Accurate Autonomous Landing of a Fixed-Wing Unmanned Aerial Vehicle

by

Frederik Nicolaas Alberts

Thesis presented in partial fulfilment of the requirements for the degree of

Master of Science in Engineering

in the Faculty of Engineering at Stellenbosch University

Supervisor:

Prof T. Jones

Department Electrical and Electronic Engineering

December 2012

Declaration

By submitting this thesis electronically, I declare that the entirety of the work contained therein is my own, original work, that I am the sole author thereof (save to the extent explicitly otherwise stated), that reproduction and publication thereof by Stellenbosch University will not infringe any third party rights and that I have not previously in its entirety or in part submitted it for obtaining any qualification.

December 2012

Abstract

This thesis presents the analysis, design, simulation and practical implementation of a control system to achieve an accurate autonomous landing of a fixed-wing unmanned aerial vehicle in the presence of wind gust atmospheric disturbances.

Controllers which incorporate the concept of direct-lift control were designed based on a study of the longitudinal dynamics of the UAV constructed as a testbed. Direct-lift control offers the prospect of an improvement in the precision with which aircraft height and vertical velocity can be controlled by utilising actuators which generate *lift* directly, instead of the conventional method whereby the *moment* produced by an actuator results in lift being indirectly generated. Two normal specific acceleration controllers were designed. The first being a conventional moment-based controller, and the second a direct-lift-augmented controller. The moment-based controller makes use of the aircraft's elevator while the direct-lift augmented controller in addition makes use of the flaps of the aircraft which serve as the direct-lift actuator.

Controllers were also designed to regulate the airspeed, altitude, climb rate, and roll angle of the aircraft as well as damp the Dutch roll mode. A guidance controller was implemented to allow for the following of waypoints. A landing procedure and methodology was developed which includes the circuit and landing approach paths and the concept of a glide path offset to calibrate the touchdown point of a landing.

All controllers and the landing procedure were tested in a hardware-in-the-loop simulation environment as well as practically in a series of flight tests. Five fully autonomous landings were performed, three of these using the conventional NSA controller, and the final two the direct-lift-augmented NSA controller.

The results obtained during the landing flight tests show that the project goal of a landing within five meters along the runway and three meters across the runway was achieved in both normal wind conditions as well as in conditions where wind gusts prevailed. The flight tests also showed that the direct-lift-augmented NSA controller appears to achieve a more accurate landing than the conventional NSA controller, especially in the presence of greater wind disturbances. The direct-lift augmented NSA controller also exhibited less pitch angle rotation during landing.

Opsomming

Hierdie tesis verteenwoordig die analise, ontwerp, simulasie en praktiese implementering van ’n beheerstelsel wat ten doel het om ’n akkurate en outonome landing van ’n onbemande vastevlerk vliegtuig in rukwind atmosferiese toestande te bewerkstellig.

Gegrond op ’n studie van die longitudinale dinamika van die vliegtuig wat as proeftuig gebruik is, is beheerders ontwerp wat die beginsel van direkte-lig insluit. Direkte-lig beheer hou die potensiaal in om die vliegtuig se hoogte en vertikale snelheid akkuraat te beheer deur gebruik te maak van aktueerders wat lig direk genereer in teenstelling met die konvensionele metode waar die moment van die aktueerder indirek lig genereer. Twee normaal-versnellings beheerders is ontwerp. Die eerste is ’n konvensionele moment-gebaseerde beheerder wat gebruik maak van die hys-aktueerder van die vliegtuig, en die tweede is ’n direkte-lig-bygestaande beheerder wat addisioneel gebruik maak van die flappe van die vliegtuig wat as die direkte-lig aktueerder dien.

Vedere beheerders is ontwerp wat die lugspoed, hoogte, klimkoers, en rolhoek van die vliegtuig reguleer asook die “Dutch roll” gedrag afklam. ’n Leiding-beheerder wat die volg van vliegbakens hanteer, is ingestel. Die landingsprosedure en -metodologie is ontwikkel wat die landingspad sowel as die sweef-pad bepaal en wat terselfdertyd ’n metode daarstel om die posisie van die landingspunt te kalibreer.

Die beheerders en landingsprosedure is in ’n hardeware-in-die-lus omgewing gesimuleer en deur middel van ’n reeks proefvlugte getoets. Vyf ten volle outonome landings is uitgevoer waarvan drie van die konvensionele normaal-versnellings beheerder gebruik gemaak het, en die laaste twee die direkte-lig-bygestaande normaal-versnellings beheerder.

Die vlugtoetsuitslae bevestig dat die navorsingsdoel om ’n landing binne vyf meter in lyn met en drie meter dwarsoor die landingstrook te bewerkstellig, behaal is. Hierdie akkuraatheid is verkry in beide goeie atmosferiese toestande sowel as toestande met rukwinde. Volgens die vlugtoetse blyk dit dat die direkte-lig-bygestaande normaal-versnellings beheerder ’n meer akkurate landing kan bewerkstellig as die konvensionele normaal-versnellings beheerder, veral dan in toestande met rukwinde. Die direkte-lig-bygestaande normaal-versnellings beheerder het ook ’n laer hei-hoek rotasie tydens die landing vertoon.

Contents

List of Figures

List of Tables

Nomenclature

Abbreviations and Acronyms

AVL	Athena Vortex Lattice
CAN	Controller Area Network
DC	Direct Current
DCM	Direction Cosine Matrix
DGPS	Differential Global Positioning System
DLC	Direct-Lift Control
GPS	Global Positioning System
HIL	Hardware-In-the-Loop
IMU	Inertial Measurement Unit
LQR	Linear Quadratic Regulator
LSA	Lateral Specific Acceleration
MIMO	Multi-Input, Multi-Output
NMP	Non-Minimum Phase
NP	Neutral Point
NSA	Normal Specific Acceleration
PC	Personal computer
OBC	On-Board Computer
RC	Remote Controlled
RF	Radio Frequency
RTK	Real Time Kinematic
SU	Stellenbosch University
UAV	Unmanned Aerial Vehicle

Vector Notation

$\mathbf{X}_C^{AB}$	Denotes vector X with data about axis system A relative to axis system B, coordinated in axis system C

Coordinate Vectors

P_x,P_y,P_z	Position vector components in the X,Y and Z axes
$\bar{V}$,α,β	Airspeed magnitude, angle of attack, angle of sideslip
ψ,θ,ϕ	Yaw, pitch and roll angles
P,Q,R	Roll, pitch and yaw rates
L,M,N	Rolling, pitching and yawing moments
X,Y,Z	Roll, pitch and yaw rates
P,Q,R	X,Y and Z-axis forces
A,B,C	Specific accelerations in the X,Y and Z-axis directions

Vectors and Matrices

DCM	Direction cosine matrix
F,**M**	Force and moment vectors
G	Gravitational acceleration vector
H	Angular momentum vector
I	Moment of inertia matrix
P,**V**,**A**	Position, velocity and acceleration vectors
S	Cross product matrix
ω	Angular rate vector

Landing Symbols

h	Altitude above touchdown point
Ψ_R	Runway heading angle
γ	Glide path angle
$WP_{x,y}$	Waypoint location

Aircraft Modelling Symbols

$\mathcal{AR}$	Aspect ratio
b	Wing span
$\bar{c}$	Mean aerodynamic chord
δ_A,δ_E,δ_F,δ_R	Aileron, elevator, flaps, rudder deflection angles
e	Oswald efficiency factor
g	Gravitational acceleration
I_x,I_y,I_z	Moments of inertia about the X,Y and Z axes
m	Mass
q	Dynamic pressure
ρ	Air density
S	Reference wing area
T_c,T	Commanded and actual thrust
$\tau_{_T}$	Engine time constant
$\bar{V}$	Airspeed magnitude
C_D	Aerodynamic drag coefficient
C_y	Aerodynamic side force coefficient
C_L	Aerodynamic lift coefficient
C_l	Aerodynamic roll moment coefficient
C_m	Aerodynamic pitch moment coefficient
C_n	Aerodynamic yaw moment coefficient

System Dynamics

ζ	Damping ratio
ω_n	Natural frequency
p	Pole location
z	Zero location

Subscripts and Superscripts

I,R,B,W,N	Inertial, runway, body, wind, and navigation axis systems
A	Aerodynamic forces and moments
G	Gravitational forces and moments
T	Engine forces and moments

Acknowledgements

I would like to thank the following people and organisations:

- Prof Thomas Jones for your support, guidance and advice throughout the project.
- Dr Iain Peddle and Mr Japie Engelbrecht, for your input and guidance during our research group meetings.
- Armscor, The Defence Research and Development Board (DRDB) and the South African Navy for providing the funding that made this project possible.
- AM de Jager, Anton Runhaar and Lionel Basson, for all your assistance during the flight tests.
- The technical staff at the EE Department, including Wessel Kroukamp and Lincoln Saunders for providing technical assistance with various aspects of the project.
- Micheal Basson for doing an excellent job as the safety pilot of the aircraft.
- All my friends in the ESL for creating a fun and enjoyable working atmosphere.
- My family for all their support and motivation during the project.
- My girlfriend, Sarah Boyd, for believing in me.

Chapter 1

Introduction

1.1 Background

The Centre of Expertise in Autonomous Systems within the Department of Electrical and Electronic Engineering at Stellenbosch University performs ongoing research in the field of autonomous systems. Active research is being conducted on topics related to the control and automation of commercial aircraft, terrestrial and underwater vehicles, and unmanned aircraft.

Previous research projects on fixed-wing unmanned aircraft focused on issues such as: Autonomous Flight of a Model Aircraft [4]; Autonomous Take-Off and Landing of a Fixed-Wing Unmanned Aerial Vehicle [5]; Autonomous Aerobatic Flight of a Fixed Wing Unmanned Aerial Vehicle [6]; Acceleration Based Manoeuvre Flight Control System for Unmanned Aerial Vehicles [2]; Die Presisie Landing van 'n Onbemande Vliegtuig "The Precision Landing of an Unmanned Aircraft" [7]; Flight Control System for a Variable Stability Blended-Wing-Body Unmanned Aerial Vehicle [8]; Aggressive Flight Control Techniques for a Fixed-Wing Unmanned Aerial Vehicle [1]; Advanced Take-off and Flight Control Algorithms for Fixed Wing Unmanned Aerial Vehicles [9]; and Fault Tolerant Adaptive Control of an Unmanned Aerial Vehicle [10].

This project is a further progression in this area of research. In particular, it is a continuation of research into the autonomous *landing* of a fixed-wing unmanned aerial vehicle (UAV). Ultimately, there is a need for a high degree of accuracy in autonomous landings under various flight conditions to expand the operational capabilities of UAV's. Landing must for example be possible in operational circumstances that necessitate the landing of a UAV on the deck of a ship or on a short or improvised runway in a land-based application. This project aims to contribute to the achievement of this goal.

Research in autonomous landings was started by [5], where the successful take-off and landing of a fixed-wing UAV was demonstrated. However, the sensors used to determine the aircraft's position limited the accuracy of the landings to the extent that a runway width of at least $20\,\mathrm{m}$ was required to guarantee a landing. In an attempt to address this

limitation, [7] successfully developed an infra-red vision-based system to improve the accuracy with which the aircraft's position, velocity and attitude states can be determined. However, no landing flight tests were conducted.

The aim of this research project is to build upon the knowledge base of the Centre of Expertise in the field of autonomous fixed-wing aircraft landings. In particular, it will endeavour to further develop the ability to accurately land a UAV even under adverse atmospheric conditions, and also demonstrate this with practical flight tests.

1.2 Overview

The successful landing of a UAV presents two challenges: the accurate control of the aircraft in the presence of atmospheric disturbances and the accurate determination of, in particular, the position and velocity states of the aircraft. In this project, the focus will be on the first part of the landing challenge: developing a control system which can achieve an accurate landing in the presence of atmospheric disturbances. Wind gusts and crosswinds are the two major atmospheric disturbances that impact on the landing. This research will be limited to addressing the disturbances caused by wind gusts.

In this thesis an advanced GPS system is used to address the challenge of accurately determining the position and velocity of the aircraft. This system is an implementation of Real Time Kinematic (RTK) differential GPS (DGPS) by the Autonomous Systems Research Group at Stellenbosch University (SU Research Group), and it is accurate to the order of a few centimeters. It involves having one GPS unit on the ground, and another on board of the aircraft. The GPS units measure and compare the phase of the satellite signals which allow the relative position of the two units to be calculated to a high degree of precision [11].

The primary goal of this thesis is to practically demonstrate an accurate autonomous landing, and the research focusses on the development of a landing control system which can achieve accurate aircraft control in the presence of atmospheric disturbances. Progress has been made in the development of aircraft controllers since those used by [5]. These enhanced controllers were developed by [2] and have been utilised practically by [1] and [8]. They function on the acceleration level of the aircraft, and will be used as the basis for the controller design in this project. The research also explores the concept of direct-lift control, which offers the prospect of an improvement in the precision with which aircraft height and vertical velocity can be controlled in the presence of wind gusts [12].

For the purpose of this project, an accurate autonomous landing is defined as achieving a landing touchdown within five meters along the runway and two meters across the runway from the intended touchdown point.

1.3 Research Outcomes

This research project requires the following milestones to be attained in order to successfully achieve an accurate autonomous landing of a fixed-wing UAV,

Aircraft:

- Construction of a UAV to serve as the testbed for the various controllers developed. This involves modifying and strengthening a model aircraft, incorporating an electric motor system as well as assembling and integrating sensors and avionics. These include,
  - Inertial Measurement Unit (IMU) providing 3-axis acceleration and rotation measurements
  - Magnetometer
  - Differential pressure sensor for calculating airspeed and pressure altitude
  - RTK DGPS system
- Calibration of all sensors and actuators.

Modelling and controllers:

- Determination of the aircraft model. This involves,
  - Determining the stability and control derivatives through the use of Athena Vortex Lattice (AVL).
  - Conducting a static thrust test of the aircraft's motor and propeller.
  - Finding the moment of inertia through the double pendulum method.
- Analysis of the dynamics of the aircraft in order to formulate a control strategy. This also involves an in-depth study of the longitudinal dynamics of the aircraft in order to design aircraft controllers which incorporate the concept of direct-lift control.
- Design of two normal specific acceleration controllers. The first being a conventional elevator-based NSA controller, and the second a direct-lift-augmented NSA controller which makes use of both the elevator and the flaps of the aircraft.
- Design of controllers to regulate the airspeed, altitude, climb rate, and roll angle of the aircraft, as well as a Dutch roll damper.
- Implementation of a guidance controller to allow for the following of waypoints.

Landing:

- Developing a landing procedure and methodology to accomplish an accurate landing. This includes the circuit and landing approach paths and the concept of a glide path offset to calibrate the touchdown point of a landing.

Simulation and flight tests:

- Implementation of all controllers and the landing procedure on an OBC.
- Testing of all controllers in a hardware-in-the-loop (HIL) simulation environment as well as practically in a series of flight tests in order to verify the controller design and the aircraft model.
- Testing of the landing procedure in a HIL simulation environment and practically in a series of flight tests.
- Conducting practical autonomous landings using the conventional NSA controller as well as the direct-lift augmented NSA controller.

1.4 Testbed

The UAV constructed to act as the testbed for this project is shown in Figure 1.1 and the details are contained in Appendix B.

Figure 1.1 – UAV photo

1.5 Thesis Outline

The description of the research conducted unfolds in six chapters as depicted in Figure 1.2.

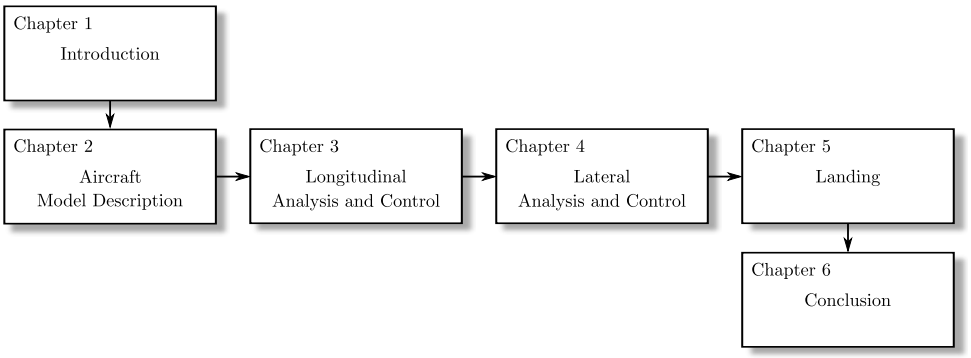

Figure 1.2 – Thesis chapter outline

Chapter 2 describes the definitions required to model the aircraft and its environment. This comprises the axis system and actuator definitions. The six degree of freedom equations of motion are then developed in such a way that they can be split into an outer- and an inner-loop model. The outer-loop model consists of the slower, aircraft independent, point mass dynamics, while the inner-loop model consists of the fast aircraft-specific dynamics. The chapter concludes by simplifying and decoupling the model such that the control systems of Chapters 3 and 4 can be designed.

Chapter 3 addresses longitudinal analysis and control. During landing, it is intuitive that the control of the aircraft occurs primarily in its longitudinal axis. Therefore, in order to land accurately, it is essential that the longitudinal motion of the aircraft is controlled accurately. The analysis of the longitudinal dynamics of the aircraft and the subsequent design of appropriate controllers focus on this prerequisite. This chapter therefore explores the concept of direct-lift control (DLC) and how it could be applied to this thesis. This is followed by the design, HIL simulation, and practical flight test results of the normal specific acceleration (NSA), climb rate, altitude and airspeed controllers.

Chapter 4 provides an analysis of the lateral dynamics of the aircraft, followed by the design, HIL simulation and practical flight test results of the roll angle controller and the Dutch roll damper. This is followed with by outline, HIL simulation and practical flight test results of the guidance controller.

The procedure followed during a landing is presented in Chapter 5. The flight and descent paths are investigated, followed by an overview of the landing state machine. The flight test results of several autonomous landings where both the conventional and the direct-lift-augmented NSA controllers were utilised are presented and analysed.

The concluding Chapter 6 presents a summary of the research, the results obtained and the contributions made by this project to the knowledgebase of the SU Research Group. Recommendations for further research are also made.

Chapter 2

Aircraft Model Description

This chapter describes the aircraft model presented by [2], the core feature of which is the ultimate design of attitude-independent inner-loop acceleration controllers. These controllers reduce the aircraft to a point mass with a steerable acceleration vector as viewed from an outer-loop guidance controller's perspective. It was demonstrated that, for normal flight conditions, the inner-loop dynamics decouple and become linear, thereby allowing for the design of inner-loop *axial*, *normal* and *lateral* specific acceleration controllers. Similar controllers have been practically implemented by [1; 8] in which certain limitations of this strategy were encountered and discussed. These limitations have been taken into account in the design of the controllers of Chapters 3 and 4. This thesis follows the same derivation of the aircraft model as that presented by [2] with the addition of a flaps actuator, the use of which is covered in the controller designs of Chapter 3.

This chapter furthermore describes the axis system and actuator definitions required to model the aircraft and its environment. The six degree of freedom equations of motion are then developed in such a way that they can be split into an outer- and an inner-loop model. The outer-loop model consists of the slower, aircraft independent, point mass dynamics, while the inner-loop model consists of the fast, aircraft-specific dynamics. The chapter concludes by simplifying and decoupling the model such that the control systems of Chapters 3 and 4 can be designed.

2.1 Axis System Definitions

Several appropriate reference frames are required to formulate the equations of motion of the aircraft. The aircraft model presented by [2] requires that the motion of the aircraft be split into the motion of a gross point mass with a superimposed rotational motion relative to the commonly used wind axis system. This requirement is met by defining a frame of reference relative to inertial space, as well as two aircraft fixed axis

systems. The motion of the aircraft is thus captured completely by the inertial reference frame and the aircraft fixed reference frames rotating relative to the inertial frame.

2.1.1 Inertial and Runway Axes

An inertial axis system needs to be defined so that the aircraft's position, velocity and attitude can be described relative to a fixed reference frame. The inertial axis system is defined as right-hand orthogonal with the horizontal plane tangential to the surface of the earth and the origin at some convenient location such as the middle of the runway. In order for Newton's law of motion to be applied, it must be assumed that the earth is flat and non-rotating. This assumption is valid in the case of this project where the flight will involve short distances and durations, and where the sensors used are incapable of registering the earth's motion [13].

For the purpose of this project a runway axis system is also defined and will be used in Chapter 5 where the aircraft landing geometry is explored. It is essentially the same as the inertial axis system, except for a rotation angle (Ψ_R) around the Z_I-axis to account for cases where the runway and inertial axes do not line up (see Figure 2.1).

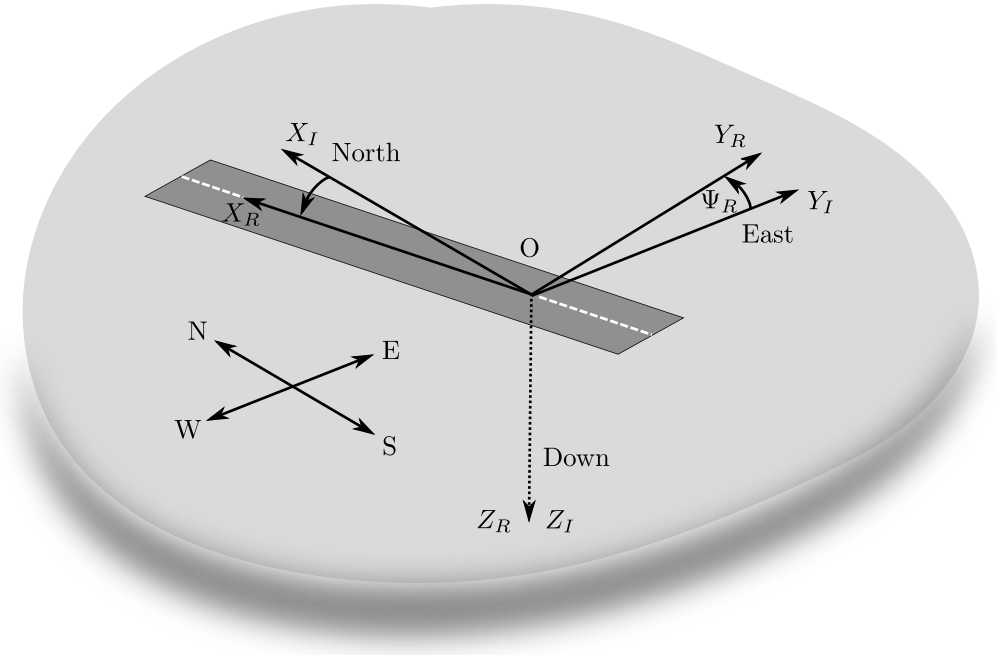

Figure 2.1 – Inertial and runway axes

2.1.2 Body Axes

The body axis system is defined as right-hand orthogonal with its origin fixed at the centre of gravity of the aircraft. The X_B-axis points towards the nose of the aircraft and is parallel to the horizontal fuselage line [13]. The Y_B-axis points out along the right wing and the Z_B-axis points down. The body axis system is depicted in Figure 2.2 along with the associated notations and positive directions for the aircraft's body axis forces and moments.

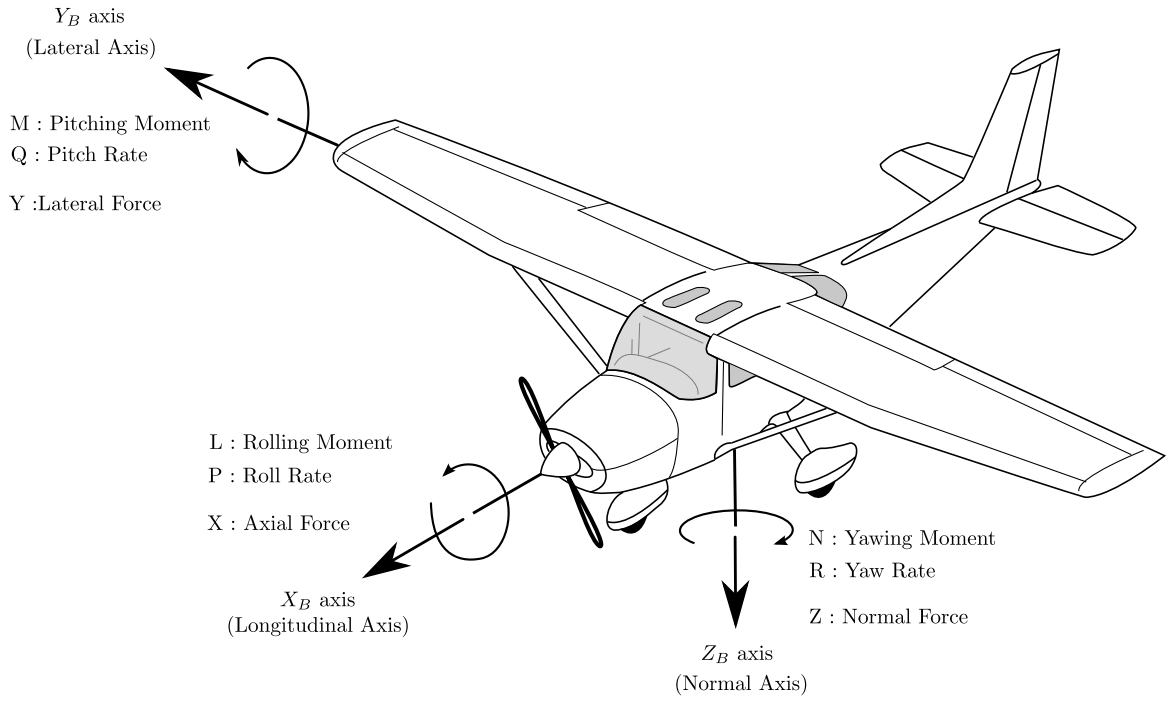

Figure 2.2 – Body axis system[1]

2.1.3 Wind and Stability Axes

Similar to the body axis system, the wind and stability axis systems are defined as right-hand orthogonal with their origins fixed at the center of gravity of the aircraft. The stability axis system is reached by rotating the body axes around the Y_B-axis through the angle of attack (α). The X_S-axis therefore points towards the direction of the oncoming free-stream velocity vector projected into the X_BZ_B-plane, whereas the Z_W-axis lies in the aircraft's plane of symmetry. The wind axis system is a further extension of the stability axis system. It is reached by rotating the stability axes around the Z_W-axis through the angle of sideslip (β). The X_W-axis therefore points towards the direction of the oncoming free-stream velocity vector. The wind and stability axis systems are illustrated in Figure 2.3.

[1] Public Domain Image adapted. Source: Wikimedia.org

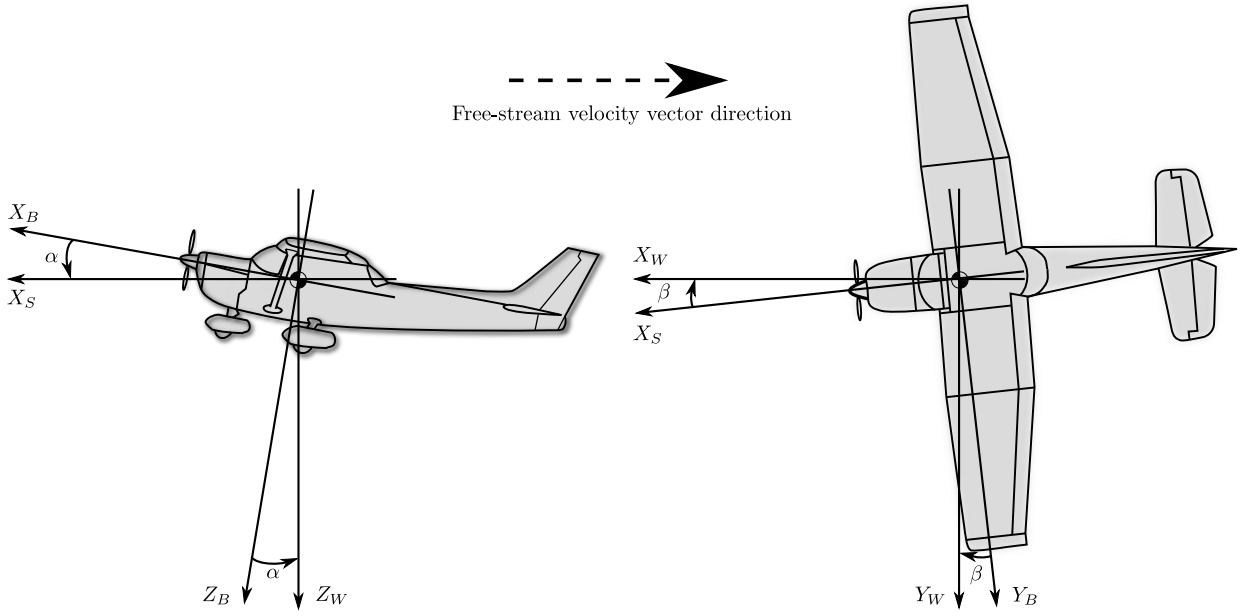

Figure 2.3 – Wind and stability axes[2]

2.1.4 Navigation Axes

Similar to the other aircraft-fixed axis systems, the navigation axis system is defined as right-hand orthogonal with its origin fixed at the centre of gravity of the aircraft. The Z_N-axis is always parallel to the Z_I-axis of the inertial axis system, and the X_N-axis remains in the aircraft's plane of symmetry. The navigation axis system is illustrated in Figure 2.4

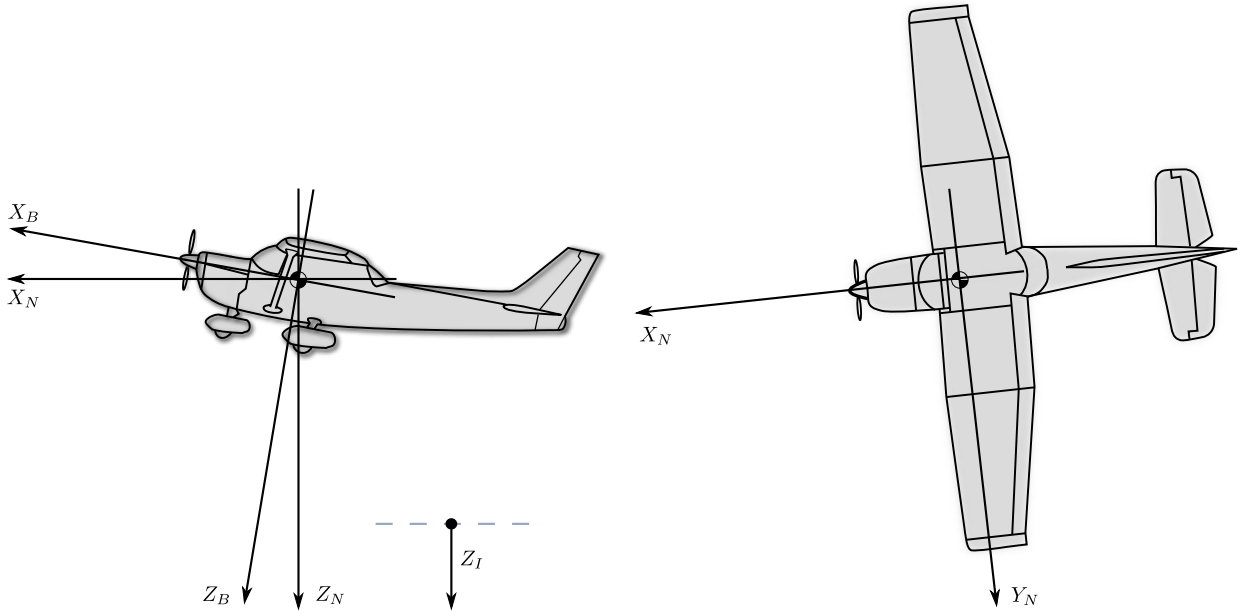

Figure 2.4 – Navigation axes[2]

[2]Public Domain Image adapted. Source: Wikimedia.org

2.2 Actuator Definitions

The aircraft used in this project is equipped with five conventional actuators. Four of these are aerodynamic actuators, namely the *elevator*, *rudder*, *aileron* and *flaps*. The final actuator is the *throttle*.

The flaps actuator is of special significance in this thesis. It is usually fairly inactive in the sense that the flaps are typically set to specific deflection angles during certain phases of flight, such as take-off or landing. The flaps of a conventional aircraft typically have a very low rate of deflection when compared to its other aerodynamic actuators. By contrast, in this project the flaps will be used *actively*. This is done to improve upon the longitudinal path following performance of the aircraft, and is explored further in Chapter 3. Using the flaps in this manner is possible due to the particular aircraft used in this project, which is equipped with flaps that can be actuated at the same rate as the other aerodynamic actuators. The flaps can also deflect upwards instead of the usual downwards-only movement.

The aerodynamic actuators are defined such that a *negative* control surface deflection creates a *positive* moment around the corresponding axis as shown in Figure 2.5. Establishing the correct deflection direction is intuitive for the elevator, aileron and rudder. However, for the flaps it is somewhat more complicated since they are located much closer to the center of gravity of the aircraft than the other aerodynamic actuators. This is investigated further in §3.2.2.

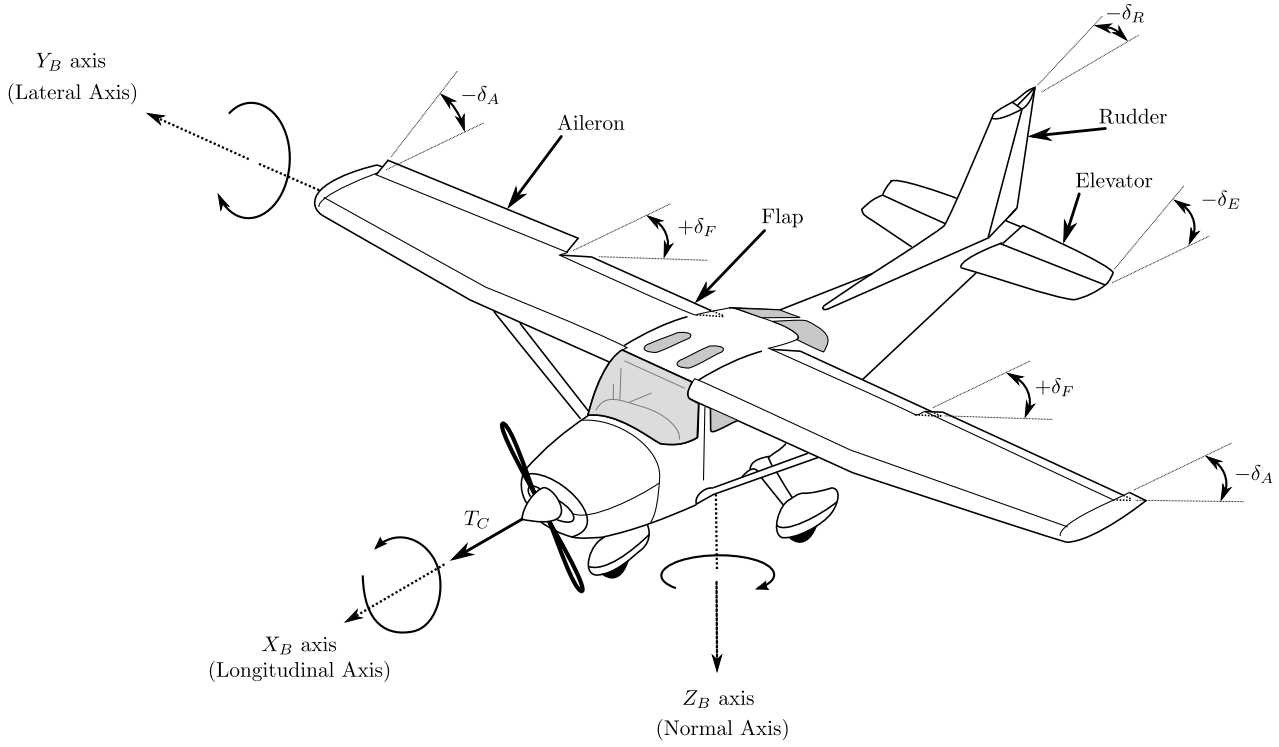

Figure 2.5 – Actuator definitions[3]

[3]Public Domain Image adapted. Source: Wikimedia.org

2.3 Six Degree of Freedom Equations of Motion

This section presents the six degree of freedom equations of motion for a rigid body in the form described by [2]. This form works on the basis that the motion of the body can be seen as the superposition of the body's slower point mass motion (kinematics) and its faster rigid body rotational motion (kinetics). The point mass motion of the body is described by the position and attitude of the wind axis system over time and the rigid body motion is described by the attitude of the body axis system with respect to the wind axis system.

A block diagram overview of the six degree of freedom equations of motion is shown in Figure 2.6. The point mass kinematics depicted on the right side of the diagram describe the gross motion of the aircraft. They are aircraft independent and are driven by the specific accelerations (A_W, B_W and C_W) as well as the roll rate (P_W). The rigid body rotational dynamics depicted on the left side of the diagram contain the aircraft-specific parameters, and therefore all of the aircraft-specific uncertainty [2]. It can be seen that the rigid body rotational dynamics describe how the various forces and moments acting on the aircraft translate into specific accelerations and roll rate. These accelerations and roll rate then propagate over time into velocity, position and attitude in the kinematic equations.

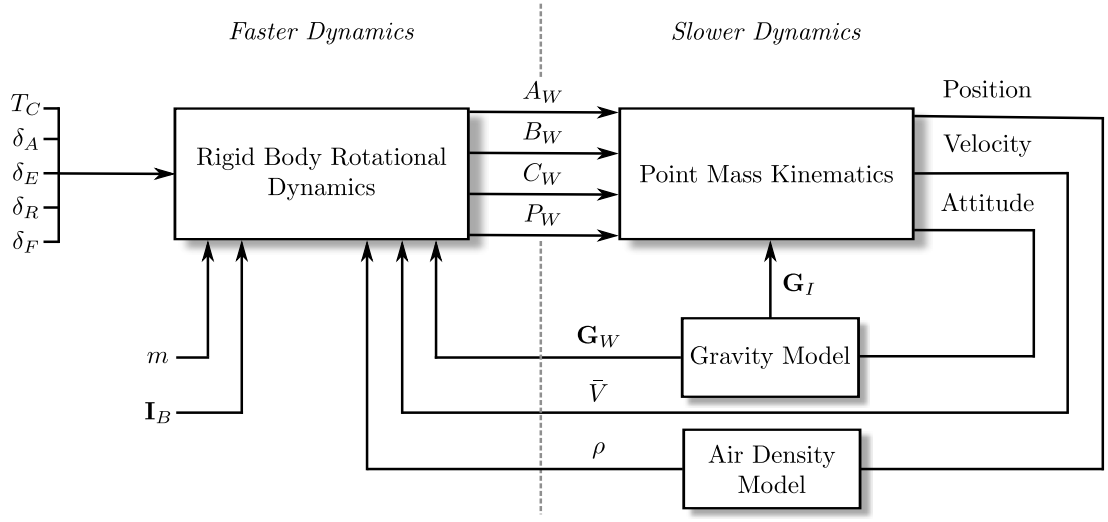

Figure 2.6 – Block diagram overview of the six degree of freedom equations of motion [2]

As demonstrated by [2], the effect of wind axis attitude parameters coupling into the rigid body rotational dynamics through the gravitational acceleration vector ($\mathbf{G}_W$) can be cancelled via dynamic inversion. It was also demonstrated that the velocity magnitude and air density feedback couplings of the point mass kinematics back into the rigid body rotational dynamics can be ignored due to the timescale separation which exists between these parameters and the rigid body rotational dynamics.

It was proposed by [2] that a set of high-bandwidth controllers be designed around the rigid body rotational dynamics which would encapsulate all of the aircraft specific uncertainty. Since these controllers operate at the acceleration and angular rate level, they would reject disturbances before they appear in the slower dynamics as error in position, velocity and attitude. In this thesis, a similar approach is followed for some of the controller designs of Chapters 3 and 4.

2.3.1 Point Mass Kinematics

Kinematics describe the motion of a rigid body, in this case the aircraft's position, velocity, acceleration and attitude, in three dimensional space. The aircraft is represented by its wind axis system which translates and rotates relative to the inertial axis system. The point mass kinematics are aircraft independent and are driven by the specific accelerations (A_W, B_W and C_W) acting on the aircraft as well as the roll rate (P_W). These inputs originate from the rigid body rotational dynamics of §2.3.2.

2.3.1.1 Point Mass Dynamics

The point mass dynamics describe the kinematic relationship which exists between the position, velocity and acceleration of the aircraft's center of mass with respect to the inertial axis system. The aircraft is represented by its wind axis system since the origin of the wind axis system coincides with the aircraft's center of mass. It is assumed that the aircraft is a rigid body with a fixed center of mass. The kinematic relationship can therefore be written as,

$$\left.\frac{\mathrm{d}}{\mathrm{d}t}\mathbf{P}^{WI}\right|_I = \mathbf{V}^{WI} \tag{2.3.1}$$

and,

$$\left.\frac{\mathrm{d}}{\mathrm{d}t}\mathbf{V}^{WI}\right|_I = \mathbf{A}^{WI} \tag{2.3.2}$$

where $\mathbf{P}^{WI}$, $\mathbf{V}^{WI}$ and $\mathbf{A}^{WI}$, are the position, velocity and acceleration vectors of the wind axis system with respect to the inertial axis system. If it is assumed that the aircraft's mass remains constant, then by Newton's second law, the applied resultant force vector ($\mathbf{F}$) can be written as,

$$\mathbf{F} = m\mathbf{A}^{WI} \tag{2.3.3}$$

Substituting the equation above into Equation 2.3.2 yields,

$$\left.\frac{\mathrm{d}}{\mathrm{d}t}\mathbf{V}^{WI}\right|_I = \frac{1}{m}\mathbf{F} \tag{2.3.4}$$

For the control architecture presented by [2] it is more intuitive to work with a velocity magnitude and the attitude of the wind axis system when describing the velocity vector.

The inertially coordinated derivative of the velocity vector of Equation 2.3.2 is now converted into a derivative with respect to wind axes by making use of Equation A.1.1 and substituting in Equation 2.3.4,

$$\frac{\mathrm{d}}{\mathrm{d}t}\mathbf{V}^{WI}\bigg|_{W} = -\omega^{WI} \times \mathbf{V}^{WI} + \frac{1}{m}\mathbf{F}_{W} \tag{2.3.5}$$

where ω^{WI} is the angular velocity of the wind axis system with respect to the inertial axis system. The above equation is now rewritten in matrix format with all terms coordinated in the wind axis system. The cross product can be simplified by making use of Equation A.2.2,

$$\begin{bmatrix} \dot{\bar{V}} \\ 0 \\ 0 \end{bmatrix} = \begin{bmatrix} 0 & -R_W & Q_W \\ R_W & 0 & -P_W \\ -Q_W & P_W & 0 \end{bmatrix} \begin{bmatrix} \bar{V} \\ 0 \\ 0 \end{bmatrix} + \frac{1}{m} \begin{bmatrix} X_W \\ Y_W \\ Z_W \end{bmatrix} \tag{2.3.6}$$

where $\bar{V}$ is the magnitude of the aircraft's velocity vector, X_W, Y_W and Z_W are the components of the force vector applied to the aircraft, and P_W, Q_W and R_W are the roll, pitch and yaw rates of the wind axis system with respect to the inertial axis system. The equation above can be split into the dynamic equation for the velocity magnitude in wind axes,

$$\dot{\bar{V}} = \frac{1}{m} X_W \tag{2.3.7}$$

and two algebraic constraint equations,

$$\begin{bmatrix} R_W \\ Q_W \end{bmatrix} = \frac{1}{m\bar{V}} \begin{bmatrix} Y_W \\ -Z_W \end{bmatrix} \tag{2.3.8}$$

The velocity dynamics of Equation 2.3.5 are coordinated in the wind axis system. In order to arrive at the position dynamics, the velocity vector must therefore be transformed back to the inertial axis system. This is accomplished by making use of the direction cosine matrix (DCM) defined in Equation A.3.5. The position dynamics of Equation 2.3.1 are rewritten as,

$$\dot{\mathbf{P}}_I^{WI} = \left[\mathbf{DCM}^{WI}\right]^{\mathsf{T}} \mathbf{V}_W^{WI} \tag{2.3.9}$$

After simplification, the position dynamics become,

$$\begin{bmatrix} \dot{P}_x \\ \dot{P}_y \\ \dot{P}_z \end{bmatrix} = \begin{bmatrix} \cos(\psi_W)\cos(\theta_W) \\ \sin(\psi_W)\cos(\theta_W) \\ -\sin(\theta_W) \end{bmatrix} \bar{V} \tag{2.3.10}$$

where P_x, P_y and P_z are the position coordinates of the wind axis system in inertial space, also often denoted as N (north), E (east) and D (down), and ψ_W and θ_W are the yaw and pitch angles of the wind axis system with respect to the inertial axis system.

2.3.1.2 Attitude and Attitude Dynamics

Attitude Amongst the various methods available for describing the attitude of one axis system relative to another, Euler angles are chosen for their simplicity and intuitive nature. Euler angles have a disadvantage over other methods such as Quaternions in the sense that they exhibit a singularity under certain orientations [14]. However, by selecting the appropriate Euler angle sequence, the singularity can be positioned such that it will never be encountered during conventional flight. To this end, the Euler 3-2-1 angle sequence will be used.

Euler angles use three angles and a specific order of rotation to describe the attitude of the wind axis system with respect to the inertial axis system. The two axis systems are initially aligned. The wind axis system is then rotated positively about the Z_W-axis through the yaw angle (ψ), followed by a positive rotation about the Y_W-axis through the pitch angle (θ), and finally a positive rotation about the X_W-axis through the roll angle (ϕ).

Attitude Dynamics The following dynamic equation describes the relation between the angular rates of the wind axis system, and the time derivatives of the Euler angles which represent the attitude of the wind axis system with respect to the inertial axis system [2],

$$\begin{bmatrix} \dot{\phi} \\ \dot{\theta} \\ \dot{\psi} \end{bmatrix}_{(321)} = \begin{bmatrix} 1 & \sin\phi\tan\theta & \cos\phi\tan\theta \\ 0 & \cos\phi & -\sin\phi \\ 0 & \sin\phi\sec\theta & \cos\phi\sec\theta \end{bmatrix}_{(321)} \begin{bmatrix} P_W \\ Q_W \\ R_W \end{bmatrix} \qquad |\theta| \neq \frac{\pi}{2} \tag{2.3.11}$$

where the subscript (321) denotes the Euler 3-2-1 angle sequence, and P_W, Q_W and R_W are the roll, pitch and yaw rates of the wind axis system. It can be seen that the Euler 3-2-1 sequence exhibits a singularity at such a large pitch angle that it will not be encountered during conventional flight.

2.3.2 Kinetics

Kinetics describe how the various forces and moments acting on a body translate into linear and angular accelerations. These accelerations then propagate over time into velocity, position and attitude in the kinematic equations of §2.3.1.

2.3.2.1 Rigid Body Rotational Dynamics

The rigid body rotational dynamics of the aircraft describe the rotational motion of the body axis system relative to the wind axis system as a result of the moments applied to the aircraft. These dynamics together with the point mass dynamics of §2.3.1.1 then completely describe the six degree of freedom motion of the aircraft.

The kinetic relationship between an applied external moment ($\mathbf{M}$) and the aircraft's angular momentum ($\mathbf{H}$) is given by [15],

$$\mathbf{M} = \frac{\mathrm{d}}{\mathrm{d}t}\mathbf{H}\bigg|_I \tag{2.3.12}$$

where,

$$\mathbf{H} = \int_v \mathbf{r}^{dmB} \times \left(\omega^{BI} \times \mathbf{r}^{dmB}\right) \mathrm{d}m \tag{2.3.13}$$

where $\mathbf{r}^{dmB}$ is the position vector of a mass element $\mathrm{d}m$ relative to the center of mass of the rigid body with volume v, and ω^{BI} is the angular velocity of the body axis system with respect to the inertial axis system.

As argued by [2], the angular momentum vector takes on its simplest form when coordinated in body axes. Because the aircraft is regarded as a rigid body, the moment arm to all mass elements will remain fixed and independent of other translation or rotation motion variables. By making use of Equation A.1.1, Equation 2.3.12 can be rewritten as,

$$\mathbf{M} = \frac{\mathrm{d}}{\mathrm{d}t}\mathbf{H}\bigg|_B + \omega^{BI} \times \mathbf{H} \tag{2.3.14}$$

Combining Equation 2.3.13 and Equation 2.3.14 and rearranging as shown by [2], the dynamics of the body axis system angular velocity with respect to the inertial axis system can be found,

$$\dot{\omega}_B^{BI} = \mathbf{I}_B^{-1}\left(\mathbf{M}_B - \mathbf{S}_{\omega_B^{BI}}\mathbf{I}_B\omega_B^{BI}\right) \tag{2.3.15}$$

where $\mathbf{I}_B$ is the moment of inertia matrix referenced in body axes as shown in Equation A.4.2, and $\mathbf{S}_{\omega_B^{BI}}$ implements the cross product as given by Equation A.2.2.

The orientation of the wind axis system relative to the body axis system is defined by two rotations as shown in §2.1.3. The first is a negative rotation around the Y_B-axis through the angle of attack (α), followed by a positive rotation around the new Z_W-axis (see Figure 2.3) through the angle of sideslip (β). The angular velocity vector of the wind axis system with respect to the body axis system can therefore be written as the sum of the angular rates ($\dot{\alpha}$ and $\dot{\beta}$) about their respective unit vectors,

$$\omega^{WB} = -\dot{\alpha}\mathbf{j}^B + \dot{\beta}\mathbf{k}^W \tag{2.3.16}$$

The angular velocity of the wind axis system with respect to the inertial axis system (ω^{WI}) can be thought of as the sum of the angular velocity of the body axis system with respect to the inertial axis system (ω^{BI}) and the angular velocity of the wind axis system with respect to the body axis system (ω^{WB}),

$$\omega^{WI} = \omega^{BI} + \omega^{WB} \tag{2.3.17}$$

Substituting Equation 2.3.16 into Equation 2.3.17 and analysing in the body axis system gives,

$$\omega_B^{BI} = \dot{\alpha}\mathbf{j}_B^B - \dot{\beta}\mathbf{k}_B^W + \omega_B^{WI} \tag{2.3.18}$$

This equation can be rewritten by making use of the DCM of Equation A.3.3 to convert the vectors to the desired axis systems,

$$\omega_B^{BI} = \dot{\alpha}\mathbf{j}_B^B - \dot{\beta}\mathbf{DCM}^{BW}\mathbf{k}_W^W + \mathbf{DCM}^{BW}\omega_W^{WI} \tag{2.3.19}$$

Expanding and rearranging the equation above yields,

$$\begin{bmatrix} P \\ Q \\ R \end{bmatrix} = \begin{bmatrix} 0 & \sin\alpha \\ 1 & 0 \\ 0 & -\cos\alpha \end{bmatrix} \begin{bmatrix} \dot{\alpha} \\ \dot{\beta} \end{bmatrix} + \begin{bmatrix} \cos\alpha\cos\beta & -\cos\alpha\sin\beta & -\sin\alpha \\ \sin\beta & \cos\beta & 0 \\ \sin\alpha\cos\beta & -\sin\alpha\sin\beta & \cos\alpha \end{bmatrix} \begin{bmatrix} P_W \\ Q_W \\ R_W \end{bmatrix} \tag{2.3.20}$$

where P, Q and R are the roll, pitch and yaw rates of the body axis system, respectively, with respect to the inertial axis system. The equations are now rearranged so as to make $\dot{\alpha}$, $\dot{\beta}$ and P_W the subject of the formula, while the two algebraic constraints from Equation 2.3.8 (for Q_W and R_W) are substituted in. The resultant equation is combined with the angular velocity dynamics of Equation 2.3.15 to form the complete rigid body rotational dynamics,

$$\begin{bmatrix} \dot{\alpha} \\ \dot{\beta} \end{bmatrix} = \begin{bmatrix} -\cos\alpha\tan\beta & 1 & -\sin\alpha\tan\beta \\ \sin\alpha & 0 & -\cos\alpha \end{bmatrix} \begin{bmatrix} P \\ Q \\ R \end{bmatrix} + \frac{1}{m\bar{V}} \begin{bmatrix} \sec\beta & 0 \\ 0 & 1 \end{bmatrix} \begin{bmatrix} Z_W \\ Y_W \end{bmatrix} \tag{2.3.21}$$

$$\begin{bmatrix} \dot{P} \\ \dot{Q} \\ \dot{R} \end{bmatrix} = \mathbf{I}_B^{-1} \left(\begin{bmatrix} L \\ M \\ N \end{bmatrix} - \begin{bmatrix} 0 & -R & Q \\ R & 0 & -P \\ -Q & P & 0 \end{bmatrix} \mathbf{I}_B \begin{bmatrix} P \\ Q \\ R \end{bmatrix} \right) \tag{2.3.22}$$

with constraint,

$$\begin{bmatrix} P_W \end{bmatrix} = \begin{bmatrix} \cos\alpha\sec\beta & 0 & \sin\alpha\sec\beta \end{bmatrix} \begin{bmatrix} P \\ Q \\ R \end{bmatrix} + \frac{1}{m\bar{V}} \begin{bmatrix} -\tan\beta & 0 \end{bmatrix} \begin{bmatrix} Z_W \\ Y_W \end{bmatrix} \tag{2.3.23}$$

The rigid body rotational dynamics above maintain the attitude of the body axis system with respect to the wind axis system over time (α and β), as a function of the components of the applied moment vector in the body axis system (L, M, N) and the lateral and normal force vector coordinates in wind axes (Y_W and Z_W).

2.3.3 Forces and Moments

The forces and moments acting on the aircraft encompass all of the aerodynamic, thrust and gravitational effects on the aircraft. The sum of the different forces and moments acting on the aircraft result in linear and angular accelerations which propagate into velocity, position and attitude over time through the rigid body rotational dynamics and point mass kinematics of §2.3.1.1 and §2.3.2.1.

The equations of motion derived in §2.3.1.1 and §2.3.2.1 require the force vector coordinated in the wind axis system and the moment vector coordinated in body axis system. The total forces and moments acting on the aircraft can therefore be written as,

$$\mathbf{F}_W = \mathbf{F}^A + \mathbf{F}^T + \mathbf{F}^G \tag{2.3.24}$$

$$\mathbf{M}_B = \mathbf{M}^A + \mathbf{M}^T + \mathbf{M}^G \tag{2.3.25}$$

where $\mathbf{F}_W$ is the total force vector coordinated in the wind axis system, $\mathbf{M}_B$ is the total moment vector coordinated in the body axis system and the superscripts A, T and G denote the aerodynamic, thrust and gravitational components of the force and moment vectors.

2.3.3.1 Aerodynamic Forces and Moments

The aerodynamic forces and moments are those created due to the movement of air across the aircraft's various surfaces. These forces and moments are modelled in the wind axis system [14],

$$\begin{bmatrix} X_W^A \\ Y_W^A \\ Z_W^A \end{bmatrix} = qS \begin{bmatrix} -C_D \\ C_y \\ -C_L \end{bmatrix} \tag{2.3.26}$$

$$\begin{bmatrix} L_W^A \\ M_W^A \\ N_W^A \end{bmatrix} = qS \begin{bmatrix} b & 0 & 0 \\ 0 & \bar{c} & 0 \\ 0 & 0 & b \end{bmatrix} \begin{bmatrix} C_l \\ C_m \\ C_n \end{bmatrix} \tag{2.3.27}$$

where,

$$q = \frac{1}{2}\rho \bar{V}^2 \tag{2.3.28}$$

Here, q is the dynamic pressure, S the wing area, b the wing span, $\bar{c}$ the mean aerodynamic chord, ρ the air density and $\bar{V}$ the airspeed magnitude. The dimensionless coefficients C_D, C_y and C_L are the drag, lift and side-force coefficients, respectively, with C_l , C_m and C_n the dimensionless roll, pitch and yaw moment coefficients, respectively. It follows from the equations above that the aerodynamic forces and moments are proportional to the dynamic pressure, which in turn is a function of the air density and the airspeed magnitude. The aerodynamic forces are the product of dynamic pressure, wing area and the dimensionless force coefficients. Similarly, the aerodynamic moments are products of dynamic pressure, wing area, the dimensionless moment coefficients, as well as a moment arm. This moment arm is the mean aerodynamic chord in the case of the pitching moment, and the wing span in the case of the roll and yaw moments.

The equations of motion derived in §2.3.2.1 require the moment vector to be coordinated in the body axis system. Transforming the aerodynamic moment vector from the wind axis system to the body axis system can be accomplished by making use of the DCM of

Equation A.3.3,

$$\begin{bmatrix} L^A \\ M^A \\ N^A \end{bmatrix} = \left[\mathbf{DCM}^{BW}\right] \begin{bmatrix} L_W^A \\ M_W^A \\ N_W^A \end{bmatrix} \tag{2.3.29}$$

where L^A, M^A and N^A are the aerodynamic moment vector coordinates in the body axis system.

The dimensionless aerodynamic force and moment coefficients are defined by using dimensionless stability and control derivatives. The stability and control derivatives describe a change in a force or moment due to a change in a normalised motion variable or actuator deflection. The aerodynamic force and moment coefficients can therefore be defined as the sum of the various aircraft motion variables and actuator deflections as given in [16],

$$C_D = C_{D_0} + \frac{C_L^2}{\pi \mathit{A}\!\mathit{R} e} \tag{2.3.30}$$

$$\begin{bmatrix} C_y \\ C_L \end{bmatrix} = \begin{bmatrix} 0 \\ C_{L_0} \end{bmatrix} + \begin{bmatrix} 0 & C_{y_\beta} & \frac{b}{2\bar{V}_a} C_{y_P} & 0 & \frac{b}{2\bar{V}_a} C_{y_R} \\ C_{L_\alpha} & 0 & 0 & \frac{\bar{c}}{2\bar{V}_a} C_{L_Q} & 0 \end{bmatrix} \begin{bmatrix} \alpha \\ \beta \\ P \\ Q \\ R \end{bmatrix} + \begin{bmatrix} C_{y_{\delta_A}} & 0 & C_{y_{\delta_R}} & 0 \\ 0 & C_{L_{\delta_E}} & 0 & C_{L_{\delta_F}} \end{bmatrix} \begin{bmatrix} \delta_A \\ \delta_E \\ \delta_R \\ \delta_F \end{bmatrix} \tag{2.3.31}$$

$$\begin{bmatrix} C_l \\ C_m \\ C_n \end{bmatrix} = \begin{bmatrix} 0 \\ C_{m_0} \\ 0 \end{bmatrix} + \begin{bmatrix} 0 & C_{l_\beta} & \frac{b}{2\bar{V}_a} C_{l_P} & 0 & \frac{b}{2\bar{V}_a} C_{l_R} \\ C_{m_\alpha} & 0 & 0 & \frac{\bar{c}}{2\bar{V}_a} C_{m_Q} & 0 \\ 0 & C_{n_\beta} & \frac{b}{2\bar{V}_a} C_{n_P} & 0 & \frac{b}{2\bar{V}_a} C_{n_R} \end{bmatrix} \begin{bmatrix} \alpha \\ \beta \\ P \\ Q \\ R \end{bmatrix} + \begin{bmatrix} C_{l_{\delta_A}} & 0 & C_{l_{\delta_R}} & 0 \\ 0 & C_{m_{\delta_E}} & 0 & C_{m_{\delta_F}} \\ C_{n_{\delta_A}} & 0 & C_{n_{\delta_R}} & 0 \end{bmatrix} \begin{bmatrix} \delta_A \\ \delta_E \\ \delta_R \\ \delta_F \end{bmatrix} \tag{2.3.32}$$

where e is the Oswald efficiency factor, $\mathit{A}\!\mathit{R}$ is the aspect ratio of the wing, C_{L_0} is the static lift coefficient and C_{m_0} is the static moment coefficient. The following notation is used for the non-dimensional stability and control derivatives,

$$C_{\mathcal{A}_\mathcal{B}} = \frac{\partial C_\mathcal{A}}{\partial \mathcal{B}'} \tag{2.3.33}$$

with,

$$\mathcal{B}' = n\mathcal{B} \tag{2.3.34}$$

where n is the applicable normalising coefficient of $\mathcal{B}$. The normalising coefficient for incident and control deflection angles is unity, for the pitch rate it is $\frac{\bar{c}}{2V}$ and for the roll and yaw angles it is $\frac{b}{2V}$.

To arrive at the model above, it is assumed that the added mass effects [14] as well as the effects of downwash lag [17] of the main wing on the horizontal tail are negligible for control design purposes. It is also assumed that the aircraft will fly at small incidence angles, therefore the stability and control derivatives are considered to be independent of the rigid body rotational dynamics.

The stability and control derivatives specific to the aircraft used in this project were obtained by modelling the aircraft in the vortex lattice program *Athena Vortex Lattice* (AVL), the results of which are given in Appendix B.6.3.

2.3.3.2 Thrust Model

The aircraft used in this project is equipped with a brushless DC electrical motor and propeller (see Appendix B.1.1). This propulsion source can be modelled by a simple first order lag (low pass filter) from thrust command to thrust output [8]. This accounts for the significantly band-limited response of most propulsion sources. The dynamic effect of airspeed on the thrust output is ignored since its effect is often negligible for control purposes [2]. The thrust model is therefore given as,

$$\dot{T} = -\frac{1}{\tau_{_T}} T + \frac{1}{\tau_{_T}} T_c \tag{2.3.35}$$

where T is the thrust in Newton, T_c is the thrust command and $\tau_{_T}$ is the time constant of the thrust dynamics. The time constant $\tau_{_T}$ is determined experimentally by commanding a step of the aircraft's throttle and then analysing the resulting thrust [1].

The motor of the aircraft used in this project is mounted such that the thrust vector acts through the center of mass and along the X_B-axis. Therefore, the motor creates a force along the X_B-axis equal to the thrust output, while all other thrust forces and moments are zero,

$$\begin{bmatrix} X^T \\ Y^T \\ Z^T \end{bmatrix} = \begin{bmatrix} T \\ 0 \\ 0 \end{bmatrix} \tag{2.3.36}$$

$$\begin{bmatrix} L^T \\ M^T \\ N^T \end{bmatrix} = \begin{bmatrix} 0 \\ 0 \\ 0 \end{bmatrix} \tag{2.3.37}$$

The equations of motion derived in §2.3.1.1 and §2.3.2.1 require the force vector coordinated in the wind axis system, therefore the body axis thrust vector is coordinated into

the wind axis system as follows,

$$\begin{bmatrix} X_W^T \\ Y_W^T \\ Z_W^T \end{bmatrix} = \begin{bmatrix} \cos\alpha\cos\beta \\ -\cos\alpha\sin\beta \\ -\sin\alpha \end{bmatrix} T \tag{2.3.38}$$

2.3.3.3 Gravitational Forces and Moments

The gravitational field is assumed to be uniform and acting in the direction of the Z_I-axis of the inertial axis system,

$$\begin{bmatrix} X_I^G \\ Y_I^G \\ Z_I^G \end{bmatrix} = \begin{bmatrix} 0 \\ 0 \\ mg \end{bmatrix} \tag{2.3.39}$$

where g is the gravitational force per unit mass (m). The moments produced by the gravitational force are all zero since it acts through the center of mass of the aircraft.

The equations of motion derived in §2.3.1.1 and §2.3.2.1 require the force vector coordinated in the wind axis system, therefore the inertial axis system gravitational vector is coordinated into the wind axis system by means of the DCM of Equation A.3.5,

$$\begin{bmatrix} X_W^G \\ Y_W^G \\ Z_W^G \end{bmatrix} = \left[\mathbf{DCM}^{WI}\right] \begin{bmatrix} 0 \\ 0 \\ mg \end{bmatrix} \tag{2.3.40}$$

2.4 Simplifying and Decoupling the Model

According to [2] the rigid body rotational dynamics of §2.3.2.1 can be simplified by ignoring the inertial cross coupling terms of Equation 2.3.22. These cross coupling terms are negligible during normal flight where the very high angular velocities required to see the effect of the cross coupling terms are not encountered. The rigid body rotational dynamics of Equations 2.3.21 and 2.3.22 therefore become,

$$\begin{bmatrix} \dot\alpha \\ \dot\beta \end{bmatrix} = \begin{bmatrix} -\cos\alpha\tan\beta & 1 & -\sin\alpha\tan\beta \\ \sin\alpha & 0 & -\cos\alpha \end{bmatrix} \begin{bmatrix} P \\ Q \\ R \end{bmatrix} + \frac{1}{m\bar V} \begin{bmatrix} \sec\beta & 0 \\ 0 & 1 \end{bmatrix} \begin{bmatrix} Z_W \\ Y_W \end{bmatrix} \tag{2.4.1}$$

$$\begin{bmatrix} \dot P \\ \dot Q \\ \dot R \end{bmatrix} = \begin{bmatrix} \frac{1}{I_x} & 0 & 0 \\ 0 & \frac{1}{I_y} & 0 \\ 0 & 0 & \frac{1}{I_z} \end{bmatrix} \begin{bmatrix} L \\ M \\ N \end{bmatrix} \tag{2.4.2}$$

The aerodynamic, thrust and gravitational forces and moments of §2.3.3 are now summed according to Equations 2.3.24 and 2.3.25 and become,

$$\begin{bmatrix} X_W \\ Y_W \\ Z_W \end{bmatrix} = qS \begin{bmatrix} -C_D \\ C_y \\ -C_L \end{bmatrix} + \begin{bmatrix} \cos\alpha\cos\beta \\ -\cos\alpha\sin\beta \\ -\sin\alpha \end{bmatrix} T + \begin{bmatrix} -\sin\theta \\ \cos\theta\sin\phi \\ \cos\theta\cos\phi \end{bmatrix} mg \tag{2.4.3}$$

$$\begin{bmatrix} L \\ M \\ N \end{bmatrix} = \left[\mathbf{DCM}^{BW}\right] qS \begin{bmatrix} b & 0 & 0 \\ 0 & \bar{c} & 0 \\ 0 & 0 & b \end{bmatrix} \begin{bmatrix} C_l \\ C_m \\ C_n \end{bmatrix} \tag{2.4.4}$$

The dimensionless aerodynamic force and moment coefficients of Equations 2.3.30 to 2.3.32 are now substituted into the equations above, and the result is in turn substituted into the simplified rigid body rotational dynamics of Equations 2.4.1 and 2.4.2. The assumption is made that the wind axis system moments can be used without conversion to the body axis system since, for small incidence angles, the inaccuracy added by the assumption is far less than the inherent uncertainty in the aerodynamic model [2]. These steps yield,

$$\begin{bmatrix} \dot{\alpha} \\ \dot{Q} \\ \dot{\beta} \\ \dot{P} \\ \dot{R} \end{bmatrix} = \begin{bmatrix} -\frac{1}{mV}\sec\beta\bar{L}_\alpha & 1-\frac{1}{mV}\sec\beta\bar{L}_Q & 0 & -\cos\alpha\tan\beta & -\sin\alpha\tan\beta \\ \frac{1}{I_y}M_\alpha & \frac{1}{I_y}M_Q & 0 & 0 & 0 \\ 0 & 0 & \frac{1}{mV}\bar{Y}_\beta & \sin\alpha+\frac{1}{mV}\bar{Y}_P & -\cos\alpha+\frac{1}{mV}\bar{Y}_R \\ 0 & 0 & \frac{1}{I_x}L_\beta & \frac{1}{I_x}L_P & \frac{1}{I_x}L_R \\ 0 & 0 & \frac{1}{I_z}N_\beta & \frac{1}{I_z}N_P & \frac{1}{I_z}N_R \end{bmatrix} \begin{bmatrix} \alpha \\ Q \\ \beta \\ P \\ R \end{bmatrix}$$
$$+ \begin{bmatrix} -\frac{1}{mV}\sec\beta\sin\alpha & -\frac{1}{mV}\sec\beta\bar{L}_{\delta_E} & 0 & 0 & -\frac{1}{mV}\sec\beta\bar{L}_{\delta_F} \\ 0 & \frac{1}{I_y}M_{\delta_E} & 0 & 0 & \frac{1}{I_y}M_{\delta_F} \\ -\frac{1}{mV}\cos\alpha\sin\beta & 0 & \frac{1}{mV}\bar{Y}_{\delta_A} & \frac{1}{mV}\bar{Y}_{\delta_R} & 0 \\ 0 & 0 & \frac{1}{I_x}L_{\delta_A} & \frac{1}{I_x}L_{\delta_R} & 0 \\ 0 & 0 & \frac{1}{I_z}N_{\delta_A} & \frac{1}{I_z}N_{\delta_R} & 0 \end{bmatrix} \begin{bmatrix} T \\ \delta_E \\ \delta_A \\ \delta_R \\ \delta_F \end{bmatrix}$$
$$+ \begin{bmatrix} -\frac{1}{mV}\sec\beta qSC_{L_0} + \frac{1}{mV}\sec\beta\cos\theta\cos\phi mg \\ \frac{1}{I_y}qS\bar{c}C_{m_0} \\ \frac{1}{mV}\cos\theta\sin\phi mg \\ 0 \\ 0 \end{bmatrix} \tag{2.4.5}$$

where use has been made of the dimensional derivative notation as outlined in Appendix B.6.4 in order to simplify the representation of the equation. Several assumptions are now made to further simplify and decouple the model [2]:

a) The standard trigonometric small angle assumptions are made with regard to the two incidence angles α and β. The assumption is also made that the product of small angles is negligible (see Appendix A.5).

b) It is assumed that during normal flight, the angle of sideslip is negligibly small as long as the control system enforces coordinated turns. Therefore, in the dynamic equation

for the angle of attack, the angle of sideslip is regarded as zero, thereby ignoring the nonlinear couplings to the roll and yaw rates.

c) The zero angle of attack lift and pitching moment coefficients C_{L_0} and C_{m_0} are removed from the model under the assumption that the controllers will remove any steady state errors caused by their omission.

d) The coupling of the thrust into the normal and lateral dynamics is ignored. This assumption is made on the basis of the large timescale separation which exists between the throttle dynamics, and the normal and lateral dynamics.

Taking into account these simplifications, the aircraft's dynamics can be decoupled into axial, normal and lateral dynamics,

Axial

$$\dot{T} = \left[-\frac{1}{\tau_T}\right] T + \left[\frac{1}{\tau_T}\right] T_C \tag{2.4.6}$$

$$A_W = \left[\frac{1}{m}\right] T + \left[-\frac{qS}{m} C_D\right] - g\sin\theta \tag{2.4.7}$$

Normal

$$\begin{bmatrix}\dot{\alpha}\\ \dot{Q}\end{bmatrix} = \begin{bmatrix} -\frac{1}{m\bar{V}}\bar{L}_\alpha & 1-\frac{1}{m\bar{V}}\bar{L}_Q \\ \frac{1}{I_y}M_\alpha & \frac{1}{I_y}M_Q\end{bmatrix}\begin{bmatrix}\alpha\\ Q\end{bmatrix} + \begin{bmatrix} -\frac{1}{m\bar{V}}\bar{L}_{\delta_E} & -\frac{1}{m\bar{V}}\bar{L}_{\delta_F} \\ \frac{1}{I_y}M_{\delta_E} & \frac{1}{I_y}M_{\delta_F}\end{bmatrix}\begin{bmatrix}\delta_E\\ \delta_F\end{bmatrix} + \begin{bmatrix}\frac{g}{\bar{V}}\cos\theta\cos\phi\\ 0\end{bmatrix} \tag{2.4.8}$$

$$\begin{bmatrix}C_W\end{bmatrix} = \begin{bmatrix} -\frac{1}{m}\bar{L}_\alpha & -\frac{1}{m}\bar{L}_Q\end{bmatrix}\begin{bmatrix}\alpha\\ Q\end{bmatrix} + \begin{bmatrix} -\frac{1}{m}\bar{L}_{\delta_E} & -\frac{1}{m}\bar{L}_{\delta_F}\end{bmatrix}\begin{bmatrix}\delta_E\\ \delta_F\end{bmatrix} \tag{2.4.9}$$

Lateral

$$\begin{bmatrix}\dot{\beta}\\ \dot{P}\\ \dot{R}\end{bmatrix} = \begin{bmatrix} \frac{1}{m\bar{V}}\bar{Y}_\beta & \frac{1}{m\bar{V}}\bar{Y}_P & -1+\frac{1}{m\bar{V}}\bar{Y}_R \\ \frac{1}{I_x}L_\beta & \frac{1}{I_x}L_P & \frac{1}{I_x}L_R \\ \frac{1}{I_z}N_\beta & \frac{1}{I_z}N_P & \frac{1}{I_z}N_R\end{bmatrix}\begin{bmatrix}\beta\\ P\\ R\end{bmatrix} + \begin{bmatrix} \frac{1}{m\bar{V}}\bar{Y}_{\delta_A} & \frac{1}{m\bar{V}}\bar{Y}_{\delta_R} \\ \frac{1}{I_x}L_{\delta_A} & \frac{1}{I_x}L_{\delta_R} \\ \frac{1}{I_z}N_{\delta_A} & \frac{1}{I_z}N_{\delta_R}\end{bmatrix}\begin{bmatrix}\delta_A\\ \delta_R\end{bmatrix} + \begin{bmatrix}\frac{g}{\bar{V}}\cos\theta\sin\phi\\ 0\\ 0\end{bmatrix} \tag{2.4.10}$$

$$\begin{bmatrix}B_W\\ P_W\end{bmatrix} = \begin{bmatrix}\frac{\bar{Y}_\beta}{m} & \frac{\bar{Y}_P}{m} & \frac{\bar{Y}_R}{m}\\ 0 & 1 & 0\end{bmatrix}\begin{bmatrix}\beta\\ P\\ R\end{bmatrix} + \begin{bmatrix}\frac{\bar{Y}_{\delta_A}}{m} & \frac{\bar{Y}_{\delta_R}}{m}\\ 0 & 0\end{bmatrix}\begin{bmatrix}\delta_A\\ \delta_R\end{bmatrix} \tag{2.4.11}$$

Chapter 3

Longitudinal Analysis and Control

During landing, it is intuitive that the control of the aircraft occurs primarily in its longitudinal axis. Therefore, in order to land accurately, it is essential that the longitudinal motion of the aircraft is controlled accurately. The analysis of the longitudinal dynamics of the aircraft and the subsequent design of appropriate controllers will focus on this point of departure.

During landing the aircraft must essentially follow an *altitude* reference path which guides it down to the runway. The strategy to achieve this longitudinal control involves designing two sets of controllers. The first set is a series of controllers based around the longitudinal aerodynamic control surfaces (elevator δ_E and flaps δ_F), and the second is a controller based around the throttle actuator (T_C). The two sets of controllers are shown highlighted in Figure 3.1 where the first set consists of an *altitude* (h), *climb rate* ($\dot{h}$) and *normal specific acceleration* (C_W) controller, and the second consists of an *airspeed* ($\bar{V}$) controller.

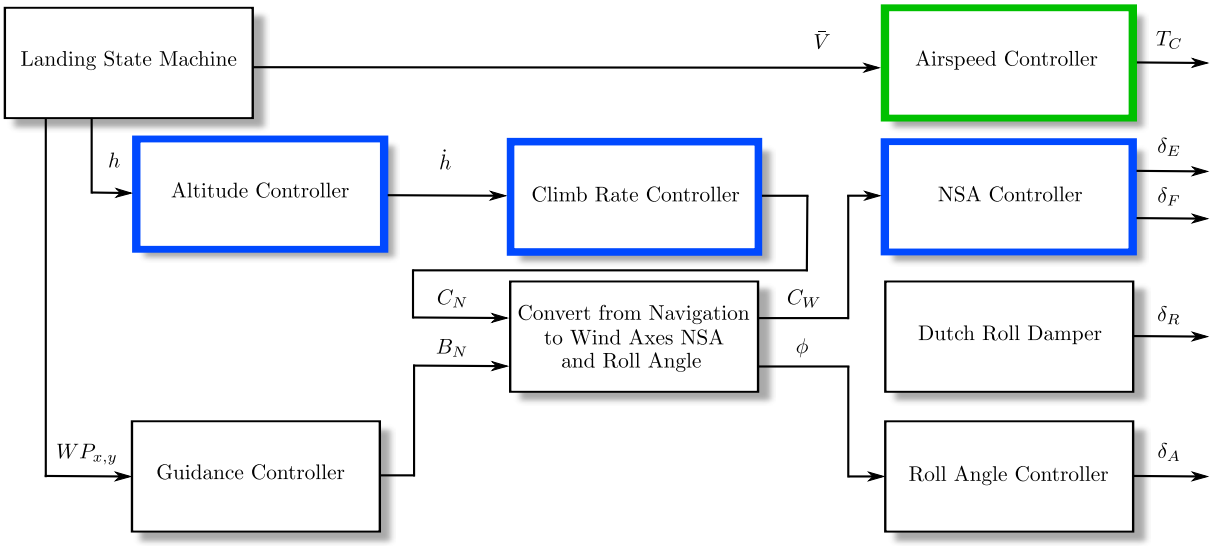

Figure 3.1 – Longitudinal control system overview

The *normal specific acceleration* (NSA) controller is designed around the linear, decoupled normal dynamics of Equations 2.4.8 and 2.4.9 as proposed by [2]. This controller possesses a high bandwidth and encapsulates all of the aircraft specific uncertainty. Since the NSA controller operates at the acceleration level it has the benefit of rejecting disturbances before they appear in the slower dynamics as an error in climb rate and altitude. This controller is capable of using the aircraft's elevator and flaps in order to create a commanded NSA, and receives its input from the *climb rate* controller. The *climb rate* controller creates a commanded climb rate by commanding the NSA controller, and receives its input from the *altitude* controller. In turn, the *altitude* controller creates a commanded altitude by commanding the climb rate controller. The *airspeed* controller is independent of the other controllers, and makes use of the aircraft's throttle in order to create a commanded airspeed. Both the airspeed and the altitude controllers receive their input from the landing state machine as discussed in Chapter 5.

As mentioned in §2.2, the flaps actuator is of special significance in this thesis. The mechanism through which it is used is known as *Direct-Lift Control* (DLC). DLC offers the prospect of an improvement in the precision with which aircraft height and vertical velocity can be controlled [12]. It does so by addressing some of the limitations faced by traditional longitudinal motion control, as discussed in §3.1.

This chapter explores the concept of DLC and how it could be applied to this thesis. This is followed by the design, HIL simulation, and practical flight test results of the NSA, climb rate, altitude and airspeed controllers.

3.1 Direct-Lift Control

If it is assumed that the airspeed of a conventional fixed-wing aircraft remains constant, then longitudinal control of the aircraft is essentially accomplished by varying the amount of lift produced by the aircraft as a whole. For a conventional aircraft, this is realised by means of a rear elevator. An elevator deflection by itself produces some change in lift of the tailplane, however, this lift is relatively small and in the *opposite sense* to what is ultimately intended. This lift does however act with a relatively large moment arm with respect to the centre of gravity of the aircraft, thereby causing a significant pitching moment. This pitching moment can change the angle of attack of the aircraft and thereby change the amount of lift produced by the aircraft. Conventional elevator-based longitudinal control is therefore accomplished by α*-generated* lift produced primarily by the wing of the aircraft. This is also known as pitch-moment-based longitudinal control.

Another mechanism by which longitudinal control can be accomplished is DLC. DLC utilises a control mechanism by which lift is generated without, or largely without, a significant change of aircraft incidence, and ideally should not generate pitching moment [12].

The flaps are an example of an actuator with inherent direct-lift properties. Operating the flaps causes a change in the camber of the wing, which results in an instantaneous change in the lift of the wing. Since the flaps are located close to the centre of gravity of the aircraft, the corresponding moment produced is relatively small when compared to actuators such as the elevator.

An important difference between pitch-moment-based and direct-lift-based longitudinal control is the transient response to a control input. In the case of pitch-moment-based control, the transient response is largely defined by the short period mode of the aircraft. There is in essence a second order lag imposed between a control input and achieving the desired output. This lag is proportional to the period of the short period mode. It is not unreasonable to imagine that this lag could have an adverse effect on any attempts to control the longitudinal motion aircraft very precisely. In the case of an idealised *pure* direct-lift control, [12] argues that the response is in essence only defined by the amount of lift commanded by the actuator. In this case the aircraft can simply be considered a mass with an applied force. This force causes a normal acceleration, which in turn causes a vertical velocity and finally a height change. The prospect of controlling the aircraft's height and vertical velocity independent of any pitch rate dynamics holds great promise for improvements in the precision with which these parameters can be controlled. Such improvements could impact directly on the accuracy with which the landing altitude reference path is followed, and consequently an improvement in the accuracy with which the landing touchdown point can be reached.

The design and implementation of a practically feasible DLC system is more complicated than the idealised scenario described, would suggest. The complexity arises from the fact that a practical direct-lift control surface, such as the flaps, also generates a pitch moment in addition to lift. These adverse effects are evaluated further during the design of the NSA controller in §3.2.

3.2 Normal Specific Acceleration Controller

This section describes the design, simulation and practical testing of a NSA controller based on the principles of DLC as outlined in §3.1. The NSA of the aircraft acts normal to the wing along the Z_W-axis of the wind axis system. The NSA controller is designed around the linear, decoupled normal dynamics of Equations 2.4.8 and 2.4.9 as proposed by [2]. This controller possesses a high bandwidth and encapsulates all of the aircraft specific uncertainty. Since the NSA controller operates at the acceleration level it has the benefit of rejecting disturbances before they appear in the slower dynamics as an error in climb rate and altitude. The input to the NSA controller stems from the *climb rate* controller of §3.3, which creates a commanded climb rate by commanding the NSA controller. The NSA controller then makes use of the aircraft's elevator and flaps to create the commanded NSA.

Previous implementations of this type of NSA controller [2; 1] made use of only the aircraft's elevator as the control surface. As discussed in §3.1, it is expected that with the addition of the flaps as a control surface, a direct-lift NSA controller can be designed which will show improved performance over the conventional NSA controller.

It must be noted that the controller design is not specific to the use of flaps as the direct-lift actuator. In general, any actuator or actuator combination which causes a change in lift force with a minimal change in pitch moment can be used. These could include spoilers and hybrid actuators such as spoilerons or flaperons (where the ailerons can move both differentially and in tandem).

3.2.1 Overview and Strategy

Several approaches to implement a direct-lift control system are discussed by [12], the most promising of which is a method of using DLC systems with relatively restricted authority. This involves combining traditional pitch-moment-based longitudinal control with direct-lift-based longitudinal control in order to form a hybrid longitudinal motion controller. The direct-lift control part of this hybrid controller only has a limited authority, whereas the pitch moment control part can respond to commands beyond the point where the direct-lift control authority is exhausted.

It is suggested by [12] that the most efficient use of a limited amount of direct-lift would be to superimpose it in *transient* form upon conventional moment-based control. This essentially means that the NSA controller signals must be filtered such that the direct-lift portion of the controller will only respond to higher frequency signals, whereas the moment-based portion of the controller will respond to lower frequency and steady state signals. In such a configuration the long term longitudinal response of the aircraft will remain as without direct-lift control, only the *initial* response will be affected by the direct-lift.

To illustrate this control concept, consider a step input to the NSA controller. The filter passes the higher frequency part of this signal to the direct-lift portion of the NSA controller. The direct-lift portion of the controller then allows the aircraft to achieve an immediate normal acceleration. Assuming that the direct-lift actuator possesses sufficient control authority, the commanded acceleration will be achieved. The effect of the filter is then to return the direct-lift actuator to its neutral position since the control signal now no longer contains any higher frequency components. Simultaneously, the lower frequency part of the control signal is passed to the moment-based portion of the controller. The moment-based actuator then simply holds the steady state acceleration demand. In the absence of the direct-lift portion of the controller, the nature of the response is in essence a second order lag which is proportional to the period of the short period mode. The effect of the direct-lift is thus to speed up the transient response to a control demand. This is also the case when the direct-lift actuator does not possess

sufficient control authority to achieve the commanded acceleration. In such a case, the response is a combination between the direct-lift and moment-based control responses.

An additional advantage of a direct-lift-augmented NSA controller is that, for small normal acceleration demands, there is less pitch angle variation than for a conventional moment-based controller. This attribute is especially useful in the presence of disturbances such as wind gusts, as the disturbance can be counteracted without affecting the pitch angle (and therefore the flight path angle) of the aircraft [18]. This results in improved altitude path following ability when compared to moment-based longitudinal control [19].

For a DLC system with relatively restricted authority, the strategy proposed by [12] is to use the moment-based control actuator to cancel out any unwanted moment produced by the DLC actuator. The NSA controller design presented makes use of the elevator as the pitch-moment-based control actuator, and the flaps as the direct-lift-based control actuator. Therefore, by using the elevator to cancel out the moment produced by the flaps, the flaps can be approximated as a *pure* direct-lift actuator.

In general, making use of two control actuators simultaneously to control the same parameter leads to the inherent problem of proper control allocation. However, for the strategy proposed in this section, this is overcome through the frequency separation between the elevator- and flaps-based portions of the controller. This frequency separation is the result of a complementary filter pair on the NSA controller signals and allows the two portions of the controller to be designed independently, before simply being superimposed.

Based on the preceding discussion, the NSA controller can be presented conceptually as shown in Figure 3.2. Both the commanded and the actual NSA signals are passed through a complementary filter pair. The low frequency parts of signals enter the elevator-based portion of the NSA controller, while the high-frequency parts enter the flaps-based portion. The resultant elevator and flaps deflections are then inputs to the NSA dynamics of the aircraft. The true NSA of the aircraft is again passed through the complementary filter pair before being fed back to the controllers. The gain K_M represents the gearing required between the flaps and the elevator in order for the elevator to cancel out any unwanted moment produced by the flaps.

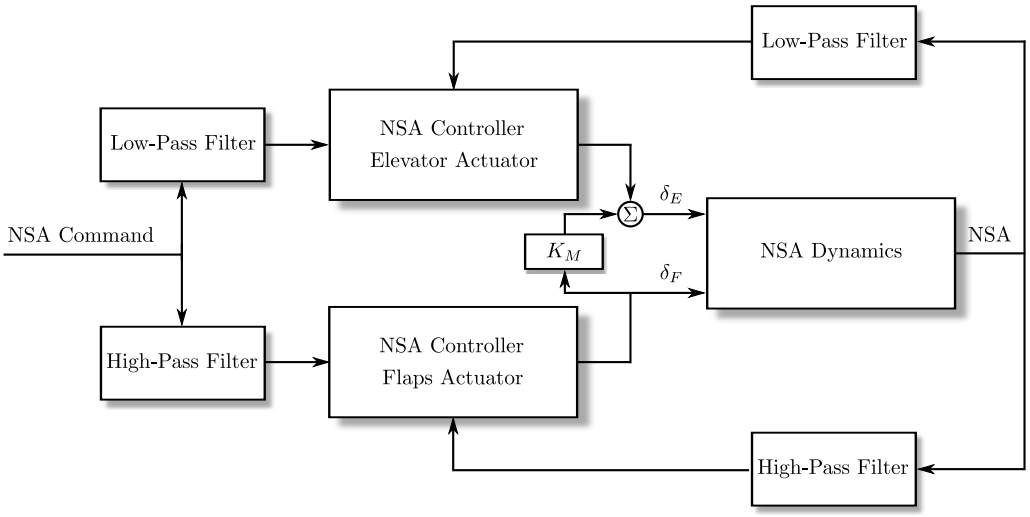

Figure 3.2 – Block diagram of NSA controller strategy

3.2.2 Investigation of the Elevator and Flap Actuators

In the control strategy of §3.2.1 it is stated that the aircraft's elevator is used as a moment-based longitudinal actuator and the flaps as a direct-lift-based longitudinal actuator. In this section these actuators are studied further to confirm their suitability for this controller design.

The longitudinal actuator configuration is shown in Figure 3.3 where L_W, L_T and L_{Total} are the lift forces of the wing, tailplane and the total lift force of the aircraft respectively, ac_W and ac_T the aerodynamic centre of the wing and tailplane respectively and NP the neutral point of the aircraft.

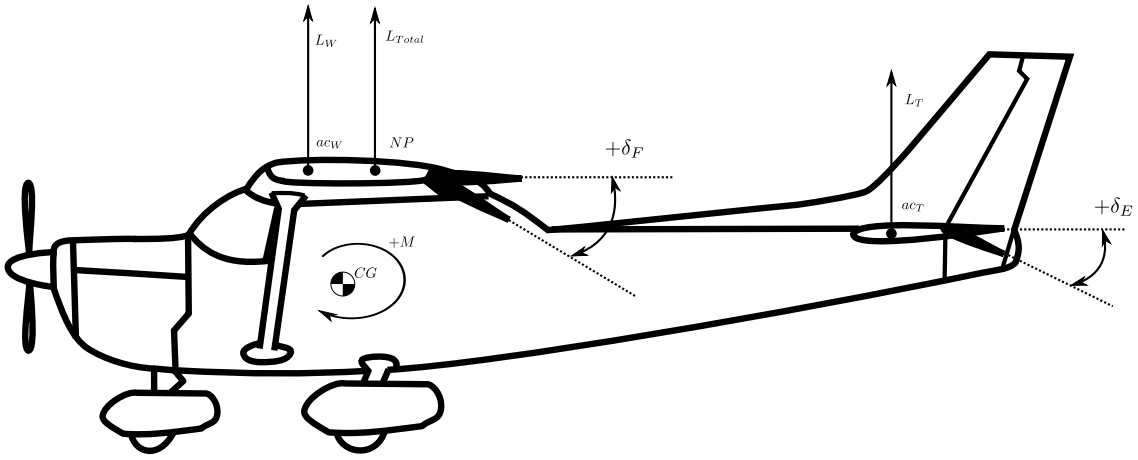

Figure 3.3 – Longitudinal actuator configuration of the aircraft[1]

To gauge the relative effects of the longitudinal actuators, it is necessary to determine the dimensionless stability and control derivatives of the aircraft. This is accomplished by modelling and analysing the aircraft in the vortex lattice program AVL (see Appendix B.6.3). The stability and control derivatives obtained describe a change in a force or

[1] Public Domain Image adapted. Source: Wikimedia.org

moment due to a change in a normalised motion variable or actuator deflection. The derivatives of interest in the design of the NSA controller are contained in Tables B.3 and B.5, and summarised in Table 3.1 for convenience.

Lift Force	Value	Pitch Moment	Value
C_{L_α}	4.808411	C_{m_α}	-0.664939
C_{L_Q}	7.812170	C_{m_Q}	-7.438796
$C_{L_{\delta_E}}$	0.456085	$C_{m_{\delta_E}}$	-0.957351
$C_{L_{\delta_F}}$	1.078236	$C_{m_{\delta_F}}$	0.172092

Table 3.1 – Longitudinal stability and control derivatives

From the relative values of the derivatives, it can be seen that for an equivalent deflection angle, the flaps generate more than twice the amount of lift than the elevator. Similarly it can be seen that moment generated by a flap deflection is more than five times less than that of the elevator. It can also be seen that the lift generated directly by an elevator deflection is in the opposite direction to what is intended. These attributes are in agreement with those of direct-lift-based and moment-based longitudinal control actuators as discussed in §3.1. It can also be safely assumed that the elevator possesses sufficient margin with which to counter any moments produced by a flaps deflection as discussed in §3.2.1.

It was shown in [4; 6; 8] that the stability and control derivatives generated by AVL are sufficiently accurate to enable the design of the aircraft's controllers. However, there is some uncertainty as to the direction of the flaps moment coefficient. With reference to Figure 3.3, the coefficients in Table 3.1 show that a positive flaps deflection will increase the lift of the aircraft whilst also generating a positive pitching moment. However, the actual pitching moment produced depends on how the change in lift and drag caused by the flaps deflection is positioned around the centre of gravity of the aircraft. It is therefore possible that the direction of the flaps moment coefficient can change for a different aircraft mass distribution. An additional complication is the difference in downwash on the tailplane between a small and a large flaps deflection. It is thus necessary to confirm the nature of the flaps moment coefficient through practical flight tests.

3.2.3 Investigation of the Natural NSA Dynamics

In this section the natural NSA dynamics are studied in order to gain further insight into the behaviour of the aircraft in respect of both elevator and flaps control deflections. This insight will be required in the controller designs of §3.2.4 and §3.2.5.

The decoupled model of the NSA dynamics from Equations 2.4.8 and 2.4.9 are restated below for convenience,

$$\begin{bmatrix}\dot{\alpha}\\ \dot{Q}\end{bmatrix} = \begin{bmatrix}-\frac{1}{m\bar{V}}\bar{L}_{\alpha} & 1-\frac{1}{m\bar{V}}\bar{L}_{Q}\\ \frac{1}{I_y}M_{\alpha} & \frac{1}{I_y}M_{Q}\end{bmatrix}\begin{bmatrix}\alpha\\ Q\end{bmatrix} + \begin{bmatrix}-\frac{1}{m\bar{V}}\bar{L}_{\delta_E} & -\frac{1}{m\bar{V}}\bar{L}_{\delta_F}\\ \frac{1}{I_y}M_{\delta_E} & \frac{1}{I_y}M_{\delta_F}\end{bmatrix}\begin{bmatrix}\delta_E\\ \delta_F\end{bmatrix} + \begin{bmatrix}\frac{g}{\bar{V}}\cos\theta\cos\phi\\ 0\end{bmatrix} \tag{3.2.1}$$

$$\begin{bmatrix}C_W\\ Q\end{bmatrix} = \begin{bmatrix}-\frac{1}{m}\bar{L}_{\alpha} & -\frac{1}{m}\bar{L}_{Q}\\ 0 & 1\end{bmatrix}\begin{bmatrix}\alpha\\ Q\end{bmatrix} + \begin{bmatrix}-\frac{1}{m}\bar{L}_{\delta_E} & -\frac{1}{m}\bar{L}_{\delta_F}\\ 0 & 0\end{bmatrix}\begin{bmatrix}\delta_E\\ \delta_F\end{bmatrix} \tag{3.2.2}$$

The effect of gravitational acceleration in the system can be removed by means of direct feedback linearisation as shown by [2]. However, provided that the flight path angle remains small, the gravitational acceleration effect can be considered static [8]. The gravitational acceleration term can thus be ignored under the assumption that the longitudinal controllers will remove any steady state error caused by its omission. An assumption is also made that,

$$\left|\frac{\bar{L}_Q}{m\bar{V}}\right| \ll 1 \tag{3.2.3}$$

since its effect is negligibly small for most conventional aircraft [14]. After these simplifications the normal dynamics are given by,

$$\begin{bmatrix}\dot{\alpha}\\ \dot{Q}\end{bmatrix} = \begin{bmatrix}-\frac{1}{m\bar{V}}\bar{L}_{\alpha} & 1\\ \frac{1}{I_y}M_{\alpha} & \frac{1}{I_y}M_{Q}\end{bmatrix}\begin{bmatrix}\alpha\\ Q\end{bmatrix} + \begin{bmatrix}-\frac{1}{m\bar{V}}\bar{L}_{\delta_E} & -\frac{1}{m\bar{V}}\bar{L}_{\delta_F}\\ \frac{1}{I_y}M_{\delta_E} & \frac{1}{I_y}M_{\delta_F}\end{bmatrix}\begin{bmatrix}\delta_E\\ \delta_F\end{bmatrix} \tag{3.2.4}$$

$$\begin{bmatrix}C_W\\ Q\end{bmatrix} = \begin{bmatrix}-\frac{1}{m}\bar{L}_{\alpha} & -\frac{1}{m}\bar{L}_{Q}\\ 0 & 1\end{bmatrix}\begin{bmatrix}\alpha\\ Q\end{bmatrix} + \begin{bmatrix}-\frac{1}{m}\bar{L}_{\delta_E} & -\frac{1}{m}\bar{L}_{\delta_F}\\ 0 & 0\end{bmatrix}\begin{bmatrix}\delta_E\\ \delta_F\end{bmatrix} \tag{3.2.5}$$

To analyse the natural NSA behavior, the transfer function matrix is found as shown in Appendix C.1, and can be written as,

$$\mathbf{G}(s) = \frac{1}{\Delta(s)}\mathbf{N}(s) \tag{3.2.6}$$

where $\mathbf{N}(s)$ is a polynomial matrix whose elements consist of the response transfer function numerators, and where $\Delta(s)$ is the characteristic polynomial common to all transfer functions. For the NSA dynamics as shown in Equations 3.2.4 and 3.2.5 four transfer functions exist,

$$\mathbf{G}(s) = \frac{1}{\Delta(s)}\begin{bmatrix}N^{C_W}_{\delta_E}(s) & N^{C_W}_{\delta_F}(s)\\ N^{Q}_{\delta_E}(s) & N^{Q}_{\delta_F}(s)\end{bmatrix} \tag{3.2.7}$$

where $N^{\mathcal{A}}_{\mathcal{B}}(s)$ is the response transfer function numerator of state variable $\mathcal{A}$ to control input $\mathcal{B}$. Calculating the characteristic equation and the response transfer function numerators yields,

$$\Delta(s) = s^2 + \left(\frac{\bar{L}_{\alpha}}{m\bar{V}} - \frac{M_Q}{I_y}\right)s - \left(\frac{\bar{L}_{\alpha}}{m\bar{V}}\frac{M_Q}{I_y} + \frac{M_{\alpha}}{I_y}\right) \tag{3.2.8}$$

and,

$$\mathbf{N}(s) = \begin{bmatrix} -\frac{\bar{L}_{\delta_E}}{m}\left[s^2 - \frac{\bar{L}_Q}{I_y}\left(\frac{M_Q}{\bar{L}_Q} - \frac{M_{\delta_E}}{\bar{L}_{\delta_E}}\right)s - \frac{\bar{L}_\alpha}{I_y}\left(\frac{M_\alpha}{\bar{L}_\alpha} - \frac{M_{\delta_E}}{\bar{L}_{\delta_E}}\right)\right] & -\frac{\bar{L}_{\delta_F}}{m}\left[s^2 - \frac{\bar{L}_Q}{I_y}\left(\frac{M_Q}{\bar{L}_Q} - \frac{M_{\delta_F}}{\bar{L}_{\delta_F}}\right)s - \frac{\bar{L}_\alpha}{I_y}\left(\frac{M_\alpha}{\bar{L}_\alpha} - \frac{M_{\delta_F}}{\bar{L}_{\delta_F}}\right)\right] \\ \frac{M_{\delta_E}}{I_y}\left[s + \frac{\bar{L}_\alpha}{m\bar{V}} - \frac{\bar{L}_{\delta_E}}{m\bar{V}}\frac{M_\alpha}{M_{\delta_E}}\right] & \frac{M_{\delta_F}}{I_y}\left[s + \frac{\bar{L}_\alpha}{m\bar{V}} - \frac{\bar{L}_{\delta_F}}{m\bar{V}}\frac{M_\alpha}{M_{\delta_F}}\right] \end{bmatrix} \tag{3.2.9}$$

It follows from Equation 3.2.8 that the normal dynamic poles are not affected by the lift due to pitch rate ($\bar{L}_Q$) or either of the control deflections (δ_E and δ_F). It can also be seen in Equation 3.2.9 that the response transfer functions for the elevator and flaps are identical except for the respective control deflection lift and pitching moment derivatives. The NSA response to both the elevator and flaps control input is further looked at in the following sections.

3.2.3.1 NSA Response to Elevator Input

The transfer function for the NSA response to an elevator input can be determined from Equations 3.2.7 to 3.2.9, and is given by,

$$G_{\delta_E}^{C_W}(s) = \frac{N_{\delta_E}^{C_W}(s)}{\Delta(s)} = \frac{-\frac{\bar{L}_{\delta_E}}{m}\left[s^2 - \frac{\bar{L}_Q}{I_y}\left(\frac{M_Q}{\bar{L}_Q} - \frac{M_{\delta_E}}{\bar{L}_{\delta_E}}\right)s - \frac{\bar{L}_\alpha}{I_y}\left(\frac{M_\alpha}{\bar{L}_\alpha} - \frac{M_{\delta_E}}{\bar{L}_{\delta_E}}\right)\right]}{s^2 + \left(\frac{\bar{L}_\alpha}{m\bar{V}} - \frac{M_Q}{I_y}\right)s - \left(\frac{\bar{L}_\alpha}{m\bar{V}}\frac{M_Q}{I_y} + \frac{M_\alpha}{I_y}\right)} \tag{3.2.10}$$

To gain a better appreciation for the nature of the transfer function, the values for the aerodynamic derivatives, standard flight conditions and aircraft parameters (see Appendix B.6) are substituted into the above equation. Thus,

$$G_{\delta_E}^{C_W}(s) = \frac{-9.65s^2 + 85.88s + 8794}{s^2 + 13.04s + 106} = \frac{-9.65(s - 34.96)(s + 26.06)}{(s + 6.52 + 7.97\mathrm{i})(s + 6.52 - 7.97\mathrm{i})} \tag{3.2.11}$$

The location of the poles and zeros of $G_{\delta_E}^{C_W}(s)$ as well as the NSA response to an elevator step input can now be determined as shown in Figures 3.4a and 3.4b. The damped pole pair depicted in Figure 3.4a represents the short period mode of the aircraft. The short period mode is a damped pitch oscillation of the aircraft which is excited whenever the aircraft is disturbed from its pitch equilibrium state. It manifests itself as a classical second order oscillation in which the principal variables are angle of attack (α), pitch rate (Q) and pitch attitude (θ) [13]. The airspeed magnitude remains approximately constant in the timescale of this mode due to the effects of inertia and momentum.

The right half plane zero depicted in Figure 3.4a indicates the non-minimum phase (NMP) nature of the NSA response to an elevator input. The NMP nature results from the small amount of lift produced by an elevator deflection where the lift is in the *opposite* sense to what is ultimately intended. The effect of this portion of the lift can be seen in Figure 3.4b as the small initial dip in NSA which occurs before the dominant portion of the response. As discussed in §3.1, the dominant portion of the response results from the pitch moment created by that lift. This moment can change the angle of attack of

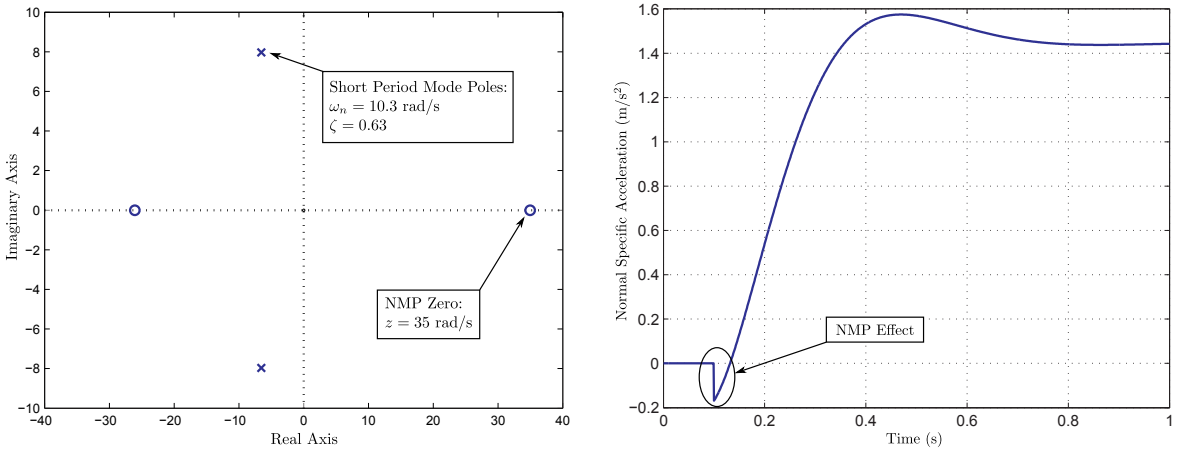

(a) Pole-zero map **(b)** Step response

Figure 3.4 – Pole-zero map and step response of the NSA to elevator input transfer function

the aircraft and thereby change the amount of lift produced by the aircraft. As shown by [2], the NMP nature of the NSA dynamics can be ignored if the natural frequency of both the open- and the closed-loop dominant poles of the system is at least three times slower than that of the NMP zero. Figure 3.4a shows an approximate NMP zero location of,

$$Z_{NMP} \approx 35\,\text{rad/s} \tag{3.2.12}$$

which is more than three times faster than the open-loop poles. If it is assumed that the controller design of §3.2.4 will ensure that the closed-loop poles also meet the above requirement, then the NMP zero can be ignored by assuming that,

$$C_{L_{\delta_E}} = 0 \tag{3.2.13}$$

This assumption reinforces the notion expressed in §3.2.1 that the elevator is used as a *pitch moment* based actuator. In general, as the airspeed increases, the frequency of the short period mode poles increases while their damping increases slightly. The two zeros move further away from the origin as the airspeed increases, and the NMP zero remains sufficiently far from the poles across the conventional airspeed range of the aircraft in order for the assumption to remain valid.

A left half plane zero is also depicted in Figure 3.4a. This zero is located at a much higher frequency than the poles of the NSA dynamics. As such, its effects will be negligible due to the presence of other high-frequency poles, such as those from servo lag, which remain unmodelled. This zero represents the lift generated by the aircraft due to the induced angle of attack created when the aircraft is experiencing a pitch rate. It can therefore be ignored by assuming that,

$$C_{L_Q} = 0 \tag{3.2.14}$$

After the simplifications above, the NSA dynamic equations for an elevator input are given by,

$$\begin{bmatrix}\dot{\alpha}\\ \dot{Q}\end{bmatrix} = \begin{bmatrix}-\frac{1}{m\bar{V}}\bar{L}_\alpha & 1\\ \frac{1}{I_y}M_\alpha & \frac{1}{I_y}M_Q\end{bmatrix}\begin{bmatrix}\alpha\\ Q\end{bmatrix} + \begin{bmatrix}0\\ \frac{1}{I_y}M_{\delta_E}\end{bmatrix}\delta_E \tag{3.2.15}$$

$$\begin{bmatrix}C_W\\ Q\end{bmatrix} = \begin{bmatrix}-\frac{1}{m}\bar{L}_\alpha & 0\\ 0 & 1\end{bmatrix}\begin{bmatrix}\alpha\\ Q\end{bmatrix} + \begin{bmatrix}0\\ 0\end{bmatrix}\delta_E \tag{3.2.16}$$

In order to compare these simplified dynamics with the full dynamics of Equations 3.2.4 and 3.2.5, the transfer function for the NSA response to an elevator input of the simplified dynamics is determined,

$$G_{\delta_E}^{C_W}(s) = \frac{N_{\delta_E}^{C_W}(s)}{\Delta(s)} = \frac{-\frac{M_{\delta_E}\bar{L}_\alpha}{I_y m}}{s^2 + \left(\frac{\bar{L}_\alpha}{m\bar{V}} - \frac{M_Q}{I_y}\right)s - \left(\frac{\bar{L}_\alpha}{m\bar{V}}\frac{M_Q}{I_y} + \frac{M_\alpha}{I_y}\right)} \tag{3.2.17}$$

Substituting in the values for the aerodynamic derivatives, standard flight conditions and aircraft parameters (see Appendix B.6) gives,

$$G_{\delta_E}^{C_W}(s) = \frac{9414}{s^2 + 13.04s + 106} = \frac{9414}{(s + 6.52 + 7.97\mathrm{i})(s + 6.52 - 7.97\mathrm{i})} \tag{3.2.18}$$

The NSA response to an elevator step input for both the full and the simplified dynamics can now be determined as shown in Figure 3.5. It can be seen that there is only a slight difference in the open-loop step response between the full and simplified dynamics. The most significant difference is the absence of the NMP effect in the response of the simplified dynamics. The simplified dynamics of Equations 3.2.15 and 3.2.16 are therefore used in the elevator-based portion of NSA controller design in §3.2.4.

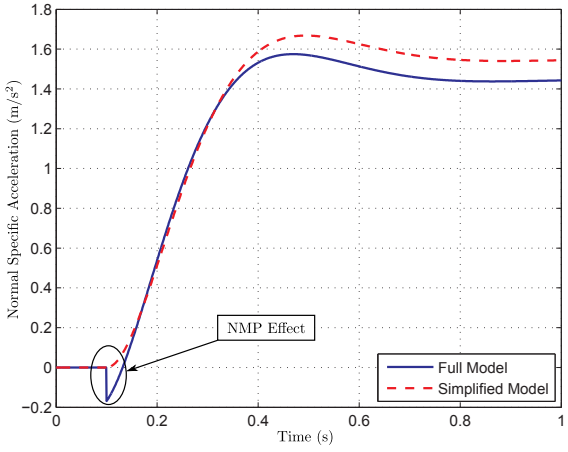

Figure 3.5 – Step response of the full and simplified NSA to elevator input transfer functions

3.2.3.2 NSA Response to Flaps Input

The transfer function for the NSA response to a flaps input can be determined from Equations 3.2.7 to 3.2.9, and is given by,

$$G_{\delta_F}^{C_W}(s) = \frac{N_{\delta_F}^{C_W}(s)}{\Delta(s)} = \frac{-\frac{\bar{L}_{\delta_F}}{m}\left[s^2 - \frac{\bar{L}_Q}{I_y}\left(\frac{M_Q}{\bar{L}_Q} - \frac{M_{\delta_F}}{\bar{L}_{\delta_F}}\right)s - \frac{\bar{L}_\alpha}{I_y}\left(\frac{M_\alpha}{\bar{L}_\alpha} - \frac{M_{\delta_F}}{\bar{L}_{\delta_F}}\right)\right]}{s^2 + \left(\frac{\bar{L}_\alpha}{m\bar{V}} - \frac{M_Q}{I_y}\right)s - \left(\frac{\bar{L}_\alpha}{m\bar{V}}\frac{M_Q}{I_y} + \frac{M_\alpha}{I_y}\right)} \tag{3.2.19}$$

In order to gain a better appreciation for the nature of the transfer function, the values for the aerodynamic derivatives, standard flight conditions and aircraft parameters (see Appendix B.6) are substituted into the above equation. Thus,

$$G_{\delta_F}^{C_W}(s) = \frac{-22.81s^2 - 196.8s - 3158}{s^2 + 13.04s + 106} = \frac{-22.81(s + 4.31 + 10.95\mathrm{i})(s + 4.31 - 10.95\mathrm{i})}{(s + 6.52 + 7.97\mathrm{i})(s + 6.52 - 7.97\mathrm{i})} \tag{3.2.20}$$

The pole-zero map as well as the NSA response to a flaps step input of $G_{\delta_F}^{C_W}(s)$ are shown in Figures 3.6a and 3.6b. It can be seen in Figure 3.6a that the transfer function, $G_{\delta_F}^{C_W}(s)$, displays a pair of complex poles as well as a pair of complex zeros, and that these are located in the same general area on the pole-zero map. As discussed in §3.2.3.1, the damped pole pair represent the short period mode of the aircraft. From Figure 3.6b it can be seen that the NSA response to a flap step input consists of a quick initial step in NSA followed by a slower rise to some final value. This means that, for a downwards flap deflection, the aircraft will experience an instantaneous upwards NSA followed by an upwards pitch rate which then causes the NSA to rise even more.

To understand the origin of this response, the NSA dynamics of Equations 3.2.4 and 3.2.5 must be considered for a step flap deflection. It can be seen in the output equation that this flap deflection causes an instantaneous increase to NSA due to the lift produced by a flap deflection term $\bar{L}_{\delta_F}$. This is the direct-lift effect as described in §3.1 and can be seen in Figure 3.6b as the initial jump in NSA. The $\bar{L}_{\delta_F}$ term also affects the angle of attack directly. This angle of attack effect is relatively small, and its effect on the NSA is in the opposite sense to that intended. It can be seen in Figure 3.6b as the small bump in the NSA response directly after the direct-lift part of the response. The angle of attack and pitch rate both affect one another and, in the absence of the moment produced by the flaps, will cause the pitch rate to continue to rise in the opposite direction to that intended and eventually settle at a constant value. The moment produced by the flaps, as reflected by the M_{δ_F} term, is the largest contributor to pitch rate. This pitch rate causes a change in the angle of attack of the aircraft, and this then reflects as a change in the NSA. This effect on the NSA is in the same direction as that intended and can be seen in Figure 3.6b as the slow rise in NSA following the small bump in the response. At a certain point, the moment due angle of attack and pitch rate, as reflected by the M_Q and M_α terms, becomes high enough to oppose further increase in the pitch rate. This results in the response settling at a constant pitch rate and NSA. The effect of the lift

due to pitch rate term, $\bar{L}_Q$ is negligibly small as was the case for the NSA response to elevator input of §3.2.3.1.

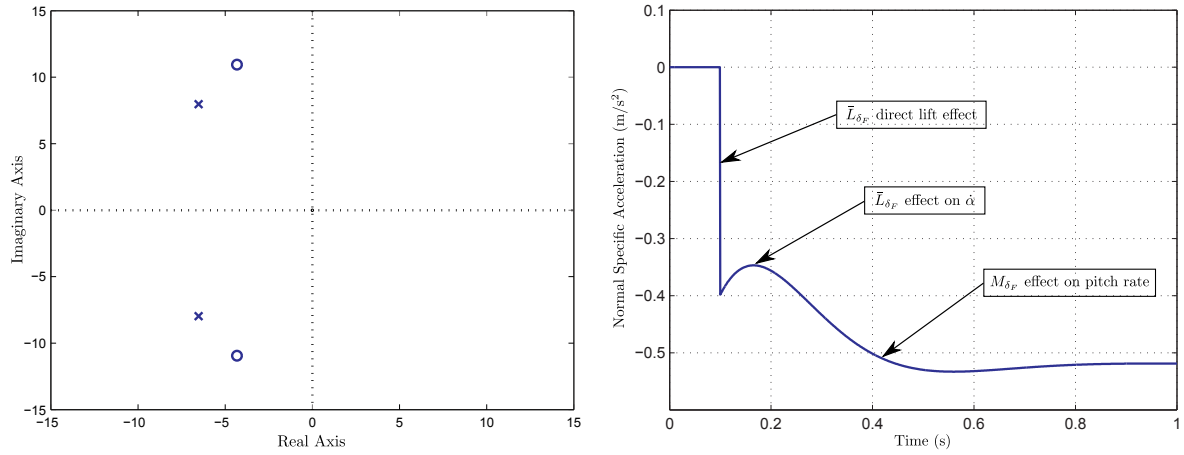

(a) Pole-zero map **(b)** Step response

Figure 3.6 – Pole-zero map and step response of the NSA to flaps input transfer function

As stated in §3.2.2 the direction of the flaps moment coefficient $C_{M_{\delta_F}}$ can change for a different aircraft configuration. This means that, for a downwards flap deflection, the aircraft will experience an instantaneous upwards NSA followed by a *downwards* pitch rate. This is in contrast to the scenario discussed previously, where a downwards flap deflection causes the aircraft to pitch *upwards*. In order to illustrate the consequences of this, the values for the aerodynamic derivatives, standard flight conditions and aircraft parameters are again substituted into Equation 3.2.19. Thus,

$$G_{\delta_F}^{C_W}(s) = \frac{-22.81s^2 - 140.3s + 226}{s^2 + 13.04s + 106} = \frac{-22.81(s + 7.48)(s - 1.33)}{(s + 6.52 + 7.97\text{i})(s + 6.52 - 7.97\text{i})} \tag{3.2.21}$$

The pole-zero map as well as the NSA response to a flaps step input of $G_{\delta_F}^{C_W}(s)$ are shown in Figures 3.7a and 3.7b. It can be seen in Figure 3.7a that the transfer function $G_{\delta_F}^{C_W}(s)$ now possesses two real zeros instead of a pair of complex zeros as in Figure 3.6a. From Figure 3.7b it can be seen that the NSA response to a flap step input consists of a quick initial step in NSA followed by a slower rise to some final value which is in the opposite direction to that intended. The previous discussion regarding the response of Equation 3.2.20 holds here as well. The only difference is that the moment produced by the flap deflection is now in the opposite direction. This moment then causes the steady state NSA response to be in the opposite direction than intended.

As discussed in the NSA controller strategy of §3.2.1, the NSA controller makes use of the elevator to cancel out any moment produced by the flaps. If it is assumed that the flap moment is cancelled out perfectly, then the NSA dynamic equations for a flaps input

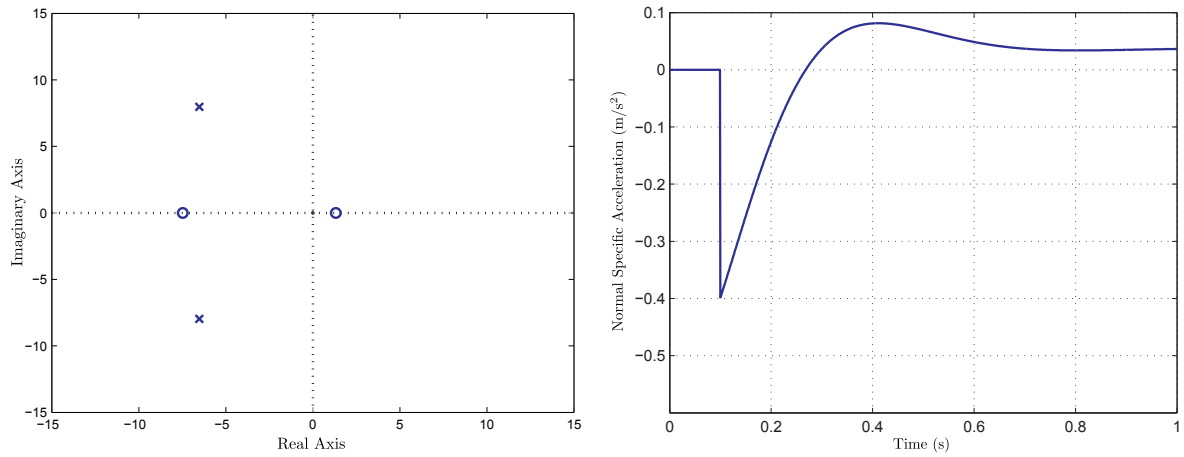

(a) Pole-zero map **(b)** Step response

Figure 3.7 – Pole-zero map and step response of the NSA to flaps input transfer function where the flaps moment coefficient is of opposite direction

become,

$$\begin{bmatrix}\dot{\alpha}\\ \dot{Q}\end{bmatrix} = \begin{bmatrix} -\frac{1}{m\bar{V}}\bar{L}_\alpha & 1 \\ \frac{1}{I_y}M_\alpha & \frac{1}{I_y}M_Q \end{bmatrix}\begin{bmatrix}\alpha\\ Q\end{bmatrix} + \begin{bmatrix} -\frac{1}{m\bar{V}}\bar{L}_{\delta_F} \\ 0 \end{bmatrix}\delta_F \tag{3.2.22}$$

$$\begin{bmatrix}C_W\\ Q\end{bmatrix} = \begin{bmatrix} -\frac{1}{m}\bar{L}_\alpha & 0 \\ 0 & 1 \end{bmatrix}\begin{bmatrix}\alpha\\ Q\end{bmatrix} + \begin{bmatrix} -\frac{1}{m}\bar{L}_{\delta_F} \\ 0 \end{bmatrix}\delta_F \tag{3.2.23}$$

The transfer function for the NSA response to a flaps input of this simplified model is given by,

$$G_{\delta_F}^{C_W}(s) = \frac{N_{\delta_F}^{C_W}(s)}{\Delta(s)} = \frac{-\frac{\bar{L}_{\delta_F}}{m}\left[s^2 - \frac{M_Q}{I_y}s - \frac{M_\alpha}{I_y}\right]}{s^2 + \left(\frac{\bar{L}_\alpha}{m\bar{V}} - \frac{M_Q}{I_y}\right)s - \left(\frac{\bar{L}_\alpha}{m\bar{V}}\frac{M_Q}{I_y} + \frac{M_\alpha}{I_y}\right)} \tag{3.2.24}$$

To gain a better appreciation for the nature of the transfer function, the values for the aerodynamic derivatives, standard flight conditions and aircraft parameters (see Appendix B.6) are substituted into the above equation. Thus,

$$G_{\delta_F}^{C_W}(s) = \frac{-22.81s^2 - 168.6s - 1466}{s^2 + 13.04s + 106} = \frac{-22.81(s + 3.70 + 7.11\mathrm{i})(s + 3.70 - 7.11\mathrm{i})}{(s + 6.52 + 7.97\mathrm{i})(s + 6.52 - 7.97\mathrm{i})} \tag{3.2.25}$$

The pole-zero map as well as the NSA response to a flaps step input of $G_{\delta_F}^{C_W}(s)$ are shown in Figures 3.8a and 3.8b. It can be seen in Figure 3.8b that the NSA response to a flap input now consists of two parts, the first being the initial jump in NSA caused by the direct-lift component of the flaps deflection. The second part is the result of the effect of the flap deflection on the angle of attack. The angle of attack and pitch rate interact in a way which lowers the angle of attack, eventually settling to some constant angle of attack and pitch rate. The effect of this reduction in angle of attack is then to reduce the NSA. It must be noted that if the moment produced by a flaps deflection is perfectly cancelled out by the elevator, then the responses are identical for either direction of

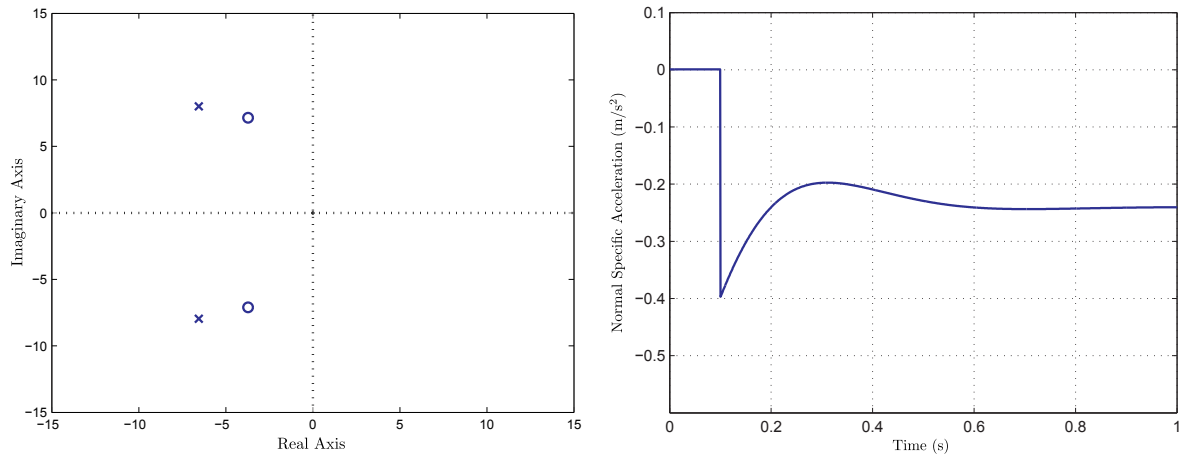

(a) Pole-zero map **(b)** Step response

Figure 3.8 – Pole-zero map and step response of the NSA to flaps input transfer function where the flaps moment is cancelled out

flaps moment coefficient $C_{M_{\delta_F}}$. It is therefore possible to design a direct-lift controller regardless of this coefficient's direction.

As discussed in §3.2.1 the NSA controller strategy involves superimposing the flaps-based direct-lift portion of the controller in *transient* form upon the elevator-based moment portion of the controller. The direct-lift portion of the controller only acts on higher frequency NSA commands and therefore the long term response of the aircraft is entirely conventional. This means that the direct-lift portion of the controller can be optimised to simply yield an improved control response. One such optimisation involves changing the gearing between the flaps and the elevator. This means that the elevator does not cancel out the moment produced by the flaps perfectly, but rather increases or decreases the net moment acting on the aircraft. In this way the response can be tuned to obtain a satisfactory result. This is demonstrated in Figures 3.9a and 3.9b where the pole-zero map and the NSA response to a flaps step input are shown for different moment gearings. It can be seen in Figure 3.9b that increasing the gearing makes the steady state NSA value shift upwards. This allows a satisfactory response to be found through simulation as shown in §3.2.6.

3.2.4 NSA Controller Design - Elevator Actuator

This section presents the design of the elevator-based portion of the NSA controller. This controller uses the aircraft's elevator to create a commanded wind axes NSA through the principles of moment-based longitudinal control as outlined in §3.1. As discussed in section §3.2.1, this controller will be superimposed with the direct-lift based NSA controller of §3.2.5. The detailed derivation of this controller is given in Appendix C.2.

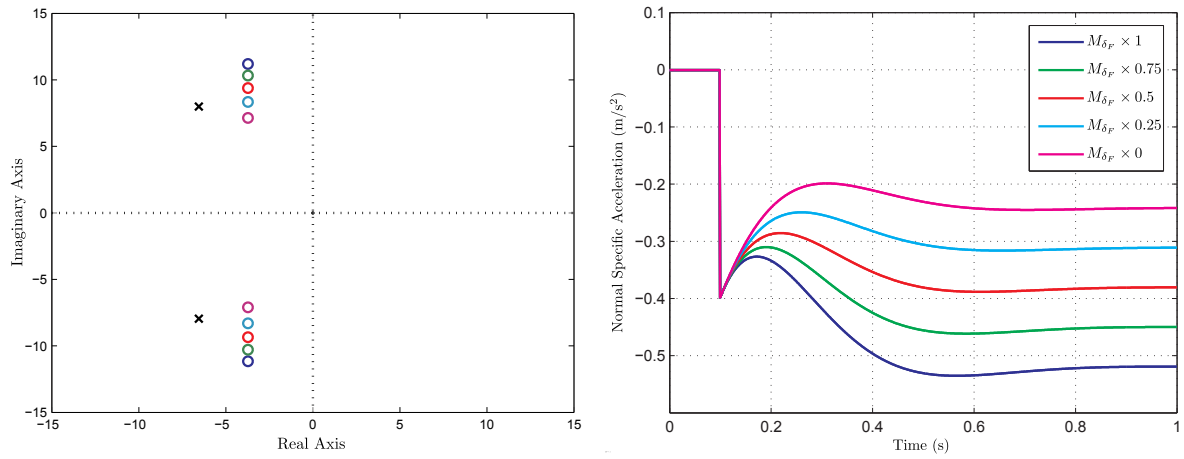

(a) Pole-zero map **(b)** Step response

Figure 3.9 – Pole-zero map and step response of the NSA to flaps input transfer function for a range of moment gearings

The simplified NSA dynamic equations from §3.2.3.1 are restated below,

$$\begin{bmatrix}\dot{\alpha}\\ \dot{Q}\end{bmatrix} = \begin{bmatrix}-\frac{1}{m\bar{V}}\bar{L}_\alpha & 1\\ \frac{1}{I_y}M_\alpha & \frac{1}{I_y}M_Q\end{bmatrix}\begin{bmatrix}\alpha\\ Q\end{bmatrix} + \begin{bmatrix}0\\ \frac{1}{I_y}M_{\delta_E}\end{bmatrix}\delta_E \tag{3.2.26}$$

$$\begin{bmatrix}C_W\\ Q\end{bmatrix} = \begin{bmatrix}-\frac{1}{m}\bar{L}_\alpha & 0\\ 0 & 1\end{bmatrix}\begin{bmatrix}\alpha\\ Q\end{bmatrix} + \begin{bmatrix}0\\ 0\end{bmatrix}\delta_E \tag{3.2.27}$$

To remove steady state errors on NSA, the state vector is augmented with an integrator x_I which obeys the differential equation,

$$\dot{x}_I = C_W - C_W^{ref} \tag{3.2.28}$$

where C_W^{ref} is the reference NSA input. The augmented NSA dynamics are now given by,

$$\begin{bmatrix}\dot{x}_I\\ \dot{\alpha}\\ \dot{Q}\end{bmatrix} = \begin{bmatrix}0 & -\frac{1}{m}\bar{L}_\alpha & 0\\ 0 & -\frac{1}{m\bar{V}}\bar{L}_\alpha & 1\\ 0 & \frac{1}{I_y}M_\alpha & \frac{1}{I_y}M_Q\end{bmatrix}\begin{bmatrix}x_I\\ \alpha\\ Q\end{bmatrix} + \begin{bmatrix}0\\ 0\\ \frac{1}{I_y}M_{\delta_E}\end{bmatrix}\delta_E - \begin{bmatrix}1\\ 0\\ 0\end{bmatrix}C_W^{ref} \tag{3.2.29}$$

$$\begin{bmatrix}C_W\\ Q\end{bmatrix} = \begin{bmatrix}0 & -\frac{1}{m}\bar{L}_\alpha & 0\\ 0 & 0 & 1\end{bmatrix}\begin{bmatrix}x_I\\ \alpha\\ Q\end{bmatrix} + \begin{bmatrix}0\\ 0\end{bmatrix}\delta_E \tag{3.2.30}$$

An elevator control law is defined which uses feedback from the integrator and pitch rate states as well as feed-forward from the reference input. The integrator state feedback will ensure that any steady state errors are removed from the closed-loop system, whereas the pitch rate feedback will allow the damping of the NSA dynamics to be selected. The feed-forward from the reference input will allow a closed-loop zero to be placed. This control strategy was proposed by [1] in response to difficulties that were encountered when using feedback directly from NSA. It was found that using NSA feedback without filtering it first made the controller very sensitive to noise on the NSA measurement. It was also found that attempts to increase the system's natural frequency can

result in undesirable pole placements, due to unmodelled effects such as delays. The elevator control law is thus given by,

$$\delta_E = -\begin{bmatrix} K_{I_{\delta_E}} & 0 & K_{Q_{\delta_E}} \end{bmatrix} \begin{bmatrix} x_I \\ \alpha \\ Q \end{bmatrix} + \bar{N}_{C_{\delta_E}} C_W^{ref} \tag{3.2.31}$$

The control law is now substituted into the dynamics and the closed-loop system becomes,

$$\begin{bmatrix} \dot{x}_I \\ \dot{\alpha} \\ \dot{Q} \end{bmatrix} = \begin{bmatrix} 0 & -\frac{1}{m}\bar{L}_\alpha & 0 \\ 0 & -\frac{1}{m\bar{V}}\bar{L}_\alpha & 1 \\ -\frac{1}{I_y}M_{\delta_E}K_{I_{\delta_E}} & \frac{1}{I_y}M_\alpha & \frac{1}{I_y}M_Q - \frac{1}{I_y}M_{\delta_E}K_{Q_{\delta_E}} \end{bmatrix} \begin{bmatrix} x_I \\ \alpha \\ Q \end{bmatrix} - \begin{bmatrix} 1 \\ 0 \\ -\frac{1}{I_y}M_{\delta_E}\bar{N}_{C_{\delta_E}} \end{bmatrix} C_W^{ref} \tag{3.2.32}$$

$$\begin{bmatrix} C_W \\ Q \end{bmatrix} = \begin{bmatrix} 0 & -\frac{1}{m}\bar{L}_\alpha & 0 \\ 0 & 0 & 1 \end{bmatrix} \begin{bmatrix} x_I \\ \alpha \\ Q \end{bmatrix} \tag{3.2.33}$$

Calculating the closed-loop characteristic equation gives,

$$\begin{aligned} p(s) = s^3 + \left(\frac{\bar{L}_\alpha}{m\bar{V}} - \frac{M_Q}{I_y} + \frac{M_{\delta_E}}{I_y}K_{Q_{\delta_E}}\right)s^2 + \left(-\frac{\bar{L}_\alpha M_Q}{m\bar{V}I_y} + \frac{\bar{L}_\alpha M_{\delta_E}}{m\bar{V}I_y}K_{Q_{\delta_E}} - \frac{M_\alpha}{I_y}\right)s \\ - \frac{\bar{L}_\alpha M_{\delta_E}}{mI_y}K_{I_{\delta_E}} \end{aligned} \tag{3.2.34}$$

In order to place the closed-loop poles a desired characteristic equation for the NSA dynamics is defined as,

$$\alpha_c(s) = (s^2 + 2\zeta\omega_n s + \omega_n^2)(s + a) \tag{3.2.35}$$

where the complex pole pair corresponds to the short period mode and the single real pole to the closed-loop integrator. Expanding Equation 3.2.35 equation gives,

$$\alpha_c(s) = s^3 + (2\zeta\omega_n + a)s^2 + (2\zeta\omega_n a + \omega_n^2)s + \omega_n^2 a \tag{3.2.36}$$

Equating the coefficients of Equations 3.2.34 and 3.2.36 results in the following two equations for $K_{Q_{\delta_E}}$,

$$K_{Q_{\delta_E}} = \frac{I_y}{M_{\delta_E}}\left(2\zeta\omega_n + a - \frac{\bar{L}_\alpha}{m\bar{V}} + \frac{M_Q}{I_y}\right) \tag{3.2.37}$$

and,

$$K_{Q_{\delta_E}} = \frac{m\bar{V}}{\bar{L}_\alpha}\frac{I_y}{M_{\delta_E}}\left(2\zeta\omega_n a + \omega_n^2 + \frac{\bar{L}_\alpha}{m\bar{V}}\frac{M_Q}{I_y} + \frac{M_\alpha}{I_y}\right) \tag{3.2.38}$$

If the damping of the short period mode (ζ) and the location of the closed-loop integrator pole (a) are selected, the resulting natural frequency can be solved by setting Equations 3.2.37 and 3.2.38 equal to one another yielding,

$$\omega_n^2 + \omega_n\left(2\zeta a - 2\zeta\frac{\bar{L}_\alpha}{m\bar{V}}\right) + \frac{M_\alpha}{I_y} + \left(\frac{\bar{L}_\alpha}{m\bar{V}}\right)^2 - a\frac{\bar{L}_\alpha}{m\bar{V}} = 0 \tag{3.2.39}$$

Solving for positive values of ω_n the closed-loop natural frequency of the short period mode is given by,

$$\omega_n = \zeta\eta + \sqrt{(\zeta\eta)^2 - \frac{M_\alpha}{I_y} - \frac{\bar{L}_\alpha}{m\bar{V}}\eta} \tag{3.2.40}$$

where,

$$\eta = \frac{\bar{L}_\alpha}{m\bar{V}} - a \tag{3.2.41}$$

The natural frequency of the short period mode (ω_n), along with the previously selected damping of the short period mode (ζ) and the location of the closed-loop integrator pole (a) can now be used in conjunction with either of the pitch rate equations, Equations 3.2.37 and 3.2.38, to determine the pitch rate feedback gain $K_{Q_{\delta_E}}$. The integrator feedback gain can be solved by equating the coefficients of the final terms of Equations 3.2.34 and 3.2.36 and is given by,

$$K_{I_{\delta_E}} = -a\frac{\omega_n^2 m I_y}{\bar{L}_\alpha M_{\delta_E}} \tag{3.2.42}$$

The integrator's response can be removed from the reference input by placing a feed-forward zero as follows,

$$\bar{N}_{C_{\delta_E}} = -\frac{K_{I_{\delta_E}}}{z_f} \tag{3.2.43}$$

where z_f is the location of the desired zero.

3.2.4.1 Pole/Zero Placement

Placement of the closed-loop poles and zero essentially involves selecting the damping ratio of the short period mode (ζ), the location of the close loop integrator pole (a) and the location of feed-forward zero (z_f). The pole/zero placements which follow are for the aircraft parameters and standard flight conditions as outlined in Appendix B.6.

From Figure 3.4a it can be seen that the open-loop poles of the short period mode have the following attributes,

$$\omega_{n_{ol}} \approx 10.3\,\text{rad/s} \qquad \zeta_{ol} \approx 0.63 \tag{3.2.44}$$

The closed-loop poles are now chosen to have a somewhat higher damping ratio of,

$$\zeta_{cl} = 0.707 \tag{3.2.45}$$

The integrator pole is placed at a frequency lower than that of the short period mode poles,

$$a = -4\,\text{rad/s} \tag{3.2.46}$$

The feed-forward zero is placed at a frequency twice that of the integrator pole to avoid excessive feed-forward whilst still removing some of the integrator dynamics from the reference input,

$$z_f = -8\,\text{rad/s} \tag{3.2.47}$$

The results of the pole/zero placement are shown in Figure 3.10. It can be seen that the natural frequency of the short period mode poles has decreased slightly whilst the damping has increased. The assumption made in §3.2.3.1 that the NMP nature of the NSA dynamics can be ignored if the natural frequency of both the open- and the closed-loop dominant poles of the system is at least three times slower than that of the NMP zero remains valid.

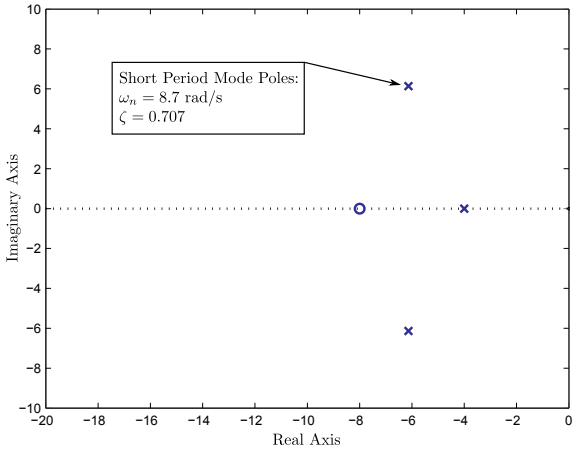

Figure 3.10 – Pole-zero map of the closed-loop elevator-based NSA controller

The NSA response to a reference step input can be seen in Figure 3.11a. The response is well damped, and has a rise time of,

$$t_{r_{63.2\%}} = 0.3\,\text{s} \tag{3.2.48}$$

The corresponding elevator deflection for this step input is shown in Figure 3.11b. It can be seen that for a NSA step of $1\,\text{m/s}^2$ the elevator remains well within the limits defined in Appendix B.5. The effect of the feed-forward term in the control law can also be seen clearly as the immediate jump in elevator deflection following the NSA command.

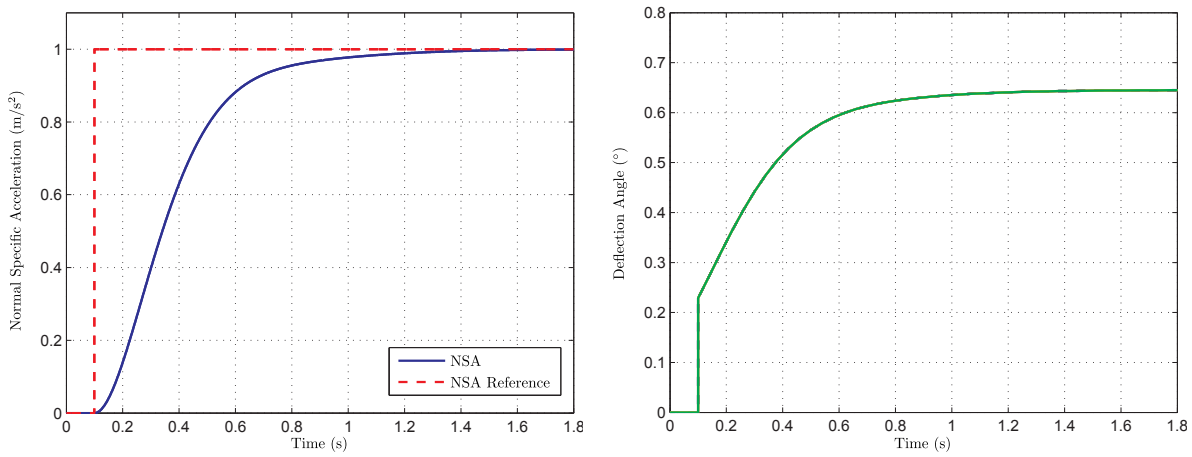

(a) Step response **(b)** Elevator deflection

Figure 3.11 – NSA step response to a reference NSA with corresponding elevator deflection for the elevator-based NSA controller

During HIL simulation and practical flight tests the control gains are often tuned slightly in order to achieve a satisfactory aircraft response. Figures 3.12a to 3.12c show what effect varying the control gains has on the closed-loop poles and zeros of the NSA controller. It can be seen in Figure 3.12a that increasing the pitch rate feedback gain $K_{Q_{\delta_E}}$ increases the damping and natural frequency of the short period mode poles, while it decreases the frequency of the closed-loop integrator pole. This gain therefore has the effect of slowing down the NSA step response and increasing the damping. Figure 3.12b shows that increasing the integrator feedback gain $K_{I_{\delta_E}}$ decreases the damping and natural frequency of the closed-loop short period mode poles and increases the frequency of the closed-loop integrator pole and feed-forward zero. This gain therefore has the effect of speeding up the NSA step response while increasing the overshoot. It can be seen in Figure 3.12c that increasing the feed-forward gain $\bar{N}_{C_{\delta_E}}$, decreases the frequency of the feed-forward zero. This has the effect of speeding up the NSA response.

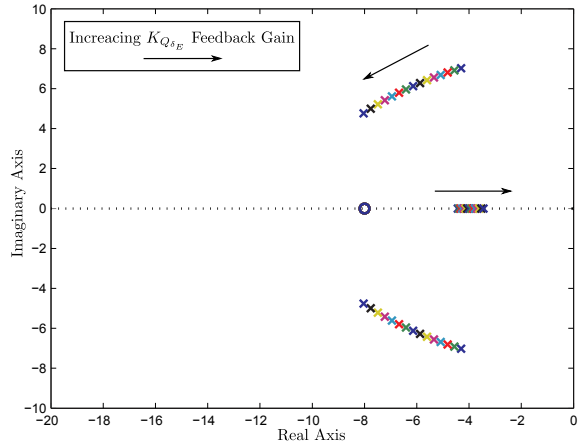

(a) Pitch rate feedback gain

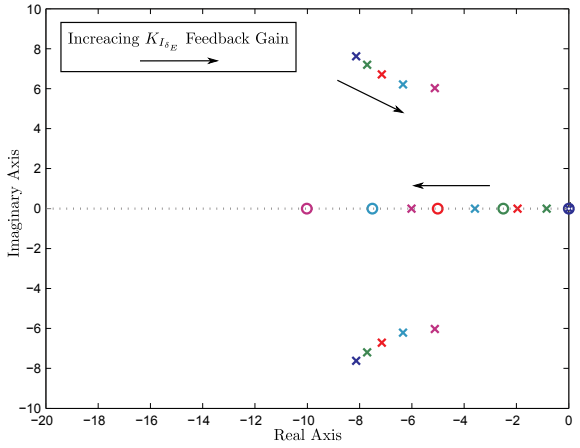

(b) Integrator feedback gain

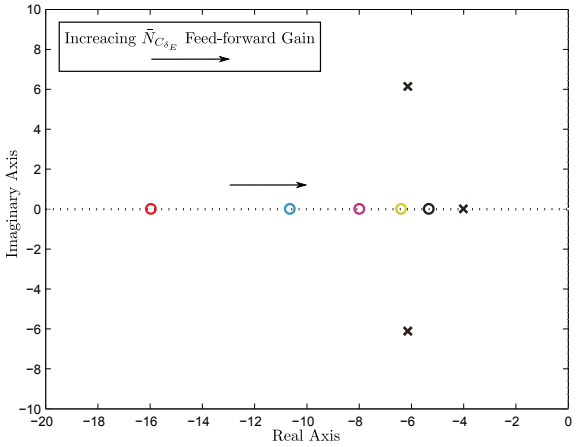

(c) Feed-forward gain

Figure 3.12 – Pole-zero map of the closed-loop elevator-based NSA controller for a change in the control gains

3.2.4.2 HIL Simulation and Practical Flight Test Results

The NSA controller was implemented on an OBC and tested in the HIL simulation environment as well as practically in a series of flight tests. The HIL simulation environment, aircraft, avionics and other hardware used in this project are outlined in Appendix B, only the results are presented in this section. The HIL tests allow the controller to be fully tested before practical flight tests are attempted. Ideally, the practical flight test results should closely resemble those achieved in the HIL simulation.

Figures 3.13a and 3.13b show typical HIL and practical flight test results of the NSA controller. The responses shown were selected since they give an approximate indication of a step response. It is clear that the NSA signal is significantly more noisy in the practical flight test than the HIL simulation. This is most likely due to the presence of wind gusts and other such disturbances, and it is possible to adjust the HIL simulation wind disturbance parameters to reflect a similar level of disturbance. Due to the high noise level it is difficult to gauge an accurate rise time for the NSA in the practical flight test. A better comparison between the HIL simulation and flight tests can be drawn by

examining the climbrate controller as shown in §3.3. The rise time of the HIL simulation and practical flight tests appear to be very slightly slower than that of the pure simulated NSA response. The difference can be explained due to uncertainties and unmodelled effects, however the design can be considered a success.

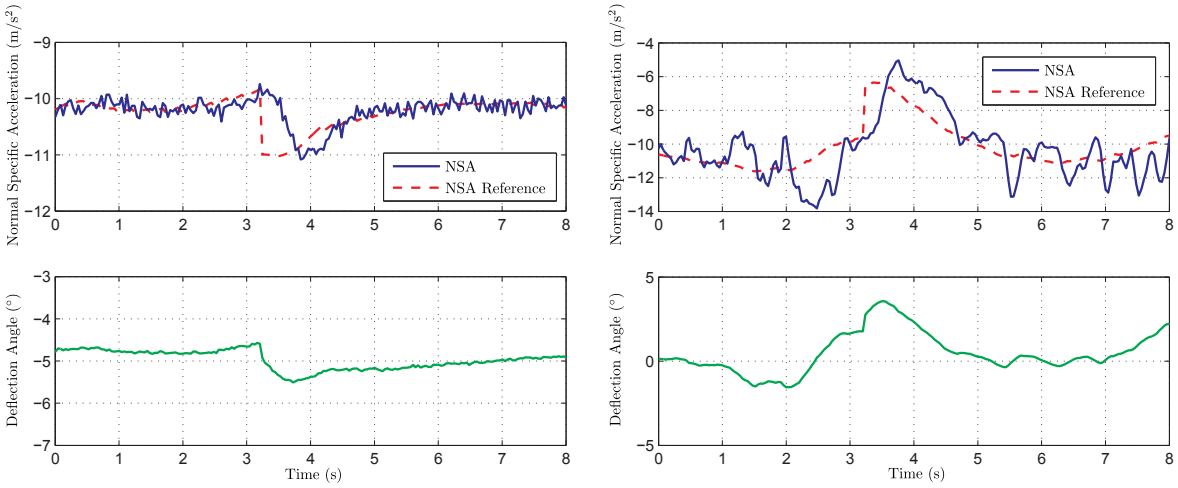

(a) HIL **(b)** Flight test

Figure 3.13 – NSA response to a reference along with corresponding elevator deflection for the elevator-based NSA controller during HIL and flight tests

3.2.5 NSA Controller Design - Flaps Actuator

This section presents the design of the flaps-based portion of the NSA controller. This controller uses the aircraft's flaps to create a commanded wind axes NSA through the principles of direct-lift longitudinal control as outlined in §3.1. As discussed in section §3.2.1, this controller will be superimposed with the moment-based NSA controller of §3.2.4. The detailed derivation of this controller is given in Appendix C.3.

After the simplifications in §3.2.3.2 the NSA dynamic equations for a flaps input are given by,

$$\begin{bmatrix}\dot{\alpha}\\ \dot{Q}\end{bmatrix} = \begin{bmatrix}-\frac{1}{mV}\bar{L}_{\alpha} & 1\\ \frac{1}{I_y}M_{\alpha} & \frac{1}{I_y}M_{Q}\end{bmatrix}\begin{bmatrix}\alpha\\ Q\end{bmatrix} + \begin{bmatrix}-\frac{1}{mV}\bar{L}_{\delta_F}\\ \frac{1}{I_y}M_{\delta_F}\end{bmatrix}\delta_F \tag{3.2.49}$$

$$\begin{bmatrix}C_W\\ Q\end{bmatrix} = \begin{bmatrix}-\frac{1}{m}\bar{L}_{\alpha} & 0\\ 0 & 1\end{bmatrix}\begin{bmatrix}\alpha\\ Q\end{bmatrix} + \begin{bmatrix}-\frac{1}{m}\bar{L}_{\delta_F}\\ 0\end{bmatrix}\delta_F \tag{3.2.50}$$

A flaps control law is now defined which uses proportional feedback from the NSA,

$$\delta_F = -K_{P_{\delta_F}}(C_W - C_W^{ref}) \tag{3.2.51}$$

Substituting the NSA output equation, C_W, from Equation 3.2.50 into Equation 3.2.51 yields,

$$\delta_F = -\frac{K_{P_{\delta_F}}}{1 - K_{P_{\delta_F}} \frac{\bar{L}_{\delta_F}}{m}} \left(\begin{bmatrix} -\frac{1}{m}\bar{L}_\alpha & 0 \end{bmatrix} \begin{bmatrix} \alpha \\ Q \end{bmatrix} - C_W^{ref} \right) \tag{3.2.52}$$

The control law is now substituted into the dynamics and the closed-loop system becomes,

$$\begin{bmatrix} \dot{\alpha} \\ \dot{Q} \end{bmatrix} = \begin{bmatrix} -\frac{\bar{L}_\alpha}{m\bar{V}} - \Delta \frac{\bar{L}_{\delta_F}\bar{L}_\alpha}{m^2\bar{V}} & 1 \\ \frac{M_\alpha}{I_y} + \Delta \frac{M_{\delta_F}\bar{L}_\alpha}{I_y m} & \frac{M_Q}{I_y} \end{bmatrix} \begin{bmatrix} \alpha \\ Q \end{bmatrix} + \begin{bmatrix} -\frac{\bar{L}_{\delta_F}}{m\bar{V}}\Delta \\ \frac{M_{\delta_F}}{I_y}\Delta \end{bmatrix} C_W^{ref} \tag{3.2.53}$$

$$\begin{bmatrix} C_W \\ Q \end{bmatrix} = \begin{bmatrix} -\frac{\bar{L}_\alpha}{m} - \Delta \frac{\bar{L}_{\delta_F}\bar{L}_\alpha}{m^2} & 0 \\ 0 & 1 \end{bmatrix} \begin{bmatrix} \alpha \\ Q \end{bmatrix} + \begin{bmatrix} -\frac{\bar{L}_{\delta_F}}{m}\Delta \\ 0 \end{bmatrix} C_W^{ref} \tag{3.2.54}$$

where,

$$\Delta = \left(\frac{K_{P_{\delta_F}}}{1 - K_{P_{\delta_F}} \frac{\bar{L}_{\delta_F}}{m}} \right) \tag{3.2.55}$$

The transfer function for the NSA response to a reference NSA input can be determined from Equations 3.2.53 to 3.2.55,

$$G_{C_W^{ref}}^{C_W}(s) = \frac{\left[-\frac{\bar{L}_{\delta_F}}{m}\Delta \right] \left[s^2 - \frac{M_Q}{I_y}s + \left(\frac{\bar{L}_\alpha}{\bar{L}_{\delta_F}} \frac{M_{\delta_F}}{I_y} - \frac{M_\alpha}{I_y} \right) \right]}{s^2 + s\left(\frac{\bar{L}_\alpha}{m\bar{V}} + \Delta \frac{\bar{L}_{\delta_F}\bar{L}_\alpha}{m^2\bar{V}} - \frac{M_Q}{I_y} \right) - \left(\frac{M_Q}{I_y}\frac{\bar{L}_\alpha}{m\bar{V}} + \frac{M_Q}{I_y}\Delta \frac{\bar{L}_{\delta_F}\bar{L}_\alpha}{m^2\bar{V}} \right) + \left(-\frac{M_\alpha}{I_y} - \Delta \frac{M_{\delta_F}\bar{L}_\alpha}{I_y m} \right)} \tag{3.2.56}$$

It can be seen in the transfer function of Equation 3.2.56 that the feedback gain $K_{P_{\delta_F}}$ does not have an effect on the location of the closed-loop zeros but does have an effect on the location of the closed-loop poles and on the steady state gain of the closed-loop system. In order to place the closed-loop poles a desired characteristic equation is defined as,

$$\alpha_c(s) = (s^2 + 2\zeta\omega_n s + \omega_n^2) \tag{3.2.57}$$

Equating the characteristic equation (the denominator of the transfer function of Equation 3.2.56) with the desired characteristic equation allows for two equations for Δ to be derived,

$$\Delta = \frac{m^2\bar{V}}{\bar{L}_{\delta_F}\bar{L}_\alpha} \left(2\zeta\omega_n - \frac{\bar{L}_\alpha}{m\bar{V}} + \frac{M_Q}{I_y} \right) \tag{3.2.58}$$

and,

$$\Delta = -\frac{\left(\omega_n^2 I_y m^2\bar{V} + M_Q\bar{L}_\alpha m + M_\alpha m^2\bar{V} \right)}{\left(M_Q\bar{L}_{\delta_F}\bar{L}_\alpha + M_{\delta_F}\bar{L}_\alpha m\bar{V} \right)} \tag{3.2.59}$$

By substituting Equation 3.2.58 into Equation 3.2.59 an equation for the natural frequency ω_n can be determined,

$$\bar{L}_{\delta_F} I_y^2 \omega_n^2 + 2\zeta\omega_n \left(M_Q\bar{L}_{\delta_F} I_y + M_{\delta_F} I_y m\bar{V} \right) + M_Q^2\bar{L}_{\delta_F} + M_Q M_{\delta_F} m\bar{V} - \bar{L}_\alpha M_{\delta_F} I_y + \bar{L}_{\delta_F} M_\alpha I_y = 0 \tag{3.2.60}$$

Solving for the positive values of ω_n the closed-loop natural frequency is given by,

$$\omega_n = \frac{-\zeta\eta + \sqrt{(\zeta\eta)^2 - \bar{L}_{\delta_F} I_y^2 \left(M_Q^2 \bar{L}_{\delta_F} + M_Q M_{\delta_F} m\bar{V} - \bar{L}_\alpha M_{\delta_F} I_y + \bar{L}_{\delta_F} M_\alpha I_y\right)}}{\bar{L}_{\delta_F} I_y^2} \tag{3.2.61}$$

where,

$$\eta = M_Q \bar{L}_{\delta_F} I_y + M_{\delta_F} I_y m\bar{V} \tag{3.2.62}$$

Substituting Equations 3.2.61 and 3.2.62 into Equations 3.2.58 and 3.2.59 respectively, allows the derivation of two equations for the feedback gain $K_{P_{\delta_F}}$,

$$K_{P_{\delta_F}} = \frac{m}{\bar{L}_{\delta_F}} - \frac{\bar{L}_\alpha}{\bar{L}_{\delta_F}\bar{V}\left(2\zeta\omega_n + \frac{M_Q}{I_y}\right)} \tag{3.2.63}$$

and,

$$K_{P_{\delta_F}} = -\frac{\omega_n^2 I_y m\bar{V} + M_Q\bar{L}_\alpha + M_\alpha m\bar{V}}{M_{\delta_F}\bar{L}_\alpha\bar{V} - \bar{L}_{\delta_F}\omega_n^2 I_y\bar{V} - \bar{L}_{\delta_F}M_\alpha\bar{V}} \tag{3.2.64}$$

3.2.5.1 Pole/Zero Placement

The direct-lift portion of the NSA controller only acts on higher frequency NSA components, therefore the long term response of the aircraft is entirely conventional and dependent on the elevator-based portion of the NSA controller of §3.2.4. The pole/zero placement strategy in this section is therefore not focused on obtaining a specific NSA response but rather to obtain a response which will yield an improvement in the *overall* NSA controller. Such improvement is explored in §3.2.6. The pole/zero placements which follow are for the aircraft parameters and standard flight conditions as outlined in Appendix B.6.

The transfer function for an NSA response to a reference NSA input is restated for convenience,

$$G_{C_W^{ref}}^{C_W}(s) = \frac{\left[-\frac{\bar{L}_{\delta_F}}{m}\Delta\right]\left[s^2 - \frac{M_Q}{I_y}s + \left(\frac{\bar{L}_\alpha}{\bar{L}_{\delta_F}}\frac{M_{\delta_F}}{I_y} - \frac{M_\alpha}{I_y}\right)\right]}{s^2 + s\left(\frac{\bar{L}_\alpha}{m\bar{V}} + \Delta\frac{\bar{L}_{\delta_F}\bar{L}_\alpha}{m^2\bar{V}} - \frac{M_Q}{I_y}\right) - \left(\frac{M_Q}{I_y}\frac{\bar{L}_\alpha}{m\bar{V}} + \frac{M_Q}{I_y}\Delta\frac{\bar{L}_{\delta_F}\bar{L}_\alpha}{m^2\bar{V}}\right) + \left(-\frac{M_\alpha}{I_y} - \Delta\frac{M_{\delta_F}\bar{L}_\alpha}{I_y m}\right)} \tag{3.2.65}$$

where,

$$\Delta = \left(\frac{K_{P_{\delta_F}}}{1 - K_{P_{\delta_F}}\frac{\bar{L}_{\delta_F}}{m}}\right) \tag{3.2.66}$$

As seen in the transfer function of Equation 3.2.65 the feedback gain $K_{P_{\delta_F}}$ does not have an effect on the location of the closed-loop zeros. It is only possible to place the poles and change the steady state gain of the system, both of which are interlinked.

To gain further insight into the behaviour of the system, it is useful to look at the pole-zero map and step response of the closed-loop transfer function for a range of feedback gains. Figure 3.14 shows the location of the poles and zeros for several different values

of the feedback gain $K_{P_{\delta_F}}$. It can be seen that as the gain increases the poles move towards the zeros. The location of the zeros remains unchanged. Therefore, as the feedback gain increases, the response will become more like a pure gain as the poles and zeros begin to cancel each other out.

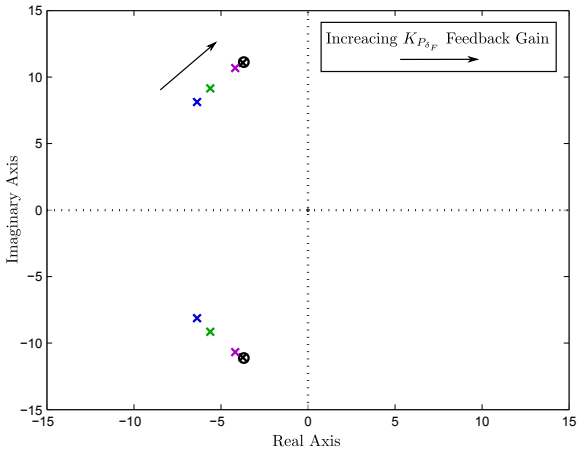

Figure 3.14 – Pole-zero map of the closed-loop flaps-based NSA controller

The insight gained in the pole-zero map of Figure 3.14 is again reflected in the step response of the transfer function as shown in Figure 3.15a. It can be seen that as the feedback gain increases, the steady state NSA value increases and the transient component of the response becomes smaller. The flap deflection angle corresponding to these step responses is shown in Figure 3.15b. Here it can be seen that as the gain increases, the required flaps deflection angle increases, and the flaps exhibit increasing damped oscillating behaviour.

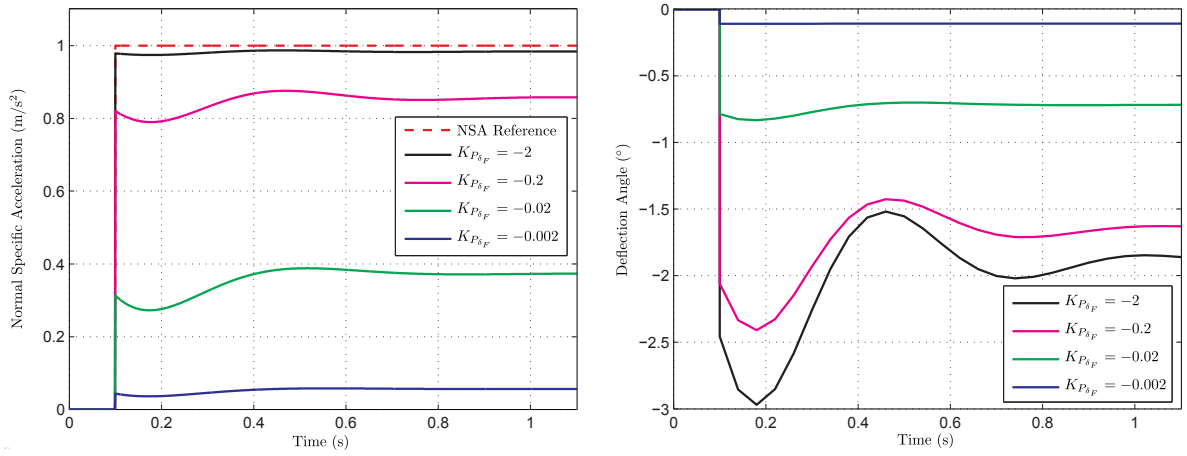

(a) Step response **(b)** Flaps deflection

Figure 3.15 – NSA step responses to a reference NSA with corresponding flaps deflection of the flaps-based NSA controller for a range of feedback gains

From the preceding analysis it follows that a high feedback gain will result in a good response with little transient components and a small steady state error. However, this

could result in a required flap deflection which is beyond the physical limits of the aircraft. Placement of the closed-loop poles is therefore a trade-off between response magnitude and control effort required. For the aircraft used in this project the limits of the flaps deflection angle are (see Appendix B.5),

$$-5^\circ \geq \delta_F \leq 5^\circ \tag{3.2.67}$$

Ideally, the feedback gain selected should be the largest possible where the reference NSA input will not cause the controller to exceed the deflection angle limits of the flaps. If a reasonable assumption is made regarding the maximum NSA demand expected during flight, the feedback gain can be selected such that the flaps deflection limits are not exceeded for such a control demand. This NSA demand will need to be established through flight tests and HIL simulation, but a reasonable assumption is made that,

$$-3\,\text{m/s}^2 \geq C_W^{ref} \leq 3\,\text{m/s}^2 \tag{3.2.68}$$

These requirements result in a feedback gain which is used during simulation of the complete NSA controller of §3.2.6. These simulations and subsequent flight tests show that a lower feedback gain resulted in a more satisfactory overall response. Therefore, this gain has been retroactively applied to be the result of the analysis of the rest of this section. For a damping ratio of,

$$\zeta_{cl} = 0.523 \tag{3.2.69}$$

the closed-loop natural frequency can be calculated using Equations 3.2.61 and 3.2.62 as,

$$\omega_{n_{cl}} \approx 10.78\,\text{rad/s} \tag{3.2.70}$$

The feedback gain can be calculated from either Equation 3.2.63 or Equation 3.2.64 giving,

$$K_{P_{\delta_F}} = -0.02 \tag{3.2.71}$$

This gain, along with the values for the aerodynamic derivatives, standard flight conditions and aircraft parameters (see Appendix B.6) are substituted into the transfer function of Equation 3.2.65 giving,

$$G_{C_W^{ref}}^{C_W}(s) = \frac{0.3133s^2 - 7.39s - 138.4}{s^2 + 11.27s + 116.2} = \frac{0.3133(s + 3.6949 + 11.1712\text{i})(s + 3.6949 - 11.1712\text{i})}{(s + 5.6354 + 9.1887\text{i})(s + 5.6354 - 9.1887\text{i})} \tag{3.2.72}$$

The pole-zero map and step response of this transfer function are also shown in Figures 3.14 and 3.15. It can be seen in Figure 3.15a that the response consists of two parts. The first is the initial jump in NSA up to the value of the steady state gain of the transfer

function, followed by a transient resulting in an initial slight decrease followed by a slight increase in NSA as the response settles. The flap deflection angle corresponding to this step responses is shown in Figure 3.15b where it can be seen that the deflection angle remains well within the limits of Equation 3.2.67.

It is apparent that the step response for this pole placement only achieves about a third of the reference NSA. This is usually unacceptable from a control design perspective, however, since the design consideration is to improve the *overall* NSA response, it proves to be a successful design as shown in §3.2.6.

3.2.6 NSA Controller Design - Elevator and Flaps Combined

This section presents the design of the overall NSA controller where both the elevator and the flaps are used as actuators. As discussed in the NSA controller strategy of §3.2.1, the flaps-based portion of the NSA controller must be superimposed on the elevator-based portion of the NSA controller. To overcome the problem of proper control allocation, and in order to superimpose the flaps-based NSA controller in transient form, the two NSA controllers are separated in frequency. This frequency separation is achieved by a complementary filter pair on the NSA controller signals. The controller configuration is shown diagrammatically in Figure 3.2.

In this design there are several parameters of interest namely the cut-off frequency of the complementary filter pair ω_C, the gain of the flaps-based portion of the NSA controller $K_{P_{\delta_F}}$ and the gearing between the flaps and the elevator K_M. The parameters of the elevator-based portion of the NSA controller are considered fixed and as shown in §3.2.4. In order to determine which combination of these parameters will yield the best result, the controller is simulated in Matlab Simulink as shown in Figure 3.16. This process is largely iterative, and is focused on the step response and disturbance rejection characteristics of the controller.

During the HIL and subsequent flight tests of this controller it was found that the following set of parameters lead to an acceptable controller response,

$$\omega_C = 4\,\text{rad/s} \qquad K_{P_{\delta_F}} = -0.02 \qquad K_M = 0.2 \tag{3.2.73}$$

These gains are somewhat lower than what the simulation suggests is feasible. However, the parameters of Equation 3.2.73 still lead to an improvement over the conventional elevator-based NSA controller of §3.2.4. The cause of this discrepancy is discussed in §3.2.6.1. Each of these parameters is now investigated in order to illustrate their effect on the response of the NSA controller.

Complementary Filter The complementary filter pair consists of first order low-pass filters on the NSA reference and feedback signals of the elevator-based portion of the controller, and first order high-pass filters on the NSA signals of the flaps-based portion

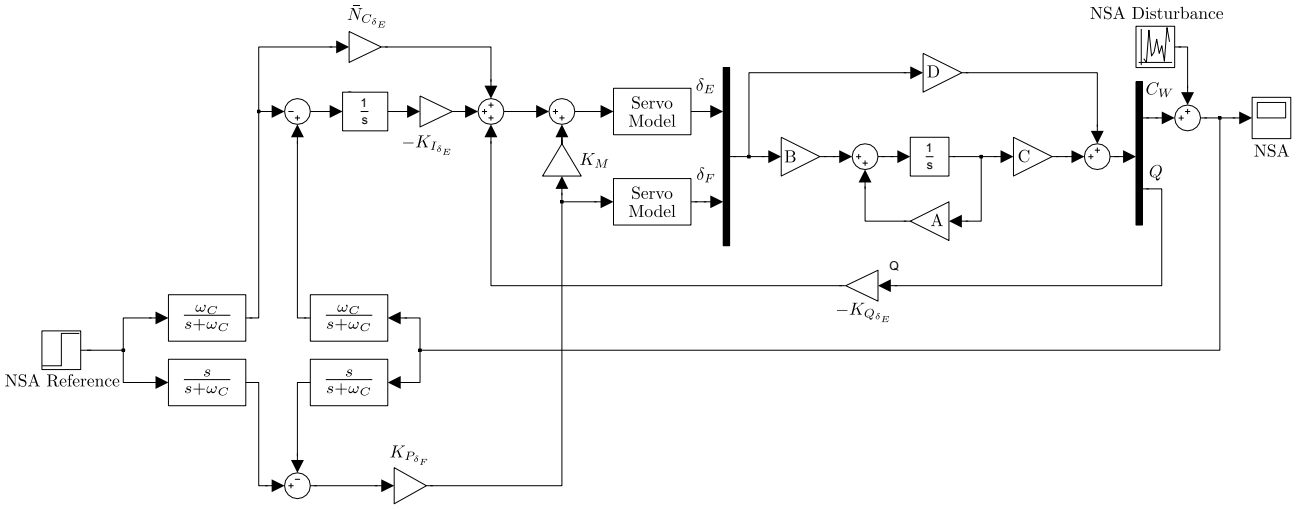

Figure 3.16 – Simulink block diagram of the direct-lift-augmented NSA controller

of the controller. These filters have the effect that the elevator will respond to NSA signals below the cut-off frequency and the flaps to NSA signals above the cut-off frequency of the filter, with some overlap in between.

During simulation it was found that, for relatively low values of flaps feedback gain, applying a low-pass filter on the NSA signals of the elevator-based portion of the controller leads to weakened response characteristics. This is due to the limited amount of direct-lift available at low flaps feedback gains which means that only a part of the NSA demand is achieved as shown in Figure 3.15. Under these conditions limiting the frequency range in which the elevator-based portion of the controller acts, results in degraded performance since the flaps do not have sufficient control authority to compensate for the loss of higher frequency elevator control. If the flaps feedback gain were made sufficiently high, then enough direct-lift is available for the filter to be used without degrading performance. Unfortunately practical limitations exist which prohibit the flaps gain from being made high enough as discussed in §3.2.6.1. Alternatively, placing the cut-off frequency of the filter much higher also eliminates this problem, however this then also means that disturbances available to the flaps-based controller to be rejected are far fewer, therefore under-utilising its disturbance rejection capabilities.

To overcome this limitation, the NSA signals to the elevator-based portion of the controller are not filtered. This can be considered an acceptable deviation from the control strategy of §3.2.1 since the dominant closed-loop pole of the elevator-based controller effectively acts as a low-pass filter. In light of this, the cut-off frequency for the high-pass filters is chosen to coincide with that of the dominant closed-loop pole of the elevator-based NSA controller as shown in Figure 3.10. Omitting the low-pass filter means that there will now be a greater overlap between the elevator and flaps portions of the controller. This will result in situations where the flaps and the elevator portions of the controller act on the same signal which raises the question of interference between them. However, it was found during simulations that since the flaps only produce a part of the

NSA demand there is never a situation where it overpowers the elevator portion of the controller. The flaps serve to simply augment the elevator at higher frequencies.

Flaps Feedback Gain The flaps-based portion of the controller makes use of proportional feedback from the high-pass filtered NSA reference and feedback signals. In order to illustrate the effect of the flaps feedback gain $K_{P_{\delta_F}}$ the step response for a range of feedback gains is shown in Figure 3.17. Here the cut-off frequency is as in Equation 3.2.73 and there is no gearing between the flaps and the elevator. It can be seen that as the gain increases, the initial step in NSA due to the direct-lift component of the flaps controller becomes more pronounced. This results in faster rise times, however it comes at the cost of greatly increased settling time due to oscillation induced in the response, as well as greater flaps deflection demand. It is possible to design a controller with the higher feedback gains which functions in simulation, however, practical limitations encountered during flight tests indicate that the gain be chosen as,

$$K_{P_{\delta_F}} = -0.02 \tag{3.2.74}$$

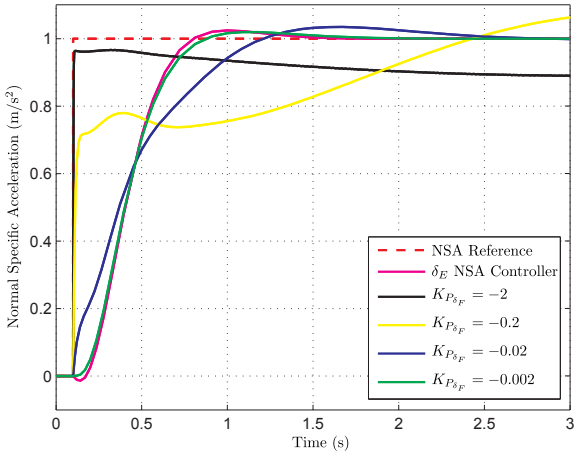

Figure 3.17 – Step response of the combined elevator and flaps NSA controller for a range of flaps feedback gains

Flaps to elevator gearing The gain K_M represents the gearing required between the flaps and the elevator in order for the elevator to cancel out any unwanted moment produced by the flaps. As stated in §3.2.3.2 this gearing can be selected such that the elevator does not cancel out the moment produced by the flaps perfectly, but rather increases or decreases the net moment acting on the aircraft. In this way the response can be tuned to obtain a satisfactory result. In order to illustrate this effect, the NSA step response is shown for a range of gearing ratios. Here the cut-off frequency and flaps feedback gain are as Equation 3.2.73.

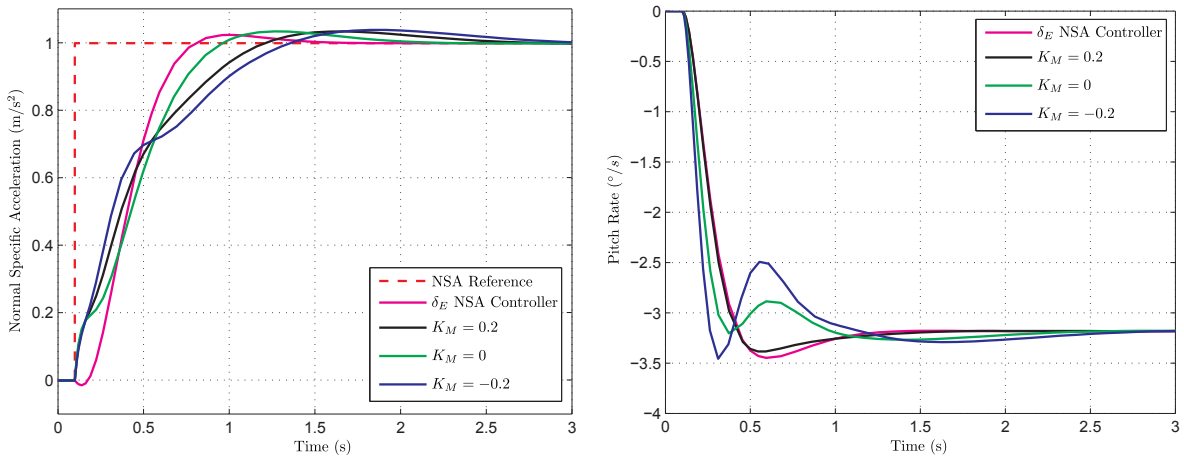

(a) NSA step response **(b)** Pitch rate response

Figure 3.18 – NSA step response with corresponding pitch rate response of the combined elevator and flaps NSA controller for a range of flaps to elevator gearing ratios

It can be seen in Figure 3.18b that for a gearing ratio of 0.2 the pitch rate response of the elevator-based controller is nearly identical to that of the elevator and flaps combined controller. This shows that the moment produced by the flaps deflection has been mostly cancelled out by the gearing to the elevator. Examination of the dimensionless pitch moment derivative of the elevator and flaps as given by Table 3.1 shows that the ratio between these derivatives is, as expected, also approximately 0.2. It can be seen that for a gearing ratio of -0.2 the elevator is adding to the moment produced by the flap deflection. This has the effect of speeding up the pitch rate as well as the NSA response up to a point. HIL simulation and practical flight tests indicate that the gearing ratio be chosen as,

$$K_M = 0.2 \tag{3.2.75}$$

Disturbance rejection With the controller parameters now fixed, the disturbance rejection capabilities of the controller are demonstrated. Figure 3.19 shows the controller attempting to follow a constant NSA reference in the presence of a disturbance. It can be seen that the controller, making use of both flaps and elevator, follows the reference signal more closely. The disturbance rejection can be improved greatly by increasing the flaps feedback gain, however certain practical limitations to this arise as discussed in §3.2.6.1.

3.2.6.1 HIL Simulation and Practical Flight Test Results

The NSA controller was implemented on an OBC and tested in the HIL simulation environment as well as practically in a series of flight tests. The HIL simulation environment, aircraft, avionics and other hardware used in this project are outlined in Appendix B, only the results are presented in this section. The HIL tests allow the controller to be

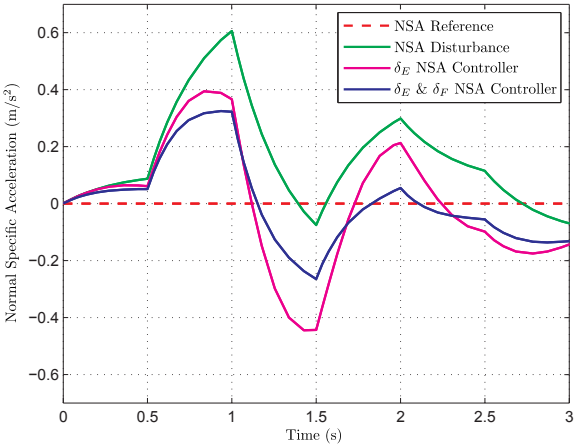

Figure 3.19 – NSA reference following in the presence of an NSA disturbance

fully tested before practical flight tests are attempted. Ideally, the practical flight test results should closely resemble those achieved in the HIL simulation.

The amount of noise and disturbances on the NSA signal make it difficult to evaluate the controller's performance directly. It is therefore useful to simultaneously examine the climb rate performance of the aircraft since the NSA controller has a direct effect on how well the climb rate controller functions. This allows a comparison to be made between the conventional and direct-lift-augmented NSA controllers. Figures 3.20a and 3.20b show the climb rate and corresponding NSA response of the conventional and direct-lift-augmented NSA controllers during HIL simulation, and Figures 3.20c and 3.20d show the same during practical flight tests. Firstly, it can be seen that in general the responses of the HIL simulation correspond very well with those obtained during flight tests, thus confirming the validity of the aircraft model used to design the controllers. The exception to this is the NSA signals where it can be seen that during the flight tests the NSA signal is significantly more noisy than during the HIL simulation. It is however possible to obtain similar NSA signals in the HIL simulation environment by adjusting the model's noise parameters. The origin of this noise is examined further in the subsequent analysis of the direct-lift-augmented NSA controller.

Secondly, a comparison can be made between the conventional and direct-lift-augmented NSA controllers by examining the flight test plots since the differences are more apparent than in the HIL simulation. The data shown are of two separate flight tests where the reference climb rates are very similar. Unfortunately, atmospheric conditions differ between the two flight tests, such that an exact comparison cannot be made but is is still possible to gauge the general performance of the two controllers. It must be noted that the atmospheric conditions during the conventional NSA controller test were more favourable than during the direct-lift-augmented NSA controller test. It can be seen in Figure 3.20c that the direct-lift-augmented NSA controller shows a somewhat faster climb rate response than the conventional NSA controller. The corresponding NSA response shown in Figure 3.20d does not reveal much other than the presence of

significant disturbances.

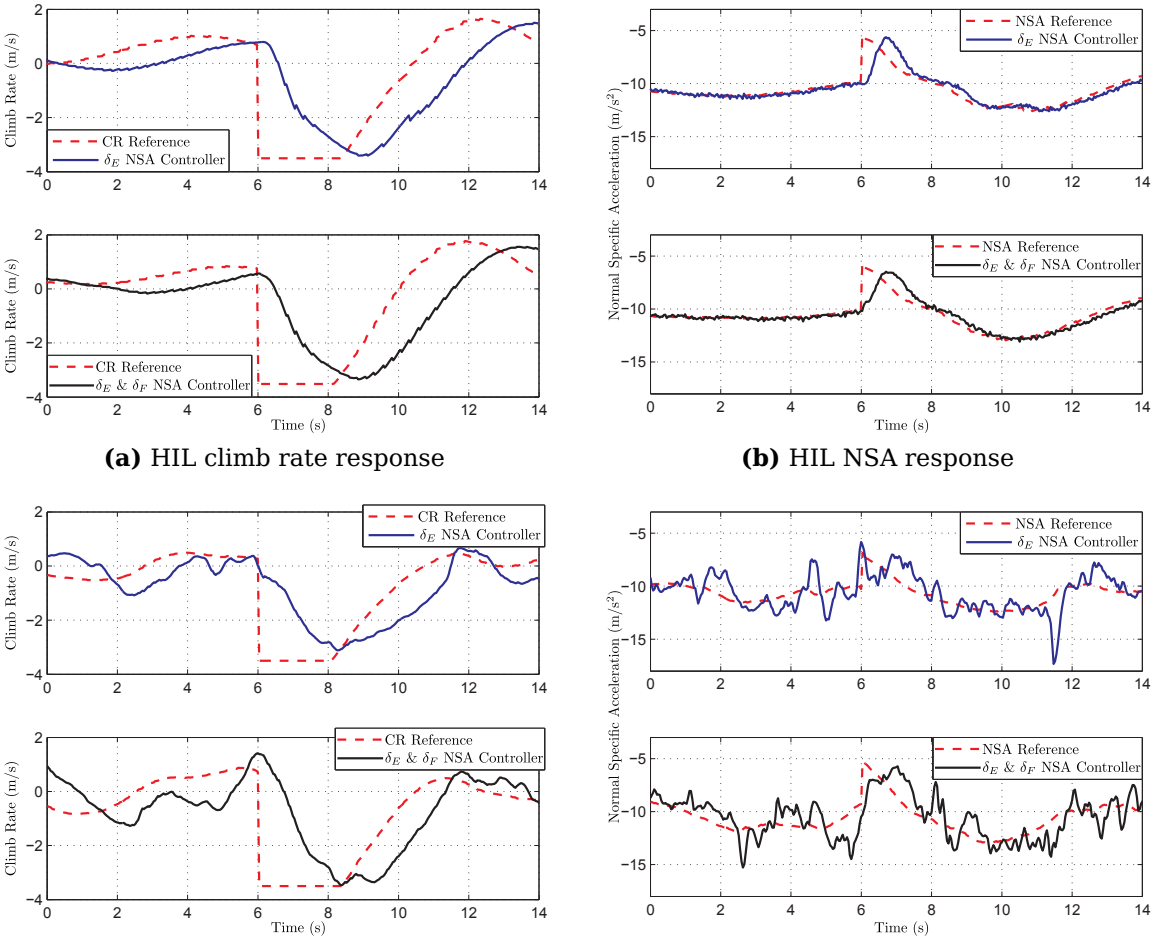

(a) HIL climb rate response

(b) HIL NSA response

(c) Flight test climb rate response

(d) Flight test NSA response

Figure 3.20 – Climb rate and corresponding NSA response for the conventional and direct-lift-augmented NSA controllers during HIL and flight tests

The flaps-based portion of the NSA controller makes use of high-pass filtered NSA and reference NSA signals as shown in Figure 3.16. These signals are shown in Figure 3.21 for the same HIL simulation and flight tests as in Figure 3.20. It can be seen in the upper plot of Figure 3.21a that in the HIL simulation there is a slight difference in the high-pass filtered NSA signals of the conventional and direct-lift-augmented NSA controllers after the climb rate step time. The direct-lift-augmented NSA controller responds faster than the conventional NSA controller as can be seen in the initial jump in NSA after the climb rate step. This response is similar in form to that seen during the controller design as depicted in Figure 3.18a and is the result of the direct-lift component of the flaps deflection.

It can be seen in the upper plot of Figure 3.21b that during the flight tests, the magnitude of the high-pass filtered NSA signal is on average slightly less for the direct-lift-augmented NSA controller than for the conventional NSA controller. This is to be expected since one of the functions of the flaps is to counter high-frequency NSA dis-

turbances. It must be noted that there is an improvement over the conventional NSA controller in spite of the fact that the atmospheric conditions were less favourable during the direct-lift-augmented NSA controller test.

The lower plot in Figures 3.21a and 3.21b show the high-pass filtered NSA reference signal which originates from the climb rate controller of §3.3. The error between this signal and that of the high-pass filtered NSA signal in the upper plot of Figures 3.21a and 3.21b, is used in conjunction with the flaps feedback gain in order to determine the required flaps deflection. As expected, this signal remains fairly small for most climb rate controller demands, however during the climb rate step it can be seen that an immediate NSA demand is generated which subsequently dies down due the effect of the high-pass filter. The direct-lift portion of the NSA controller therefore receives a large input which it can immediately respond to due to the direct-lift component of the flaps deflection. This allows the direct-lift-augmented NSA controller to achieve a faster response as demonstrated by the faster climb rate step shown in Figure 3.20c.

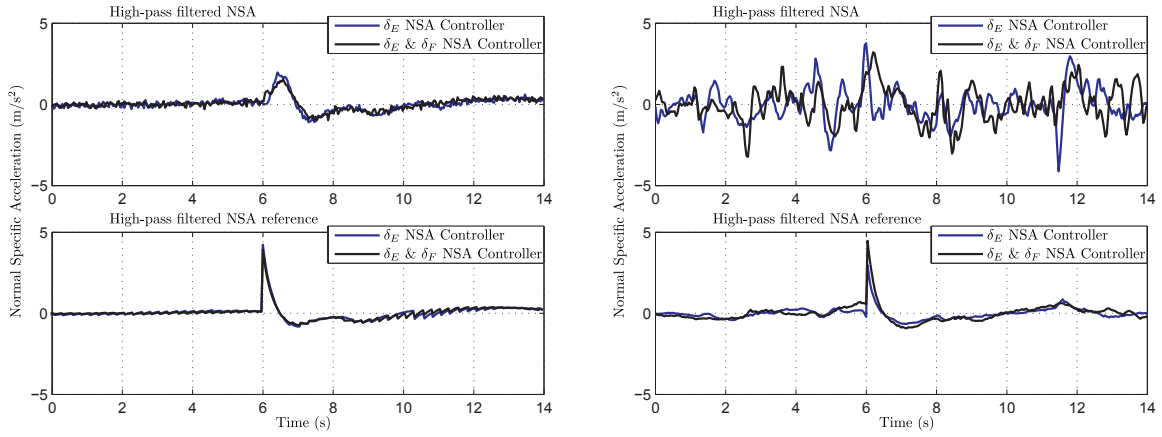

(a) HIL NSA signals **(b)** Flight test NSA signals

Figure 3.21 – High-pass filtered NSA and NSA reference signals during HIL and flight tests

Figures 3.22a and 3.22b show the error between the high-pass filtered NSA and NSA reference signals, and the corresponding actuator deflections for the HIL simulation, and Figures 3.22c and 3.22d show the same during practical flight tests. In these figure it can again be seen that there is a large amount of noise on the NSA signal since the error fluctuates considerably. It can also be seen that the maximum error is greater for the conventional NSA controller than for the direct-lift-augmented NSA controller. The actuator deflection plots show that both the elevator and the flaps remain well within their respective deflection limits. The elevator deflection for the direct-lift augmented NSA controller shows small fluctuations on top of its main response. These are the component of the elevator deflection which is geared from the flaps in order to cancel out the moment produced by the flaps.

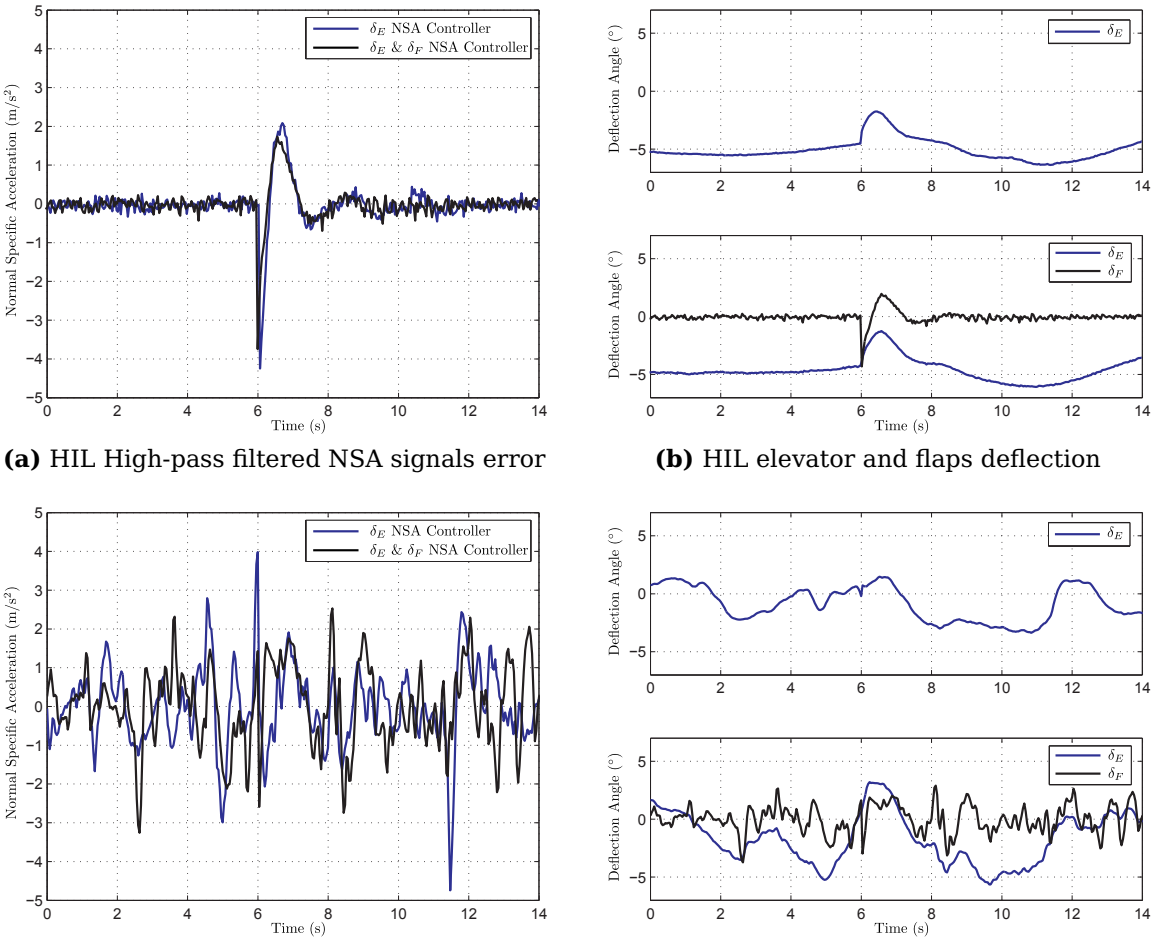

(a) HIL High-pass filtered NSA signals error

(b) HIL elevator and flaps deflection

(c) Flight test High-pass filtered NSA signals error

(d) Flight test elevator and flaps deflection

Figure 3.22 – Step response of the combined elevator and flaps NSA controller for a range of flaps to elevator gearing ratios

As discussed previously, there is a fairly large amount of noise on the NSA signal. This noise is far greater than the measurement noise of the accelerometers used in this project (see Appendix B). The origin of this noise is therefore most likely a combination of atmospheric disturbances and unmodelled effects such as engine noise. True atmospheric disturbances should be attenuated by the flaps-based NSA controller, and this effect is seen in the results of this section. However, it was expected that this effect would be greater. A possible explanation for this is that some of the excess noise is not aerodynamic in origin, therefore when the flaps attempt to counteract this disturbance they might instead be adding to the true disturbance. This is also suggested by the fact that the flaps feedback gain used had to be much lower than the simulation suggested in order to achieve a stable controller. It might therefore be necessary to revise the control law of the flaps-based portion of the NSA controller to mitigate this effect. One such option would be to augment a fast integrator on the NSA signal similar to that of the elevator-based NSA controller of §3.2.4. The time constraints of this project do not allow such a controller to be tested but initial simulations show that the strategy does hold promise and that further investigation is warranted.

3.3 Climb Rate Controller

This section describes the design, simulation and practical testing of a climb rate controller. This controller regulates the climb rate of the aircraft by making use of either the conventional NSA controller of §3.2.4 or the direct-lift-augmented NSA controller of §3.2.6. The input to the climb rate controller stems from the *altitude* controller of §3.4, which creates a commanded altitude by commanding the climb rate controller. The controller is designed in the navigation axis system as shown in Figure 2.4. It is therefore assumed that the NSA vector of the aircraft is always pointing up normal to the flat earth. This assumption is valid as long as the flight path angle remains small and the effect of the aircraft's roll orientation is compensated for by the guidance controller as shown in §4.4.

It must be noted that the climb rate controller is designed independent of the airspeed dynamics. This is despite the coupling which exists between the airspeed and climb rate dynamics. Typically, this coupling is addressed by designing a multi-input-multi-output (MIMO) airspeed and climb rate controller. Linear Quadratic Regulator (LQR) theory is often used for this purpose as demonstrated by [8]. In such a controller strategy, the airspeed and climb rate commands are both achieved by a combination of the throttle and longitudinal aerodynamic actuators. To illustrate this, consider an airspeed step; the throttle command will increase to achieve the greater airspeed demand, and the elevator actuator will cause a downwards climb rate which *also* serves to increase the airspeed. The relative amounts of actuation used is determined by the weighting matrices of the LQR design. It is therefore clear that applying such a controller to this project will make the relationship between the NSA controller and the climb rate of the aircraft become significantly less clear. This is especially important since the conventional moment-based NSA controller must be adequately compared to the direct-lift-augmented NSA controller. The climb rate and airspeed controllers will therefore be designed completely separately from one another under the assumption that the airspeed is maintained sufficiently well by the airspeed controller. As shown in the airspeed controller design of §3.5, the gravitational coupling into the airspeed dynamics is also compensated for, which further aids in separating the airspeed and climb rate controllers.

3.3.1 Design

The basic model for the aircraft's climb rate dynamics is given by,

$$\dot{V}_h = \begin{bmatrix} 0 \end{bmatrix} \begin{bmatrix} V_h \end{bmatrix} + \begin{bmatrix} 1 \end{bmatrix} C_N \tag{3.3.1}$$

where V_h is the climb rate and C_N the normal specific acceleration of the aircraft in the navigation axis system.

The dominant closed-loop pole of the NSA controller is located at $4\,$rad/s as shown in §3.10. If the climb rate dynamics are to be timescale separated from the normal dynam-

ics, then by the generally held design rule, the climb rate dynamics bandwidth should be at least five times less than that of the normal dynamics. Such a pole placement will lead to an unacceptably slow climb rate response. If however the dynamics of the NSA controller are taken into account during the design of the climb rate controller, then the frequency separation requirement falls away and the climb rate controller poles can be placed at a somewhat higher frequency. To accomplish this the NSA controller can be approximated with a simple first order lag and the climb rate dynamics augmented accordingly,

$$\begin{bmatrix} \dot{V}_h \\ \ddot{V}_h \end{bmatrix} = \begin{bmatrix} 0 & 1 \\ 0 & -\dfrac{1}{\tau_{\text{NSA}}} \end{bmatrix} \begin{bmatrix} V_h \\ \dot{V}_h \end{bmatrix} + \begin{bmatrix} 0 \\ \dfrac{1}{\tau_{\text{NSA}}} \end{bmatrix} C_N^{ref} \tag{3.3.2}$$

$$V_h = \begin{bmatrix} 1 & 0 \end{bmatrix} \begin{bmatrix} V_h \\ \dot{V}_h \end{bmatrix} \tag{3.3.3}$$

where τ_{NSA} is the time constant of the dominant closed-loop pole of the NSA controller and C_N^{ref} is the component of commanded NSA in the navigation axis system. C_N^{ref} can be considered a virtual actuator of this system and it is assumed that any command is instantly met. Approximating the NSA controller with a first order lag is only truly valid for the conventional moment-based NSA controller since for the direct-lift-augmented NSA controller a part of the NSA is generated almost instantaneously as shown in Figure 3.18a. This means that the climb rate response for the direct-lift-augmented NSA controller will be somewhat faster than the design in this section suggests.

A control law is now defined which uses proportional feedback from the climb rate,

$$\begin{aligned} C_N^{ref} &= -K_{P_{CR}} \left(V_h - V_h^{ref} \right) \\ &= -K_{P_{CR}} \left(\begin{bmatrix} 1 & 0 \end{bmatrix} \begin{bmatrix} V_h \\ \dot{V}_h \end{bmatrix} - V_h^{ref} \right) \end{aligned} \tag{3.3.4}$$

where V_h^{ref} is the reference climb rate command. The control law is now substituted into the dynamics and the closed-loop system becomes,

$$\begin{bmatrix} \dot{V}_h \\ \ddot{V}_h \end{bmatrix} = \begin{bmatrix} 0 & 1 \\ -K_{P_{CR}}\, a_{\text{NSA}} & -a_{\text{NSA}} \end{bmatrix} \begin{bmatrix} V_h \\ \dot{V}_h \end{bmatrix} + \begin{bmatrix} 0 \\ K_{P_{CR}}\, a_{\text{NSA}} \end{bmatrix} V_h^{ref} \tag{3.3.5}$$

where,

$$a_{\text{NSA}} = \frac{1}{\tau_{\text{NSA}}} \tag{3.3.6}$$

is the location of the closed-loop integrator pole of the NSA dynamics as described in §3.2.4.

Calculating the closed-loop characteristic equation gives,

$$p(s) = s^2 + a_{\text{NSA}} s + K_{P_{CR}}\, a_{\text{NSA}} \tag{3.3.7}$$

In order to place the closed-loop poles, a desired characteristic equation for the climb rate dynamics is defined as,

$$\alpha_c(s) = s^2 + 2\zeta\omega_n s + \omega_n^2 \tag{3.3.8}$$

By equating the coefficients of Equations 3.3.7 and 3.3.8 the control gain can be calculated as,

$$K_{P_{CR}} = \frac{a_{\text{NSA}}}{4\zeta^2} \tag{3.3.9}$$

and the resulting natural frequency as,

$$\omega_n = \frac{a_{\text{NSA}}}{2\zeta} \tag{3.3.10}$$

3.3.2 Pole Placement

Placement of the closed-loop poles essentially involves selecting the damping ratio (ζ) of the climb rate dynamics. The location of the closed-loop integrator pole of the NSA controller (a_{NSA}) was determined in §3.2.4.1 and is therefore fixed for this design. The climb rate feedback gain can then be calculated from Equation 3.3.9. The pole placements which follow are for the aircraft parameters and standard flight conditions as outlined in Appendix B.6.

The damping ratio is selected so that there is no overshoot in the response. Thus,

$$\zeta_{cl} = 1 \tag{3.3.11}$$

From Equations 3.3.9 and 3.3.10 the climb rate feedback gain and resulting natural frequency of the climb rate dynamics are then calculated to be,

$$K_{P_{CR}} = 1 \qquad \omega_n = 2\,\text{rad/s} \tag{3.3.12}$$

During HIL simulation and flight tests the control gains are often tuned slightly in order to achieve a satisfactory aircraft response. Figures 3.23a and 3.23b show what effect varying the feedback gain has on the closed-loop poles and zeros as well as on the step response of the climb rate controller. It can be seen that when the feedback gain is increased, the system's poles move towards one another, eventually becoming a complex pole pair. Increasing the climb rate feedback gain therefore increases the frequency and decreases the damping of the dominant closed-loop pole(s). This has the effect of speeding up the climb rate response, while also increasing the overshoot.

3.3.3 HIL Simulation and Practical Flight Test Results

The climb rate controller was implemented on an OBC and tested in the HIL simulation environment as well as practically in a series of flight tests. The HIL simulation environment, aircraft, avionics and other hardware used in this project are outlined in Appendix

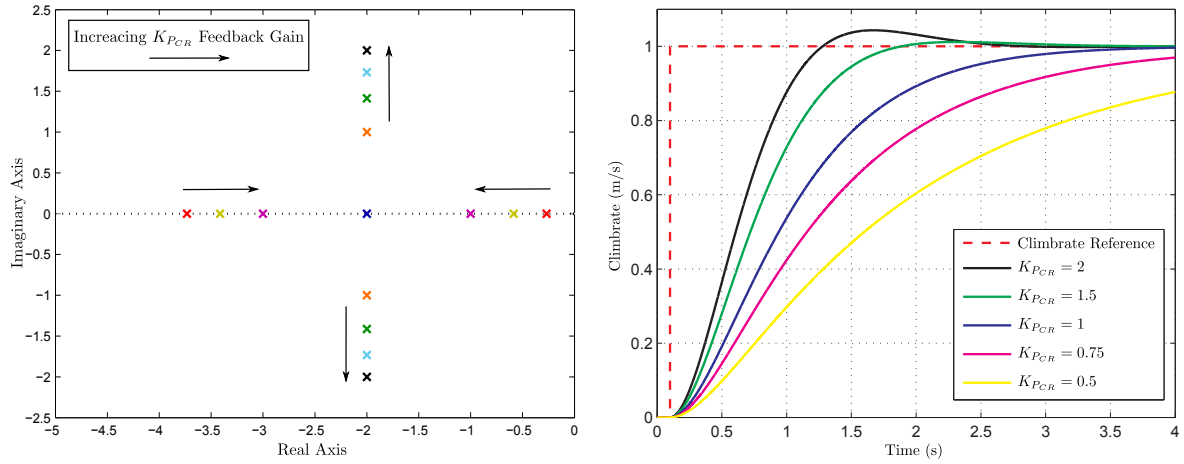

(a) Pole-zero map **(b)** Step response

Figure 3.23 – Pole-zero map and step response of the climb rate controller for a range of feedback gains

B, only the results are presented in this section. The HIL tests allow the controller to be fully tested before practical flight tests are attempted. Ideally, the practical flight test results should closely resemble those achieved in the HIL simulation.

With reference to Figure 3.20 it has already been show in the HIL and practical flight tests of the NSA controller in §3.2.6.1 that the responses of the climb rate controller during HIL simulation correspond very well with those obtained during flight tests. Figures 3.20c and 3.20d are presented again as Figures 3.24a and 3.24b so that a more detailed comparison can be made between the climb rate controller making use of a conventional NSA controller, and a direct-lift-augmented NSA controller. The practical fight test data shown in Figure 3.24 are of two separate flight tests where the reference climb rates are very similar. Unfortunately, atmospheric conditions differ between the two flight tests, and as such an exact comparison cannot be made but is is still possible to gauge the general performance of the two NSA controllers. It must be noted that the atmospheric conditions during the conventional NSA controller test were more favourable than during the direct-lift-augmented NSA controller test. It can be seen that the direct-lift-augmented NSA controller shows a somewhat faster climb rate response than the conventional NSA controller or the pole placement design suggests. This is due to the direct-lift component present in the augmented NSA controller, and it demonstrates one of the advantages that the direct-lift-augmented NSA controller holds over the conventional NSA controller. The corresponding NSA response shown in Figure 3.24b does not reveal much other than the presence of significant disturbances which are discussed in §3.2.6.1

Figure 3.25 shows the effect of the climb rate feedback gain on the response during practical flight tests. The conventional NSA controller is used and its response is shown in Figure 3.25b. The results are very similar to those of the the pole placement design. This controller design can thus be considered a success.

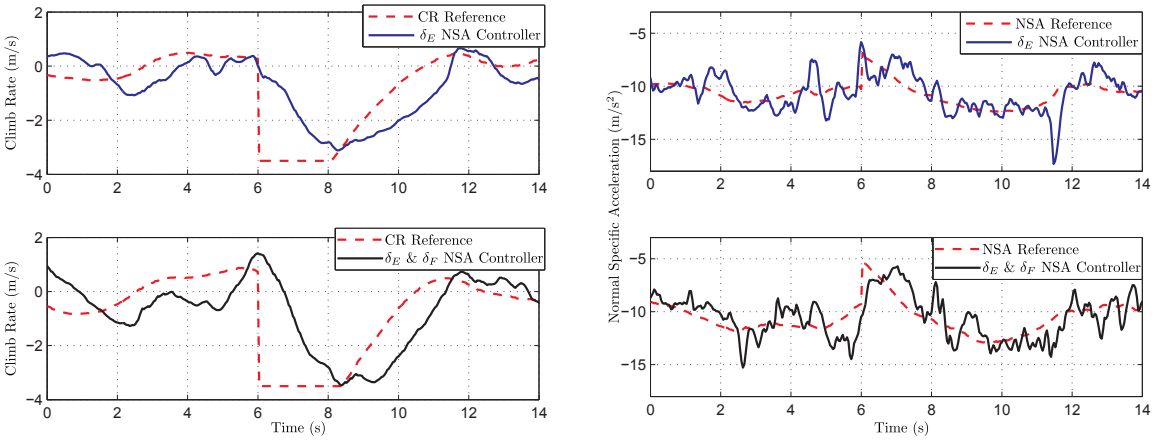

(a) Climb rate response **(b)** NSA response

Figure 3.24 – Climb rate response and corresponding NSA response for the conventional and direct-lift-augmented NSA controllers during practical flight tests

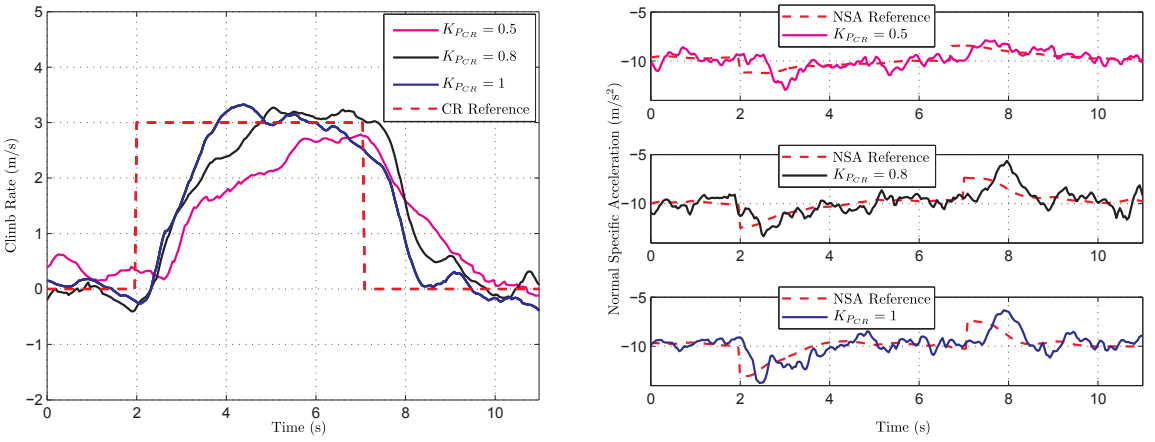

(a) Step response **(b)** NSA response

Figure 3.25 – Climb rate step response and corresponding NSA response for a series of climb rate feedback gains during practical flight tests

3.4 Altitude Controller

This section describes the design, simulation and practical testing of an altitude controller. This controller regulates the altitude of the aircraft by making use of the climb rate controller of §3.3. The input to the altitude controller stems from the aircraft landing state machine of §5.4. The controller is designed in the inertial axis system as shown in Figure 2.1. It is therefore assumed that the climb rate vector of the aircraft is always normal to the flat earth. This assumption is valid as long as the flight path angle remains small and the effect of the aircraft's roll orientation is compensated for by the guidance controller as shown in §4.4.

3.4.1 Design

The basic model for the aircraft's altitude dynamics is given by,

$$\dot{h} = \begin{bmatrix} 0 \end{bmatrix} \begin{bmatrix} h \end{bmatrix} + \begin{bmatrix} 1 \end{bmatrix} V_h \tag{3.4.1}$$

where h is the altitude and V_h the climb rate of the aircraft in the inertial and navigation axis systems respectively.

The dominant closed-loop pole of the climb rate controller of §3.3 is located at 2 rad/s as shown in Equation 3.3.12. If the altitude dynamics are to be timescale separated from the climb rate dynamics, then by the generally held design rule, the altitude dynamics bandwidth should be at least five times less than that of the climb rate dynamics. This pole placement will lead to an unacceptably slow altitude response. If however, the dynamics of the climb rate controller are taken into account, the frequency separation requirement falls away and the altitude controller poles can be placed at a somewhat higher frequency. To accomplish this the climb rate dynamics can be approximated with a simple first order lag and the altitude dynamics augmented accordingly,

$$\begin{bmatrix} \dot{h} \\ \dot{V}_h \end{bmatrix} = \begin{bmatrix} 0 & 1 \\ 0 & -\dfrac{1}{\tau_{\text{CR}}} \end{bmatrix} \begin{bmatrix} h \\ V_h \end{bmatrix} + \begin{bmatrix} 0 \\ \dfrac{1}{\tau_{\text{CR}}} \end{bmatrix} V_h^{ref} \tag{3.4.2}$$

$$h = \begin{bmatrix} 1 & 0 \end{bmatrix} \begin{bmatrix} h \\ V_h \end{bmatrix} \tag{3.4.3}$$

where τ_{CR} is the time constant of the dominant closed-loop climb rate dynamics pole and V_h^{ref} is the commanded climbrate in the navigation axis system. V_h^{ref} can be considered a virtual actuator of this system and it is assumed that any command is instantly met.

In this project accurate altitude following is of paramount importance. An argument can therefore be made that the control law of the altitude controller should contain integrator feedback in order to eliminate steady state errors which will arise when a ramp command, such as the landing approach path, is followed. However, the control law defined makes use of only proportional feedback from the climb rate which means that the landing approach path will be followed with a constant altitude offset. The reasoning behind this decision is discussed in §5.3. Thus,

$$\begin{aligned} V_h^{ref} &= -K_{P_h} \left(h - h^{ref} \right) \\ &= -K_{P_h} \left(\begin{bmatrix} 1 & 0 \end{bmatrix} \begin{bmatrix} h \\ V_h \end{bmatrix} - h^{ref} \right) \end{aligned} \tag{3.4.4}$$

where h^{ref} is the reference altitude command. The control law is now substituted into the dynamics and the closed-loop system becomes,

$$\begin{bmatrix} \dot{h} \\ \dot{V}_h \end{bmatrix} = \begin{bmatrix} 0 & 1 \\ -K_{P_h}\, a_{\text{CR}} & -a_{\text{CR}} \end{bmatrix} \begin{bmatrix} h \\ V_h \end{bmatrix} + \begin{bmatrix} 0 \\ K_{P_h}\, a_{\text{CR}} \end{bmatrix} h^{ref} \tag{3.4.5}$$

where,

$$a_{\text{CR}} = \frac{1}{\tau_{\text{CR}}} \tag{3.4.6}$$

is the location of the closed-loop integrator pole of the climb rate dynamics as given by Equation 3.3.10.

Calculating the closed-loop characteristic equation gives,

$$p(s) = s^2 + a_{\text{CR}}s + K_{P_h}a_{\text{CR}} \tag{3.4.7}$$

In order to place the closed-loop poles, a desired characteristic equation for the altitude dynamics is defined as,

$$\alpha_c(s) = s^2 + 2\zeta\omega_n s + \omega_n^2 \tag{3.4.8}$$

By equating the coefficients of Equations 3.4.7 and 3.4.8 the control gain can be calculated as,

$$K_{P_h} = \frac{a_{\text{CR}}}{4\zeta^2} \tag{3.4.9}$$

and the resulting natural frequency as,

$$\omega_n = \frac{a_{\text{CR}}}{2\zeta} \tag{3.4.10}$$

3.4.2 Pole Placement

Placement of the closed-loop poles essentially involves selecting the damping ratio (ζ) of the altitude dynamics. The location of the closed-loop integrator pole of the climb rate controller (a_{CR}) was determined in §3.3 and is therefore fixed for this design. The altitude feedback gain can then be calculated from Equation 3.4.9. The pole placements which follow are for the aircraft parameters and standard flight conditions as outlined in Appendix B.6.

The damping ratio is selected so that there is no overshoot in the response. Thus,

$$\zeta_{cl} = 1 \tag{3.4.11}$$

From Equations 3.4.9 and 3.4.10 the altitude feedback gain and resulting natural frequency of the altitude dynamics are then calculated to be,

$$K_{P_h} = 0.5 \qquad\qquad \omega_n = 1\,\text{rad/s} \tag{3.4.12}$$

During HIL simulation and flight tests the control gains are often tuned slightly in order to achieve a satisfactory aircraft response. Figures 3.26a and 3.26b show what effect varying the feedback gain has on the closed-loop poles and zeros as well as on the step response of the altitude controller. It can be seen that when the feedback gain is increased, the systems poles move towards one another, eventually becoming a complex pole pair. Increasing the altitude feedback gain therefore increases frequency and decreases the damping of the dominant closed-loop pole(s). This has the effect of speeding up the altitude response, while also increasing the overshoot.

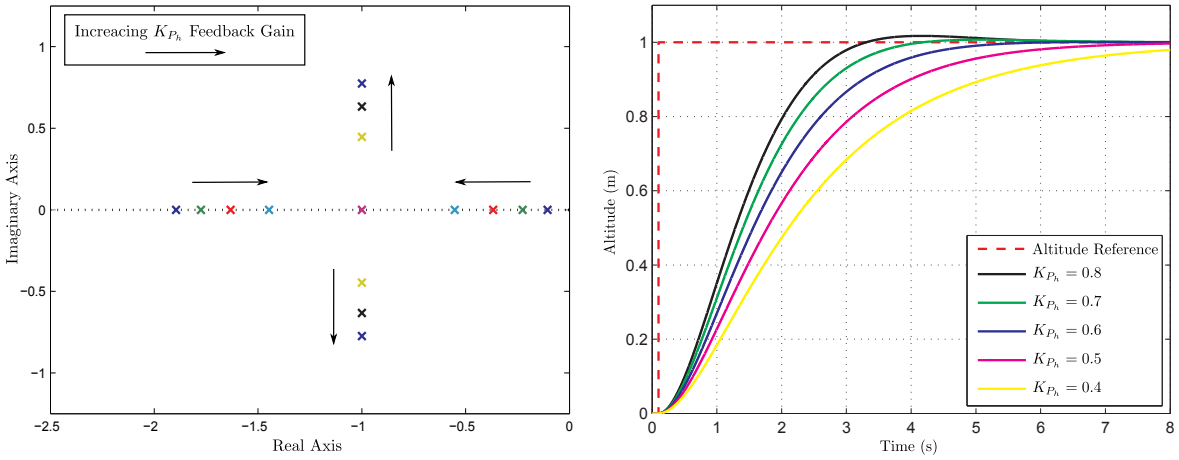

(a) Pole-zero map **(b)** Step response

Figure 3.26 – Pole-zero map and step response of the altitude controller for a range of feedback gains

3.4.3 HIL Simulation and Practical Flight Test Results

The altitude controller was implemented on an OBC and tested in the HIL simulation environment as well as practically in a series of flight tests. The HIL simulation environment, aircraft, avionics and other hardware used in this project are outlined in Appendix B, only the results are presented in this section. The HIL tests allow the controller to be fully tested before practical flight tests are attempted. Ideally, the practical flight test results should closely resemble those achieved in the HIL simulation.

Figures 3.27a and 3.27b show the altitude step and corresponding climb rate response of the aircraft for both the conventional and the direct-lift-augmented NSA controllers during HIL simulation, and Figures 3.27c and 3.27d show the same for practical flight tests. Firstly, it can be seen that the HIL simulation and practical flight test altitude steps correspond well with one another with the exception that the HIL simulation exhibits somewhat greater overshoot. The practical fight test data shown in Figure 3.27c is of two separate flight tests. Unfortunately, atmospheric conditions differ between the two flight tests, and as such an exact comparison cannot be made but it is still possible to gauge the general performance of the two NSA controllers. It can be seen that while the rise time is very similar, the altitude controller which makes use of the direct-lift-augmented NSA controller follows the reference more closely than the controller which makes use of the conventional NSA controller. This demonstrates the improved disturbance rejection capabilities of the direct-lift-augmented NSA controller compared to the conventional NSA controller. The comparisons between the climb rate controllers driven by the conventional and the direct-lift-augmented NSA controllers are discussed in §3.3.3.

A good measure of the altitude controller's performance is its ability to maintain a constant altitude during different aircraft roll angles. This is demonstrated in Figures 3.28a

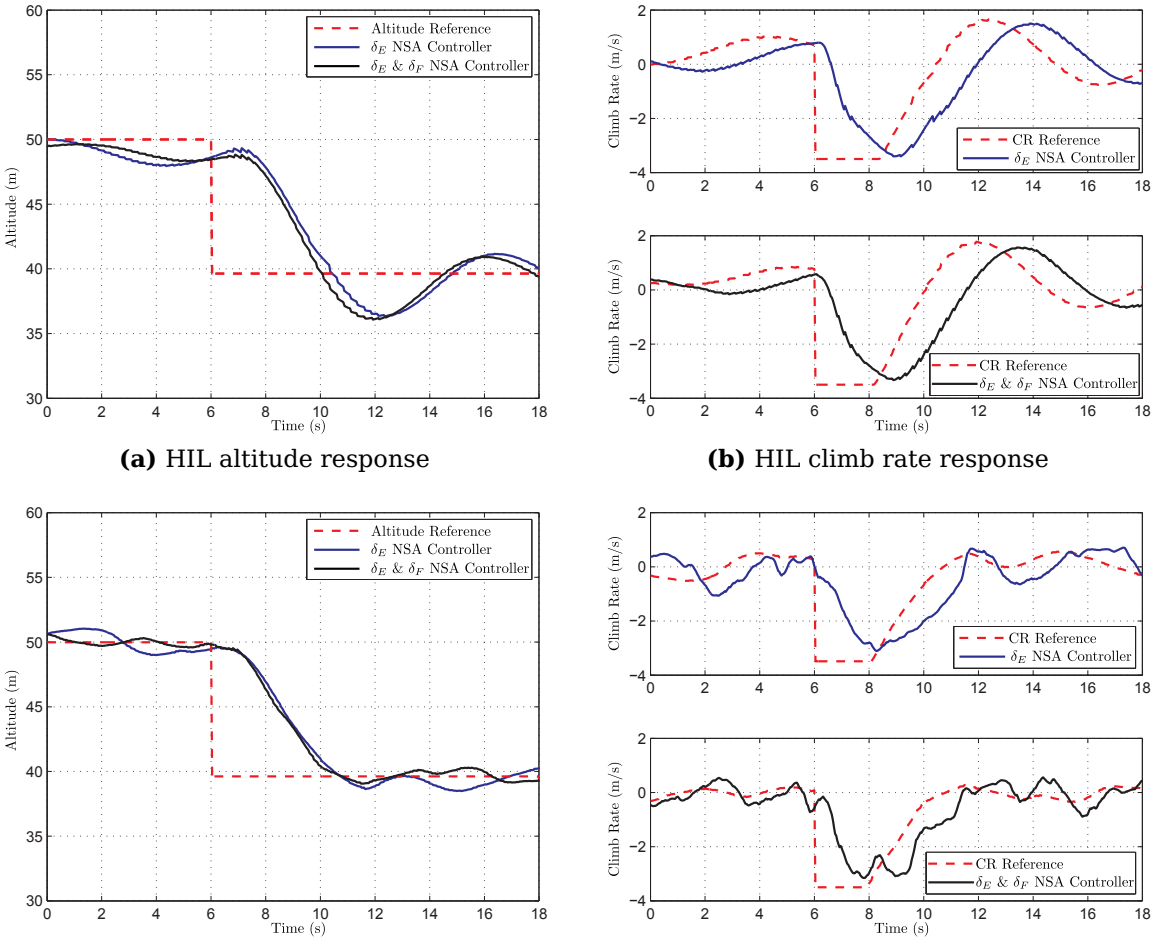

(a) HIL altitude response

(b) HIL climb rate response

(c) Flight test altitude response

(d) Flight test climb rate response

Figure 3.27 – Altitude step and corresponding climb rate response for the conventional and direct-lift-augmented NSA controllers during HIL and flight tests

and 3.28b where the altitude response of the aircraft is shown whilst the aircraft is flying a circuit. It can be seen that even during high roll angles the altitude is maintained with only a slight decrease in precision. This is of importance since any deviation in altitude during a turn will affect the landing approach path as discussed in Chapter **??**.

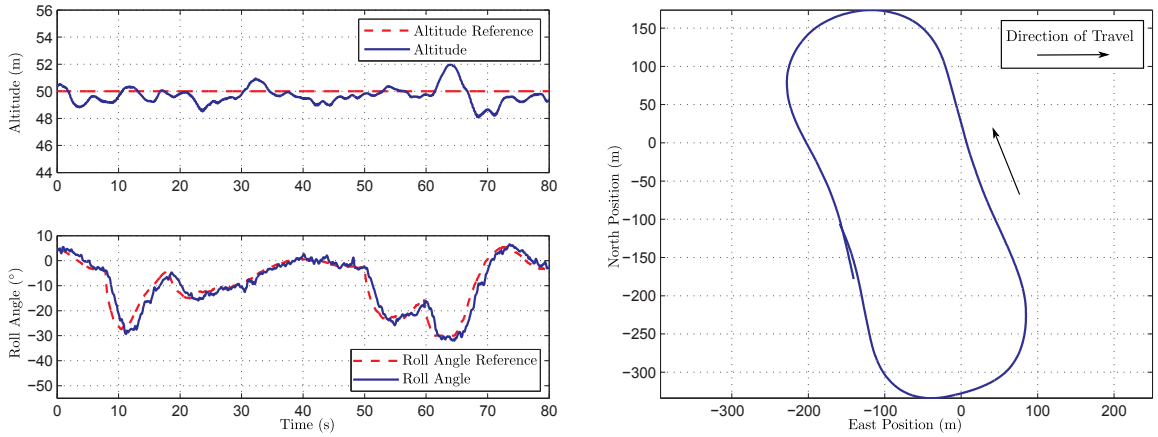

(a) Altitude and roll angle **(b)** Flight path

Figure 3.28 – Altitude response and roll angle during a looped flight path

3.5 Airspeed Controller

This section describes the design, simulation and practical testing of an airspeed controller. This controller regulates the airspeed of the aircraft by means of the throttle actuator. The input to the airspeed controller stems from the aircraft landing state machine of §5.4. The controller is designed in the aircraft's wind axis system as shown in Figure 2.3 and will make use of the measurements from a pitot tube to determine the aircraft's airspeed. As discussed in §3.3, the airspeed controller is designed independent of the climb rate dynamics despite the coupling which exists.

3.5.1 Design

The simplified and decoupled model of the aircraft's axial dynamics from Equations 2.4.6 and 2.4.7 is restated for convenience,

$$\dot{T} = \left[-\frac{1}{\tau_T}\right] T + \left[\frac{1}{\tau_T}\right] T_C \tag{3.5.1}$$

$$A_W = \left[\frac{1}{m}\right] T + \left[-\frac{qS}{m} C_D\right] - g\sin\theta \tag{3.5.2}$$

where the standard trigonometric small angle assumptions have been made with regard to the two incidence angles α and β. The dynamics for the velocity magnitude of the aircraft's wind axes can be written as,

$$\begin{bmatrix}\dot{T}\\ \dot{\bar{V}}\end{bmatrix} = \begin{bmatrix}-\frac{1}{\tau_T} & 0\\ \frac{1}{m} & 0\end{bmatrix}\begin{bmatrix}T\\ \bar{V}\end{bmatrix} + \begin{bmatrix}\frac{1}{\tau_T}\\ 0\end{bmatrix} T_c + \begin{bmatrix}0\\ -\frac{qS}{m}C_D\end{bmatrix} + \begin{bmatrix}0\\ -g\sin\theta\end{bmatrix} \tag{3.5.3}$$

The drag term above is treated as an unmodelled disturbance [2] and can be removed by augmenting an integrator to the system in order to reject this and any other disturbances to the airspeed in the steady state. The integrator is defined as,

$$\dot{E}_V = \bar{V} - \bar{V}^{ref} \tag{3.5.4}$$

where $\bar{V}^{ref}$ is the reference airspeed in wind axes. After simplifying the dynamics and augmenting the integrator the system becomes,

$$\begin{bmatrix} \dot{E}_V \\ \dot{T} \\ \dot{\bar{V}} \end{bmatrix} = \begin{bmatrix} 0 & 0 & 1 \\ 0 & -\frac{1}{\tau_T} & 0 \\ 0 & \frac{1}{m} & 0 \end{bmatrix} \begin{bmatrix} E_V \\ T \\ \bar{V} \end{bmatrix} + \begin{bmatrix} 0 \\ \frac{1}{\tau_T} \\ 0 \end{bmatrix} T_C + \begin{bmatrix} 0 \\ 0 \\ -g\sin\theta \end{bmatrix} + \begin{bmatrix} -1 \\ 0 \\ 0 \end{bmatrix} V^{ref} \tag{3.5.5}$$

A throttle control law is defined which uses feedback from the integrator and airspeed states as well as a feed-forward term which will be used to cancel out the effect of gravitational coupling. The gravitational coupling effect must be minimised in particular when the aircraft descends steeply during a landing approach in order to prevent a rapid increase in airspeed. Thus,

$$T_C = -K_V\bar{V} - K_E E_V + T_g \tag{3.5.6}$$

where T_g is the throttle command which removes the effect of gravitational coupling. The control law is now substituted into the dynamics and the closed-loop system becomes,

$$\begin{bmatrix} \dot{E}_V \\ \dot{T} \\ \dot{\bar{V}} \end{bmatrix} = \begin{bmatrix} 0 & 0 & 1 \\ -\frac{1}{\tau_T}K_E & -\frac{1}{\tau_T} & -\frac{1}{\tau_T}K_V \\ 0 & \frac{1}{m} & 0 \end{bmatrix} \begin{bmatrix} E_V \\ T \\ \bar{V} \end{bmatrix} + \begin{bmatrix} 0 \\ \frac{1}{\tau_T} \\ 0 \end{bmatrix} T_g + \begin{bmatrix} 0 \\ 0 \\ -g\sin(\theta) \end{bmatrix} + \begin{bmatrix} -1 \\ 0 \\ 0 \end{bmatrix} V^{ref} \tag{3.5.7}$$

The gravitational coupling into the airspeed dynamics can be cancelled out by letting,

$$T_g = gm\tau_T \sin\theta \tag{3.5.8}$$

Thus the closed-loop system becomes,

$$\begin{bmatrix} \dot{E}_V \\ \dot{T} \\ \dot{\bar{V}} \end{bmatrix} = \begin{bmatrix} 0 & 0 & 1 \\ -\frac{1}{\tau_T}K_E & -\frac{1}{\tau_T} & -\frac{1}{\tau_T}K_V \\ 0 & \frac{1}{m} & 0 \end{bmatrix} \begin{bmatrix} E_V \\ T \\ \bar{V} \end{bmatrix} + \begin{bmatrix} -1 \\ 0 \\ 0 \end{bmatrix} V^{ref} \tag{3.5.9}$$

Calculating the closed-loop characteristic equation gives,

$$p(s) = s^3 + \frac{1}{\tau_T}s^2 + \frac{K_V}{m\tau_T}s + \frac{K_E}{m\tau_T} \tag{3.5.10}$$

In order to place the closed-loop poles a desired characteristic equation for the airspeed dynamics is defined as,

$$\alpha_c(s) = (s^2 + 2\zeta\omega_n s + \omega_n^2)(s + a) \tag{3.5.11}$$

By equating the coefficients of Equations 3.5.10 and 3.5.11 control gains can be calculated as,

$$K_V = m\frac{(1 + (4\zeta^2 - 1)a\tau_T)(1 - a\tau_T)}{4\zeta^2\tau_T} \tag{3.5.12}$$

$$K_E = m\tau_T a\left(\frac{1 - a\tau_T}{2\zeta\tau_T}\right)^2 \tag{3.5.13}$$

and the resulting natural frequency as,

$$\omega_n = \frac{1 - a\tau_T}{2\zeta\tau_T} \tag{3.5.14}$$

The throttle actuator is prone to integrator windup especially during steep climbs and descents. Integrator anti-windup can be implemented by placing a limit on the integrator state whenever the controller commands a thrust which is outside the physical range of the aircraft's motor. This integrator state is obtained by rewriting the control law of Equation 3.5.6,

$$E_V = \frac{T_g - K_V\bar{V} - T_C}{K_E} \tag{3.5.15}$$

It must be noted that several assumptions are made regarding the thrust produced by the motor. Firstly, it is assumed that the motor's *thrust* is commanded, when in reality it is the voltage to the motor which is controlled by sending a pulse-width-modulated (PWM) signal to the speed controller. This signal is based on a fraction of the maximum thrust of the motor. There is therefore a difference between the thrust commanded and the true thrust produced, however, this is compensated for by the integrator on airspeed. Secondly, it has been assumed that the effect of airspeed on the thrust is constant. This means that the maximum dynamic thrust of the aircraft was fixed at a value somewhat lower than the maximum static thrust determined by a static thrust test. Again, any errors will be compensated for by the integrator on airspeed.

3.5.2 Pole Placement

Placement of the closed-loop poles essentially involves selecting the damping ratio (ζ) and the location of the closed-loop integrator pole (a) of the airspeed dynamics. The feedback gains (K_V and K_E) can then be calculated from Equations 3.5.12 and 3.5.13. The value of the thrust time constant (τ_T) as well as the maximum thrust were determined through tests (see Appendix B.6.2). The pole placements which follow are for the aircraft parameters and standard flight conditions as outlined in Appendix B.6.

The damping ratio and closed-loop integrator location are selected such that there is little overshoot in the response and that the throttle command remains within reasonable bounds for a typical airspeed command. Thus,

$$\zeta_{cl} = 0.8 \qquad\qquad a = 0.5\,\text{rad/s} \tag{3.5.16}$$

The pole placement and step response of the airspeed controller are shown in Figure 3.29.

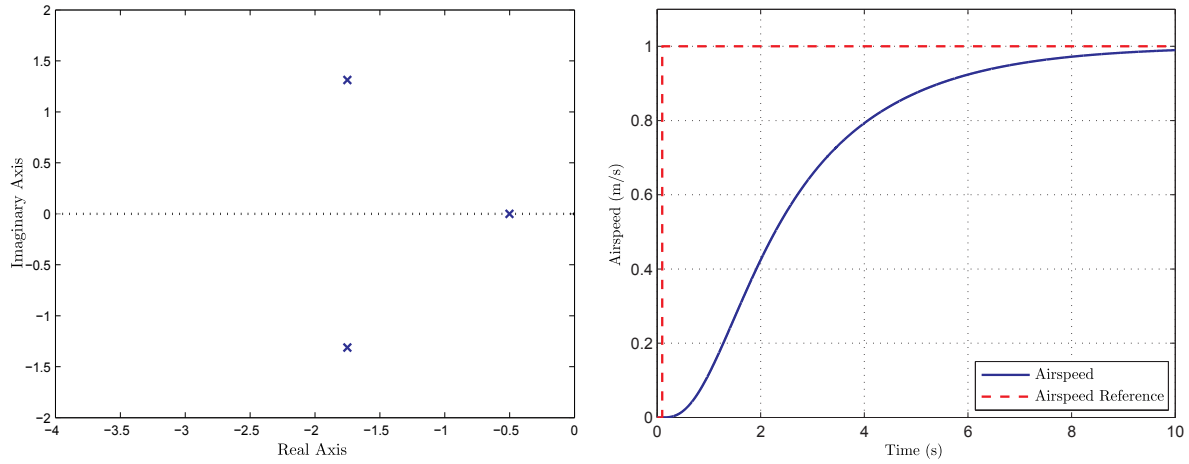

(a) Pole-zero map **(b)** Step response

Figure 3.29 – Pole-zero map and step response of the airspeed controller

3.5.3 HIL Simulation and Practical Flight Test Results

The airspeed controller was implemented on an OBC and tested in the HIL simulation environment as well as practically in a series of flight tests. The HIL simulation environment, aircraft, avionics and other hardware used in this project are outlined in Appendix B, only the results are presented in this section. The HIL tests allow the controller to be fully tested before practical flight tests are attempted. Ideally, the practical flight test results should closely resemble those achieved in the HIL simulation.

During HIL simulations the airspeed of the aircraft is maintained well, however the throttle actuator behaviour differs significantly from that of the practical flight tests. This is most likely due to modelling inaccuracies of the drag coefficient term but is ultimately of little consequence. The HIL results are thus omitted from this section.

Figure 3.30a shows the airspeed step response of the aircraft during a flight test, and Figure 3.30b shows the corresponding throttle and altitude responses. The airspeed of the aircraft as measured by the pressure sensors of a pitot tube, the velocity of the aircraft as measured inertially by the GPS as well as the velocity determined by the estimator of the aircraft, are shown in Figure 3.30a. If the aircraft is flying straight and level, and there is zero wind, then the inertially measured aircraft velocity should closely match the true airspeed measured by the pitot tube. The climb rate of the aircraft will have some effect on the inertially measured velocity, and when this is accounted for, the remaining difference is due to wind disturbances. It can be seen that the airspeed follows the reference well and that the rise time of the response resembles that of the pole placement design.

In this project, the ability of the airspeed controller to maintain the airspeed during the descent phase of the landing is of paramount importance. Figure 3.31a shows the airspeed of the aircraft for a flight path circuit similar to that of Figure 3.28b where the aircraft descends and ascends a sloped path simulating a landing approach. The

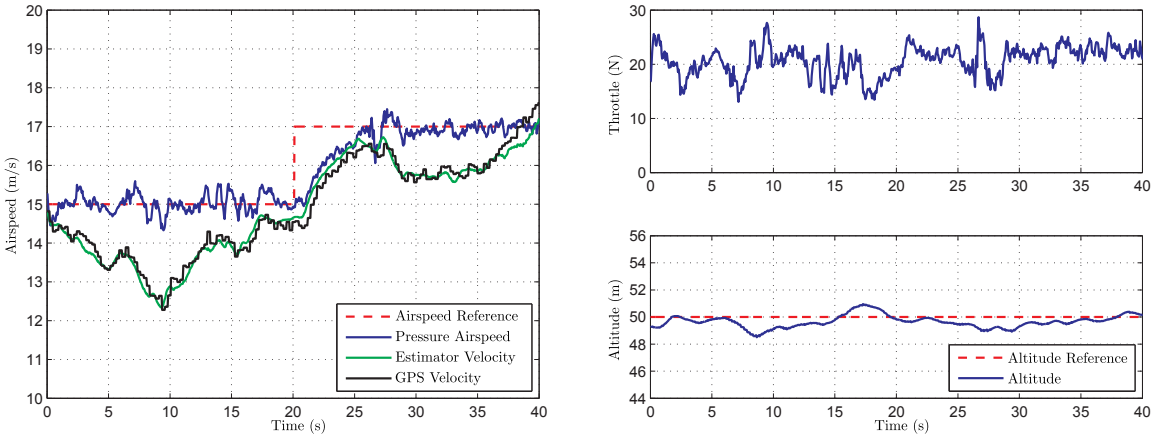

(a) Step response **(b)** Throttle actuator and altitude

Figure 3.30 – Airspeed step with corresponding throttle and altitude responses during a flight test

altitude of the aircraft during this manoeuvre is shown in Figure 3.31b along with the corresponding throttle actuator. It must be noted that this flight test plot was selected specifically because it shows a very high degree of wind disturbance. It can be seen that in spite of the presence of wind disturbances the airspeed is well maintained during the descent and ascent.

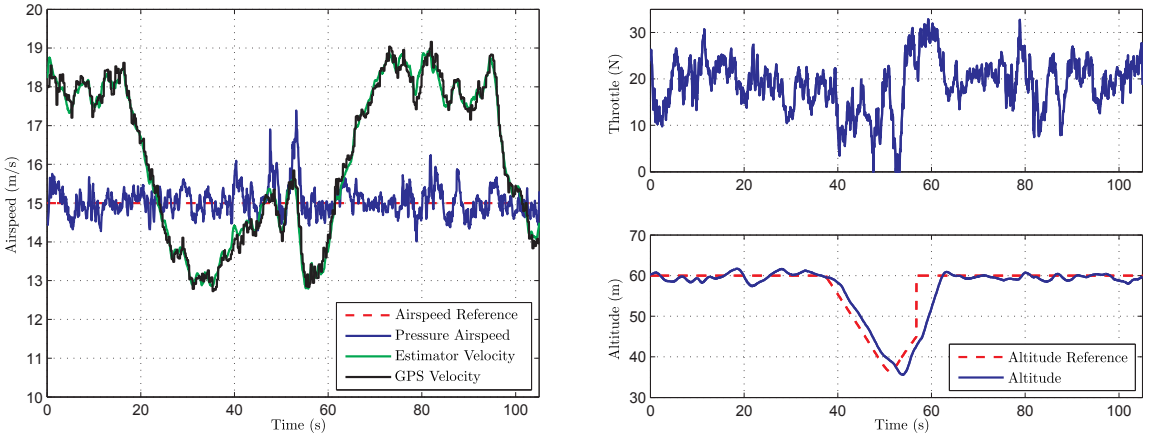

(a) Airspeed response **(b)** Throttle actuator and altitude

Figure 3.31 – Airspeed with corresponding throttle and altitude responses for sloped altitude path during a flight test

Chapter 4

Lateral Analysis and Control

During landing, the flight path of the aircraft in the inertial axis system must be controlled such that it coincides with that of the runway. In order to accomplish this, several controllers which operate in the lateral axis system of the aircraft are required. These controllers are presented in this chapter, while the specifics of the landing procedure are discussed in Chapter 5. This chapter also provides an analysis of the lateral dynamics of the aircraft, followed by the design, HIL simulation and practical flight test results of the roll angle controller and the Dutch roll damper. The chapter ends with an outline, HIL simulation and practical flight test results of the guidance controller.

As highlighted in Figure 4.1 the lateral flight control system consists of a roll angle controller, Dutch roll damper and a guidance controller.

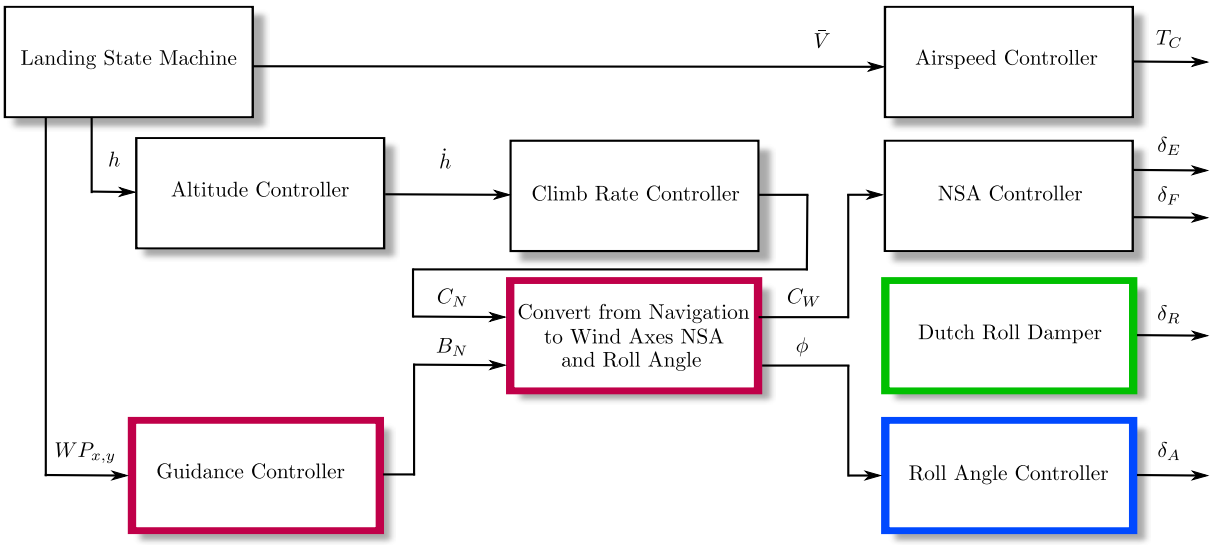

Figure 4.1 – Longitudinal Control System Overview Block Diagram

The roll angle controller and Dutch roll damper are designed around the linear, decoupled lateral dynamics of Equations 2.4.10 and 2.4.11. The roll angle controller is capable of using the aircraft's ailerons in order to create a commanded wind axes roll angle, and receives its input from the guidance controller. The Dutch roll damper makes

use of the aircraft's rudder in order to damp the Dutch roll mode of the aircraft. The guidance controller receives its input from the landing state machine as a path to be followed, and does so by commanding a lateral acceleration in the navigation axis system which, in combination with the commanded normal acceleration in the navigation axis system, is then converted to a wind axis system NSA and roll angle.

The analysis of the lateral dynamics of the aircraft, and the subsequent design of appropriate controllers has already been extensively covered by [2; 1] and the controllers presented in this section are based directly on that work. The lateral control system in [2; 1] also made use of a lateral specific acceleration (LSA) controller which enables the aircraft to fly coordinated turns. Such a controller might be useful during manouvres such as crosswind landings, but since these fall outside the scope of this project an LSA controller was not implemented. The guidance controller implemented was developed by [3].

4.1 Decoupling the Lateral Dynamics

For convenience, the simplified lateral dynamics of Equations 2.4.10 and 2.4.11 are shown again,

Lateral Dynamics

$$\begin{bmatrix}\dot{\beta}\\ \dot{P}\\ \dot{R}\end{bmatrix} = \begin{bmatrix}\frac{1}{mV}\bar{Y}_\beta & \frac{1}{mV}\bar{Y}_P & -1+\frac{1}{mV}\bar{Y}_R\\ \frac{1}{I_x}L_\beta & \frac{1}{I_x}L_P & \frac{1}{I_x}L_R\\ \frac{1}{I_z}N_\beta & \frac{1}{I_z}N_P & \frac{1}{I_z}N_R\end{bmatrix}\begin{bmatrix}\beta\\ P\\ R\end{bmatrix} + \begin{bmatrix}\frac{1}{mV}\bar{Y}_{\delta_A} & \frac{1}{mV}\bar{Y}_{\delta_R}\\ \frac{1}{I_x}L_{\delta_A} & \frac{1}{I_x}L_{\delta_R}\\ \frac{1}{I_z}N_{\delta_A} & \frac{1}{I_z}N_{\delta_R}\end{bmatrix}\begin{bmatrix}\delta_A\\ \delta_R\end{bmatrix} + \begin{bmatrix}\frac{g}{V}\cos\theta\sin\phi\\ 0\\ 0\end{bmatrix} \tag{4.1.1}$$

$$\begin{bmatrix}B_W\\ P_W\end{bmatrix} = \begin{bmatrix}\frac{\bar{Y}_\beta}{m} & \frac{\bar{Y}_P}{m} & \frac{\bar{Y}_R}{m}\\ 0 & 1 & 0\end{bmatrix}\begin{bmatrix}\beta\\ P\\ R\end{bmatrix} + \begin{bmatrix}\frac{\bar{Y}_{\delta_A}}{m} & \frac{\bar{Y}_{\delta_R}}{m}\\ 0 & 0\end{bmatrix}\begin{bmatrix}\delta_A\\ \delta_R\end{bmatrix} \tag{4.1.2}$$

According to [2], these dynamics can be decoupled into roll mode and directional dynamics. This then allows for the design of separate roll angle and lateral acceleration controllers. However, since a lateral acceleration controller is not implemented in this project, the directional dynamics will only be used in the design of the Dutch roll damper.

The lateral dynamics are simplified by assuming that the lateral force generated by an aileron deflection and roll rates is negligible. It is also assumed that the coupling between the directional and the roll rate dynamics is weak. The lateral decoupling assumption holds for most conventional aircraft such as the one used in this project. A detailed list of conditions under which the lateral decoupling assumption can be made is presented in [2]. These assumptions allow for separate controllers to be designed for the roll angle

and Dutch roll mode where any aileron and rudder couplings into the directional and roll dynamics respectively will be considered disturbances.

The decoupled models are given by,

Roll Dynamics

$$\dot{P} = \left[\frac{1}{I_x}L_P\right]\left[P\right] + \left[\frac{1}{I_x}L_{\delta_A}\right]\delta_A \tag{4.1.3}$$

$$P_W = P \tag{4.1.4}$$

Directional Dynamics

$$\begin{bmatrix}\dot{\beta}\\ \dot{R}\end{bmatrix} = \begin{bmatrix}\frac{1}{m\bar{V}}\bar{Y}_\beta & -1+\frac{1}{m\bar{V}}\bar{Y}_R\\ \frac{1}{I_z}N_\beta & \frac{1}{I_z}N_R\end{bmatrix}\begin{bmatrix}\beta\\ R\end{bmatrix} + \begin{bmatrix}\frac{1}{m\bar{V}}\bar{Y}_{\delta_R}\\ \frac{1}{I_z}N_{\delta_R}\end{bmatrix}\delta_R + \begin{bmatrix}\frac{g}{\bar{V}}\cos\theta\sin\phi\\ 0\end{bmatrix} \tag{4.1.5}$$

$$B_W = \begin{bmatrix}\frac{\bar{Y}_\beta}{m} & \frac{\bar{Y}_R}{m}\end{bmatrix}\begin{bmatrix}\beta\\ R\end{bmatrix} + \begin{bmatrix}\frac{\bar{Y}_{\delta_R}}{m}\end{bmatrix}\delta_R \tag{4.1.6}$$

4.2 Roll Angle Controller

The design, simulation and practical testing of a roll angle controller which is based on the work of [2; 1] is presented in this section. This controller regulates the roll angle of the aircraft by making use of the ailerons. The input to the roll angle controller stems from the guidance controller of §4.4.

4.2.1 Design

The decoupled equations for the roll dynamics of Equations 4.1.3 and 4.1.4 are restated for convenience,

$$\dot{P} = \left[\frac{1}{I_x}L_P\right]P + \left[\frac{1}{I_x}L_{\delta_A}\right]\delta_A \tag{4.2.1}$$

$$P_W = P \tag{4.2.2}$$

In order to remove any steady state errors such as those arising due to the cross coupling effects from the directional dynamics, and to counter other disturbances, an integrator is augmented to the system as follows,

$$\dot{E}_P = P - P^{ref} \tag{4.2.3}$$

where P^{ref} is the reference roll rate. The system now becomes,

$$\begin{bmatrix}\dot{E}_P\\ \dot{P}\end{bmatrix} = \begin{bmatrix}0 & 1\\ 0 & \frac{1}{I_x}L_P\end{bmatrix}\begin{bmatrix}E_P\\ P\end{bmatrix} + \begin{bmatrix}-1 & 0\\ 0 & \frac{1}{I_x}L_{\delta_A}\end{bmatrix}\begin{bmatrix}P^{ref}\\ \delta_A\end{bmatrix} \tag{4.2.4}$$

With an appropriate aileron control law, the derivation thus far allows for the design of a roll rate controller. In order to control the roll angle, the dynamics must however again be expanded to include the roll angle error,

$$\dot{\phi}_E = P^{ref} - P \tag{4.2.5}$$

The system thus becomes,

$$\begin{bmatrix} \dot{E}_P \\ \dot{P} \\ \dot{\phi}_E \end{bmatrix} = \begin{bmatrix} 0 & 1 & 0 \\ 0 & \frac{1}{I_x} L_P & 0 \\ 0 & -1 & 0 \end{bmatrix} \begin{bmatrix} E_P \\ P \\ \phi_E \end{bmatrix} + \begin{bmatrix} -1 & 0 \\ 0 & \frac{1}{I_x} L_{\delta_A} \\ 0 & 0 \end{bmatrix} \begin{bmatrix} P^{ref} \\ \delta_A \end{bmatrix} \tag{4.2.6}$$

Two control laws are now defined. The first is an aileron control law which will control the roll rate segment of the controller by making use of feedback from the roll rate and roll rate integrator states. The second control law is for the roll rate reference and makes use of feedback from the roll angle error. Thus,

$$\delta_A = -K_P P - K_E E_P \tag{4.2.7}$$

$$P^{ref} = K_\phi \phi_E \tag{4.2.8}$$

The control laws are now substituted into the dynamics and the closed-loop system becomes,

$$\begin{bmatrix} \dot{E}_P \\ \dot{P} \\ \dot{\phi}_E \end{bmatrix} = \begin{bmatrix} 0 & 1 & -K_\phi \\ -\frac{L_{\delta_A}}{I_x} K_E & \frac{L_P}{I_x} - \frac{L_{\delta_A}}{I_x} K_P & 0 \\ 0 & -1 & 0 \end{bmatrix} \begin{bmatrix} E_P \\ P \\ \phi_E \end{bmatrix} \tag{4.2.9}$$

Calculating the closed-loop characteristic equation gives,

$$p(s) = s^3 + \left(\frac{L_{\delta_A}}{I_x} K_P - \frac{L_P}{I_x} \right) s^2 + \left(\frac{L_{\delta_A}}{I_x} K_E \right) s + \left(K_\phi \frac{L_{\delta_A}}{I_x} K_E \right) \tag{4.2.10}$$

In order to place the closed-loop poles a desired characteristic equation for the roll dynamics is defined as,

$$\alpha_c(s) = s^3 + \alpha_2 s^2 + \alpha_1 s + \alpha_0 \tag{4.2.11}$$

By equating the coefficients of Equations 4.2.10 and 4.2.11 the control gains can be calculated as,

$$K_P = \frac{I_x}{L_{\delta_A}} \left(\alpha_2 + \frac{L_P}{I_x} \right) \tag{4.2.12}$$

$$K_E = \frac{I_x}{L_{\delta_A}} \alpha_1 \tag{4.2.13}$$

$$K_\phi = \frac{\alpha_0}{\alpha_1} \tag{4.2.14}$$

The reference roll angle of the controller enters the system as follows,

$$\phi_E = \phi^{ref} - \phi \tag{4.2.15}$$

4.2.2 Pole Placement

The pole placement strategy involves selecting the location of three closed-loop poles and then determining the coefficients of the resulting desired characteristic equation. This then allows the control gains to be determined. The three poles in question are the roll rate, roll rate integrator and the error angle pole. The pole placements which follow are for the aircraft parameters and standard flight conditions as outlined in Appendix B.6.

The roll rate pole stems from the roll rate dynamics of Equation 4.2.1 and is fixed as,

$$\begin{aligned} p_1 &= \frac{L_P}{I_x} \\ &\approx -8\,\text{rad/s} \end{aligned} \tag{4.2.16}$$

The location of the roll rate integrator and error angle poles are selected as,

$$p_2 = \frac{1}{2}p_1 = -4\,\text{rad/s} \tag{4.2.17}$$

and,

$$p_3 = \frac{1}{2}p_2 = -2\,\text{rad/s} \tag{4.2.18}$$

respectively.

The coefficients of the desired characteristic equation of Equation 4.2.11 can now be determined and the results substituted into Equations 4.2.12 to 4.2.14 in order to calculate the controller gains. The resulting pole-zero map and step response of the controller are shown in Figures 4.2a and 4.2b.

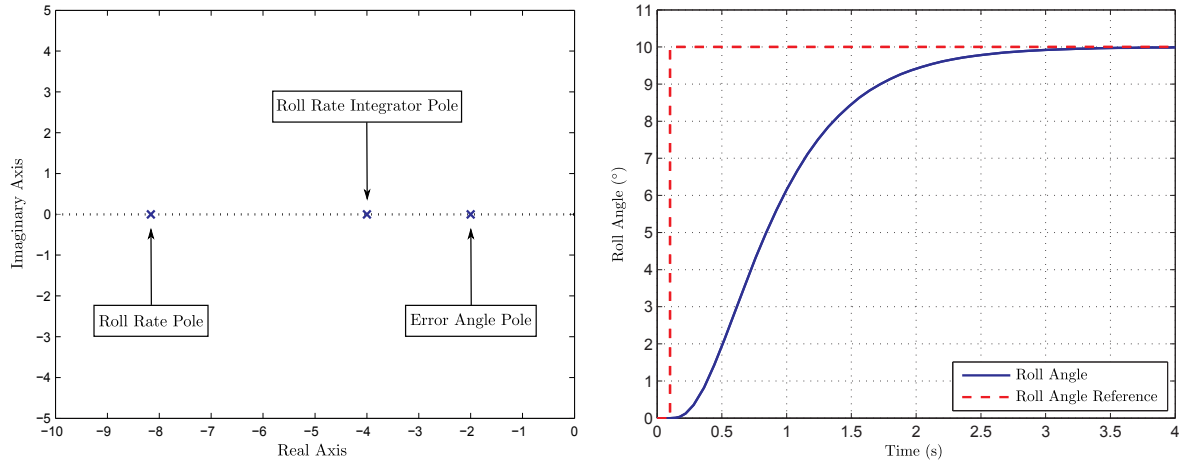

(a) Pole-zero map **(b)** Step response

Figure 4.2 – Pole-zero map and step response of the roll angle controller

4.2.3 HIL Simulation and Practical Flight Test Results

The roll angle controller was implemented on an OBC and tested in the HIL simulation environment as well as practically in a series of flight tests. The HIL simulation environment, aircraft, avionics and other hardware used in this project are outlined in Appendix B, only the results are presented in this section. The HIL tests allow the controller to be fully tested before practical flight tests are attempted. Ideally, the practical flight test results should closely resemble those achieved in the HIL simulation.

Figures 4.3a and 4.3b show the roll angle response with the corresponding roll rate response and aileron deflection angle during HIL simulation, and Figures 4.3c and 4.3d show the same for a practical flight test. Firstly, it can be seen that the HIL simulation and practical flight test roll angle responses correspond well with one another, with the exception that the flight test exhibits somewhat greater disturbances. The cause of these disturbances can be seen in the plot of the roll rate response where there is significant disturbances on the roll rate. It must be noted that the flight test data shown was selected specifically since atmospheric conditions were unfavourable during the test. The origin of this disturbance is therefore mostly aerodynamic in nature. This is confirmed by the roll angle step response shown in Figure 4.4 where it can be seen that the roll rate disturbances are significantly less than those of Equation 4.3d. This demonstrates that the controller continues to function in the presence of significant atmospheric disturbances.

Figures 4.4a and 4.4b show the roll angle response with the corresponding roll rate response and aileron deflection angle during a flight test with favourable atmospheric conditions. It can be seen that the roll angle step response corresponds well with the response obtained in the pole placement of the controller as shown in Figure 4.2b. It can also be seen that the aileron deflection angle remains well within the limits defined in Appendix B.5. This controller design can therefore be considered a success.

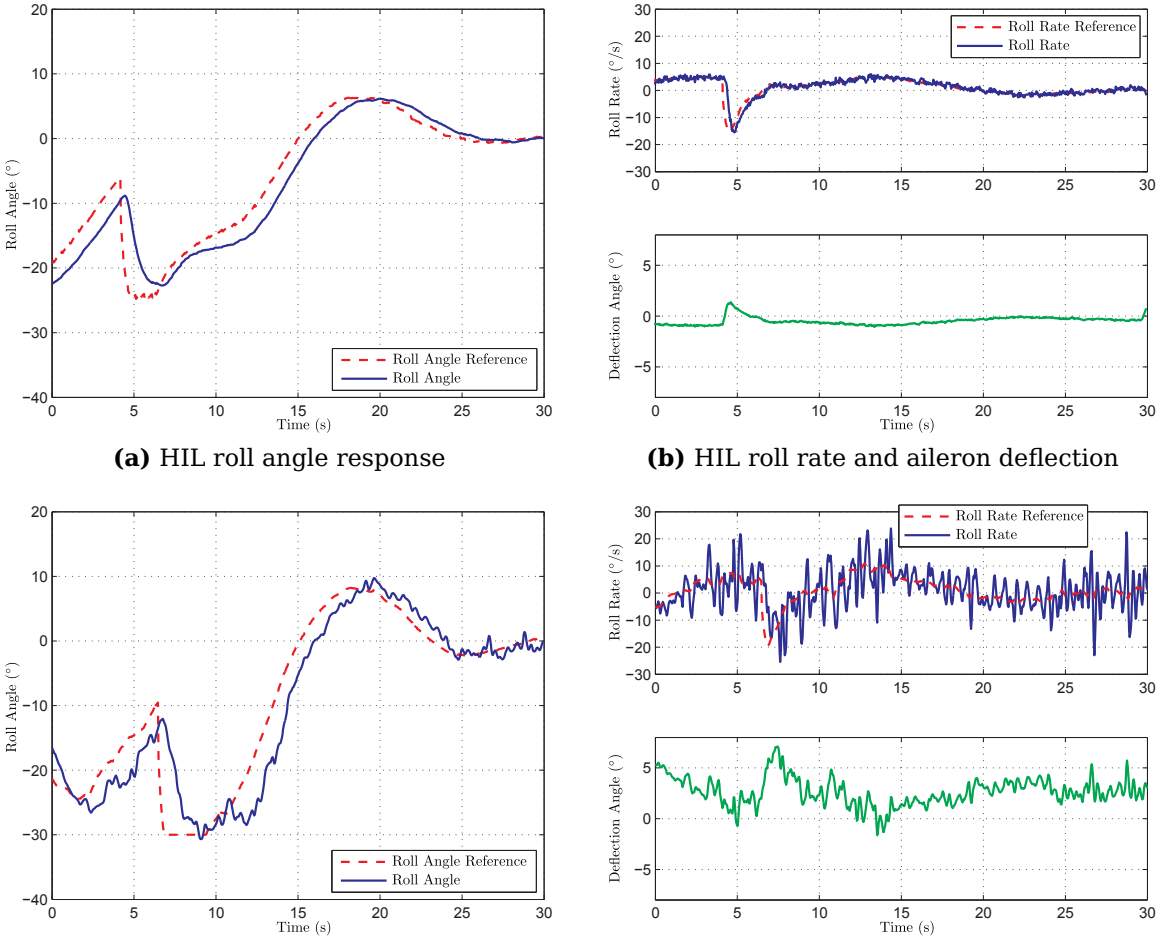

(a) HIL roll angle response

(b) HIL roll rate and aileron deflection

(c) Flight test roll angle response

(d) Flight test roll rate and aileron deflection

Figure 4.3 – Roll angle response with corresponding roll rate response and aileron deflection angle during HIL simulation and flight tests

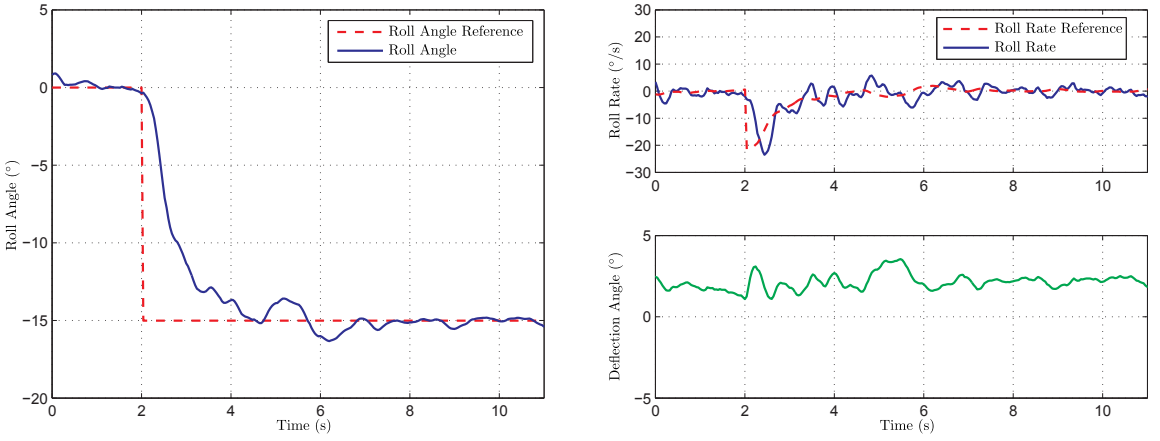

(a) Roll angle step response

(b) Roll rate and aileron deflection

Figure 4.4 – Roll angle step response with corresponding roll rate response and aileron deflection angle during flight tests

4.3 Dutch Roll Damper

This section describes the design, simulation and practical testing of a Dutch roll damper as presented by [1]. The Dutch roll mode of the aircraft is a lightly damped oscillation in yaw, which couples into roll. This controller damps the Dutch roll mode poles of the aircraft by means of the rudder actuator in order to improve the overall flying qualities of the aircraft.

4.3.1 Design

The control strategy involves utilising a high pass filter on the yaw rate feedback signal to the rudder. The transfer function of this filter is given by,

$$D(s) = \frac{K_{DR}s}{s + \omega_f} \tag{4.3.1}$$

where K_{DR} is the feedback gain and ω_f the filter's cut-off frequency. This filter has the effect of countering higher frequency Dutch roll effects while filtering out any low frequency effects. This ensures that the controller does not attempt to actively counter constant turn rates.

The decoupled equation for the directional dynamics of Equation 4.1.5 is restated below for convenience,

$$\begin{bmatrix} \dot{\beta} \\ \dot{R} \end{bmatrix} = \begin{bmatrix} \frac{1}{m\bar{V}}\bar{Y}_\beta & -1 + \frac{1}{m\bar{V}}\bar{Y}_R \\ \frac{1}{I_z}N_\beta & \frac{1}{I_z}N_R \end{bmatrix} \begin{bmatrix} \beta \\ R \end{bmatrix} + \begin{bmatrix} \frac{1}{m\bar{V}}\bar{Y}_{\delta_R} \\ \frac{1}{I_z}N_{\delta_R} \end{bmatrix} \delta_R \tag{4.3.2}$$

where the gravitational coupling term has been ignored [2]. Calculating the open-loop characteristic equation gives,

$$p(s) = s^2 + \left(-\frac{1}{I_z}N_R - \frac{1}{m\bar{V}}\bar{Y}_\beta\right)s + \frac{1}{I_z}\left(\frac{1}{m\bar{V}}\bar{Y}_\beta N_R + N_\beta - N_\beta\frac{1}{m\bar{V}}\bar{Y}_R\right) \tag{4.3.3}$$

The frequency of the open-loop Dutch roll mode poles is therefore given by,

$$\omega_{DR} = \sqrt{\frac{1}{I_z}\left(\frac{1}{m\bar{V}}\bar{Y}_\beta N_R + N_\beta - N_\beta\frac{1}{m\bar{V}}\bar{Y}_R\right)} \tag{4.3.4}$$

Since the poles and zeros of the lateral dynamics scale uniformly with airspeed, [1] presented the following general equation for the Dutch roll damper which will function over the entire airspeed range of the aircraft,

$$D(s) = \frac{K'_{DR}}{\eta_d\omega_{DR}}\frac{s}{(s + \eta_d\omega_{DR})} \tag{4.3.5}$$

where K'_{DR} is the normalised feedback gain, ω_{DR} is the frequency of the open-loop Dutch roll mode poles and η_d is the fraction of this frequency where the filter will cut off.

4.3.2 Pole Placement

The pole placements in this section are for the aircraft parameters and standard flight conditions as outlined in Appendix B.6.

The cut-off frequency of the filter is chosen as,

$$\omega_f = \eta_d \omega_{DR} \qquad \text{where,} \qquad \eta_d = \frac{1}{3} \tag{4.3.6}$$

This ensures that the Dutch roll mode response lies within the filter's passband whilst also filtering out low frequency effects such as constant turn rates.

The feedback gain of the filter at the aircraft's trim velocity must now be determined. In order to accomplish this, the root locus for a variation in the filter feedback gain of the closed-loop system is obtained as shown in Figure 4.5.

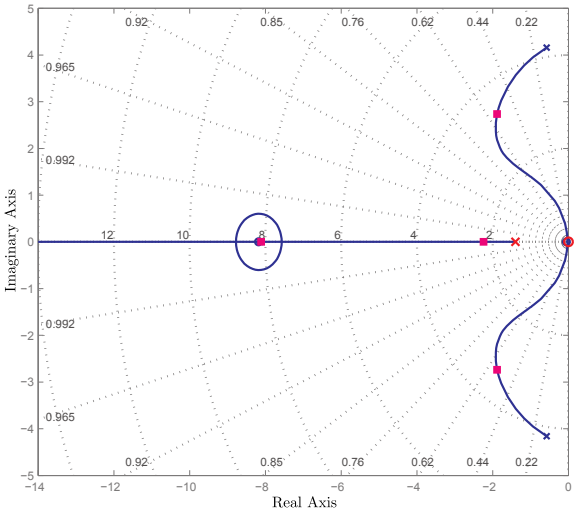

Figure 4.5 – Root locus design of the Dutch roll damper at the aircraft's trim velocity

It can be seen that the open-loop damping ratio of the Dutch roll mode poles is given by,

$$\zeta_{ol} = 0.14 \tag{4.3.7}$$

which is very lightly damped. Selecting the feedback gain as,

$$K_{DR} = -0.214 \tag{4.3.8}$$

results in the closed-loop poles shown, and yields a closed-loop damping ratio of,

$$\zeta_{cl} = 0.57 \tag{4.3.9}$$

The filter's transfer function at trim velocity is therefore given by,

$$D_{trim}(s) = \frac{-0.214s}{s + 1.4} \tag{4.3.10}$$

The normalised feedback gain can now be calculated as,

$$K'_{DR} = K_{DR}(\omega_{DR}\eta_d) \tag{4.3.11}$$

$$= -0.3 \tag{4.3.12}$$

During implementation of this controller, substituting the gain K'_{DR} from Equation 4.3.11 alongside ω_{DR} from Equation 4.3.4 as well as η_d from Equation 4.3.6 into Equation 4.3.5 leads to the transfer function of the Dutch roll damper which will function at the current airspeed of the aircraft.

4.3.3 HIL Simulation and Practical Flight Test Results

The Dutch roll damper was implemented on an OBC and tested in the HIL simulation environment as well as practically in a series of flight tests. The HIL simulation environment, aircraft, avionics and other hardware used in this project are outlined in Appendix B, only the results are presented in this section. The HIL tests allow the controller to be fully tested before practical flight tests are attempted. Ideally, the practical flight test results should closely resemble those achieved in the HIL simulation.

Figures 4.6a and 4.6b show the yaw rate and rudder deflections during a HIL simulation and flight test respectively. These responses are for the same set of HIL and flight test results shown in Figure 4.3 where the aircraft is undergoing large roll angle variations. It can be seen that the HIL simulation and flight test results are somewhat similar, but that there is significantly more disturbances in the case of the flight test.

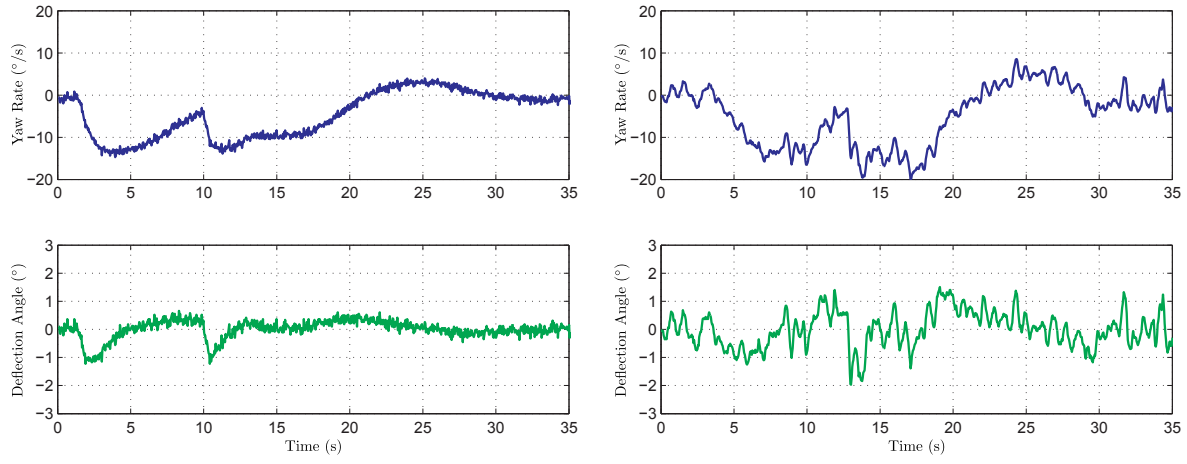

(a) Dutch roll damper during HIL **(b)** Dutch roll damper during flight test

Figure 4.6 – Yaw rate response and rudder deflection angle during HIL simulation and flight tests

Figures 4.7a and 4.7b show the yaw rate and rudder deflections during a flight test where the Dutch roll damper is disabled and enabled respectively. During these tests, the safety pilot manually generated a series of rudder deflections in order to demonstrate the effect

of the Dutch roll damper on the rudder actuator as well as to excite the Dutch roll mode dynamics of the aircraft. Figure 4.7b shows the rudder deflections commanded by the safety pilot, the rudder deflection commanded by the Dutch roll damper and the total rudder deflection. It can be seen that as the yaw rate increases so does the Dutch roll damper rudder command. This command is in the opposite direction to that of the safety pilot thereby resulting in a smaller total rudder deflection. This demonstrates the ability of the Dutch roll damper to oppose high yaw rates. Upon completion of the final safety pilot rudder step the excited Dutch roll mode of the aircraft can be observed. It can be seen that with the Dutch roll damper enabled, the yaw rate oscillations are significantly more damped than with the Dutch roll damper disabled.

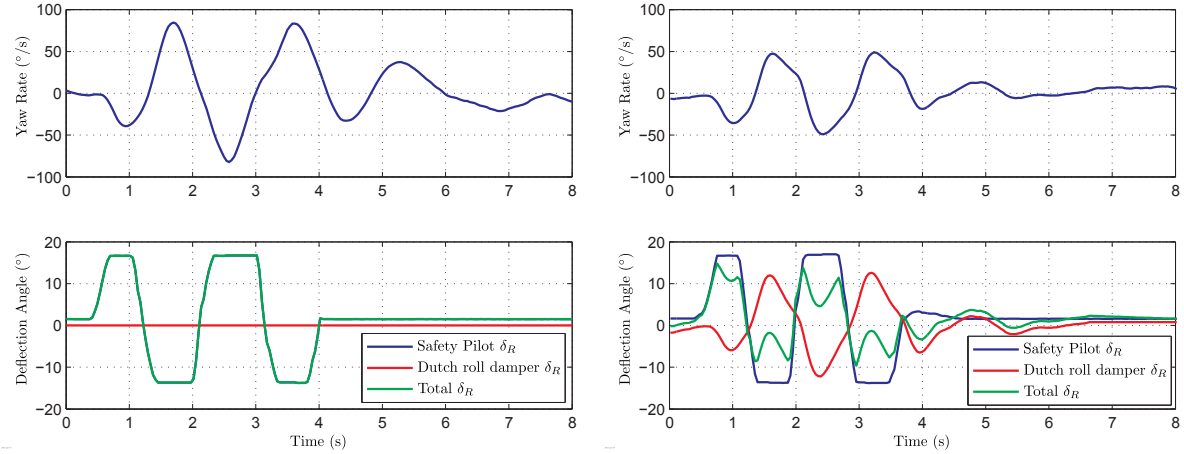

(a) Dutch roll damper disabled **(b)** Dutch roll damper enabled

Figure 4.7 – Yaw rate response to safety pilot rudder perturbations for Dutch roll damper disabled and enabled during flight test

4.4 Aircraft Guidance

Guidance Controller The purpose of the guidance controller is to control the aircraft's flight path in the XY-plane of the inertial axis system. The guidance controller used was developed by [3] and only the outline is presented in this section.

The guidance controller receives a desired flight path from the landing state machine, and then commands a lateral acceleration B_N^{ref} in order to move the aircraft towards the path. The flight path is generated between waypoints as shown in Figure 5.5.

The guidance logic consists of two parts, first a reference point is selected on the desired path at a certain distance (L_1) ahead of the aircraft. Secondly a lateral acceleration command is generated by using the aircraft's airspeed, the length (L_1) as well as the angle (η) between the velocity vector of the aircraft and the reference length. This is depicted in Figure 4.8 and the lateral acceleration command is generated by,

$$-B_N^{ref} = 2\frac{\bar{V}^2}{L_1}\sin\eta \tag{4.4.1}$$

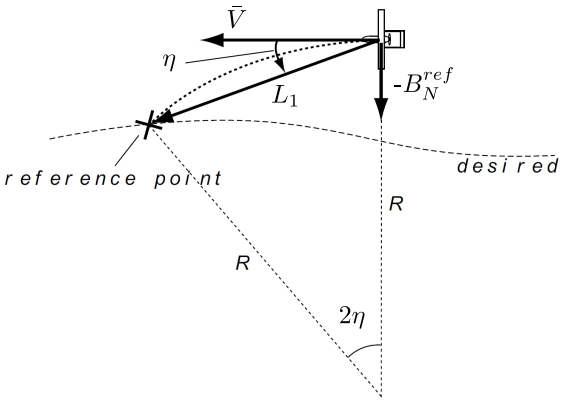

Figure 4.8 – Guidance logic [3]

The guidance controller has the effect that the aircraft will tend to align its velocity direction with the direction of the reference point length (L_1). When the aircraft is far away from the desired path, the vehicle rotates its velocity vector to approach the desired path at a large angle, and when the vehicle is close to the desired path, the vehicle rotates its velocity vector to approach the desired path at a small angle. This results in a smooth overall guidance path.

Linearisation of the nonlinear guidance logic leads to a differential equation for a controller which regulates the cross track error to zero. The poles of this controller are given by [7],

$$s = -\frac{\bar{V}}{L_1} \pm \frac{\bar{V}}{L_1}\mathrm{i} \tag{4.4.2}$$

The guidance controller is thus linearly approximated as a critically damped pole pair with natural frequency,

$$\omega_n = \sqrt{2}\frac{\bar{V}}{L_1}\text{rad/s} \tag{4.4.3}$$

The design choice for the guidance controller is selecting an appropriate length (L_1) for the distance between the aircraft and the reference point. A shorter length will result in a more aggressive controller. For the aircraft parameters and standard flight conditions as outlined in Appendix B.6 it was found during HIL simulation and practical flight tests that a satisfactory response is obtained for a length of,

$$L_1 = 100\,\text{m} \tag{4.4.4}$$

which results in a natural frequency of,

$$\omega_n = 0.25\,\text{rad/s} \tag{4.4.5}$$

NSA and Roll Angle Command Calculation The lateral acceleration command generated by the guidance controller (B_N^{ref}) and the normal acceleration command generated by the climb rate controller (C_N^{ref}) are both in the navigation axis system and cannot

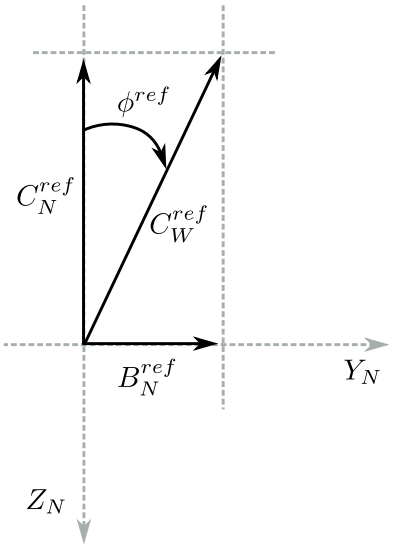

Figure 4.9 – Conversion of lateral and normal acceleration in navigation axes to wind axes NSA and roll angle

be controlled directly. These commands must therefore be converted to a NSA reference command (C_W^{ref}) and a roll angle (ϕ^{ref}) as shown in Figure 4.9.

The roll angle reference command is therefore given by,

$$\phi^{ref} = \arctan\left(-\frac{B_N^{ref}}{C_N^{ref}}\right) \tag{4.4.6}$$

where it is assumed that the roll angle remains within the controller limits as defined in Appendix B.5. The NSA reference command is given by,

$$C_W^{ref} = -\sqrt{\left(C_N^{ref}\right)^2 + \left(B_N^{ref}\right)^2} \tag{4.4.7}$$

It must be noted that since the guidance controller lacks an integrator term, the roll angle must be exactly achieved as is the case for the roll angle controller of §4.2. However, a practical constraint emerges in that during mounting, the sensors might not be exactly aligned with the axes of the aircraft. In particular, the roll angle determined by the estimator could have an offset relative to the actual roll angle of the aircraft. This will in turn result in the guidance controller following a straight path with a constant offset which is proportional to the error in roll angle. This problem is overcome via calibration; adding an appropriate offset to the roll angle measurement such that it matches the actual roll angle of the aircraft. This roll angle offset can also be exploited during landing since it allows small corrections to be made to the flight path of the aircraft as is flies along the runway.

4.4.1 HIL Simulation and Practical Flight Test Results

The guidance controller was implemented on an OBC and tested in the HIL simulation environment as well as practically in a series of flight tests. The HIL simulation environment, aircraft, avionics and other hardware used in this project are outlined in Appendix

B, only the results are presented in this section. The HIL tests allow the controller to be fully tested before practical flight tests are attempted. Ideally, the practical flight test results should closely resemble those achieved in the HIL simulation.

Figure 4.10a shows the flight path of the aircraft and Figure 4.10b the corresponding roll angle, navigation axis LSA and wind axis NSA reference commands during HIL simulation, whilst Figures 4.10c and 4.10d show the same during a practical flight test. It can be seen that the flight test results compare well with those obtained in the HIL simulation. It can also be seen that the aircraft's path only converges on the reference path after approximately $250\,\text{m}$. This is of importance during landing since sufficient distance must be allowed for in the landing procedure to allow the guidance controller to settle. Decreasing the guidance length (L_1) will decrease the distance required for the controller to settle, however, this comes at the cost of potentially higher roll angles at the touchdown point since the controller will react more aggressively to any path error.

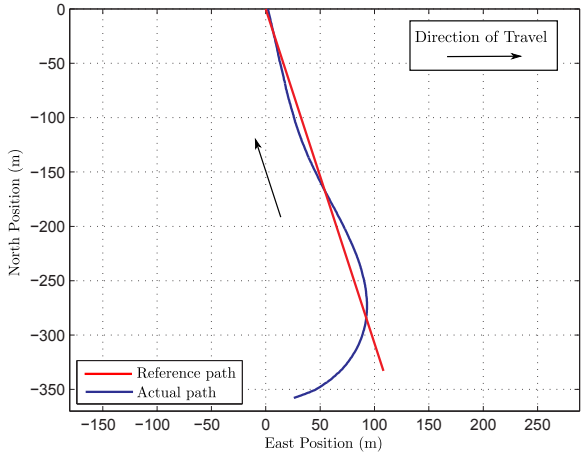

(a) HIL flight path

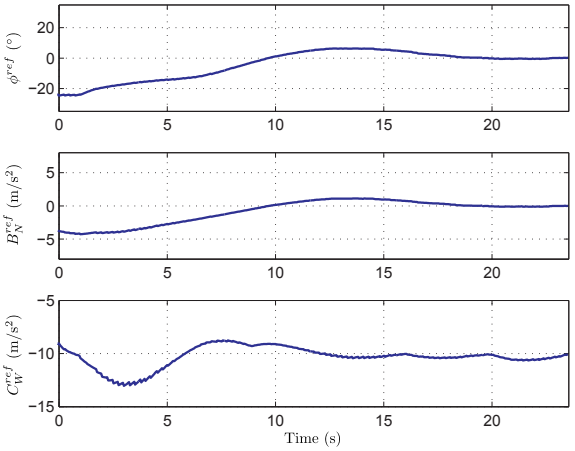

(b) HIL controller reference commands

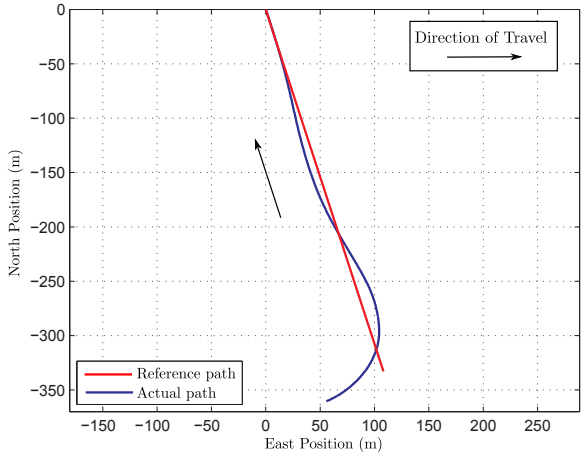

(c) Flight test flight path

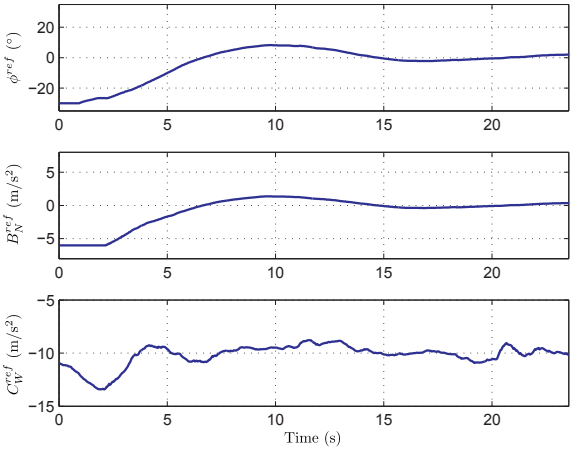

(d) Flight test controller reference commands

Figure 4.10 – Flight path and corresponding roll angle, navigation axis LSA and wind axis NSA reference commands

Chapter 5

Landing

The controllers developed in Chapters 3 and 4 allow for the control of the longitudinal and lateral motion of the aircraft respectively. This chapter shows how this control is utilised to accomplish an aircraft landing.

The landing control of the aircraft can be split into three broad categories. Firstly, the flight path of the aircraft must be controlled to coincide with the runway. This is accomplished by means of the guidance controller of §4.4. Secondly, the altitude of the aircraft must be controlled such that the aircraft descends along a specific path onto the runway. This control is accomplished by means of the altitude controller of §3.4. Thirdly, the airspeed of the aircraft must be maintained throughout the landing. This is accomplished be means of the airspeed controller of §3.5.

For an accurate landing to be performed, the controllers must strictly regulate their respective parameters. The biggest threat to this is the presence of wind disturbances of which crosswinds and wind gusts are of greatest concern. Crosswind landings fall outside the scope of this project and have been discussed in [5]. The focus falls on wind gusts, the impact of which is more pronounced during landing due to the small size and weight of the aircraft used in this project. The direct-lift-augmented NSA controller of §3.2.6 was designed to provide improved rejection of these disturbances when compared to the conventional NSA controller of §3.2.4. These two controllers will be tested and compared.

The procedure followed during a landing is discussed in this chapter. The flight and descent paths are thereafter investigated, followed by an overview of the landing state machine. The chapter ends with the flight test results of several autonomous landings where both the conventional and the direct-lift-augmented NSA controllers were utilised.

5.1 Landing Procedure

5.1.1 Standard Aircraft Landing Procedure

Whilst developing a suitable landing procedure for this project, it is useful to cross-reference the procedures used by piloted aircraft at small airfields. Such a standard aircraft landing procedure is presented in [20] and consists of several phases. These phases are discussed briefly with reference to the standard rectangular airfield traffic pattern illustrated in Figure 5.1, and its corresponding landing path geometry as illustrated in Figure 5.2.

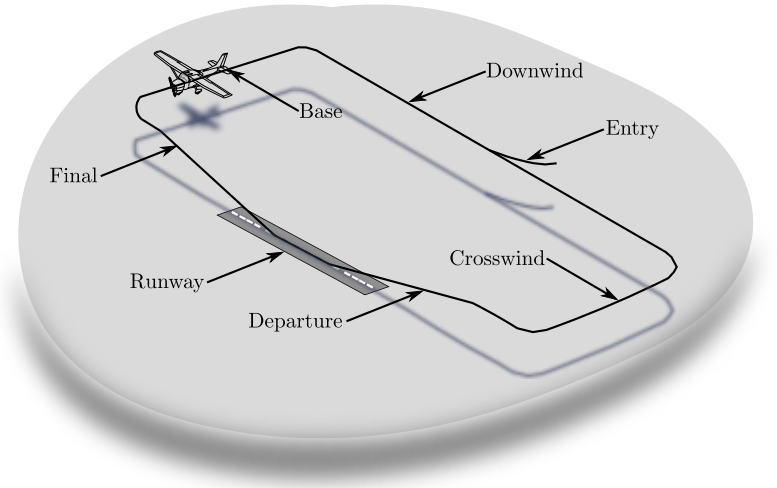

Figure 5.1 – Standard rectangular airfield traffic pattern

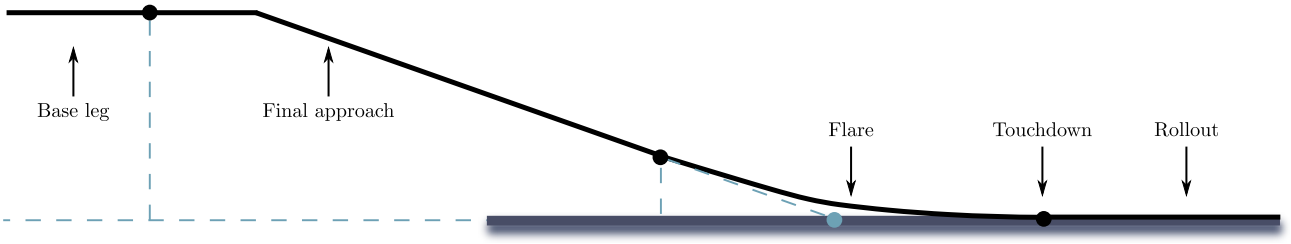

Figure 5.2 – Standard landing path geometry

Enter and maintain circuit The purpose of the landing circuit is to allow the aircraft's position, airspeed and altitude to settle into a controlled state such that only small corrections are required as the aircraft transitions into the final phase of the landing sequence. The aircraft enters the landing circuit on the downwind leg. It then follows the circuit at a constant altitude until permission to land is granted by the air traffic control authority. Once this permission is obtained, the airplane will commence the actual landing when it reaches the subsequent base leg.

Base leg When the aircraft enters the base leg for a landing approach its airspeed is reduced to the recommended landing airspeed. This is typically 1.4 times the stall speed of the aircraft. The aircraft then flies perpendicular to the runway, and at the appropriate distance from the runway centreline turns onto the final approach leg. During this turn the aircraft must not exceed a shallow to medium roll angle since the stall speed of the aircraft increases at higher roll angles. After completion of the turn, the aircraft's flight path must be aligned with the centreline of the runway.

Final approach Assuming that there is no crosswind, the longitudinal axis of the aircraft should be kept aligned with the centreline of the runway during the final approach. The final approach leg consists of a descending flight path which originates from the base-to-final turn, and extends down towards the intended touchdown point on the runway. This point should be within the first one-third of the runway. Precise control of the aircraft is essential during the final approach.

Flare The flare is a smooth transition from the approach attitude to a landing attitude. During the flare, the descending flight path of the final approach is gradually rounded out until the flight path of the aircraft is parallel with the runway. This sheds much of the remaining kinetic energy of the aircraft. At this point the aircraft touches down on the runway.

Touchdown Ideally, the aircraft should touch down gently on the main landing gear first, and at the lowest controllable airspeed.

Rollout After touchdown, control of the aircraft must be maintained whilst it decelerates to the normal taxi speed. The landing is now complete.

Go-arounds If at any point during the landing procedure the aircraft's airspeed, position or attitude deviate significantly from the normal state, or if any landing condition is not satisfactory, the landing is rejected and a go-around initiated. The aircraft then re-enters the circuit, and the landing is attempted again.

5.1.2 Modified Aircraft Landing Procedure

The standard aircraft landing procedure described in §5.1.1 is now modified to more effectively accommodate the project goals and the aircraft used as a testbed. One of the primary goals of this thesis is an *accurate* autonomous landing and the adaptation of the standard landing procedure will focus on achieving this outcome.

The standard rectangular landing circuit will be used as is, only the path of the final approach leg is modified in order to minimise any potential path following errors which may arise. These errors can have a significant effect on the accuracy with which the aircraft touches down, as illustrated in Figure 5.3 where the intended and the actual straight approach paths are shown with a constant offset error.

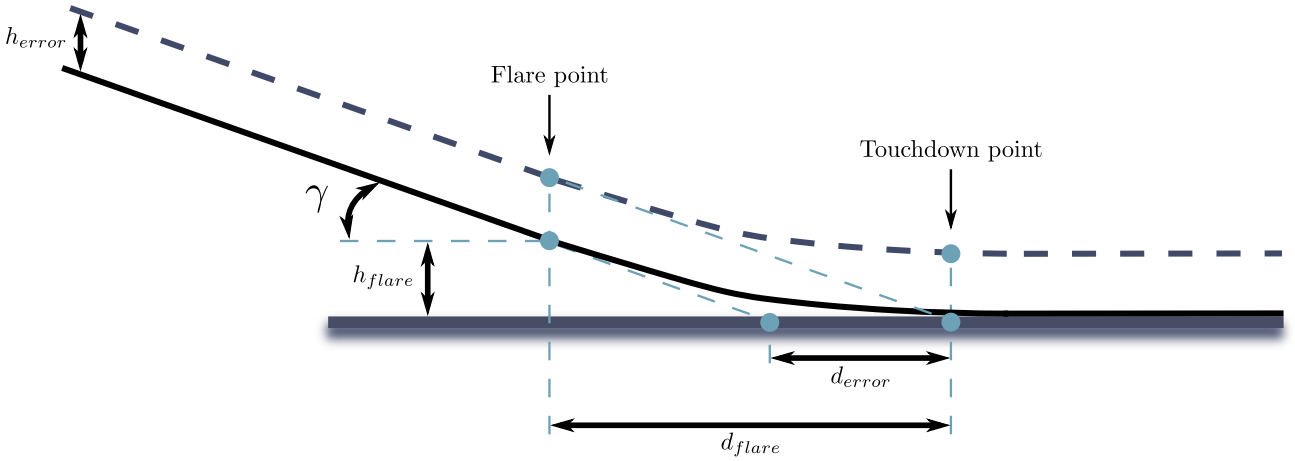

Figure 5.3 – Effect of an altitude error in the landing path on the touchdown point

The angle of the approach path γ is typically around 3° [19]. This means that a small error in height will cause a large error between the actual and the intended landing point. With reference to Figure 5.3, this is expressed mathematically as,

$$d_{error} = \frac{h_{error}}{\tan\gamma} \tag{5.1.1}$$

Figure 5.3 also shows the effect of a height error when a flare is performed. Any error between the intended and the actual approach paths is now of even greater consequence due to the fact that the angle of the flight path approaches 0° towards the end of the flare. This means that for even a small error in height, the aircraft could potentially travel a great distance along the runway before touching down. This is usually of little consequence during normal landings. However, if an accurate landing is desired, the flare manouvre presents a significant drawback.

Another significant drawback of the flare manouvre is that, due to the nonlinear nature of the wing when it is close to stall, the precise trajectory of the flare is unknown [7]. This means that the relationship between the flare height h_{flare} and the distance d_{flare} cannot be accurately determined. This is aggravated further when the effects of wind disturbances are taken into account. Therefore, to aid in the landing accuracy of the aircraft, the flare is omitted from the landing procedure, and the aircraft is simply flown along the straight path of the final approach leg. This omission comes at the cost of the gentle touchdown which would otherwise have occurred with the use of the flare, and increases the likelihood of undercarriage damage or bouncing of the aircraft during landing.

The standard landing path is further modified to accommodate the specific layout of the airfield where the practical flight tests are conducted (see Appendix D.1). Firstly, the glide path is split into two phases of descent as shown in Figure 5.4. The first descent phase is at a steeper angle than the last phase so as to provide sufficient obstacle clearance during the landing. This intermediate slope also means that the aircraft flies

at a higher altitude when it is still far away from the runway than it would have done without this slope. This provides an additional altitude margin for the safety pilot to be able to observe, and act to recover the aircraft from, any anomalies during flight. Secondly, the base leg, and those that precede it, is set at a higher altitude than the start of the final approach leg. This is again done to reduce the risks associated with low level flight, especially at the large distance between the aircraft and the safety pilot.

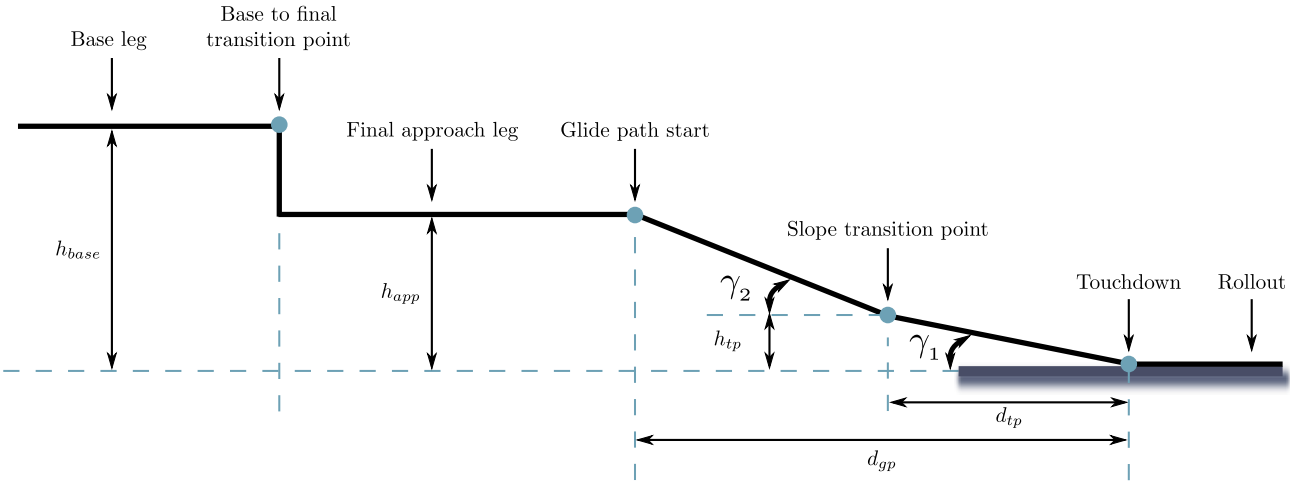

Figure 5.4 – Landing path geometry

The runway circuit is defined by four waypoints as shown in Figure 5.5. These waypoints are also set to allow for the specific layout of the airfield where flight tests are conducted. The waypoint locations allow for the avoidance of obstacles, and also allow for sufficient distance for the guidance controller to settle once the aircraft has turned from the base onto the final leg.

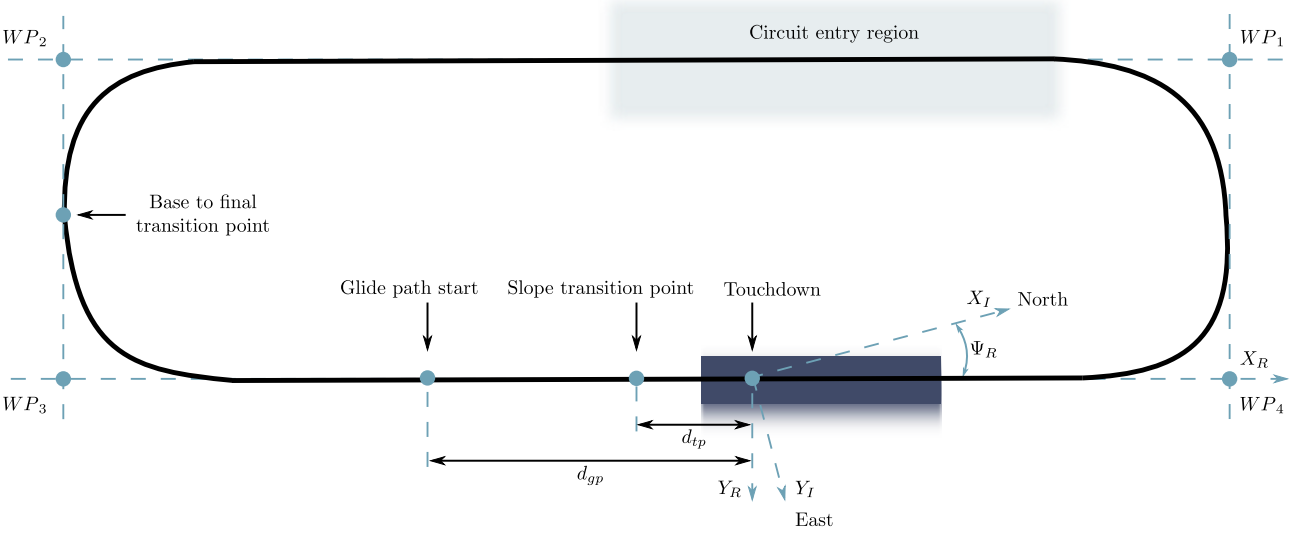

Figure 5.5 – Landing circuit geometry

It must be noted that the landing approach followed is very similar to that employed by an aircraft landing on the deck of an aircraft carrier. An outline of the specific procedure is presented by [19]. In essence, such a landing also makes use of a straight approach path with no flare so as to ensure the accuracy of the touchdown point. When the aircraft touches down, it is captured by an arrestor cable by means of a hook attached to the rear of the aircraft. This cable then brings the aircraft to a stop. This means that the aircraft does not perform any runway control. If a similar arrestor mechanism is used in this project, the need for runway control also falls away and the entire landing could be conducted autonomously. Although such a mechanism falls outside the scope of this project, the effect of using an arrestor mechanism is in essence simulated during the practical flight tests where the safety pilot performs the same function by stopping the aircraft after touchdown has been achieved by the autopilot.

After the modifications to the standard landing procedure, the landing circuit is as shown in Figure 5.5, and the corresponding landing path geometry is as shown in Figure 5.4. The specific details contained in these figures are discussed in the relevant sections which follow.

5.2 Landing Circuit

The landing circuit is the horizontal path followed by the aircraft during landing. The procedure followed is best explained in the context of a practical flight test. During a practical flight test, the safety pilot controls the aircraft during take-off, and positions it in the entry area region as shown in Figure 5.5 at a moderate altitude. Upon enabling the autopilot, the guidance controller will steer the aircraft towards the path between waypoints 1 and 2, while the altitude controller will move the aircraft towards the circuit altitude. The airspeed controller will maintain the aircraft's airspeed at the circuit airspeed. When the aircraft is sufficiently close to waypoint 2, the guidance controller will transition to the base leg causing the aircraft to turn. The same occurs for every waypoint reached, and the aircraft will maintain this guidance circuit until a landing command is issued. When a landing command is received, the same circuit is flown, however, instead of following a constant altitude, the longitudinal landing path controller will cause the aircraft to descend towards the runway as discussed in §5.3. This altitude control is completely independent of the landing circuit control. Upon touchdown the aircraft's controllers are disabled, and the safety pilot brings the aircraft to a stop.

As shown in Figure 5.5 the landing circuit is defined in the runway axis system of §2.1.1. It can be seen that the runway axis system is rotated from the inertial axis system by an angle Ψ_R. The waypoints are converted from the runway to the inertial axis system on the groundstation before being sent to the OBC.

The values for the waypoints used are,

$$WP_{1_{North}} = 220\,\text{m} \qquad WP_{1_{East}} = -180\,\text{m} \tag{5.2.1}$$

$$WP_{2_{North}} = -350\,\text{m} \qquad WP_{2_{East}} = -180\,\text{m} \tag{5.2.2}$$

$$WP_{3_{North}} = -350\,\text{m} \qquad WP_{3_{East}} = 0\,\text{m} \tag{5.2.3}$$

$$WP_{4_{North}} = 220\,\text{m} \qquad WP_{4_{East}} = 0\,\text{m} \tag{5.2.4}$$

and the angle between the runway and the inertial axis system is given by,

$$\Psi_R = 19^\circ \tag{5.2.5}$$

5.2.1 HIL Simulation and Practical Flight Test Results

The HIL simulation and practical flight test results of all of the controllers involved in executing the landing circuit are shown in Chapters 3 and 4. In order to confirm the proper execution of the landing circuit, the waypoints were entered into the OBC, and the circuit flown in the HIL simulation environment as well as practically in a series of flight tests. The HIL simulation environment, aircraft, avionics and other hardware used in this project are outlined in Appendix B, only the results are presented in this section. The HIL tests allow the landing circuit controllers to be fully tested before practical flight tests are attempted. Ideally, the practical flight test results should closely resemble those achieved in the HIL simulation.

Figures 5.6a and 5.6b show the landing circuit of the aircraft during a HIL simulation and a practical flight test respectively. In these tests, the autopilot is enabled at the point indicated. The aircraft then flies the entire circuit, and on the second pass descends and lands. It can be seen that the flight test result corresponds well with that obtained during HIL simulation, and that the path of the aircraft is aligned closely with the centreline of the runway at the touchdown point.

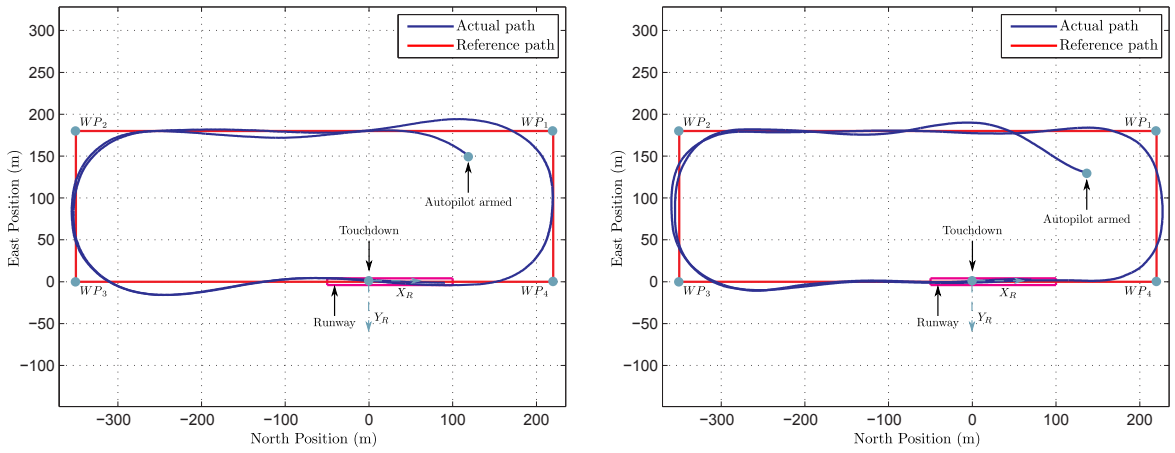

(a) HIL landing circuit **(b)** Flight test landing circuit

Figure 5.6 – Landing circuit in runway axis system during HIL simulation and flight test

5.3 Longitudinal Landing Path

The longitudinal landing path is the altitude path followed by the aircraft as it descends during the landing. This path is shown in Figure 5.4, and the path variables are defined as,

Base leg height (h_{base}) - the height of the base leg above the touchdown point

Final approach leg height (h_{app}) - the height of the final approach leg above the touchdown point, this is also the height of the start of the glide path

Slope transition point height (h_{tp}) - the height of the slope transition point above the touchdown point

Glide path start distance (d_{gp}) - the distance between the start of the glide path, and the touchdown point

Slope transition point distance (d_{tp}) - the distance between the slope transition point, and the touchdown point

Initial glide path angle (γ_2) - the angle of the glide path directly following the glide path start point

Final glide path angle (γ_1) - the angle of the glide path directly following the slope transition point

The values of the longitudinal path variables are,

$$\gamma_1 = 3\,^\circ \tag{5.3.1}$$

$$\gamma_2 = 7\,^\circ \tag{5.3.2}$$

$$d_{tp} = 70\,\mathrm{m} \tag{5.3.3}$$

$$d_{gp} = 200\,\mathrm{m} \tag{5.3.4}$$

The final glide path angle (γ_1) was selected to provide a relatively gentle touchdown. This angle could be increased which would allow a more accurate landing due the reduction in the relationship between a height error and the actual and intended touchdown points as shown in Figure 5.3. However, the landing gear of the aircraft would first need to be strengthened to absorb the increased impact force which will result.

During a practical flight test, the aircraft is positioned on the runway at the point where touchdown during the landing is intended. The aircraft's sensors are then zeroed, and the estimator started (see Appendix B). The touchdown point therefore serves as the reference point for the landing circuit and longitudinal landing paths, and the altitude commands are calculated based on the horizontal distance between the aircraft and this point.

During the design of the altitude controller of §3.4 it was noted that the altitude control law intentionally lacks integrator feedback, and makes use of only proportional feedback from the climb rate. This results in the altitude controller tracking a ramp command with a steady state error which means that the landing approach path will be followed with a constant altitude offset. The motivation behind this control law design choice is twofold. Firstly, the total duration of the glide path is not very long, therefore an integrator term on the altitude might not have sufficient time to settle the altitude to the reference value before touchdown occurs. Secondly, an integrator will have almost no effect on minimising random disturbances such as wind gusts. The practical implication of this control decision is that, for the aircraft to land at a specific point on the runway, the commanded touchdown point must be positioned below the runway by the same distance as the altitude offset. This is illustrated in Figure 5.7.

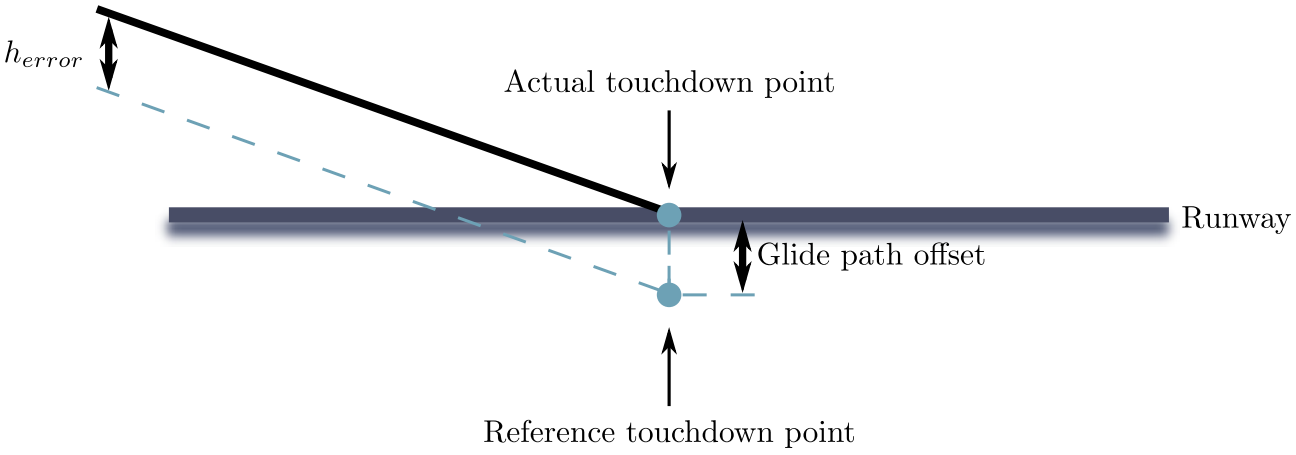

Figure 5.7 – Glide path reference offset

The altitude control is a type one system, therefore the steady state error to a ramp input $r(t) = At$ is given by,

$$e_{SS} = \frac{A}{K_{V_{ec}}} \tag{5.3.5}$$

where $K_{V_{ec}}$ is the velocity error constant. As shown in Appendix C.4,

$$K_{V_{ec}} = K_{P_h}\tau_{\text{CR}} \tag{5.3.6}$$

where τ_{CR} is the time constant of the dominant closed-loop climb rate dynamics pole and K_{P_h} is the altitude feedback gain. The actual steady state error is greater than Equation 5.3.5 suggests, due to inaccuracies in the model. It is therefore best determined experimentally during flight tests.

Figure 5.7 reveals an additional implication of the glide path offset. It is evident that the actual touchdown position of the aircraft can be directly affected by simply changing the glide path offset. An increase in the glide path offset will result in the aircraft touching down ahead of the reference touchdown point, whereas a decrease will result in the aircraft touching down beyond the reference point. Alternatively, it means that any constant error acting on the aircraft and affecting the accuracy of the touchdown point can be compensated for by an appropriate glide path offset. Such errors arise mainly from constant wind, ground effect and aircraft configuration changes. Therefore, to achieve improved landing accuracy, a runway flyby can be performed with a mock landing at a moderate altitude. The glide path offset can then be determined and the reference updated accordingly. This is shown in Figures 5.8a and 5.8b where the actual and reference glide paths are shown for both a HIL simulation and a flight test, and where the glide path offset at the mock touchdown point is shown. Next, a landing is performed. The error in touchdown position can then be used to calculate the required change in offset in order to compensate for any additional sources of error such as ground effect. In this manner, the accuracy of the touchdown point can be improved.

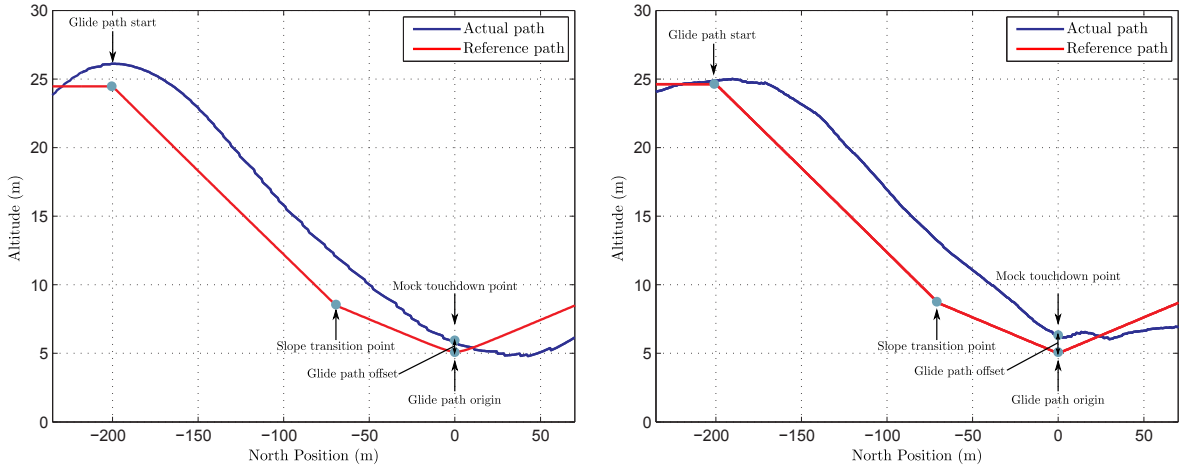

(a) HIL landing offset

(b) Flight test landing offset

Figure 5.8 – Landing longitudinal path for a mock landing during HIL simulation and flight test

5.4 Landing State Machine

The landing state machine is responsible for the overall control of the aircraft to accomplish a landing. It does so by providing the reference commands of the airspeed, altitude and guidance controller as shown in Figure 5.9. These references are set on the groundstation and can be updated during flight. During a landing, the altitude reference is calculated on board the aircraft and is based on the longitudinal landing path shown in Figure 5.4, whereas the guidance controller's reference is based on the landing circuit shown in Figure 5.5. The airspeed reference is typically fixed for the duration of the landing.

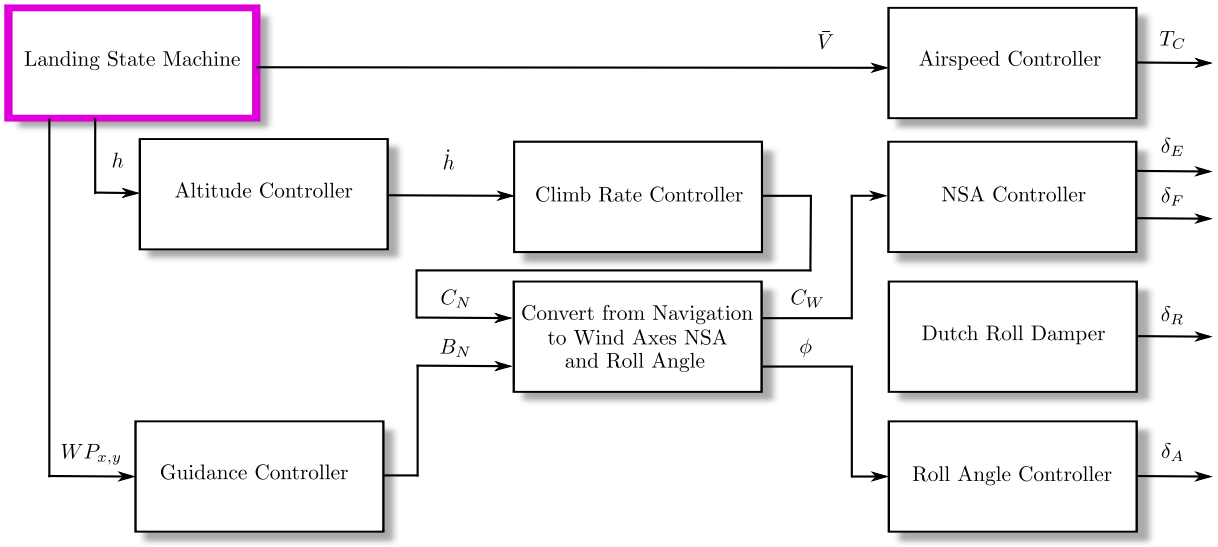

Figure 5.9 – Control System Overview Block Diagram

The logic of the landing state machine is depicted in Figure 5.10. The aircraft is positioned in the air by the safety pilot in the region shown in Figure 5.5. When the autopilot is armed, the state machine is entered, and the airspeed and altitude references sent to their respective controllers. The first two waypoints are sent to the guidance controller and the aircraft begins following the reference path. The landing state machine will update the waypoints when the aircraft is sufficiently close to its current destination waypoint. In this manner the circuit is flown at a constant airspeed and altitude. When the landing command is issued, the airspeed and circuit are maintained as before, however, the altitude reference now becomes dependent on the current position of the aircraft. When the aircraft reaches the final approach leg, the altitude command is calculated based on the glide path offset, the glide path angles (γ_1,γ_2) and the horizontal distance that the aircraft is away from the glide path origin. The aircraft therefore follows the longitudinal landing path shown in Figure 5.4. If at any point the position, airspeed or attitude of the aircraft is outside a set of safety limits, the landing is aborted and the safety pilot assumes control of the aircraft. The altitude descends along the glide path until the aircraft touches down. When a touchdown is registered, the controllers are

disabled and the safety pilot takes control, guiding the aircraft down the runway and bringing it to a stop.

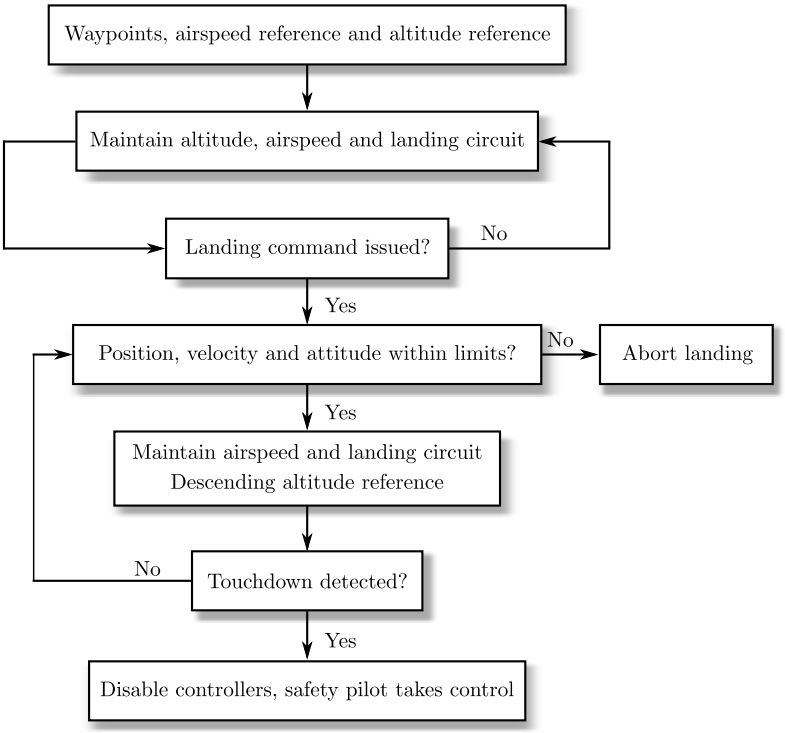

Figure 5.10 – Landing state machine overview

5.5 Landing Flight Test Results

In addition to all the controller verification flight tests presented in Chapters 3 and 4, five fully autonomous landings were performed over two days. Three of these made use of the conventional NSA controller of §3.2.4 and the final two landings were performed using the direct-lift-augmented NSA controller of §3.2.6. The results of these flight tests are presented in the sections which follow. Only the plots with direct bearing on the landing circuit and landing path are shown and evaluated.

The procedure for all flight tests is as follows,

1. The aircraft is placed on the runway and the OBC is initialised from a laptop running the ground station software.
2. The correct functioning of all sensors and actuators is confirmed, the DGPS is allowed time to lock and the estimator is started.
3. The waypoint locations, altitude and airspeed references, as well as the controller gains are uploaded to the OBC.
4. The safety pilot manually takes off and positions the aircraft in a predetermined area in the air.

5. The autopilot is enabled on the ground station, and the safety pilot flips the autopilot switch on the RC transmitter. This enables the autopilot and the aircraft begins to follow the waypoints at a constant airspeed and altitude.

6. When the aircraft enters the landing approach leg it begins to follow an altitude reference which will result in a mock landing. This mock landing serves to confirm the correct functioning of the landing controllers, and also to confirm that the heading and path of the aircraft coincide acceptably with the runway.

7. If adjustments to the heading or path are required, the relevant parameters are updated and another mock landing performed. If the heading and path are acceptable, an actual landing command is issued.

8. The aircraft descends along the glide path and impacts the runway.

9. At, or shortly after touchdown, the safety pilot retakes control of the aircraft, guiding it down the runway until it stops.

Further details of the tests are contained in the flight test cards shown in Appendix D.3.

5.5.1 Landing Test 1 - 28 November Flight 1

During this flight test the conventional elevator-based NSA controller was used. As this was the first landing attempt, the goal was merely to achieve a landing regardless of the accuracy thereof.

The aircraft performed three mock landings with the glide path origin set 5 meters above the runway. As the aircraft passed the glide path origin, the reference altitude began to increase at the same slope as during the approach. This caused the aircraft to ascend back to the circuit reference altitude. The actual landing was performed with the glide path origin set 1.3 meters *below* the runway. This is an intentionally conservative setpoint which will result in the aircraft overshooting the touchdown point, but touching down at a lower climb rate and higher pitch angle than it would otherwise. This is the result of the glide path reference increasing again as the origin is passed.

Figure 5.11a shows the altitude and airspeed of the aircraft for the duration of the flight test. The three mock landings can be seen in the altitude plot. It can also be seen that the airspeed was regulated well throughout the flight, including during the steep descent phases of the final approach legs. Figure 5.12a shows the altitude of the aircraft during the landing approach legs of the mock landings where it can be seen that the paths coincide reasonably well with one another.

The circuit path flown by the aircraft is shown in Figure 5.11b. During each of the mock landings the aircraft's path along the runway was observed and adjustments made to the runway angle and roll angle offset (see §5.2 and §4.4 respectively). It can be seen that

each successive lap of the circuit is flown with the path more aligned with the runway. This is again illustrated in Figure 5.12b where the flight paths across the runway are shown. It can be seen that the path of the third mock landing corresponded sufficiently well with the runway that an actual landing could be performed.

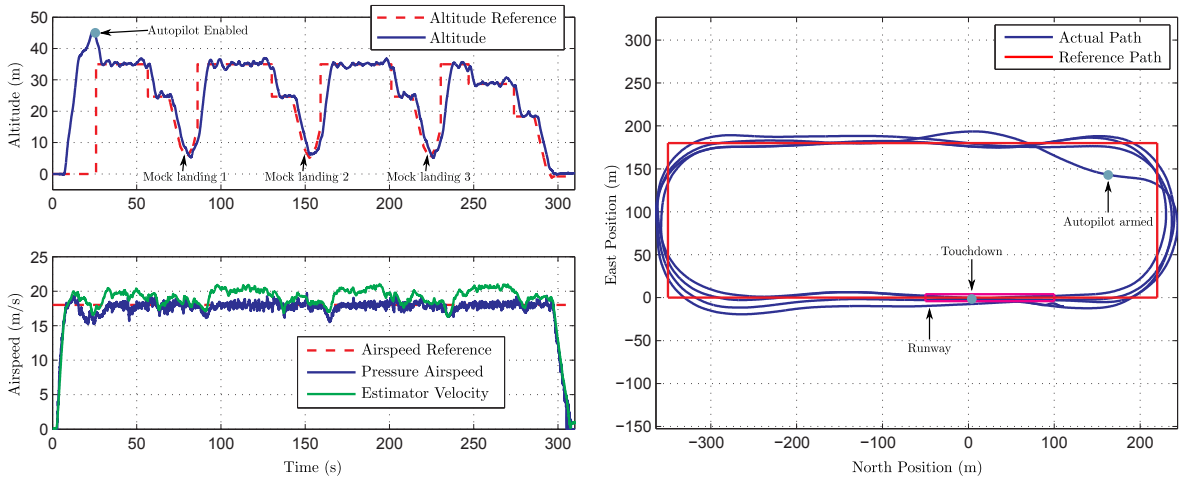

(a) Altitude and airspeed **(b)** Circuit flight path

Figure 5.11 – Landing Test 1 - Altitude, airspeed and circuit flight path for the entire duration of the flight

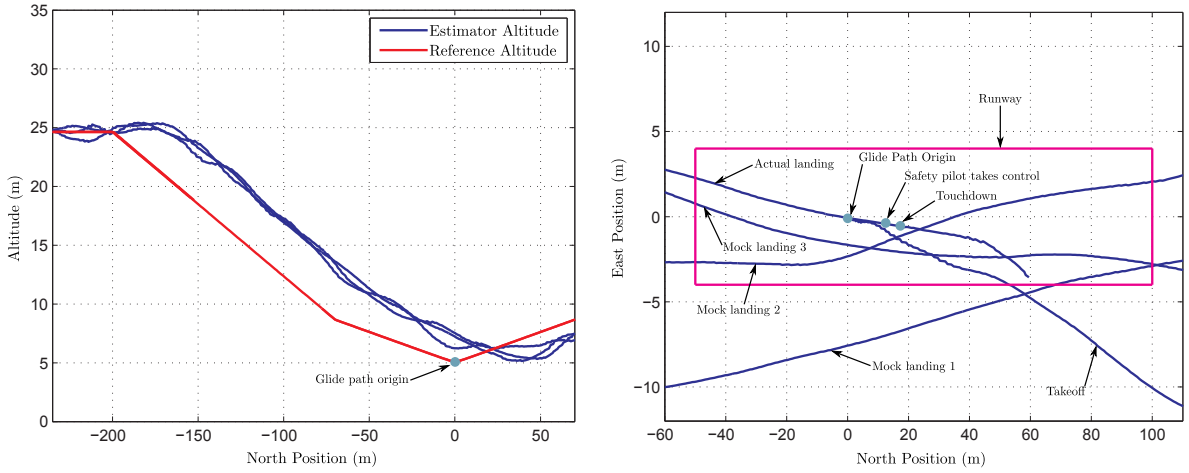

(a) Altitude during mock landings **(b)** Flight paths across runway

Figure 5.12 – Landing Test 1 - Altitude during landing leg of the mock landings, and all flight paths across the runway

The altitude of the aircraft during the actual landing leg is shown in Figure 5.13a. It can be seen that the aircraft followed the steeper reference glide path well with a constant offset. When the aircraft reached a lower altitude, the slope of its flight path is reduced somewhat. This is likely caused by the ground effect[1] which causes an increase in lift

[1] An increase in lift and decrease in drag due to the interaction of the wingtip vortices with the ground. Takes effect when the wing is within one wingspan length of the ground [5].

when the aircraft is close to the ground. The flight path of the aircraft during the actual landing, and the corresponding roll angle of the aircraft is shown in Figure 5.13b. It can be seen that the aircraft touched down close to the centre of the runway, but that the heading of the path is not aligned with the centreline of the runway. The roll angle plot indicates that the wings of the aircraft were not completely level at the touchdown point.

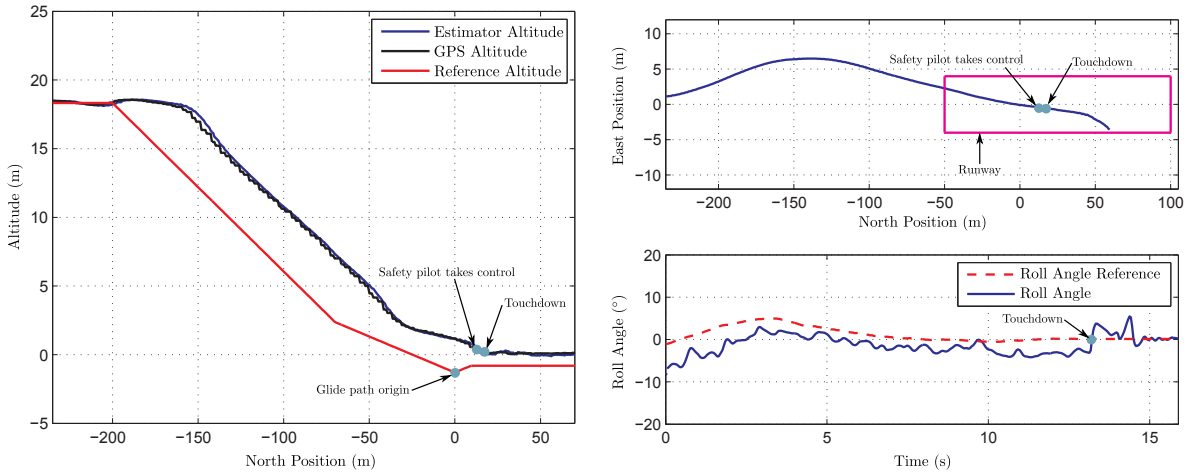

(a) Altitude during landing leg

(b) Flight path and roll angle during landing leg

Figure 5.13 – Landing Test 1 - Altitude, flight path and roll angle during landing leg

Figure 5.14a shows the climb rate and NSA of the aircraft during the final approach leg. The touchdown point is clearly visible in the NSA plot as the large spike in acceleration when the aircraft touches down. The pitch rate, pitch angle and elevator deflection are shown in Figure 5.14b. It can be seen that at the touchdown point the pitch angle is very slightly negative. This is one of the consequences of the straight line landing path, since the aircraft does not flare in order for its rear landing gear to strike the runway first. In practice this angle is small enough to not have any negative effect on the landing. However, should this angle be problematic, it can be increased by reducing the landing airspeed which in turn would cause the aircraft to fly at a higher angle of attack.

Figure 5.15 shows the altitude of the aircraft in the moments before and after touchdown. It can be seen that the aircraft touches down approximately 17 meters from the desired point at the glide path origin. This was expected due to the conservative value of the glide path offset. If the glide path offset is increased, the aircraft will touch down closer the intended touchdown point.

This flight test confirms the functioning of the landing controllers and state machine, and resulted in a successful landing. The subsequent flight tests will focus on improving the accuracy of the landing.

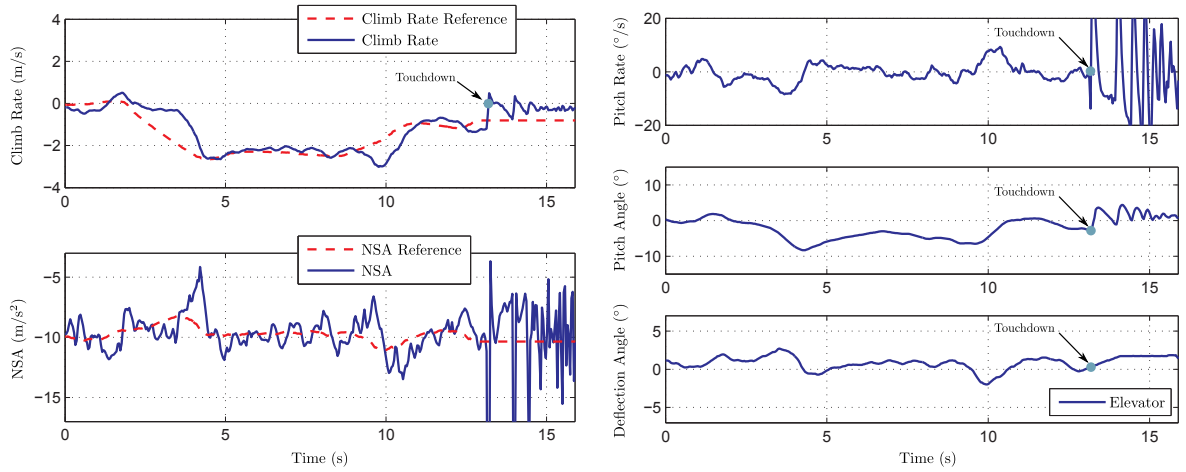

(a) Climb rate and NSA during landing leg

(b) Pitch rate, pitch angle and elevator deflection during landing leg

Figure 5.14 – Landing Test 1 - Climb rate and NSA, and pitch rate, pitch angle and elevator deflection during landing leg

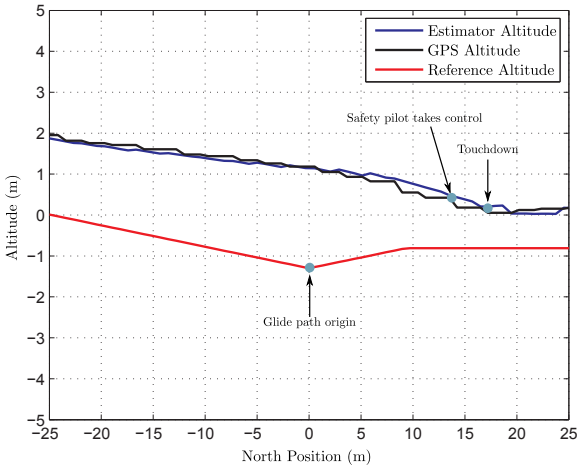

Figure 5.15 – Landing Test 1 - Altitude during touchdown

5.5.2 Landing Test 2 - 28 November Flight 2

During this flight test the conventional elevator-based NSA controller was again used. This test was conducted with the parameters as in Landing Test 1.

Only one mock landing was required since the runway heading parameters had been established in Landing Test 1. This mock landing was performed with the glide path origin set 5 meters above the runway. The actual landing was performed with the glide path origin set 1.5 meters *below* the runway. This is a slightly more aggressive setpoint which should result in an improved landing accuracy when compared to Landing Test 1. However, atmospheric conditions during this landing were less favourable and some wind disturbances prevailed.

Figure 5.16a shows the altitude and airspeed of the aircraft for the duration of the flight test. The mock landing can be seen in the altitude plot. It can also be seen that the airspeed was regulated well throughout the flight, including during the steep descent

phases of the final approach legs. When compared to the airspeed plot of Landing Test 1 as shown in Figure 5.11a, the impact of wind gusts can be seen. Figure 5.17a shows the altitude of the aircraft during the landing approach leg of the mock landing.

The circuit path flown by the aircraft is shown in Figure 5.16b. It can be seen that the flight path corresponds well with the reference path. This is again illustrated in Figure 5.17b where the flight paths of the mock and actual landing across the runway are shown. It can the seen that the path of the mock landing corresponded sufficiently well with the runway that an actual landing could be performed.

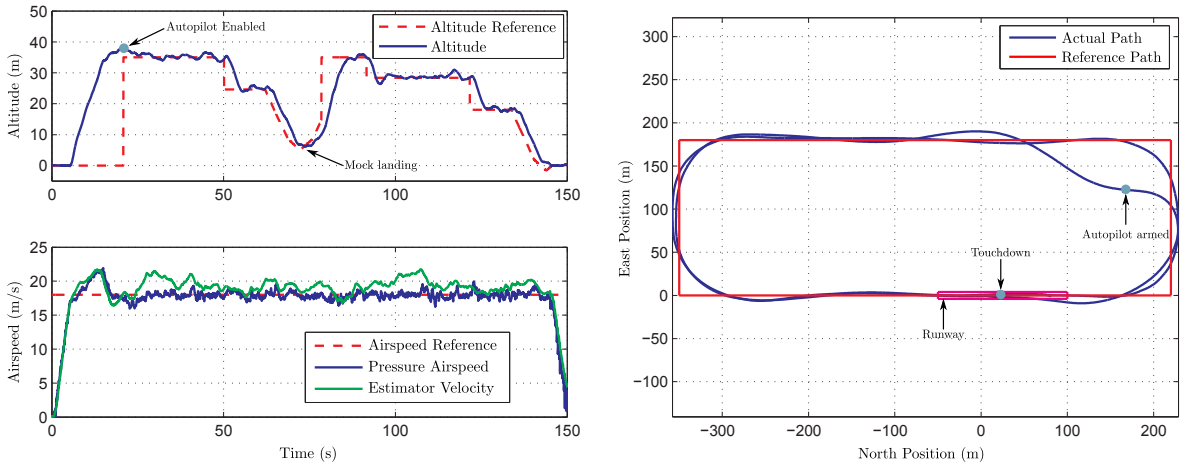

(a) Altitude and airspeed **(b)** Circuit flight path

Figure 5.16 – Landing Test 2 - Altitude, airspeed and circuit flight path for the entire duration of the flight

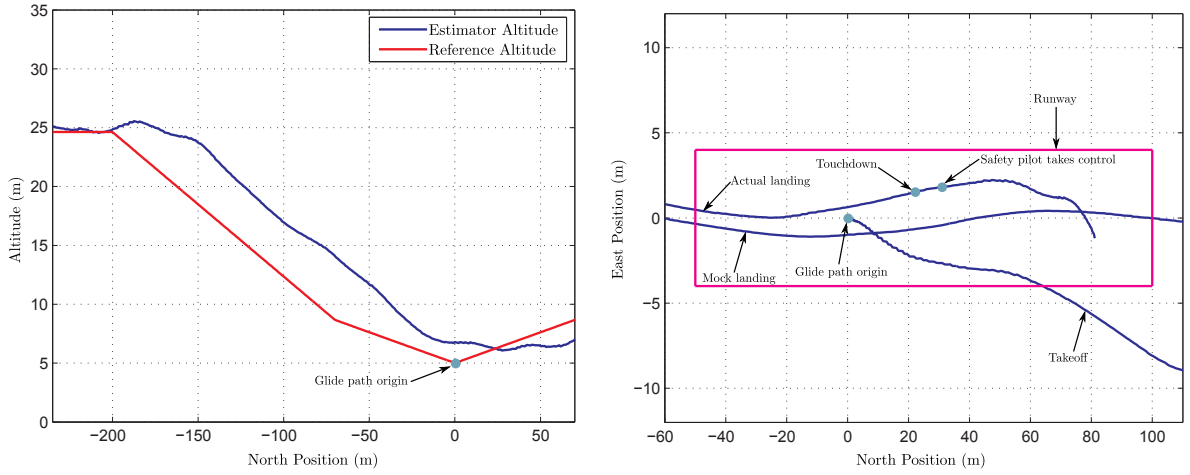

(a) Altitude during mock landings **(b)** Flight path across runway

Figure 5.17 – Landing Test 2 - Altitude during landing leg of the mock landings, and all flight paths across the runway

The altitude of the aircraft during the actual landing leg is shown in Figure 5.18a. It can be seen that the aircraft followed the steeper reference glide path well with a constant

offset. However, the effect of the increased wind disturbance is evident when compared to Landing Test 1 shown in Figure 5.13a. The flattening out of the aircraft's path caused by the ground effect is again evident. The flight path of the aircraft during the actual landing, and the corresponding roll angle of the aircraft is shown in Figure 5.18b. It can be seen that the aircraft touched down close to the centre of the runway, but that the heading of the path is not aligned with the centreline of the runway. The roll angle plot indicates that the wings of the aircraft were not perfectly level at the touchdown point. This is caused by the presence of the wind disturbances as can be seen in the larger roll angle fluctuations when compared to those in Landing Test 1 shown in Figure 5.13b.

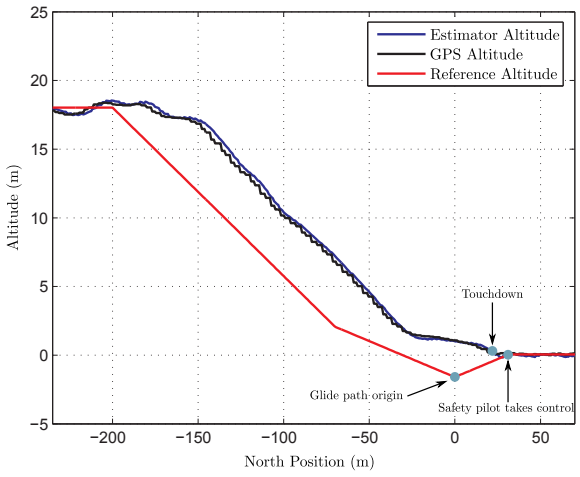

(a) Altitude during landing leg

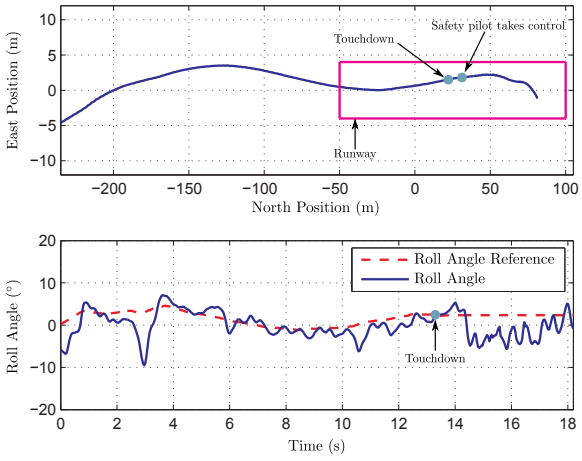

(b) Flight path and roll angle during landing leg

Figure 5.18 – Landing Test 2 - Altitude, flight path and roll angle during landing leg

Figure 5.19a shows the climb rate and NSA of the aircraft during the final approach leg. The touchdown point is clearly visible in the NSA plot as the large spike in acceleration when the aircraft touches down. The pitch rate, pitch angle and elevator deflection are shown in Figure 5.19b. It can be seen that at the touchdown point the pitch angle is very slightly negative. The effect of the wind disturbance can be clearly seen when comparing these plots to those of Landing Test 1 shown in Figures 5.14a and 5.14b.

Figure 5.20 shows the altitude of the aircraft in the moments before and after touchdown. It can be seen that the aircraft touches down approximately 22 meters from the desired point at the glide path origin. It was expected that this point would be closer to the desired touchdown point when compared to Landing Test 1, however, the presence of significant wind disturbances meant that it fared slightly worse.

This flight test confirms that the controllers function sufficiently well in the presence of wind disturbances in order for a landing to be conducted successfully.

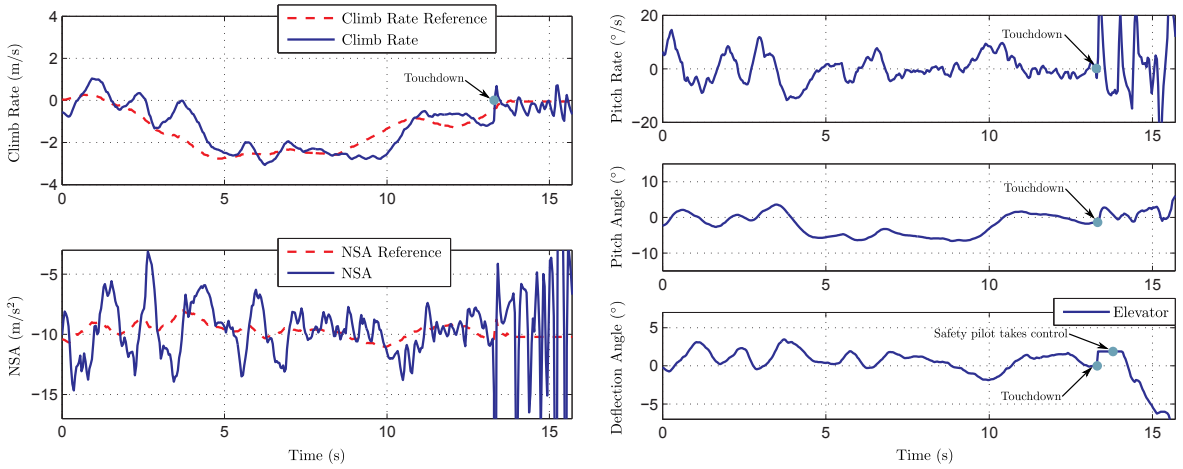

(a) Climb rate and NSA during landing leg

(b) Pitch rate, pitch angle and elevator deflection during landing leg

Figure 5.19 – Landing Test 2 - Climb rate and NSA, and pitch rate, pitch angle and elevator deflection during landing leg

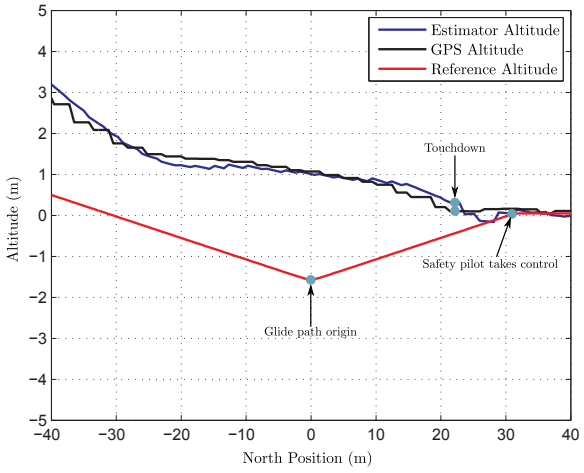

Figure 5.20 – Landing Test 2 - Altitude during touchdown

5.5.3 Landing Test 3 - 29 November Flight 1

During this flight test the conventional elevator-based NSA controller was once again used. This test was conducted using the parameters of Landing Test 2 and is in essence a repeat of that test under more favourable wind conditions.

The aircraft performed two mock landings with the glide path origin set 5 meters above the runway. The actual landing was performed with the glide path origin set 1.5 meters *below* the runway. This is the same as during Landing Test 2 and should result in an improved landing accuracy when compared to Landing Test 1, which did not occur in Landing Test 2 due to the presence of atmospheric disturbances.

Figure 5.21a shows the altitude and airspeed of the aircraft for the duration of the flight test. The two mock landings can be seen in the altitude plot. It can also be seen that the airspeed was regulated well throughout the flight, including during the steep descent phases of the final approach legs. Figure 5.22a shows the altitude of the aircraft during

the landing approach legs of the mock landings where it can be seen that the paths coincide well with one another.

The circuit path flown by the aircraft is shown in Figure 5.21b. During each of the mock landings the aircraft's path along the runway was observed and adjustments made to the runway angle and roll angle offset. It can be seen that each successive lap of the circuit is flown with the path more aligned with the runway. This is again illustrated in Figure 5.22b where the flight paths across the runway are shown. It can the seen that the path of the second mock landing corresponded sufficiently well with the runway that an actual landing could be performed.

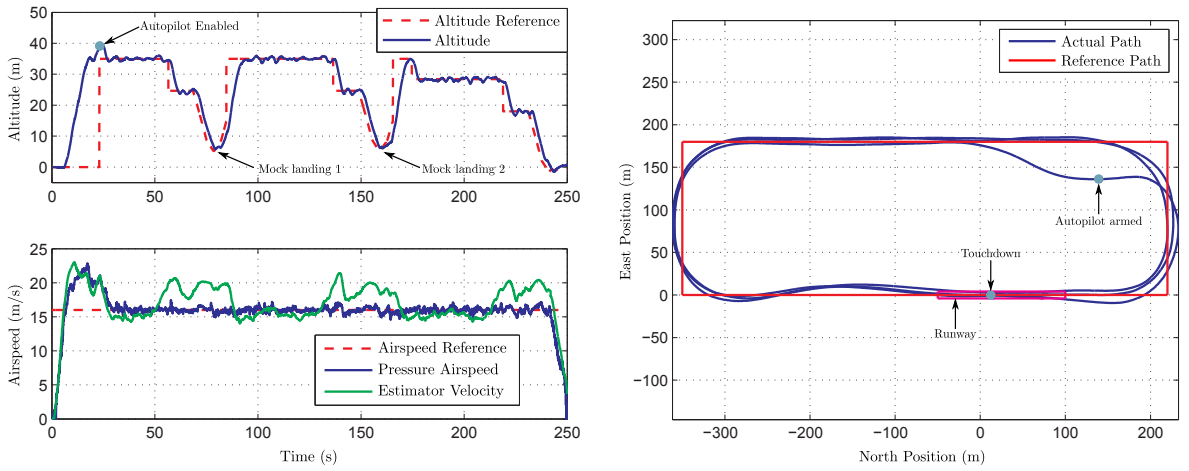

(a) Altitude and airspeed **(b)** Circuit flight path

Figure 5.21 – Landing Test 3 - Altitude, airspeed and circuit flight path for the entire duration of the flight

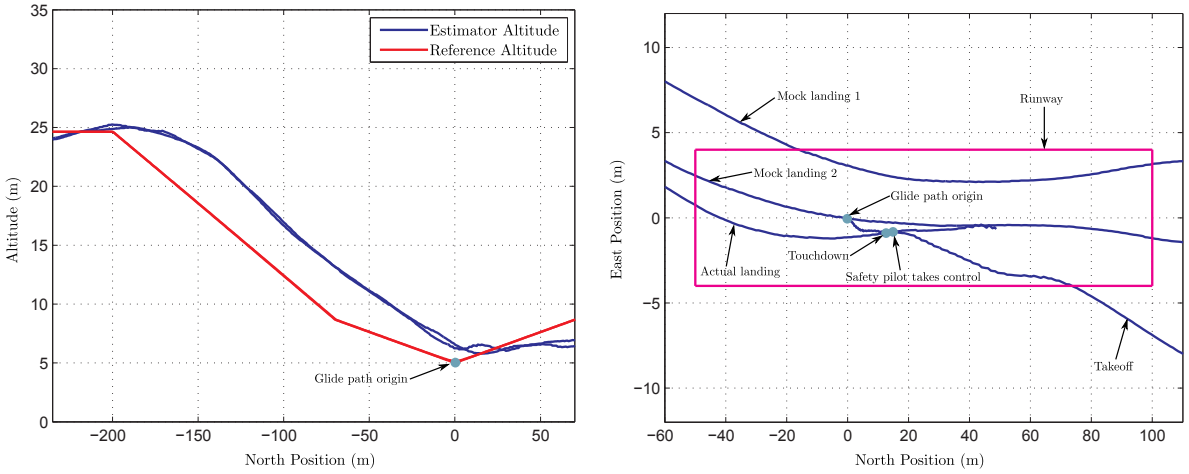

(a) Altitude during mock landings **(b)** Flight path across runway

Figure 5.22 – Landing Test 3 - Altitude during landing leg of the mock landings, and all flight paths across the runway

The altitude of the aircraft during the actual landing leg is shown in Figure 5.23a. It can be seen that the aircraft followed the steeper reference glide path well with a constant offset. The flattening out of the aircraft's path caused by the ground effect is again noticeable. The flight path of the aircraft during the actual landing, and the corresponding roll angle of the aircraft is shown in Figure 5.23b. It can be seen that the aircraft touched down close to the centre of the runway, and that the heading of the path is well aligned with the centreline of the runway. The roll angle plot indicates that the wings of the aircraft are nearly level at the touchdown point.

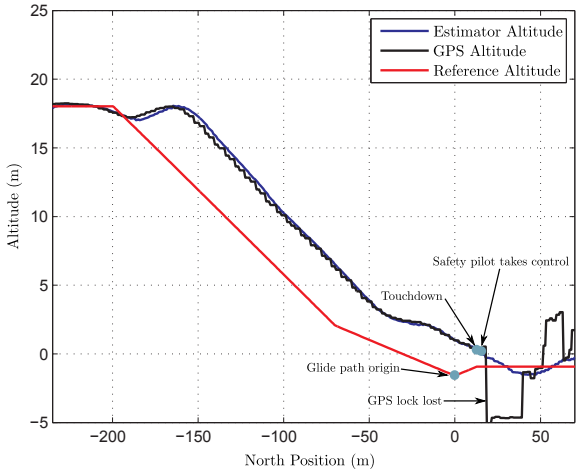

(a) Altitude during landing leg

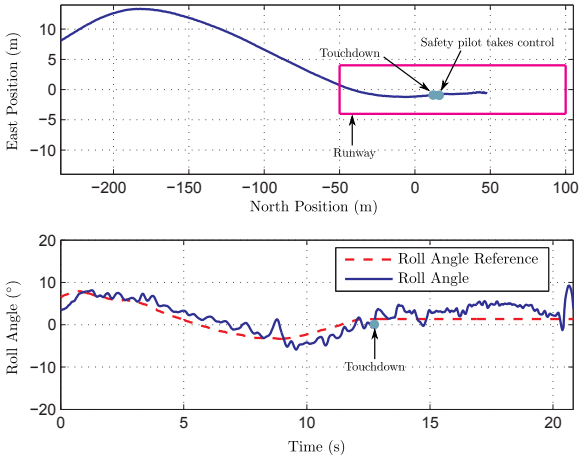

(b) Flight path and roll angle during landing leg

Figure 5.23 – Landing Test 3 - Altitude, flight path and roll angle during landing leg

Figure 5.24a shows the climb rate and NSA of the aircraft during the final approach leg. The touchdown point is clearly visible in the NSA plot as the large spike in acceleration when the aircraft touches down. The pitch rate, pitch angle and elevator deflection are shown in Figure 5.24b. It can be seen that at the touchdown point the pitch angle is very slightly negative. It is further evident that there is significantly less wind disturbance during this test than during Landing Test 2 as shown in Figures 5.19a and 5.19b.

Figure 5.25 shows the altitude of the aircraft in the moments before and after touchdown occurs. It can be seen that the aircraft touches down approximately 12.5 meters from the desired point at the glide path origin. This point is closer to the desired touchdown point when compared to Landing Test 1. This was accomplished by increasing the glide path offset from 1.3 meters to 1.5 meters.

This flight test thus confirms that the touchdown point can be controlled by changing the glide path offset. Subsequent flight tests attempt to achieve an even more accurate landing by further increasing the glide path offset.

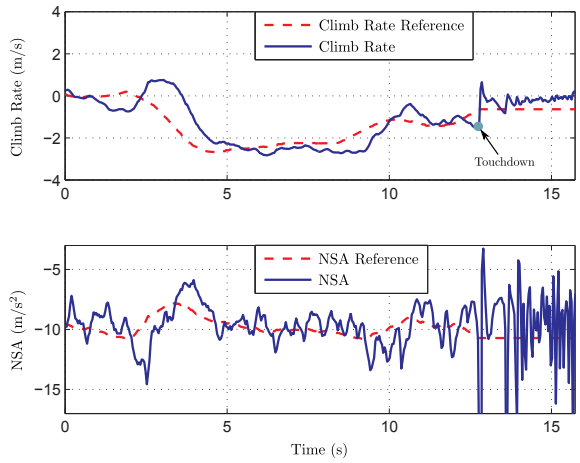

(a) Climb rate and NSA during landing leg

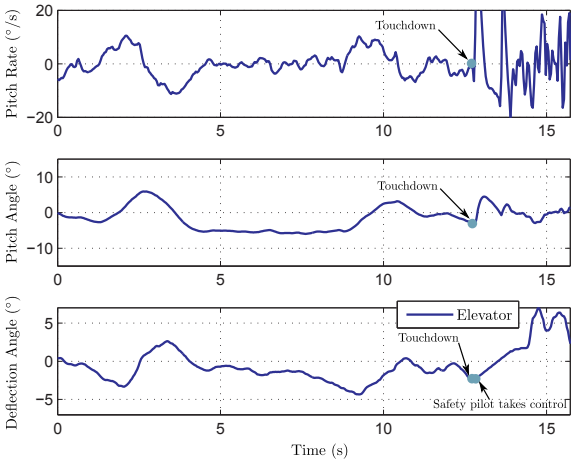

(b) Pitch rate, pitch angle and elevator deflection during landing leg

Figure 5.24 – Landing Test 3 - Climb rate and NSA, and pitch rate, pitch angle and elevator deflection during landing leg

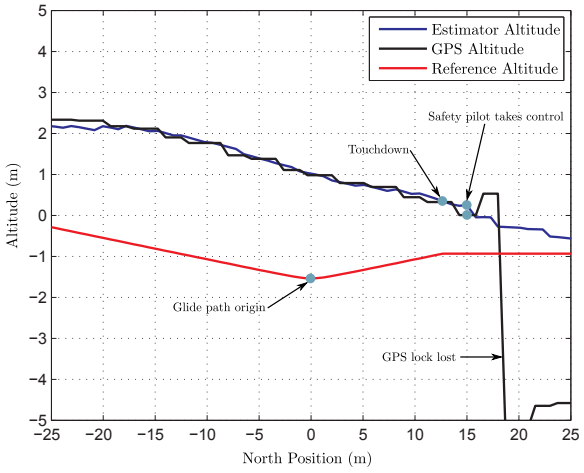

Figure 5.25 – Landing Test 3 - Altitude during touchdown

5.5.4 Landing Test 4 - 29 November Flight 2

The direct-lift-augmented NSA controller was used during this flight test. This test was conducted using the parameters of Landing Test 3 and is intended to allow a direct comparison between the conventional and the direct-lift-augmented NSA controllers. It must be noted that the atmospheric conditions during this flight test were less favourable than during Landing Test 3. The wind conditions as measured by a small weather station at the airfield are shown in Figure D.2.

The aircraft performed two mock landings with the glide path origin firstly set at 20 meters, and then at 5 meters above the runway. The higher initial mock landing was to provide an additional safety margin since the direct-lift-augmented NSA controller had not been tested before during a landing. The actual landing was performed with the glide path origin again set 1.5 meters *below* the runway. This is the same as during Landing Test 3 and a comparison between the conventional and the direct-lift-augmented NSA

controllers can therefore be made.

Figure 5.26a shows the altitude and airspeed of the aircraft for the duration of the flight test. The two mock landings can be seen in the altitude plot. It can also be seen that the airspeed was regulated well throughout the flight, including during the steep descent phases of the final approach legs. Figure 5.27a shows the altitude of the aircraft during the landing approach legs of the mock landings.

The circuit path flown by the aircraft is shown in Figure 5.26b. The adjustments to the runway angle and roll angle offset were determined during Landing Test 3, and only a small adjustment to the runway angle was required. This is again illustrated in Figure 5.27b where the flight paths across the runway are shown. It can be seen that the paths for the mock and actual landings fall very close to one another and are well aligned with the centreline of the runway.

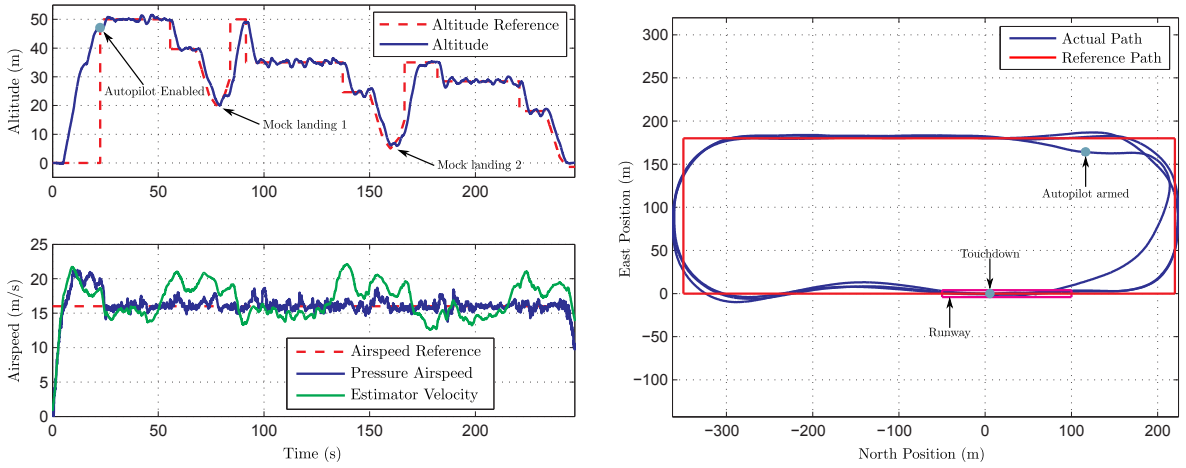

(a) Altitude and airspeed **(b)** Circuit flight path

Figure 5.26 – Landing Test 4 - Altitude, airspeed and circuit flight path for the entire duration of the flight

The altitude of the aircraft during the actual landing leg is shown in Figure 5.28a. It can be seen that the aircraft followed the steeper reference glide path well with a constant offset. Unlike the previous landings, the flattening out of the aircraft's path caused by the ground effect is less pronounced. This is likely due to the smaller pitch rotation performed by the aircraft due to the utilisation of the direct-lift-augmented NSA controller. A full comparison of the pitch behavior of the conventional and direct-lift-augmented NSA controllers is made in §5.5.5. The flight path of the aircraft during the actual landing and the corresponding roll angle is reflected in Figure 5.28b. It can be seen that the aircraft touched down nearly in the centre of the runway, and that the heading of the path is well aligned with the centreline of the runway. The roll angle plot indicates that the wings of the aircraft are nearly level at the touchdown point.

Figure 5.29a shows the climb rate and NSA of the aircraft during the final approach leg. The touchdown point is clearly visible in the NSA plot as the large spike in acceleration as

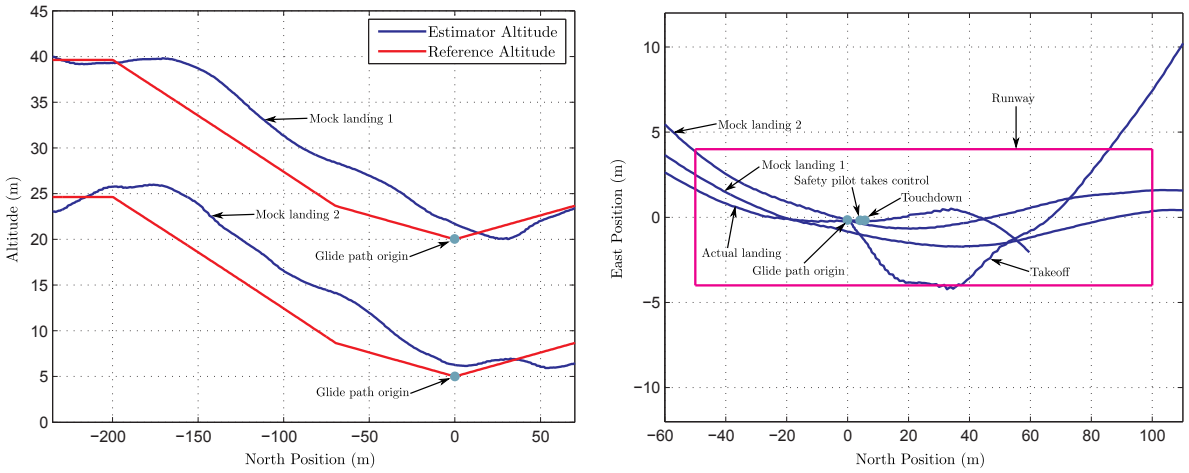

(a) Altitude during mock landings **(b)** Flight path across runway

Figure 5.27 – Landing Test 4 - Altitude during landing leg of the mock landings, and all flight paths across the runway

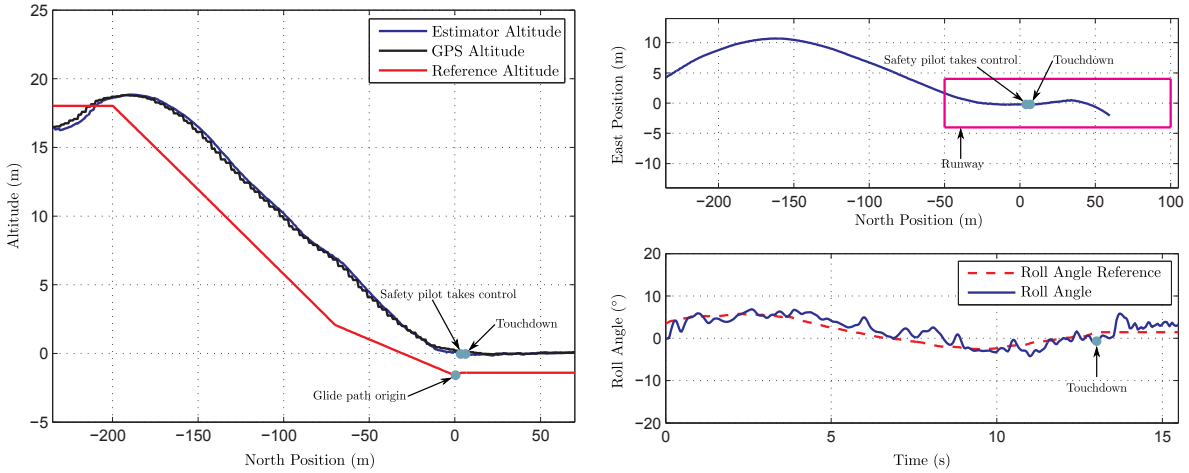

(a) Altitude during landing leg **(b)** Flight path and roll angle during landing leg

Figure 5.28 – Landing Test 4 - Altitude, flight path and roll angle during landing leg

the aircraft touches down. The pitch rate, pitch angle, and elevator and flaps deflection are shown in Figure 5.29b. It can be seen that at the touchdown point the pitch angle is very slightly positive. This is in contrast to the previous Landing Tests where the pitch angle is slightly negative at touchdown. This is possibly a consequence of using the direct-lift-augmented NSA controller and is discussed further in §5.5.5.

Figure 5.30 shows the altitude of the aircraft in the moments before and after touchdown occurs. It can be seen that the aircraft touches down approximately 5 meters from the desired point at the glide path origin. This point is closer to the desired touchdown point than that achieved in Landing Test 3.

This flight test shows that, for the same parameters, the direct-lift-augmented NSA controller appears to achieve a more accurate landing than the conventional NSA controller. However, the uncertainty about the exact atmospheric conditions during the tests means

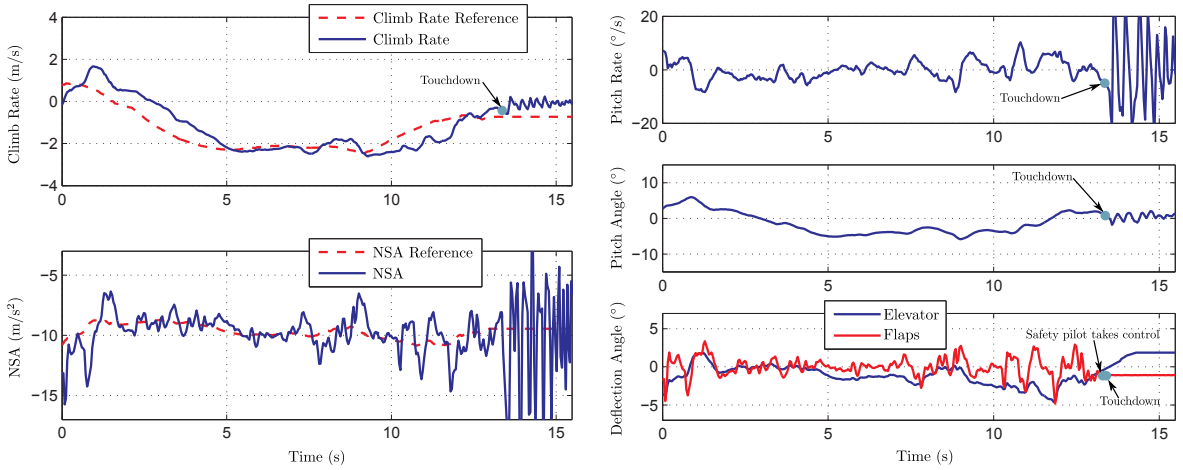

(a) Climb rate and NSA during landing leg

(b) Pitch rate, pitch angle and elevator deflection during landing leg

Figure 5.29 – Landing Test 4 - Climb rate and NSA, and pitch rate, pitch angle and elevator deflection during landing leg

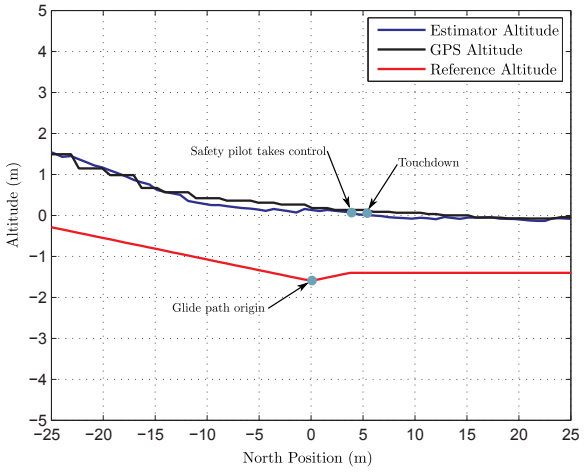

Figure 5.30 – Landing Test 4 - Altitude during touchdown

that it cannot be stated with absolute certainty. Such an assertion would require more landings than the time constraints of this project allow for.

5.5.5 Landing Test 5 - 29 November Flight 3

The direct-lift-augmented NSA controller was again used during this flight test. During this test, the glide path offset is increased in order to achieve an even more accurate landing. It must be noted that the atmospheric conditions during this flight test were significantly less favourable than during any of the other Landing Tests (see Figure D.2).

The aircraft performed two mock landings with the glide path origin firstly set at 20 meters, and then at 5 meters above the runway. The actual landing was performed with the glide path origin set 2 meters *below* the runway. This is greater than for any of the previous Landing Tests and should result in the most accurate landing.

Figure 5.31a shows the altitude and airspeed of the aircraft for the duration of the flight test. The two mock landings can be seen in the altitude plot. The airspeed plot shows the presence of significant wind gusts as evidenced by the large fluctuations of the estimator velocity when compared to the airspeed measured by the pitot tube sensor. Figure 5.32a shows the altitude of the aircraft during the landing approach legs of the mock landings.

The circuit path flown by the aircraft is shown in Figure 5.31b. The adjustments to the runway angle and roll angle offset were determined during Landing Test 4. Figure 5.32b shows the flight paths across the runway. It can be seen seen that at the touchdown point the paths of the mock and actual landings fall very close to one another and are well aligned with the centreline of the runway. However, the path of mock landing 1 diverged from the others after the glide path origin was passed. This was likely caused by a strong wind gust.

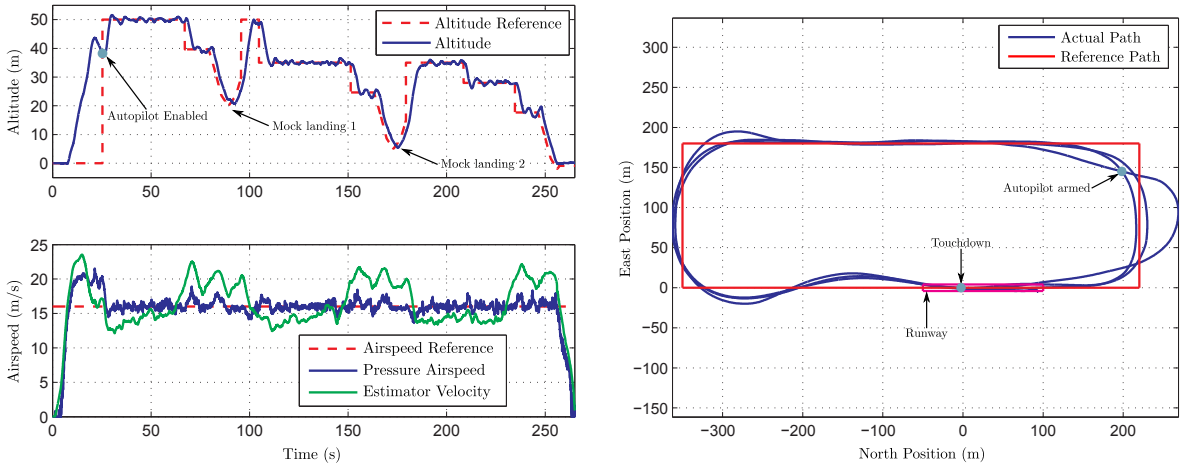

(a) Altitude and airspeed

(b) Circuit flight path

Figure 5.31 – Landing Test 5 - Altitude, airspeed and circuit flight path for the entire duration of the flight

The altitude of the aircraft during the actual landing leg is shown in Figure 5.33a. It can be seen that the aircraft followed the steeper reference glide path well with a constant offset. Similar to Landing Test 4, the flattening out of the aircraft's path caused by the ground effect is less pronounced. The flight path of the aircraft during the actual landing, and the corresponding roll angle of the aircraft is shown in Figure 5.33b. It can be seen that the aircraft touched down nearly in the centre of the runway, and that the heading of the path is well aligned with the centreline of the runway. The roll angle plot indicates that the wings of the aircraft were not level at the touchdown point which resulted in a sharp roll angle in the opposite direction as the aircraft touched down.

Figure 5.34a shows the climb rate and NSA of the aircraft during the final approach leg. The touchdown point is clearly visible in the NSA plot as the large spike in acceleration as the aircraft touches down. The pitch rate, pitch angle, and elevator and flaps deflection are shown in Figure 5.34b. It can be seen that at the touchdown point the pitch angle is

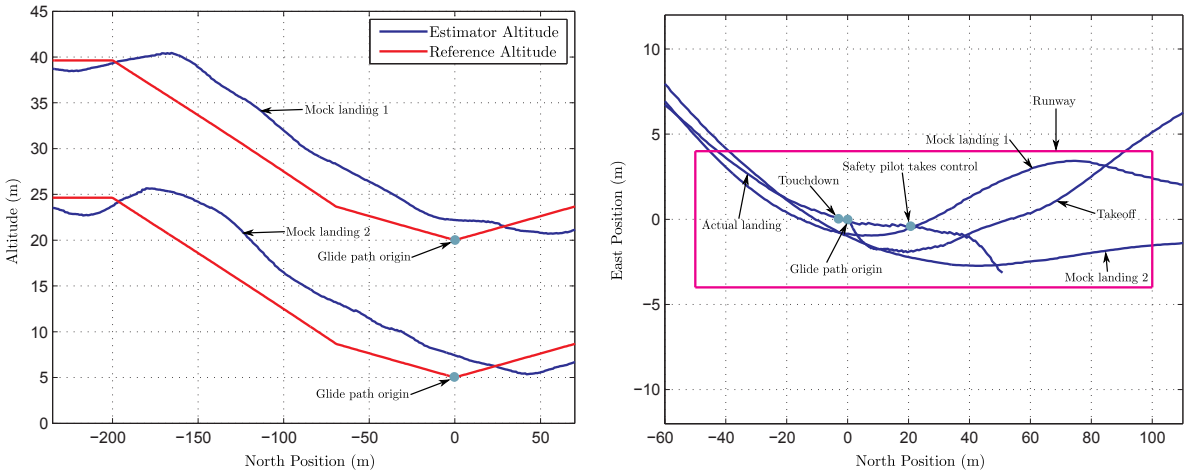

(a) Altitude during mock landings **(b)** Flight path across runway

Figure 5.32 – Landing Test 5 - Altitude during landing leg of the mock landings, and all flight paths across the runway

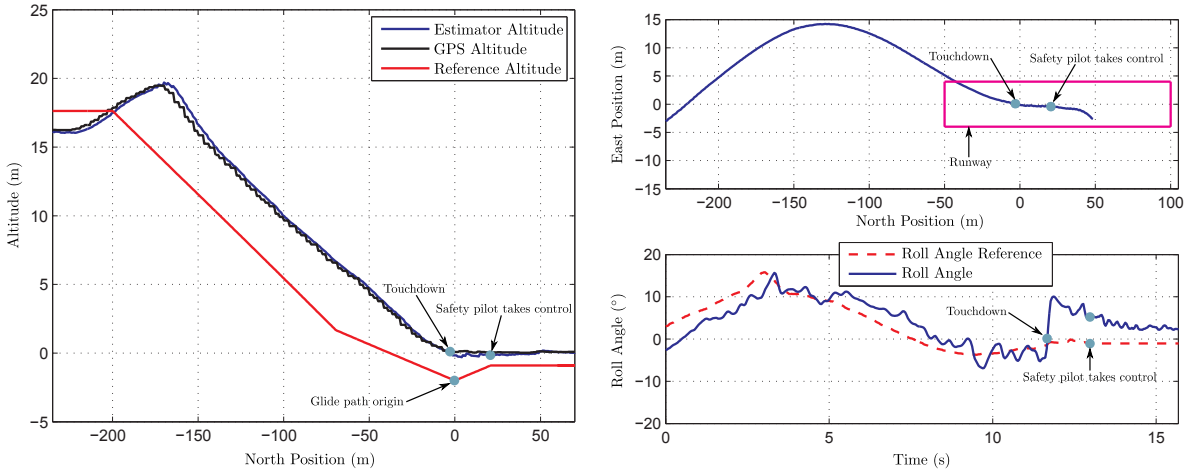

(a) Altitude during landing leg **(b)** Flight path and roll angle during landing leg

Figure 5.33 – Landing Test 5 - Altitude, flight path and roll angle during landing leg

very slightly negative. This is in contrast with Landing Test 4 where the pitch angle was slightly positive. This is likely due to different wind conditions during the glide path.

Figure 5.35 shows the altitude of the aircraft in the moments before and after touchdown occurs. It can be seen that the aircraft touches down approximately 3 meters from the desired point at the glide path origin. This is closer to the desired touchdown point than that achieved in Flight Test 4, but is ahead of the glide slope origin instead of behind. This means that the glide path offset was larger than necessary and must be reduced slightly in order to achieve a more accurate landing.

This flight test confirms that the direct-lift-augmented NSA controller continues to function even in the presence of significant wind disturbances. This test achieved the greatest accuracy, and it is clear that with the appropriate glide path offset, further improvements are possible.

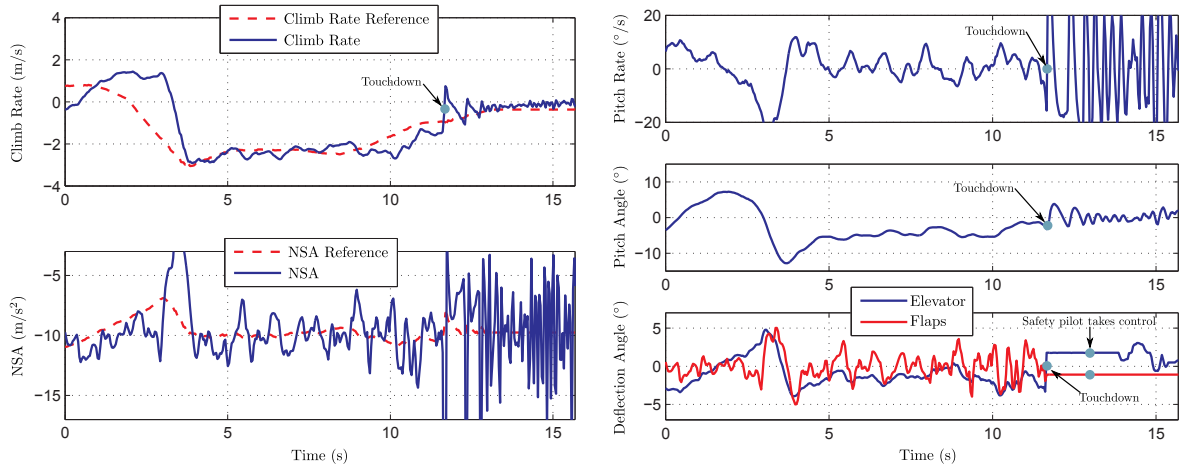

(a) Climb rate and NSA during landing leg

(b) Pitch rate, pitch angle and elevator deflection during landing leg

Figure 5.34 – Landing Test 5 - Climb rate and NSA, and pitch rate, pitch angle and elevator deflection during landing leg

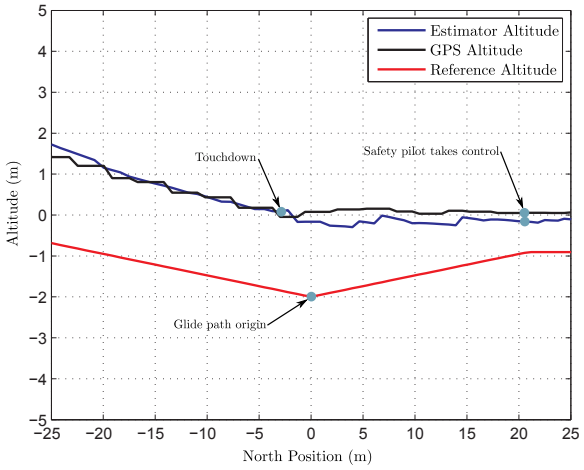

Figure 5.35 – Landing Test 5 - Altitude during touchdown

Whilst further tests would be desirable, the landings which were achieved in both normal wind conditions as well as in conditions where wind gusts prevail can, for the purposes of this thesis, be considered a success. Further improvements in accuracy are possible, however, at some point the random nature of wind disturbances will prevent any further repeatable landing improvements.

The flight test also show that the direct-lift-augmented NSA controller appears to achieve a more accurate landing than the conventional NSA controller. The wind measurements reflected in Figure D.2 also strongly suggest that the direct-lift-augmented NSA controller offers superior performance in the presence of wind disturbances. However, this cannot be stated with absolute certainty since the respective atmospheric conditions during the tests cannot be truly quantified and compared. To be confident of such an assertion would require more landings than the time constraints of this project allow for.

In addition to the landing accuracy achieved, the conventional and direct-lift-augmented

NSA controllers can also be compared by examining the pitch response of the aircraft during landing. This is of importance since part of the motivation behind employing a direct-lift type controller is to minimise aircraft high speed pitch rotation during landing. Such pitch changes can greatly influence airspeed control, and can also lead to dangerous situations such as striking the runway with the nose wheel first. To make this comparison, the pitch angle, pitch rate and airspeed of the aircraft for Landing Test 3 and 4 are shown in Figures 5.36a and 5.36b. These Landing Tests were selected since they allow the comparison of the NSA controllers under the most similar conditions. Landing Test 3 utilised the conventional NSA controller, and Landing Test 4 utilised the direct-lift-augmented NSA controller. It must be noted that the atmospheric conditions during Landing Test 4 were less favourable than during Landing Test 3. This is shown in the windspeed plot of Figure D.2. It can be seen in Figure 5.36a that the conventional NSA controller exhibited far greater pitch angle changes than the direct-lift-augmented NSA controller. This is again shown in the upper plot of Figure 5.36b where it can be seen that the conventional NSA controller showed greater pitch rates. It can be seen in Figure 5.36b that the airspeed regulation for the conventional and direct-lift NSA controllers exhibited similar variations. These results suggest that the direct-lift augmented NSA controller provides improved landing performance over the conventional NSA controller.

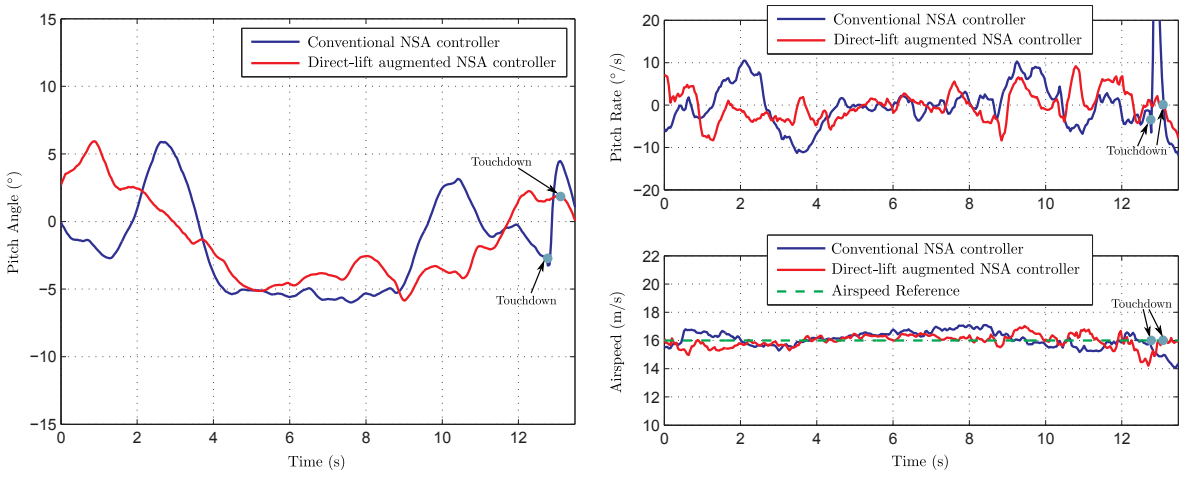

(a) Pitch angle during landing leg **(b)** Pitch rate and airspeed landing leg

Figure 5.36 – Landing Test 3 and 4 - Pitch angle, pitch rate and airspeed during landing leg

Chapter 6

Conclusion

This thesis presents the design, practical implementation and testing of a control system to achieve an accurate autonomous landing of a fixed-wing UAV in the presence of wind gust atmospheric disturbances. This chapter presents a summary of the work done and highlights the results achieved. It concludes with a list of contributions made to the research group at the Centre of Expertise in Autonomous Systems at Stellenbosch University, as well as recommendations for further research.

6.1 Summary

During the research project the following milestones were attained leading to the successful execution of accurate autonomous landings of a fixed-wing UAV.

Aircraft:

- The construction of a UAV to serve as the testbed for the various controllers developed. This involved modifying and strengthening a model aircraft, incorporating an electric motor system as well as assembling and integrating sensors and avionics. These include,
  - IMU providing 3-axis acceleration and rotation measurements
  - Magnetometer
  - Pressure sensors for calculating airspeed and pressure altitude
  - RTK DGPS system for providing accurate position and velocity state measurements

  All sensors and actuators of the aircraft were also calibrated.

Modelling and controllers:

- The aircraft model was determined on the basis of the model presented by [2]. This also involved,
  - Determining the stability and control derivatives through the use of AVL.
  - Conducting a static thrust test of the aircraft's motor and propeller.
  - Finding the moment of inertia through the double pendulum method.
- The dynamics of the aircraft were analysed in order to formulate a control strategy. This also involved an in-depth study of the longitudinal dynamics of the aircraft in order to design aircraft controllers which incorporate the concept of direct-lift control.
- Controllers were designed to regulate the airspeed, altitude, climb rate, normal specific acceleration and roll angle of the aircraft as well as damp the Dutch roll mode.
- Two normal specific acceleration controllers were designed. The first being a conventional elevator-based NSA controller, and the second a direct-lift-augmented NSA controller which makes use of both the elevator and the flaps of the aircraft.
- A guidance controller was implemented to allow for the following of waypoints.

Landing:

- A landing procedure and methodology was developed. This includes the circuit and landing approach paths and the concept of a glide path offset to calibrate the touchdown point of a landing.

Simulation and flight tests:

- All controllers and the landing procedure were implemented on an OBC.
- All controllers were tested in a HIL simulation environment as well as practically in a series of flight tests in order to verify the controller design and the aircraft model.
- The landing procedure was tested in a HIL simulation environment and practically in a series of flight tests.
- Five fully autonomous landings were performed. Three of these using the conventional NSA controller, and the final two the direct-lift-augmented NSA controller.

6.2 Results

The results of the landing flight tests show that the project goal of a landing within five meters along the runway and three meters across the runway was achieved in both normal wind conditions as well as in conditions where wind gusts prevailed. The flight tests show that the direct-lift-augmented NSA controller appears to achieve a more accurate landing than the conventional NSA controller, especially in the presence of greater wind disturbances. However, the inability to quantify and directly compare the respective atmospheric conditions during the tests means that this cannot be stated with absolute certainty. Such an assertion would require more landings than the time constraints of this project allowed for.

In addition to the landing accuracy achieved, the conventional and direct-lift-augmented NSA controllers were also compared by examining the pitch response of the aircraft during landing. It was seen that the conventional NSA controller exhibited far greater pitch angle changes than the direct-lift-augmented NSA controller. This suggests that the direct-lift augmented NSA controller provides improved landing performance over the conventional NSA controller.

6.3 Contributions

The work completed for this thesis offers the following contributions to the research group at the Centre of Expertise in Autonomous Systems at Stellenbosch University,

- The UAV which was constructed performed well, and can serve as a reliable testbed for future research. Through practical flight tests, it was demonstrated that the aircraft model is accurate, and that the controllers function well.
- The groundwork has been done for further research into the accurate autonomous landing of fixed-wing UAV's which could include aspects such as crosswind landings.
- The concept of direct-lift control has been explored and successfully implemented. This technique holds promise for future projects where accurate longitudinal control and the rejection of wind disturbances are required.
- The landing procedure and strategy has been shown to work in practice and offers scope for further development.
- The controllers which were developed are modular and can be used in other aircraft.
- The DGPS system has been demonstrated to function well on a fixed-wing aircraft.

6.4 Recommendations for Further Research

Aircraft:

- The use of an electric motor as a propulsion source was found to have great benefits when compared to the traditional liquid fuel powered engines. The benefits include simple and reliable operation, as well as improved airspeed regulation. It is recommended that future projects follow the same approach.

Control system:

- The path following ability of the aircraft was shown to work well, but there is room for improvement. A conservative approach was followed in the design of the guidance controller in order to avoid high roll angles. This resulted in a fairly long settling time. Relaxing this requirement and adding an integrator term to the guidance controller could result in an improvement. However, care would need to be taken to avoid integrator wind-up.

  Direct-lift control:

  - The direct-lift-augmented NSA controller can be improved further. This could involve revising the control law of the flaps-based portion of the NSA controller to mitigate the effect of noise on the NSA signal. This could be accomplished by augmenting a fast integrator on the NSA signal similar to that of the elevator-based NSA controller of §3.2.4. Alternatively, direct-lift control can also be attempted by using climb rate feedback.
  - A pure direct-lift controller can be designed which primarily makes use of the flaps to achieve longitudinal control This could open up interesting new horizons for future UAV's.

Landing:

- In order to achieve greater landing accuracy, the angle of the glide path can be increased. This will reduce the effect that a height error has on the distance between the intended and actual touchdown point. However, for this to be implemented practically, the landing gear of the aircraft would need to be modified to absorb the additional landing forces.

Further expansion of operational capability:

- The vision-based system for determining the aircraft's position, developed by [7], could be revisited in order to eliminate the need for a communication link between the aircraft and the ground as is the case with the DGPS system used in this project.
- The following controllers can be considered:

  - A runway controller to steer the aircraft after touchdown.
  - Controllers to enable cross-wind landing: This could consist of a lateral specific acceleration controller which will aid in maintaining the flight path of the aircraft, a de-crab controller which would align the centreline of the aircraft with that of the runway just before touchdown, and a controller to level out the wings just before touchdown.

- Implementation of an arrestor cable mechanism to capture the aircraft after touchdown which would allow for landing on a short runway.
- Landing on a moving platform such as the deck of a ship: This would require estimation of the ship's motion. Research into this field has been done by [21; 22], and could serve as a basis for further expansion.

Appendix A

Additional Mathematical Principles [1]

A.1 Transforming the Derivative of a Vector in a Rotating Reference Frame

The following equation can be used to transform the derivative of a vector from one axis system to another axis system where the axis systems rotate relative to one another [17],

$$\left.\frac{\mathrm{d}}{\mathrm{d}t}\mathbf{R}\right|_{\mathcal{A}} = \left.\frac{\mathrm{d}}{\mathrm{d}t}\mathbf{R}\right|_{\mathcal{B}} + \omega^{\mathcal{B}\mathcal{A}} \times \mathbf{R} \tag{A.1.1}$$

where $\omega^{\mathcal{B}\mathcal{A}}$ is the angular velocity of the rotation of $\mathcal{B}$ relative to $\mathcal{A}$.

A.2 Cross Product Transformation Matrix

The cross product of two vectors coordinated in the same axis system can be written as,

$$\mathbf{J}_{\mathcal{A}} \times \mathbf{K}_{\mathcal{A}} = \mathbf{S}_{\mathbf{J}_{\mathcal{A}}}\mathbf{K}_{\mathcal{A}} \tag{A.2.1}$$

where the matrix $\mathbf{S}_{\mathbf{J}_{\mathcal{A}}}$ is given by,

$$\mathbf{S}_{\mathbf{J}_{\mathcal{A}}} = \begin{bmatrix} 0 & -Z_{\mathcal{A}} & Y_{\mathcal{A}} \\ Z_{\mathcal{A}} & 0 & -X_{\mathcal{A}} \\ -Y_{\mathcal{A}} & X_{\mathcal{A}} & 0 \end{bmatrix} \tag{A.2.2}$$

where $X_{\mathcal{A}}$, $Y_{\mathcal{A}}$ and $Z_{\mathcal{A}}$ are the components of $\mathbf{J}$ coordinated in axis system $\mathcal{A}$.

A.3 Direction Cosine Matrix (DCM)

The direction cosine matrix can be used to transform a vector from one axis system into another as follows,

$$\mathbf{V}_{\mathcal{B}} = \left[\mathbf{DCM}^{\mathcal{BA}}\right] \mathbf{V}_{\mathcal{A}} \tag{A.3.1}$$

where the rows of the $\mathbf{DCM}^{\mathcal{BA}}$ matrix consist of the unit vectors of axis system $\mathcal{B}$, co-ordinated in axis system $\mathcal{A}$.

Since it consists of three orthogonal unit vectors, the DCM it is an orthogonal matrix which implies that its inverse is given by its transpose. Therefore, the reverse transform from axis system $\mathcal{B}$ to $\mathcal{A}$ is given by,

$$\mathbf{V}_{\mathcal{A}} = \left[\mathbf{DCM}^{\mathcal{BA}}\right]^{-1} \mathbf{V}_{\mathcal{B}} = \left[\mathbf{DCM}^{\mathcal{BA}}\right]^{\mathsf{T}} \mathbf{V}_{\mathcal{B}} \tag{A.3.2}$$

The following conversions are used in this thesis:

Wind to Body Axes:

$$\mathbf{DCM}^{BW} = \begin{bmatrix} \cos\alpha\cos\beta & -\cos\alpha\sin\beta & -\sin\alpha \\ \sin\beta & \cos\beta & 0 \\ \sin\alpha\cos\beta & -\sin\alpha\sin\beta & \cos\alpha \end{bmatrix} \tag{A.3.3}$$

Body to Wind Axes:

$$\begin{aligned} \mathbf{DCM}^{WB} &= \left[\mathbf{DCM}^{BW}\right]^{\mathsf{T}} \\ &= \begin{bmatrix} \cos\alpha\cos\beta & \sin\beta & \sin\alpha\cos\beta \\ -\cos\alpha\sin\beta & \cos\beta & -\sin\alpha\sin\beta \\ -\sin\alpha & 0 & \cos\alpha \end{bmatrix} \end{aligned} \tag{A.3.4}$$

Inertial to Wind Axes:

The DCM can be written in terms of the Euler 3-2-1 sequence used in this project,

$$\mathbf{DCM}^{WI} = \begin{bmatrix} \cos\psi\cos\theta & \sin\psi\cos\theta & -\sin\theta \\ \cos\psi\sin\theta\sin\phi - \sin\psi\cos\phi & \sin\psi\sin\theta\sin\phi + \cos\psi\cos\phi & \cos\theta\sin\phi \\ \cos\psi\sin\theta\cos\phi + \sin\psi\sin\phi & \sin\psi\sin\theta\cos\phi - \cos\psi\sin\phi & \cos\theta\cos\phi \end{bmatrix}_{(321)} \tag{A.3.5}$$

A.4 Moment of Inertia

For an object with a fixed mass distribution, the moment of inertia referenced to its centre of mass and coordinated in its body axis system is given by,

$$\mathbf{I}_B = \begin{bmatrix} I_x & -I_{xy} & -I_{xz} \\ -I_{xy} & I_y & -I_{yz} \\ -I_{xz} & -I_{yz} & I_z \end{bmatrix} \tag{A.4.1}$$

For most conventional aircraft this simplifies to,

$$\mathbf{I}_B = \begin{bmatrix} I_x & 0 & 0 \\ 0 & I_y & 0 \\ 0 & 0 & I_z \end{bmatrix} \tag{A.4.2}$$

A.5 Small Angle Approximations

The standard small angle approximations are given by,

$$\cos\alpha \approx 1 \tag{A.5.1}$$

$$\sin\alpha \approx \alpha \tag{A.5.2}$$

$$\alpha\beta \approx 0 \tag{A.5.3}$$

Appendix B

UAV System Description

This appendix describes the UAV system which was constructed/utilised to serve as the testbed for this project. The system consists of the airframe, propulsion source, avionics, ground station and a HIL simulation environment.

B.1 Airframe

The airframe is a standard high-wing type model aircraft with a wingspan of just under $2\,\mathrm{m}$ as shown in Figure D.1. It was modified to accommodate the avionics and strengthened to withstand higher than normal landing impact forces.

Figure B.1 – Aircraft photo

B.1.1 Propulsion Source

The aircraft is powered by a Hyperion ZS4025-10 brushless DC outrunner motor equipped with a standard 14×7 electric motor propeller. The motor is driven by a Hyperion Titan $90\,\mathrm{A}$ electronic speed controller (ESC), which is in turn powered by a $18.5\,\mathrm{V}$ 5-cell

5000 mAh 20C lithium-polymer (LiPo) battery. This allows for a safe flight duration of 5 minutes .

B.2 Avionics

The avionics used in this project have been developed within the SU Research Group and used in previous research projects [8; 10]. Figure B.2 depicts the avionics diagrammatically.

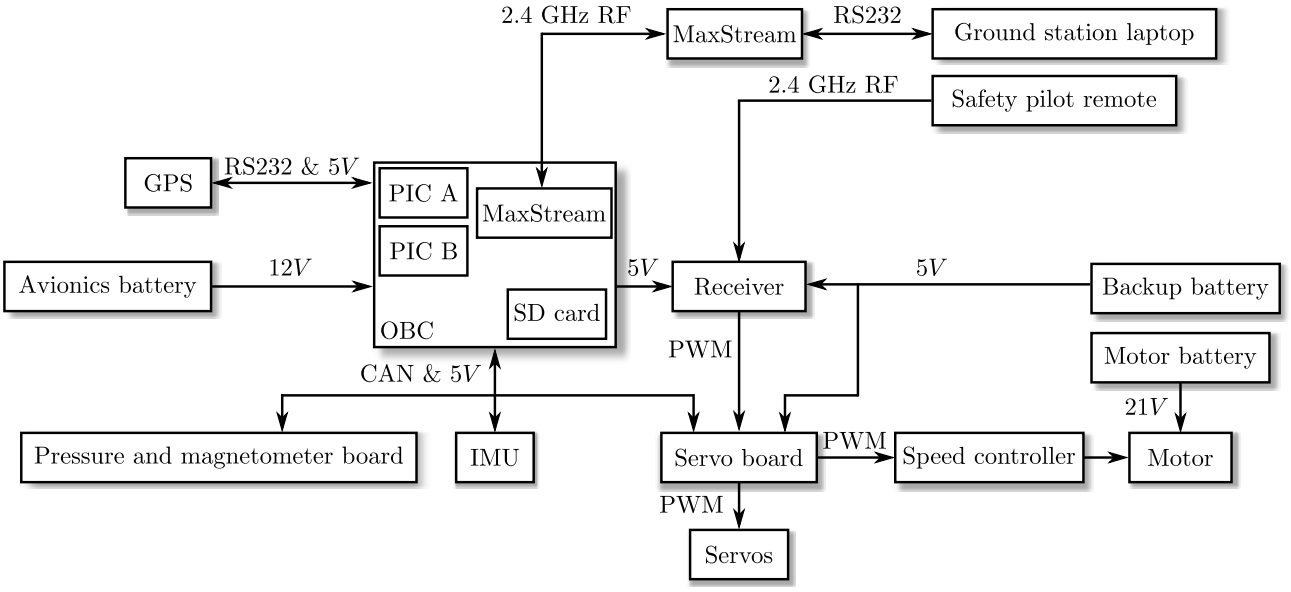

Figure B.2 – Avionics overview

The avionics consist of the following,

OBC

The OBC is based around two dsPIC30F6014 microcontrollers:

- PIC A - Communicates with the ground station laptop via a MaxStream RF module, this involves sending telemetry and receiving commands; samples the sensors via the CAN bus; monitors the voltage level of the avionics and backup batteries; receives safety pilot commands from, and sends actuator commands to the servo board; executes the controller algorithms; logs sensor, controller, actuator and other flight data on the SD card; runs an extended Kalman filter (EKF) which provides kinematic state estimation by using sensor information from the IMU, GPS and magnetometer to estimate the aircraft's position, velocity and attitude [6].
- PIC B - Performs the calculations related to the RTK DGPS and sends the result to PIC A.

IMU

The IMU is based around the Analog Devices ADIS16350AMLZ sensor. It measures the specific acceleration and rotation rates of the aircraft in the body axis system, and sends these values to the OBC via the CAN bus.

GPS

The GPS module used is a NovAtel OEMV-1G. This module is used in conjunction with another such module on the ground in order a create an RTK DGPS system with an accuracy on the order of a few centimeters.

Pressure and magnetometer board

The pressure and magnetometer board contains one static and one differential pressure sensor which are connected to a pitot tube mounted in the aircraft's wing via a series of tubes. These sensors allow the static and dynamic pressure to be determined which allows the calculation of the airspeed and pressure altitude of the aircraft. The board also contains a three-axis magnetometer that measures the earth's magnetic field vector in the aircraft's body axes. This measurement aids in determining the aircraft's attitude.

Receiver

The receiver used is a Spektrum AR 9100 which has a dual redundant power supply and four satellite receivers mounted in different orientations throughout the aircraft. This ensures a reliable link with the safety pilot remote.

Servo board

The servo board acts as the intermediary between the OBC, safety pilot RC receiver and the actuators of the aircraft. It samples the safety pilot's commands and sends them to the OBC via the CAN bus. It also sends the servo commands to the aircraft's actuators. These will either be the safety pilot commands or the autopilot commands received from the OBC. The autopilot can be armed from a switch on the safety pilot remote. The servos are powered by the servo board. Both the servo board and the receiver have a backup power supply to ensure that the safety pilot can control the aircraft even in the event of a complete failure of the rest of the avionics.

Batteries

The avionics is powered by a $11.1\,\mathrm{V}$ 3-cell $1800\,\mathrm{mAh}$ 35C LiPo battery. Backup power is provided by a 5 V $700\,\mathrm{mAh}$ nickel-cadmium (NiCad) battery which can power the servo board and the receiver if power from the main battery is lost.

B.3 Ground Station Software

The ground station software used in this project is based on the standard ground station software developed within the SU Research Group. It runs on a laptop, and communicates with the aircraft via a MaxStream RF module. This RF module is contained in an enclosure and connects to the laptop via a serial connection.

The functions of the ground station are split into several tabs described briefly below,

Main page

Side panels on the main page provide the following: start and reset the OBC; start and stop data logging on the SD card; initialise and disable the estimator; enable and disable the autopilot; toggle the avionics to HIL simulation mode; display the command history and any errors; display the status of the OBC and a summary of the sensor data.

Controller tab

This tab allows the controllers to be enabled and disabled, and the controller gains and references to be set and updated (see Figure B.3a).

Navigation tab

This tab allows the waypoints, runway heading angle and origin of the glide path to be set. The waypoints are entered in the runway axis system. The ground station then converts these to the inertial axis system before the values are sent to the OBC. (see Figure B.3b).

Estimator tab

This tab allows the kinematic state estimator used on this aircraft to be initialised and configured. The current state estimates are also displayed.

Sensors tab

This tab shows the current measurements of all the aircraft's sensors, and allows the aircraft's sensors to be zeroed.

Actuator tab

This tab shows the current safety pilot commands as well as the commands sent to the servo board from the OBC.

Actuator Setup tab

This tab is used during the calibration of the aircraft's actuators and allows the range of motion and the neutral point of all servos to be set.

The ground station also stores all telemetry data on the hard drive of the laptop.

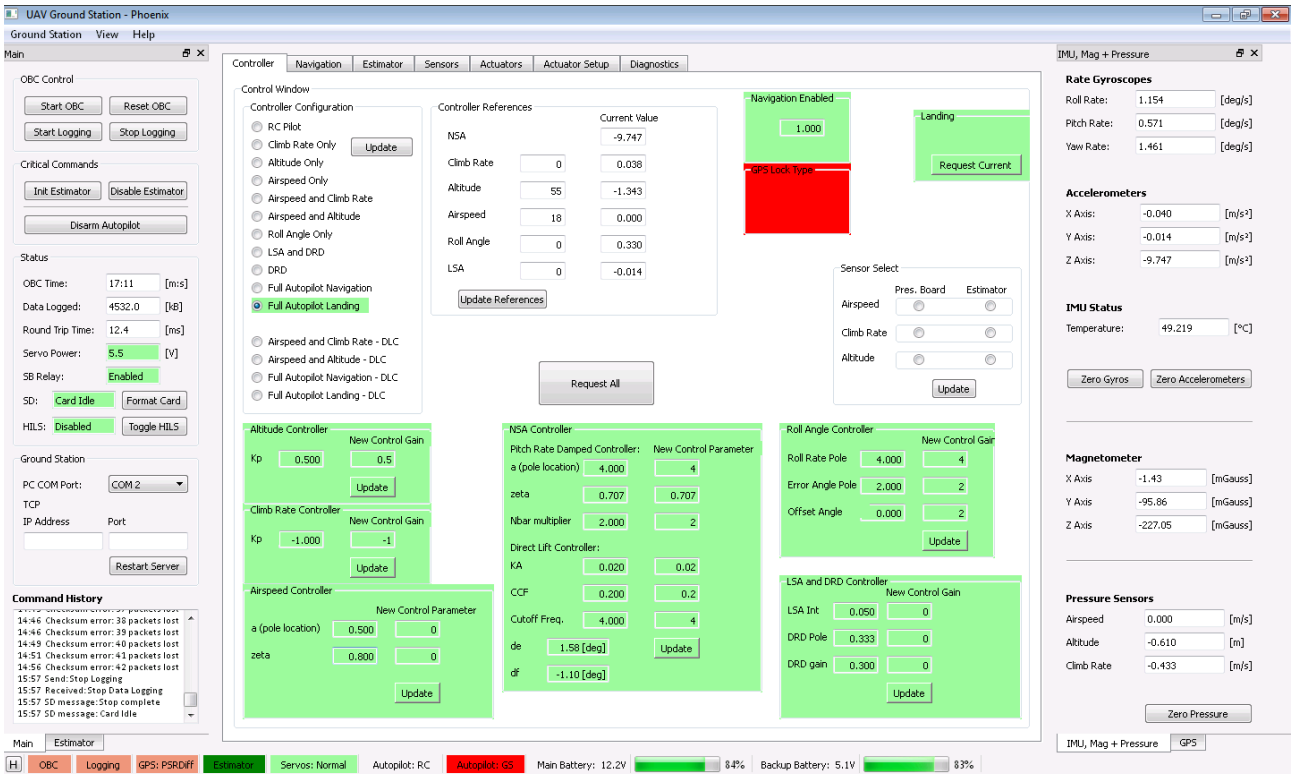

(a) Controllers tab

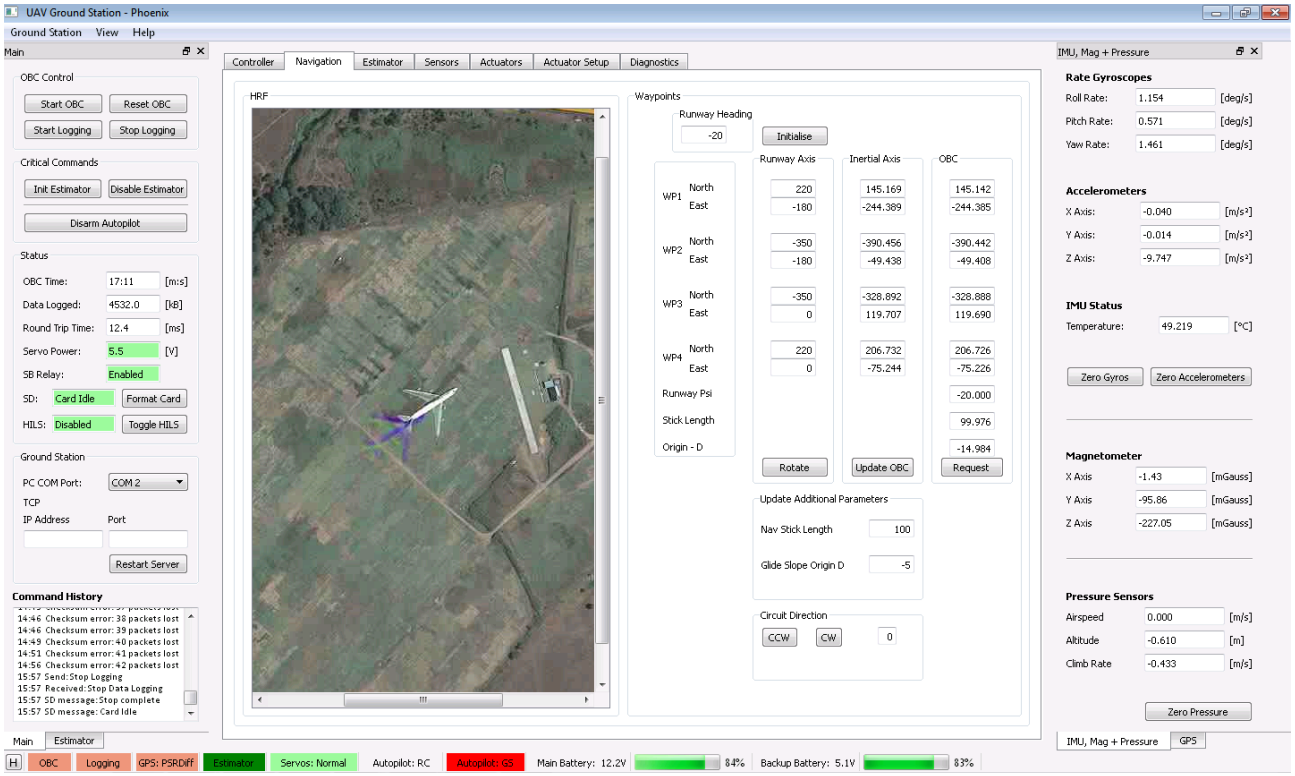

(b) Waypoints tab

Figure B.3 – Ground station graphical user interface

B.4 Hardware-in-the-Loop Simulation Environment

The HIL simulation environment allows the avionics and controllers to be tested as if the aircraft is actually flying. This is accomplished by running a non-linear aircraft simulator in Matlab Simulink on a PC [6]. This simulator generates simulated sensor signals and sends these to the OBC. The OBC then uses these sensor signals in its controller algorithms and generates actuator signals. These actuator signals are fed back into the simulator and the aircraft model responds accordingly. This allows the controllers and avionics to be fully tested before practical flight tests are attempted. Sensor noise and wind disturbances can also be set in the simulation which allows the robustness and accuracy of the controllers to be tested. The components of the HIL simulation environment are depicted in Figure B.4.

The HIL simulation environment also contains a graphical display of the aircraft and its environment as shown in Figure B.5. This allows the flight to be visualised which aids greatly in controller design and evaluation.

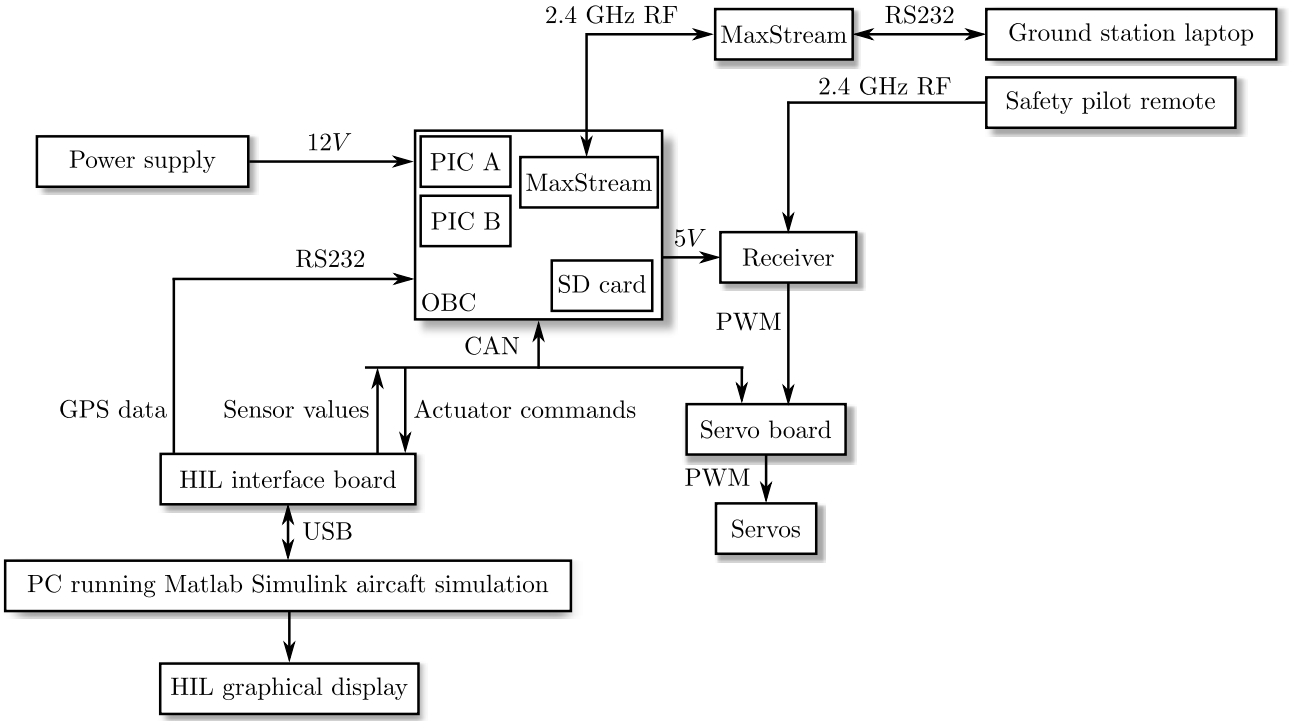

Figure B.4 – HIL overview

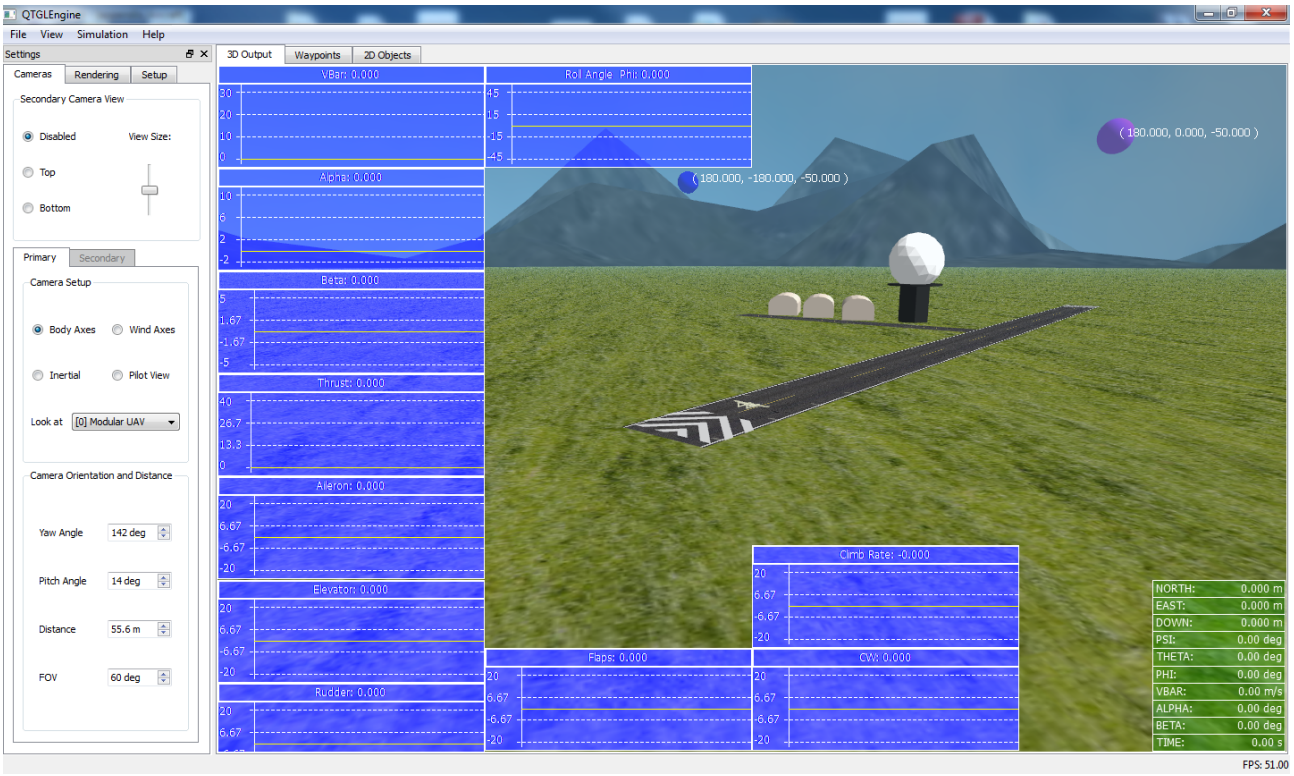

Figure B.5 – HIL graphical display

B.5 Actuator and Controller Limits

To ensure safe and controlled operation of the aircraft, limits are placed on the deflection angles of the actuators, as well as on the controller commands as shown in Table B.1.

Parameter	**Limit**
NSA controller	$-15\,\text{m/s}^2 \geq C_W^{ref} \leq -5\,\text{m/s}^2$
Climb rate controller	$-3.5\,\text{m/s} \geq V_h^{ref} \leq 3.5\,\text{m/s}$
Airspeed	$0\,\text{m/s} \geq \bar{V}^{ref} \leq 30\,\text{m/s}$
Roll angle controller	$-40\,^\circ\text{/s} \geq P^{ref} \leq 40\,^\circ\text{/s}$
Roll angle controller	$-30\,^\circ \geq \phi^{ref} \leq 30\,^\circ$
Throttle	$0\,\text{N} \geq T_C \leq 33\,\text{N}$
Elevator	$-7.5\,^\circ \geq \delta_E \leq 7.5\,^\circ$
Flaps	$-5\,^\circ \geq \delta_F \leq 5\,^\circ$
Ailerons	$-7.5\,^\circ \geq \delta_A \leq 7.5\,^\circ$
Rudder	$-7.5\,^\circ \geq \delta_R \leq 7.5\,^\circ$

Table B.1 – Actuator and controller limits

B.6 Aircraft Model

B.6.1 Standard Flight Conditions

The standard flight conditions are defined in this section. These values are used in the design of the controllers.

Air Density The density of air is considered a constant due to the small altitude ranges involved in this project. The airfield where practical flight tests are conducted is nearly at sea level. Therefore,

$$\rho = 1.225\,\text{kg/m}^3 \tag{B.6.1}$$

Gravitational Acceleration Through similar arguments as for air density, the gravitational acceleration at sea level is used,

$$g = 9.81\,\text{m/s}^2 \tag{B.6.2}$$

Trim Airspeed The aircraft's trim airspeed has been selected as,

$$\bar{V}_{trim} = 18\,\text{m/s} \tag{B.6.3}$$

B.6.2 Aircraft Parameters

This section lists the physical parameters of the aircraft.

Mass
The total flight mass of the aircraft is,

$$m = 6.35\,\text{kg} \tag{B.6.4}$$

Moment of Inertia
The moment of inertia was determined by means of the double pendulum method which is summarised by [4]. It involves suspending the aircraft by two equally long strings such that the strings are parallel to the moment of inertia axis of concern. The aircraft is then rotated slightly about this axis and released. It will begin to oscillate and this period is timed. The moment of inertia is then calculated as,

$$I = \frac{mgd^2}{4\pi^2 l}T^2 \tag{B.6.5}$$

where m is the mass of the aircraft, d the distance between each string and the axis of concern, l is the length of the string and T is the period of oscillation. Thus,

$$\mathbf{I_B} = \begin{bmatrix} 0.722 & 0 & 0 \\ 0 & 0.514 & 0 \\ 0 & 0 & 0.925 \end{bmatrix} \text{kgm}^2 \tag{B.6.6}$$

Engine Parameters

The maximum static thrust of the aircraft's motor was determined through a static thrust test as,

$$T_{\text{max}} = 33\,\text{N} \tag{B.6.7}$$

The engine can be approximated by a first order lag model with a time constant of,

$$\tau_T = 0.25\,\text{s} \tag{B.6.8}$$

B.6.3 Aerodynamic Model

The aerodynamic model of the aircraft is given by its stability and control derivatives. These were obtained by modelling the aircraft in the vortex lattice program AVL as shown in Figure B.6. During this process, the wing's span (b), mean aerodynamic chord ($\bar{c}$) and area (S) are used as non-dimensionalising coefficients. These parameters are given in Table B.2.

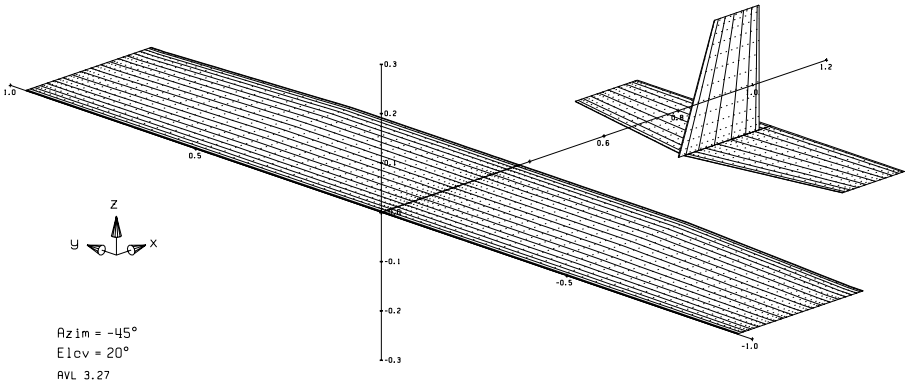

Figure B.6 – Aircraft geometry in AVL

Parameter	Value
Wing span (b)	$1.918\,\text{m}$
Mean aerodynamic chord $\bar{c}$	$0.37\,\text{m}$
Wing Reference Area (S)	$0.677\,\text{m}^2$

Table B.2 – Wing geometric data

The longitudinal and lateral stability derivatives are presented in Tables B.3 and B.4 respectively, and the control derivatives in Table B.5.

Angle of Attack (α)	Value	Pitch Rate (Q)	Value
C_{L_α}	4.808411	C_{L_Q}	7.812170
C_{m_α}	-0.664939	C_{m_Q}	-7.438796

Table B.3 – Longitudinal stability derivatives

Angle of Sideslip (β)	Value	Roll Rate (P)	Value	Yaw Rate (R)	Value
C_{y_β}	-0.167475	C_{y_P}	0.137007	C_{y_R}	0.113738
C_{l_β}	-0.062813	C_{l_P}	-0.429110	C_{l_R}	0.141714
C_{n_β}	0.058436	C_{n_P}	-0.030226	C_{n_R}	-0.063085

Table B.4 – Lateral stability derivatives

Elevator (δ_E)	Value	Flaps (δ_F)	Value
$C_{L_{\delta_E}}$	0.456085	$C_{L_{\delta_F}}$	1.078236
$C_{m_{\delta_E}}$	-0.957351	$C_{m_{\delta_F}}$	0.172092
Aileron (δ_A)	**Value**	**Rudder (δ_R)**	**Value**
$C_{y_{\delta_A}}$	0.003319	$C_{y_{\delta_R}}$	0.093545
$C_{l_{\delta_A}}$	-0.264734	$C_{l_{\delta_R}}$	0.002171
$C_{n_{\delta_A}}$	0.008785	$C_{n_{\delta_R}}$	-0.041144

Table B.5 – Control derivatives

B.6.4 Dimensional Stability and Control Derivative Notation

The dimensional stability and control derivative notation used in this thesis is defined as follows,

$$\mathcal{A}_x = qSl\frac{\partial C_{\mathcal{A}}}{\partial \mathcal{B}'}n \tag{B.6.9}$$

with,

$$\mathcal{B}' = n\mathcal{B} \tag{B.6.10}$$

where the length l is given by $\bar{c}$ for pitch moment derivatives, b for roll and yaw moment derivatives and unity for force derivatives. The normalising coefficient n for incident and control deflection angles is unity, for the pitch rate it is $\frac{\bar{c}}{2V}$ and for the roll and yaw angles it is $\frac{b}{2V}$ [1].

The dimensional stability and control derivatives for the aerodynamic forces and moments is presented in Tables B.6 and B.7 respectively.

Due to	Lift Forces	Sideslip Forces
Angle of attack (α)	$\bar{L}_\alpha = qSC_{L_\alpha}$	
Angle of sideslip (β)		$\bar{Y}_\beta = qSC_{y_\beta}$
Roll Rate (P)		$\bar{Y}_P = qS\frac{b}{2\bar{V}_a}C_{y_P}$
Pitch Rate (Q)	$\bar{L}_Q = qS\frac{\bar{c}}{2\bar{V}_a}C_{L_Q}$	
Yaw Rate (R)		$\bar{Y}_R = qS\frac{b}{2\bar{V}_a}C_{y_R}$
Elevator Deflection (δ_E)	$\bar{L}_{\delta_E} = qSC_{L_{\delta_E}}$	
Flaps Deflection (δ_F)	$\bar{L}_{\delta_F} = qSC_{L_{\delta_F}}$	
Aileron Deflection (δ_A)		$\bar{Y}_{\delta_A} = qSC_{y_{\delta_A}}$
Rudder Deflection (δ_R)		$\bar{Y}_{\delta_R} = qSC_{y_{\delta_R}}$

Table B.6 – Dimensional stability and control derivatives (forces) [1]

Due to	Roll moments	Pitch moments	Yaw moments
Angle of attack (α)		$M_\alpha = qS\bar{c}C_{m_\alpha}$	
Angle of sideslip (β)	$L_\beta = qSbC_{l_\beta}$		$N_\beta = qSbC_{n_\beta}$
Roll Rate (P)	$L_P = qSb\frac{b}{2\bar{V}_a}C_{l_P}$		$N_P = qSb\frac{b}{2\bar{V}_a}C_{n_P}$
Pitch Rate (Q)		$M_Q = qS\bar{c}\frac{\bar{c}}{2\bar{V}_a}C_{m_Q}$	
Yaw Rate (R)	$L_R = qSb\frac{b}{2\bar{V}_a}C_{l_R}$		$N_R = qSb\frac{b}{2\bar{V}_a}C_{n_R}$
Elevator Deflection (δ_E)		$M_{\delta_E} = qS\bar{c}C_{m_{\delta_E}}$	
Flaps Deflection (δ_F)		$M_{\delta_E} = qS\bar{c}C_{m_{\delta_E}}$	
Aileron Deflection (δ_A)	$L_{\delta_A} = qSbC_{l_{\delta_A}}$		$N_{\delta_A} = qSbC_{n_{\delta_A}}$
Rudder Deflection (δ_R)	$L_{\delta_R} = qSbC_{l_{\delta_R}}$		$N_{\delta_R} = qSbC_{n_{\delta_R}}$

Table B.7 – Dimensional stability and control derivatives (moments) [1]

Appendix C

Detailed Derivations

C.1 Normal Dynamics

This section presents the detailed derivation of the transfer function matrix of the normal dynamics. The simplified normal dynamics of Equations 3.2.4 and 3.2.5 are restated for convenience,

$$\begin{bmatrix}\dot{\alpha}\\ \dot{Q}\end{bmatrix} = \begin{bmatrix}-\frac{1}{m\bar{V}}\bar{L}_{\alpha} & 1\\ \frac{1}{I_y}M_{\alpha} & \frac{1}{I_y}M_{Q}\end{bmatrix}\begin{bmatrix}\alpha\\ Q\end{bmatrix} + \begin{bmatrix}-\frac{1}{m\bar{V}}\bar{L}_{\delta_E} & -\frac{1}{m\bar{V}}\bar{L}_{\delta_F}\\ \frac{1}{I_y}M_{\delta_E} & \frac{1}{I_y}M_{\delta_F}\end{bmatrix}\begin{bmatrix}\delta_E\\ \delta_F\end{bmatrix} \tag{C.1.1}$$

$$\begin{bmatrix}C_W\\ Q\end{bmatrix} = \begin{bmatrix}-\frac{1}{m}\bar{L}_{\alpha} & -\frac{1}{m}\bar{L}_{Q}\\ 0 & 1\end{bmatrix}\begin{bmatrix}\alpha\\ Q\end{bmatrix} + \begin{bmatrix}-\frac{1}{m}\bar{L}_{\delta_E} & -\frac{1}{m}\bar{L}_{\delta_F}\\ 0 & 0\end{bmatrix}\begin{bmatrix}\delta_E\\ \delta_F\end{bmatrix} \tag{C.1.2}$$

The normal dynamics can thus be written as,

$$\dot{\mathbf{x}} = \mathbf{A}\mathbf{x} + \mathbf{B}\begin{bmatrix}\delta_E\\ \delta_F\end{bmatrix} \tag{C.1.3}$$

$$\begin{bmatrix}C_W\\ Q\end{bmatrix} = \mathbf{C}\mathbf{x} + \mathbf{D}\begin{bmatrix}\delta_E\\ \delta_F\end{bmatrix} \tag{C.1.4}$$

where,

$$\mathbf{x} = \begin{bmatrix}\alpha\\ Q\end{bmatrix} \tag{C.1.5}$$

$$\mathbf{A} = \begin{bmatrix}-\frac{1}{m\bar{V}}\bar{L}_{\alpha} & 1\\ \frac{1}{I_y}M_{\alpha} & \frac{1}{I_y}M_{Q}\end{bmatrix} \quad \mathbf{B} = \begin{bmatrix}-\frac{1}{m\bar{V}}\bar{L}_{\delta_E} & -\frac{1}{m\bar{V}}\bar{L}_{\delta_F}\\ \frac{1}{I_y}M_{\delta_E} & \frac{1}{I_y}M_{\delta_F}\end{bmatrix} \tag{C.1.6}$$

$$\mathbf{C} = \begin{bmatrix}-\frac{1}{m}\bar{L}_{\alpha} & -\frac{1}{m}\bar{L}_{Q}\\ 0 & 1\end{bmatrix} \quad \mathbf{D} = \begin{bmatrix}-\frac{1}{m}\bar{L}_{\delta_E} & -\frac{1}{m}\bar{L}_{\delta_F}\\ 0 & 0\end{bmatrix} \tag{C.1.7}$$

C.1.1 Characteristic equation for the poles

The poles of the system are the roots of the characteristic equation,

$$p(s) = \det(s\mathbf{I} - \mathbf{A}) \tag{C.1.8}$$

thus,

$$\begin{aligned} p(s) &= \det\left(\begin{bmatrix} s + \frac{1}{m\bar{V}}\bar{L}_\alpha & -1 \\ -\frac{1}{I_y}M_\alpha & s - \frac{1}{I_y}M_Q \end{bmatrix}\right) \\ &= s^2 + \left(\frac{\bar{L}_\alpha}{m\bar{V}} - \frac{M_Q}{I_y}\right)s - \left(\frac{\bar{L}_\alpha}{m\bar{V}}\frac{M_Q}{I_y} + \frac{M_\alpha}{I_y}\right) \end{aligned} \tag{C.1.9}$$

C.1.2 Characteristic equation for the zeros

The zeros of the system are the roots of the equation,

$$z(s) = \mathbf{C}\text{adj}(s\mathbf{I} - \mathbf{A})\mathbf{B} + \mathbf{D}\det(s\mathbf{I} - \mathbf{A}) \tag{C.1.10}$$

solving the first part of the equation,

$$
\begin{aligned}
\mathbf{C}\text{adj}(s\mathbf{I}-\mathbf{A})\mathbf{B} &= \begin{bmatrix} -\frac{1}{m}\bar{L}_\alpha & -\frac{1}{m}\bar{L}_Q \\ 0 & 1 \end{bmatrix} \begin{bmatrix} s-\frac{1}{I_y}M_Q & 1 \\ \frac{1}{I_y}M_\alpha & s+\frac{1}{mV}\bar{L}_\alpha \end{bmatrix} \begin{bmatrix} -\frac{1}{mV}\bar{L}_{\delta_E} & -\frac{1}{mV}\bar{L}_{\delta_F} \\ \frac{1}{I_y}M_{\delta_E} & \frac{1}{I_y}M_{\delta_F} \end{bmatrix} \\
&= \begin{bmatrix} -\frac{1}{m}\bar{L}_\alpha s+\frac{1}{m}\bar{L}_\alpha\frac{1}{I_y}M_Q-\frac{1}{m}\bar{L}_Q\frac{1}{I_y}M_\alpha & -\frac{1}{m}\bar{L}_\alpha-\frac{1}{m}\bar{L}_Q s-\frac{1}{m}\bar{L}_Q\frac{1}{mV}\bar{L}_\alpha \\ \frac{1}{I_y}M_\alpha & s+\frac{1}{mV}\bar{L}_\alpha \end{bmatrix} \begin{bmatrix} -\frac{1}{mV}\bar{L}_{\delta_E} & -\frac{1}{mV}\bar{L}_{\delta_F} \\ \frac{1}{I_y}M_{\delta_E} & \frac{1}{I_y}M_{\delta_F} \end{bmatrix} \\
&= \begin{bmatrix} -\frac{\bar{L}_\alpha}{m}s+\frac{\bar{L}_\alpha}{m}\frac{M_Q}{I_y}-\frac{\bar{L}_Q}{m}\frac{M_\alpha}{I_y} & -\frac{\bar{L}_\alpha}{m}-\frac{\bar{L}_Q}{m}s-\frac{\bar{L}_Q}{m}\frac{\bar{L}_\alpha}{mV} \\ \frac{M_\alpha}{I_y} & s+\frac{\bar{L}_\alpha}{mV} \end{bmatrix} \begin{bmatrix} -\frac{\bar{L}_{\delta_E}}{mV} & -\frac{\bar{L}_{\delta_F}}{mV} \\ \frac{M_{\delta_E}}{I_y} & \frac{M_{\delta_F}}{I_y} \end{bmatrix} \\
&= \begin{bmatrix} -\frac{\bar{L}_{\delta_E}}{mV}(-\frac{\bar{L}_\alpha}{m}s+\frac{\bar{L}_\alpha}{m}\frac{M_Q}{I_y}-\frac{\bar{L}_Q}{m}\frac{M_\alpha}{I_y})+\frac{M_{\delta_E}}{I_y}(-\frac{\bar{L}_\alpha}{m}-\frac{\bar{L}_Q}{m}s-\frac{\bar{L}_Q}{m}\frac{\bar{L}_\alpha}{mV}) & -\frac{\bar{L}_{\delta_F}}{mV}(-\frac{\bar{L}_\alpha}{m}s+\frac{\bar{L}_\alpha}{m}\frac{M_Q}{I_y}-\frac{\bar{L}_Q}{m}\frac{M_\alpha}{I_y})+\frac{M_{\delta_F}}{I_y}(-\frac{\bar{L}_\alpha}{m}-\frac{\bar{L}_Q}{m}s-\frac{\bar{L}_Q}{m}\frac{\bar{L}_\alpha}{mV}) \\ -\frac{\bar{L}_{\delta_E}}{mV}\frac{M_\alpha}{I_y}+\frac{M_{\delta_E}}{I_y}(s+\frac{\bar{L}_\alpha}{mV}) & -\frac{\bar{L}_{\delta_F}}{mV}\frac{M_\alpha}{I_y}+\frac{M_{\delta_F}}{I_y}(s+\frac{\bar{L}_\alpha}{mV}) \end{bmatrix} \\
&= \begin{bmatrix} \frac{\bar{L}_{\delta_E}}{mV}\frac{\bar{L}_\alpha}{m}s-\frac{\bar{L}_{\delta_E}}{mV}\frac{\bar{L}_\alpha}{m}\frac{M_Q}{I_y}+\frac{\bar{L}_{\delta_E}}{mV}\frac{\bar{L}_Q}{m}\frac{M_\alpha}{I_y}-\frac{M_{\delta_E}}{I_y}\frac{\bar{L}_\alpha}{m}-\frac{M_{\delta_E}}{I_y}\frac{\bar{L}_Q}{m}s-\frac{M_{\delta_E}}{I_y}\frac{\bar{L}_Q}{m}\frac{\bar{L}_\alpha}{mV} & \frac{\bar{L}_{\delta_F}}{mV}\frac{\bar{L}_\alpha}{m}s-\frac{\bar{L}_{\delta_F}}{mV}\frac{\bar{L}_\alpha}{m}\frac{M_Q}{I_y}+\frac{\bar{L}_{\delta_F}}{mV}\frac{\bar{L}_Q}{m}\frac{M_\alpha}{I_y}-\frac{M_{\delta_F}}{I_y}\frac{\bar{L}_\alpha}{m}-\frac{M_{\delta_F}}{I_y}\frac{\bar{L}_Q}{m}s-\frac{M_{\delta_F}}{I_y}\frac{\bar{L}_Q}{m}\frac{\bar{L}_\alpha}{mV} \\ -\frac{\bar{L}_{\delta_E}}{mV}\frac{M_\alpha}{I_y}+\frac{M_{\delta_E}}{I_y}s+\frac{M_{\delta_E}}{I_y}\frac{\bar{L}_\alpha}{mV} & -\frac{\bar{L}_{\delta_F}}{mV}\frac{M_\alpha}{I_y}+\frac{M_{\delta_F}}{I_y}s+\frac{M_{\delta_F}}{I_y}\frac{\bar{L}_\alpha}{mV} \end{bmatrix} \\
&= \begin{bmatrix} \frac{\bar{L}_{\delta_E}}{m}\left[\left(\frac{\bar{L}_\alpha}{mV}-\frac{M_{\delta_E}}{I_y}\frac{\bar{L}_Q}{\bar{L}_{\delta_E}}\right)s+\left(-\frac{\bar{L}_\alpha}{mV}\frac{M_Q}{I_y}+\frac{\bar{L}_Q}{mV}\frac{M_\alpha}{I_y}-\frac{M_{\delta_E}}{I_y}\frac{\bar{L}_\alpha}{\bar{L}_{\delta_E}}-\frac{M_{\delta_E}}{I_y}\frac{\bar{L}_Q}{\bar{L}_{\delta_E}}\frac{\bar{L}_\alpha}{mV}\right)\right] & \frac{\bar{L}_{\delta_F}}{m}\left[\left(\frac{\bar{L}_\alpha}{mV}-\frac{M_{\delta_F}}{I_y}\frac{\bar{L}_Q}{\bar{L}_{\delta_F}}\right)s+\left(-\frac{\bar{L}_\alpha}{mV}\frac{M_Q}{I_y}+\frac{\bar{L}_Q}{mV}\frac{M_\alpha}{I_y}-\frac{M_{\delta_F}}{I_y}\frac{\bar{L}_\alpha}{\bar{L}_{\delta_F}}-\frac{M_{\delta_E}}{I_y}\frac{\bar{L}_Q}{\bar{L}_{\delta_F}}\frac{\bar{L}_\alpha}{mV}\right)\right] \\ -\frac{\bar{L}_{\delta_E}}{mV}\frac{M_\alpha}{I_y}+\frac{M_{\delta_E}}{I_y}s+\frac{M_{\delta_E}}{I_y}\frac{\bar{L}_\alpha}{mV} & -\frac{\bar{L}_{\delta_F}}{mV}\frac{M_\alpha}{I_y}+\frac{M_{\delta_F}}{I_y}s+\frac{M_{\delta_F}}{I_y}\frac{\bar{L}_\alpha}{mV} \end{bmatrix}
\end{aligned}
\tag{C.1.11}
$$

now solve for the second part of the equation,

$$
\begin{aligned}
\mathbf{D}\det(s\mathbf{I}-\mathbf{A}) &= \begin{bmatrix} -\frac{1}{m}\bar{L}_{\delta_E} & -\frac{1}{m}\bar{L}_{\delta_F} \\ 0 & 0 \end{bmatrix} \det\left(\begin{bmatrix} s+\frac{1}{mV}\bar{L}_\alpha & -1 \\ -\frac{1}{I_y}M_\alpha & s-\frac{1}{I_y}M_Q \end{bmatrix}\right) \\
&= \begin{bmatrix} -\frac{1}{m}\bar{L}_{\delta_E} & -\frac{1}{m}\bar{L}_{\delta_F} \\ 0 & 0 \end{bmatrix} \left[s^2+\left(\frac{\bar{L}_\alpha}{m\bar{V}}-\frac{M_Q}{I_y}\right)s-\left(\frac{\bar{L}_\alpha}{m\bar{V}}\frac{M_Q}{I_y}+\frac{M_\alpha}{I_y}\right)\right] \\
&= \begin{bmatrix} \frac{\bar{L}_{\delta_E}}{m}\left[-s^2-\left(\frac{\bar{L}_\alpha}{mV}-\frac{M_Q}{I_y}\right)s+\left(\frac{\bar{L}_\alpha}{mV}\frac{M_Q}{I_y}+\frac{M_\alpha}{I_y}\right)\right] & \frac{\bar{L}_{\delta_F}}{m}\left[-s^2-\left(\frac{\bar{L}_\alpha}{mV}-\frac{M_Q}{I_y}\right)s+\left(\frac{\bar{L}_\alpha}{mV}\frac{M_Q}{I_y}+\frac{M_\alpha}{I_y}\right)\right] \\ 0 & 0 \end{bmatrix}
\end{aligned}
\tag{C.1.12}
$$

Combining the result of the two parts,

$$z(s) = \mathbf{C}\text{adj}(s\mathbf{I}-\mathbf{A})\mathbf{B} + \mathbf{D}\det(s\mathbf{I}-\mathbf{A}) \tag{C.1.13}$$

$$= \begin{bmatrix} \left(\begin{array}{c} \frac{\bar{L}_{\delta_E}}{m}\left[\left(\frac{\bar{L}_\alpha}{m\bar{V}} - \frac{M_{\delta_E}}{I_y}\frac{\bar{L}_Q}{\bar{L}_{\delta_E}}\right)s + \left(-\frac{\bar{L}_\alpha}{m\bar{V}}\frac{M_Q}{I_y} + \frac{\bar{L}_Q}{m\bar{V}}\frac{M_\alpha}{I_y} - \frac{M_{\delta_E}}{I_y}\frac{\bar{L}_\alpha}{\bar{L}_{\delta_E}}\right.\right. \\ \left.\left. -\frac{M_{\delta_E}}{I_y}\frac{\bar{L}_Q}{\bar{L}_{\delta_E}}\frac{\bar{L}_\alpha}{m\bar{V}}\right) - s^2 - \left(\frac{\bar{L}_\alpha}{m\bar{V}} - \frac{M_Q}{I_y}\right)s + \left(\frac{\bar{L}_\alpha}{m\bar{V}}\frac{M_Q}{I_y} + \frac{M_\alpha}{I_y}\right)\right] \end{array}\right) & \left(\begin{array}{c} \frac{\bar{L}_{\delta_F}}{m}\left[\left(\frac{\bar{L}_\alpha}{m\bar{V}} - \frac{M_{\delta_F}}{I_y}\frac{\bar{L}_Q}{\bar{L}_{\delta_F}}\right)s + \left(-\frac{\bar{L}_\alpha}{m\bar{V}}\frac{M_Q}{I_y} + \frac{\bar{L}_Q}{m\bar{V}}\frac{M_\alpha}{I_y} - \frac{M_{\delta_F}}{I_y}\frac{\bar{L}_\alpha}{\bar{L}_{\delta_F}}\right.\right. \\ \left.\left. -\frac{M_{\delta_F}}{I_y}\frac{\bar{L}_Q}{\bar{L}_{\delta_F}}\frac{\bar{L}_\alpha}{m\bar{V}}\right) - s^2 - \left(\frac{\bar{L}_\alpha}{m\bar{V}} - \frac{M_Q}{I_y}\right)s + \left(\frac{\bar{L}_\alpha}{m\bar{V}}\frac{M_Q}{I_y} + \frac{M_\alpha}{I_y}\right)\right] \end{array}\right) \\ \left(-\frac{\bar{L}_{\delta_E}}{m\bar{V}}\frac{M_\alpha}{I_y} + \frac{M_{\delta_E}}{I_y}s + \frac{M_{\delta_E}}{I_y}\frac{\bar{L}_\alpha}{m\bar{V}}\right) & \left(-\frac{\bar{L}_{\delta_F}}{m\bar{V}}\frac{M_\alpha}{I_y} + \frac{M_{\delta_F}}{I_y}s + \frac{M_{\delta_F}}{I_y}\frac{\bar{L}_\alpha}{m\bar{V}}\right) \end{bmatrix}$$

$$= \begin{bmatrix} \left(\frac{\bar{L}_{\delta_E}}{m}\left[-s^2 + \frac{\bar{L}_Q}{I_y}\left(\frac{M_Q}{\bar{L}_Q} - \frac{M_{\delta_E}}{\bar{L}_{\delta_E}}\right)s + \frac{\bar{L}_\alpha}{I_y}\left(\frac{M_\alpha}{\bar{L}_\alpha} - \frac{M_{\delta_E}}{\bar{L}_{\delta_E}}\right)\left(1 + \frac{\bar{L}_Q}{m\bar{V}}\right)\right]\right) & \left(\frac{\bar{L}_{\delta_F}}{m}\left[-s^2 + \frac{\bar{L}_Q}{I_y}\left(\frac{M_Q}{\bar{L}_Q} - \frac{M_{\delta_F}}{\bar{L}_{\delta_F}}\right)s + \frac{\bar{L}_\alpha}{I_y}\left(\frac{M_\alpha}{\bar{L}_\alpha} - \frac{M_{\delta_F}}{\bar{L}_{\delta_F}}\right)\left(1 + \frac{\bar{L}_Q}{m\bar{V}}\right)\right]\right) \\ \left(-\frac{\bar{L}_{\delta_E}}{m\bar{V}}\frac{M_\alpha}{I_y} + \frac{M_{\delta_E}}{I_y}s + \frac{M_{\delta_E}}{I_y}\frac{\bar{L}_\alpha}{m\bar{V}}\right) & \left(-\frac{\bar{L}_{\delta_F}}{m\bar{V}}\frac{M_\alpha}{I_y} + \frac{M_{\delta_F}}{I_y}s + \frac{M_{\delta_F}}{I_y}\frac{\bar{L}_\alpha}{m\bar{V}}\right) \end{bmatrix}$$

$$= \begin{bmatrix} \left(\frac{\bar{L}_{\delta_E}}{m}\left[-s^2 + \frac{\bar{L}_Q}{I_y}\left(\frac{M_Q}{\bar{L}_Q} - \frac{M_{\delta_E}}{\bar{L}_{\delta_E}}\right)s + \frac{\bar{L}_\alpha}{I_y}\left(\frac{M_\alpha}{\bar{L}_\alpha} - \frac{M_{\delta_E}}{\bar{L}_{\delta_E}}\right)\right]\right) & \left(\frac{\bar{L}_{\delta_F}}{m}\left[-s^2 + \frac{\bar{L}_Q}{I_y}\left(\frac{M_Q}{\bar{L}_Q} - \frac{M_{\delta_F}}{\bar{L}_{\delta_F}}\right)s + \frac{\bar{L}_\alpha}{I_y}\left(\frac{M_\alpha}{\bar{L}_\alpha} - \frac{M_{\delta_F}}{\bar{L}_{\delta_F}}\right)\right]\right) \\ \left(\frac{M_{\delta_E}}{I_y}\left(s + \frac{\bar{L}_\alpha}{m\bar{V}} - \frac{\bar{L}_{\delta_E}}{m\bar{V}}\frac{M_\alpha}{M_{\delta_E}}\right)\right) & \left(\frac{M_{\delta_F}}{I_y}\left(s + \frac{\bar{L}_\alpha}{m\bar{V}} - \frac{\bar{L}_{\delta_F}}{m\bar{V}}\frac{M_\alpha}{M_{\delta_F}}\right)\right) \end{bmatrix}$$

where it is again assumed that,

$$\left|\frac{L_Q}{m\bar{V}}\right| \ll 1 \tag{C.1.14}$$

If only the location of the zeros is desired the characteristic equation for the zeros becomes,

$$z(s) = \begin{bmatrix} s^2 - \frac{\bar{L}_Q}{I_y}\left(\frac{M_Q}{\bar{L}_Q} - \frac{M_{\delta_E}}{\bar{L}_{\delta_E}}\right)s - \frac{\bar{L}_\alpha}{I_y}\left(\frac{M_\alpha}{\bar{L}_\alpha} - \frac{M_{\delta_E}}{\bar{L}_{\delta_E}}\right) & s^2 - \frac{\bar{L}_Q}{I_y}\left(\frac{M_Q}{\bar{L}_Q} - \frac{M_{\delta_F}}{\bar{L}_{\delta_F}}\right)s - \frac{\bar{L}_\alpha}{I_y}\left(\frac{M_\alpha}{\bar{L}_\alpha} - \frac{M_{\delta_F}}{\bar{L}_{\delta_F}}\right) \\ s + \frac{\bar{L}_\alpha}{m\bar{V}} - \frac{\bar{L}_{\delta_E}}{m\bar{V}}\frac{M_\alpha}{M_{\delta_E}} & s + \frac{\bar{L}_\alpha}{m\bar{V}} - \frac{\bar{L}_{\delta_F}}{m\bar{V}}\frac{M_\alpha}{M_{\delta_F}} \end{bmatrix} \tag{C.1.15}$$

The transfer function matrix can be written as,

$$\mathbf{G}(s) = \frac{1}{\Delta(s)}\mathbf{N}(s) \tag{C.1.16}$$

where $\mathbf{N}(s)$ is a polynomial matrix whose elements consist of the response transfer function numerators, and where $\Delta(s)$ is the characteristic polynomial common to all transfer functions. For the NSA dynamics as shown in Equations 3.2.4 and 3.2.5 four transfer functions exist,

$$\mathbf{G}(s) = \frac{1}{\Delta(s)}\begin{bmatrix} N_{\delta_E}^{C_W}(s) & N_{\delta_F}^{C_W}(s) \\ N_{\delta_E}^{Q}(s) & N_{\delta_F}^{Q}(s) \end{bmatrix} \tag{C.1.17}$$

where $N_{\mathcal{B}}^{\mathcal{A}}(s)$ is the response transfer function numerator of state variable $\mathcal{A}$ to control input $\mathcal{B}$. From the preceding derivations,

$$\Delta(s) = s^2 + \left(\frac{\bar{L}_\alpha}{m\bar{V}} - \frac{M_Q}{I_y}\right)s - \left(\frac{\bar{L}_\alpha}{m\bar{V}}\frac{M_Q}{I_y} + \frac{M_\alpha}{I_y}\right) \tag{C.1.18}$$

and,

$$\mathbf{N}(s) = \begin{bmatrix} -\frac{\bar{L}_{\delta_E}}{m}\left[s^2 - \frac{\bar{L}_Q}{I_y}\left(\frac{M_Q}{\bar{L}_Q} - \frac{M_{\delta_E}}{\bar{L}_{\delta_E}}\right)s - \frac{\bar{L}_\alpha}{I_y}\left(\frac{M_\alpha}{\bar{L}_\alpha} - \frac{M_{\delta_E}}{\bar{L}_{\delta_E}}\right)\right] & -\frac{\bar{L}_{\delta_F}}{m}\left[s^2 - \frac{\bar{L}_Q}{I_y}\left(\frac{M_Q}{\bar{L}_Q} - \frac{M_{\delta_F}}{\bar{L}_{\delta_F}}\right)s - \frac{\bar{L}_\alpha}{I_y}\left(\frac{M_\alpha}{\bar{L}_\alpha} - \frac{M_{\delta_F}}{\bar{L}_{\delta_F}}\right)\right] \\ \frac{M_{\delta_E}}{I_y}\left[s + \frac{\bar{L}_\alpha}{m\bar{V}} - \frac{\bar{L}_{\delta_E}}{m\bar{V}}\frac{M_\alpha}{M_{\delta_E}}\right] & \frac{M_{\delta_F}}{I_y}\left[s + \frac{\bar{L}_\alpha}{m\bar{V}} - \frac{\bar{L}_{\delta_F}}{m\bar{V}}\frac{M_\alpha}{M_{\delta_F}}\right] \end{bmatrix} \tag{C.1.19}$$

C.2 NSA Controller Design - Elevator Actuator

This section presents the detailed derivation of the elevator-based NSA controller. The simplified NSA dynamic equations form §3.2.3.1 are restated below,

$$\begin{bmatrix}\dot{\alpha}\\ \dot{Q}\end{bmatrix} = \begin{bmatrix}-\frac{1}{m\bar{V}}\bar{L}_\alpha & 1\\ \frac{1}{I_y}M_\alpha & \frac{1}{I_y}M_Q\end{bmatrix}\begin{bmatrix}\alpha\\ Q\end{bmatrix} + \begin{bmatrix}0\\ \frac{1}{I_y}M_{\delta_E}\end{bmatrix}\delta_E \tag{C.2.1}$$

$$\begin{bmatrix}C_W\\ Q\end{bmatrix} = \begin{bmatrix}-\frac{1}{m}\bar{L}_\alpha & 0\\ 0 & 1\end{bmatrix}\begin{bmatrix}\alpha\\ Q\end{bmatrix} + \begin{bmatrix}0\\ 0\end{bmatrix}\delta_E \tag{C.2.2}$$

The normal dynamics can thus be written as,

$$\dot{\mathbf{x}} = \mathbf{A}\mathbf{x} + \mathbf{B}\delta_E \tag{C.2.3}$$

$$\begin{bmatrix}C_W\\ Q\end{bmatrix} = \mathbf{C}\mathbf{x} + \mathbf{D}\delta_E \tag{C.2.4}$$

where,

$$\mathbf{x} = \begin{bmatrix}\alpha\\ Q\end{bmatrix} \tag{C.2.5}$$

$$\mathbf{A} = \begin{bmatrix}-\frac{1}{m\bar{V}}\bar{L}_\alpha & 1\\ \frac{1}{I_y}M_\alpha & \frac{1}{I_y}M_Q\end{bmatrix} \quad \mathbf{B} = \begin{bmatrix}0\\ \frac{1}{I_y}M_{\delta_E}\end{bmatrix} \tag{C.2.6}$$

$$\mathbf{C} = \begin{bmatrix}-\frac{1}{m}\bar{L}_\alpha & 0\\ 0 & 1\end{bmatrix} \quad \mathbf{D} = \begin{bmatrix}0\\ 0\end{bmatrix} \tag{C.2.7}$$

To remove steady state errors on NSA, the state vector is augmented with an integrator x_I which obeys the differential equation,

$$\dot{x}_I = C_W - C_W^{ref} \tag{C.2.8}$$

$$\dot{x}_I = \mathbf{C}'x + \mathbf{D}'\delta_E - C_W^{ref} \tag{C.2.9}$$

where C_W^{ref} is the reference NSA input, and $\mathbf{C}'$ and $\mathbf{D}'$ are the first rows of $\mathbf{C}$ and $\mathbf{D}$ respectively. The augmented NSA dynamics are now given by,

$$\begin{bmatrix}\dot{x}_I\\ \dot{\mathbf{x}}\end{bmatrix} = \begin{bmatrix}0 & \mathbf{C}'\\ \mathbf{0} & \mathbf{A}\end{bmatrix}\begin{bmatrix}x_I\\ \mathbf{x}\end{bmatrix} + \begin{bmatrix}\mathbf{D}'\\ \mathbf{B}\end{bmatrix}\delta_E - \begin{bmatrix}1\\ \mathbf{0}\end{bmatrix}C_W^{ref} \tag{C.2.10}$$

$$\begin{bmatrix}C_W\\ Q\end{bmatrix} = \begin{bmatrix}\mathbf{0} & \mathbf{C}\end{bmatrix}\begin{bmatrix}x_I\\ \mathbf{x}\end{bmatrix} + \mathbf{D}\delta_E \tag{C.2.11}$$

An elevator control law is defined which uses feedback from the integrator and pitch rate states as well as feed-forward from the reference input. Thus,

$$\delta_E = -\begin{bmatrix} K_{I_{\delta_E}} & 0 & K_{Q_{\delta_E}} \end{bmatrix} \begin{bmatrix} x_I \\ \alpha \\ Q \end{bmatrix} + \bar{N}_{C_{\delta_E}} C_W^{ref} \tag{C.2.12}$$

The control law is now substituted into the dynamics,

$$\begin{bmatrix} \dot{x}_I \\ \dot{\alpha} \\ \dot{Q} \end{bmatrix} = \begin{bmatrix} 0 & -\frac{1}{m}\bar{L}_\alpha & 0 \\ 0 & -\frac{1}{m\bar{V}}\bar{L}_\alpha & 1 \\ 0 & \frac{1}{I_y}M_\alpha & \frac{1}{I_y}M_Q \end{bmatrix} \begin{bmatrix} x_I \\ \alpha \\ Q \end{bmatrix} + \begin{bmatrix} 0 \\ 0 \\ \frac{1}{I_y}M_{\delta_E} \end{bmatrix} \begin{bmatrix} -K_{I_{\delta_E}} & 0 & -K_{Q_{\delta_E}} \end{bmatrix} \begin{bmatrix} x_I \\ \alpha \\ Q \end{bmatrix} + \begin{bmatrix} 0 \\ 0 \\ \frac{1}{I_y}M_{\delta_E} \end{bmatrix} \bar{N}_C C_W^{ref} - \begin{bmatrix} 1 \\ 0 \\ 0 \end{bmatrix} C_W^{ref} \tag{C.2.13}$$

$$\begin{bmatrix} \dot{x}_I \\ \dot{\alpha} \\ \dot{Q} \end{bmatrix} = \begin{bmatrix} 0 & -\frac{1}{m}\bar{L}_\alpha & 0 \\ 0 & -\frac{1}{m\bar{V}}\bar{L}_\alpha & 1 \\ 0 & \frac{1}{I_y}M_\alpha & \frac{1}{I_y}M_Q \end{bmatrix} \begin{bmatrix} x_I \\ \alpha \\ Q \end{bmatrix} + \begin{bmatrix} 0 & 0 & 0 \\ 0 & 0 & 0 \\ -\frac{1}{I_y}M_{\delta_E}K_{I_{\delta_E}} & 0 & -\frac{1}{I_y}M_{\delta_E}K_{Q_{\delta_E}} \end{bmatrix} \begin{bmatrix} x_I \\ \alpha \\ Q \end{bmatrix} - \begin{bmatrix} 1 \\ 0 \\ -\frac{1}{I_y}M_{\delta_E}\bar{N}_C \end{bmatrix} C_W^{ref}$$

$$\begin{bmatrix} \dot{x}_I \\ \dot{\alpha} \\ \dot{Q} \end{bmatrix} = \begin{bmatrix} 0 & -\frac{1}{m}\bar{L}_\alpha & 0 \\ 0 & -\frac{1}{m\bar{V}}\bar{L}_\alpha & 1 \\ -\frac{1}{I_y}M_{\delta_E}K_{I_{\delta_E}} & \frac{1}{I_y}M_\alpha & \frac{1}{I_y}M_Q - \frac{1}{I_y}M_{\delta_E}K_{Q_{\delta_E}} \end{bmatrix} \begin{bmatrix} x_I \\ \alpha \\ Q \end{bmatrix} - \begin{bmatrix} 1 \\ 0 \\ -\frac{1}{I_y}M_{\delta_E}\bar{N}_C \end{bmatrix} C_W^{ref}$$

The closed loop system is therefore given by,

$$\begin{bmatrix} \dot{x}_I \\ \dot{\alpha} \\ \dot{Q} \end{bmatrix} = \begin{bmatrix} 0 & -\frac{1}{m}\bar{L}_\alpha & 0 \\ 0 & -\frac{1}{m\bar{V}}\bar{L}_\alpha & 1 \\ -\frac{1}{I_y}M_{\delta_E}K_{I_{\delta_E}} & \frac{1}{I_y}M_\alpha & \frac{1}{I_y}M_Q - \frac{1}{I_y}M_{\delta_E}K_{Q_{\delta_E}} \end{bmatrix} \begin{bmatrix} x_I \\ \alpha \\ Q \end{bmatrix} - \begin{bmatrix} 1 \\ 0 \\ -\frac{1}{I_y}M_{\delta_E}\bar{N}_{C_{\delta_E}} \end{bmatrix} C_W^{ref} \tag{C.2.14}$$

$$\begin{bmatrix} C_W \\ Q \end{bmatrix} = \begin{bmatrix} 0 & -\frac{1}{m}\bar{L}_\alpha & 0 \\ 0 & 0 & 1 \end{bmatrix} \begin{bmatrix} x_I \\ \alpha \\ Q \end{bmatrix} \tag{C.2.15}$$

Calculating the closed loop characteristic equation,

$$\begin{aligned} p(s) &= \det(s\mathbf{I} - \mathbf{A}) \qquad \text{(C.2.16)} \\ &= \det\left(\begin{bmatrix} s & \frac{1}{m}\bar{L}_\alpha & 0 \\ 0 & s + \frac{1}{m\bar{V}}\bar{L}_\alpha & -1 \\ \frac{1}{I_y}M_{\delta_E}K_{I_{\delta_E}} & -\frac{1}{I_y}M_\alpha & s - (\frac{1}{I_y}M_Q - \frac{1}{I_y}M_{\delta_E}K_{Q_{\delta_E}}) \end{bmatrix}\right) \\ &= s^3 - \left(-\frac{1}{m\bar{V}}\bar{L}_\alpha + \frac{1}{I_y}M_Q - \frac{1}{I_y}M_{\delta_E}K_{Q_{\delta_E}}\right)s^2 \\ &\quad + \left((-\frac{1}{m\bar{V}}\bar{L}_\alpha)(\frac{1}{I_y}M_Q - \frac{1}{I_y}M_{\delta_E}K_{Q_{\delta_E}}) - (1)(\frac{1}{I_y}M_\alpha)\ \right)s \\ &\quad - (-\frac{1}{m}\bar{L}_\alpha)(1)(-\frac{1}{I_y}M_{\delta_E}K_{I_{\delta_E}}) \\ &= s^3 + \left(\frac{\bar{L}_\alpha}{m\bar{V}} - \frac{M_Q}{I_y} + \frac{M_{\delta_E}}{I_y}K_{Q_{\delta_E}}\right)s^2 + \left(-\frac{\bar{L}_\alpha M_Q}{m\bar{V}I_y} + \frac{\bar{L}_\alpha M_{\delta_E}}{m\bar{V}I_y}K_{Q_{\delta_E}} - \frac{M_\alpha}{I_y}\right)s - \frac{\bar{L}_\alpha M_{\delta_E}}{mI_y}K_{I_{\delta_E}} \end{aligned}$$

To place the closed loop poles, a desired characteristic equation for the NSA dynamics is defined as,

$$\alpha_c(s) = s^3 + \alpha_2 s^2 + \alpha_1 s + \alpha_0 \tag{C.2.17}$$

When equating the coefficients of the actual and desired characteristic equations the following results are obtained,

$$\alpha_2 = \frac{\bar{L}_\alpha}{m\bar{V}} - \frac{M_Q}{I_y} + \frac{M_{\delta_E}}{I_y} K_{Q_{\delta_E}} \tag{C.2.18}$$

$$\alpha_1 = -\frac{\bar{L}_\alpha M_Q}{m\bar{V} I_y} + \frac{\bar{L}_\alpha M_{\delta_E}}{m\bar{V} I_y} K_{Q_{\delta_E}} - \frac{M_\alpha}{I_y} \tag{C.2.19}$$

$$\alpha_0 = -\frac{\bar{L}_\alpha M_{\delta_E}}{m I_y} K_{I_{\delta_E}} \tag{C.2.20}$$

The desired characteristic equation can be rewritten as,

$$\alpha_c(s) = (s^2 + 2\zeta\omega_n s + \omega_n^2)(s + a) \tag{C.2.21}$$

where the complex pole pair corresponds to the short period mode and the single real pole to the closed-loop integrator. Expanding the equation gives,

$$\alpha_c(s) = s^3 + (2\zeta\omega_n + a)s^2 + (2\zeta\omega_n a + \omega_n^2)s + \omega_n^2 a \tag{C.2.22}$$

If the damping of the short period mode (ζ) as well as the integrator pole location are selected, then the resulting natural frequency can be solved for. This is accomplished by solving for the pitch rate feedback gain K_Q in the first and second order terms of the characteristic equation,

$$K_{Q_{\delta_E}} = \frac{I_y}{M_{\delta_E}}(2\zeta\omega_n + a - \frac{\bar{L}_\alpha}{m\bar{V}} + \frac{M_Q}{I_y}) \tag{C.2.23}$$

and,

$$K_{Q_{\delta_E}} = \frac{m\bar{V}}{\bar{L}_\alpha}\frac{I_y}{M_{\delta_E}}(2\zeta\omega_n a + \omega_n^2 + \frac{\bar{L}_\alpha}{m\bar{V}}\frac{M_Q}{I_y} + \frac{M_\alpha}{I_y}) \tag{C.2.24}$$

Setting these equal to one another yields an equation for the natural frequency,

$$\frac{I_y}{M_{\delta_E}}(2\zeta\omega_n + a - \frac{\bar{L}_\alpha}{m\bar{V}} + \frac{M_Q}{I_y}) = \frac{m\bar{V}}{\bar{L}_\alpha}\frac{I_y}{M_{\delta_E}}(2\zeta\omega_n a + \omega_n^2 + \frac{\bar{L}_\alpha}{m\bar{V}}\frac{M_Q}{I_y} + \frac{M_\alpha}{I_y}) \tag{C.2.25}$$

$$\frac{m\bar{V}}{\bar{L}_\alpha}\frac{I_y}{M_{\delta_E}}(2\zeta\omega_n\frac{\bar{L}_\alpha}{m\bar{V}} + a\frac{\bar{L}_\alpha}{m\bar{V}} - \frac{\bar{L}_\alpha}{m\bar{V}}\frac{\bar{L}_\alpha}{m\bar{V}} + \frac{M_Q}{I_y}\frac{\bar{L}_\alpha}{m\bar{V}}) = \frac{m\bar{V}}{\bar{L}_\alpha}\frac{I_y}{M_{\delta_E}}(2\zeta\omega_n a + \omega_n^2 + \frac{\bar{L}_\alpha}{m\bar{V}}\frac{M_Q}{I_y} + \frac{M_\alpha}{I_y})$$

$$2\zeta\omega_n\frac{\bar{L}_\alpha}{m\bar{V}} + a\frac{\bar{L}_\alpha}{m\bar{V}} - \frac{\bar{L}_\alpha}{m\bar{V}}\frac{\bar{L}_\alpha}{m\bar{V}} + \frac{M_Q}{I_y}\frac{\bar{L}_\alpha}{m\bar{V}} = 2\zeta\omega_n a + \omega_n^2 + \frac{\bar{L}_\alpha}{m\bar{V}}\frac{M_Q}{I_y} + \frac{M_\alpha}{I_y}$$

$$0 = 2\zeta\omega_n a + \omega_n^2 + \frac{\bar{L}_\alpha M_Q}{m\bar{V} I_y} + \frac{M_\alpha}{I_y} - 2\zeta\omega_n\frac{\bar{L}_\alpha}{m\bar{V}} - a\frac{\bar{L}_\alpha}{m\bar{V}} + \frac{\bar{L}_\alpha}{m\bar{V}}\frac{\bar{L}_\alpha}{m\bar{V}} - \frac{M_Q\bar{L}_\alpha}{I_y m\bar{V}}$$

$$0 = \omega_n^2 + \omega_n\left(2\zeta a - 2\zeta\frac{\bar{L}_\alpha}{m\bar{V}}\right) + \frac{M_\alpha}{I_y} + \left(\frac{\bar{L}_\alpha}{m\bar{V}}\right)^2 - a\frac{\bar{L}_\alpha}{m\bar{V}}$$

Solving for positive values of ω_n the closed loop natural frequency of the short period mode is given by,

$$\omega_n = \zeta\eta + \sqrt{(\zeta\eta)^2 - \frac{M_\alpha}{I_y} - \frac{\bar{L}_\alpha}{m\bar{V}}\eta} \tag{C.2.26}$$

where,

$$\eta = \frac{\bar{L}_\alpha}{m\bar{V}} - a \tag{C.2.27}$$

The natural frequency of the short period mode (ω_n), along with the previously selected damping of the short period mode (ζ) and the location of the closed-loop integrator pole (a) can now be used in conjunction with either of the pitch rate equations to determine the pitch rate feedback gain $K_{Q_{\delta_E}}$. The integrator feedback gain can be solved by equating the coefficients of the final terms of actual and desired characteristic equations and is given by,

$$K_{I_{\delta_E}} = -a\frac{\omega_n^2 m I_y}{\bar{L}_\alpha M_{\delta_E}} \tag{C.2.28}$$

The integrator's response can be removed from the reference input by placing a feed-forward zero as follows,

$$\bar{N}_{C_{\delta_E}} = -\frac{K_{I_{\delta_E}}}{z_f} \tag{C.2.29}$$

where z_f is the location of the desired zero.

C.3 NSA Controller Design - Flaps actuator

This section presents the detailed derivation of the flaps-based NSA controller. The simplified NSA dynamic equations from §3.2.3.2 are restated below,

$$\begin{bmatrix}\dot{\alpha}\\ \dot{Q}\end{bmatrix} = \begin{bmatrix} -\frac{1}{m\bar{V}}\bar{L}_\alpha & 1 \\ \frac{1}{I_y}M_\alpha & \frac{1}{I_y}M_Q\end{bmatrix}\begin{bmatrix}\alpha\\ Q\end{bmatrix} + \begin{bmatrix} -\frac{1}{m\bar{V}}\bar{L}_{\delta_F} \\ \frac{1}{I_y}M_{\delta_F}\end{bmatrix}\delta_F \tag{C.3.1}$$

$$\begin{bmatrix}C_W\\ Q\end{bmatrix} = \begin{bmatrix} -\frac{1}{m}\bar{L}_\alpha & 0 \\ 0 & 1\end{bmatrix}\begin{bmatrix}\alpha\\ Q\end{bmatrix} + \begin{bmatrix} -\frac{1}{m}\bar{L}_{\delta_F} \\ 0\end{bmatrix}\delta_F \tag{C.3.2}$$

The normal dynamics can thus be written as,

$$\dot{\mathbf{x}} = \mathbf{A}\mathbf{x} + \mathbf{B}\delta_F \tag{C.3.3}$$

$$\begin{bmatrix}C_W\\ Q\end{bmatrix} = \mathbf{C}\mathbf{x} + \mathbf{D}\delta_F \tag{C.3.4}$$

where,

$$\mathbf{x} = \begin{bmatrix}\alpha\\ Q\end{bmatrix} \tag{C.3.5}$$

$$\mathbf{A} = \begin{bmatrix} -\frac{1}{m\bar{V}}\bar{L}_\alpha & 1 \\ \frac{1}{I_y}M_\alpha & \frac{1}{I_y}M_Q\end{bmatrix} \quad \mathbf{B} = \begin{bmatrix} -\frac{1}{m\bar{V}}\bar{L}_{\delta_F} \\ \frac{1}{I_y}M_{\delta_F}\end{bmatrix} \tag{C.3.6}$$

$$\mathbf{C} = \begin{bmatrix} -\frac{1}{m}\bar{L}_\alpha & 0 \\ 0 & 1\end{bmatrix} \quad \mathbf{D} = \begin{bmatrix} -\frac{1}{m}\bar{L}_{\delta_F} \\ 0\end{bmatrix} \tag{C.3.7}$$

A flaps control law is now defined which uses proportional feedback from the NSA,

$$\begin{aligned}\delta_F &= -K_{P_{\delta_F}}(y - s) \\ &= -K_{P_{\delta_F}}(C_W - C_W^{ref}) \\ &= -K_{P_{\delta_F}}\left(\mathbf{C}'\mathbf{x} + \mathbf{D}'u - C_W^{ref}\right)\end{aligned} \tag{C.3.8}$$

where C_W^{ref} is the reference NSA input, and $\mathbf{C}'$ and $\mathbf{D}'$ are the first rows of $\mathbf{C}$ and $\mathbf{D}$ respectively. Thus,

$$\delta_F = -K_{P_{\delta_F}}\left(\begin{bmatrix} -\frac{1}{m}\bar{L}_\alpha & 0\end{bmatrix}\begin{bmatrix}\alpha\\ Q\end{bmatrix} + \begin{bmatrix} -\frac{1}{m}\bar{L}_{\delta_F}\end{bmatrix}\delta_F - C_W^{ref}\right) \tag{C.3.9}$$

$$\delta_F = -K_{P_{\delta_F}}\begin{bmatrix} -\frac{1}{m}\bar{L}_\alpha & 0\end{bmatrix}\begin{bmatrix}\alpha\\ Q\end{bmatrix} - K_{P_{\delta_F}}\begin{bmatrix} -\frac{1}{m}\bar{L}_{\delta_F}\end{bmatrix}\delta_F + K_{P_{\delta_F}}C_W^{ref}$$

$$\delta_F + K_{P_{\delta_F}}\begin{bmatrix} -\frac{1}{m}\bar{L}_{\delta_F}\end{bmatrix}\delta_F = -K_{P_{\delta_F}}\begin{bmatrix} -\frac{1}{m}\bar{L}_\alpha & 0\end{bmatrix}\begin{bmatrix}\alpha\\ Q\end{bmatrix} + K_{P_{\delta_F}}C_W^{ref}$$

$$\delta_F = -\frac{K_{P_{\delta_F}}}{1 - K_{P_{\delta_F}}\frac{\bar{L}_{\delta_F}}{m}}\begin{bmatrix} -\frac{1}{m}\bar{L}_\alpha & 0\end{bmatrix}\begin{bmatrix}\alpha\\ Q\end{bmatrix} + \frac{K_{P_{\delta_F}}C_{W_R}}{1 - K_{P_{\delta_F}}\frac{\bar{L}_{\delta_F}}{m}}$$

The control law is now substituted into the dynamic equation,

$$\begin{bmatrix}\dot{\alpha}\\ \dot{Q}\end{bmatrix} = \begin{bmatrix} -\frac{1}{m\bar{V}}\bar{L}_\alpha & 1 \\ \frac{1}{I_y}M_\alpha & \frac{1}{I_y}M_Q\end{bmatrix}\begin{bmatrix}\alpha\\ Q\end{bmatrix} - \frac{K_{P_{\delta_F}}}{1-K_{P_{\delta_F}}\frac{\bar{L}_{\delta_F}}{m}}\begin{bmatrix} -\frac{1}{m\bar{V}}\bar{L}_{\delta_F}\\ \frac{1}{I_y}M_{\delta_F}\end{bmatrix}\begin{bmatrix} -\frac{1}{m}\bar{L}_\alpha & 0\end{bmatrix}\begin{bmatrix}\alpha\\ Q\end{bmatrix} + \frac{K_{P_{\delta_F}}C_W^{ref}}{1-K_{P_{\delta_F}}\frac{\bar{L}_{\delta_F}}{m}}\begin{bmatrix} -\frac{1}{m\bar{V}}\bar{L}_{\delta_F}\\ \frac{1}{I_y}M_{\delta_F}\end{bmatrix}$$

$$\begin{bmatrix}C_W\\ Q\end{bmatrix} = \begin{bmatrix} -\frac{1}{m}\bar{L}_\alpha & 0 \\ 0 & 1\end{bmatrix}\begin{bmatrix}\alpha\\ Q\end{bmatrix} - \frac{K_{P_{\delta_F}}}{1-K_{P_{\delta_F}}\frac{\bar{L}_{\delta_F}}{m}}\begin{bmatrix} -\frac{1}{m}\bar{L}_{\delta_F}\\ 0\end{bmatrix}\begin{bmatrix} -\frac{1}{m}\bar{L}_\alpha & 0\end{bmatrix}\begin{bmatrix}\alpha\\ Q\end{bmatrix} + \frac{K_{P_{\delta_F}}C_W^{ref}}{1-K_{P_{\delta_F}}\frac{\bar{L}_{\delta_F}}{m}}\begin{bmatrix} -\frac{1}{m}\bar{L}_{\delta_F}\\ 0\end{bmatrix}$$

$$\begin{bmatrix}\dot{\alpha}\\ \dot{Q}\end{bmatrix} = \begin{bmatrix} -\frac{1}{m\bar{V}}\bar{L}_\alpha & 1 \\ \frac{1}{I_y}M_\alpha & \frac{1}{I_y}M_Q\end{bmatrix}\begin{bmatrix}\alpha\\ Q\end{bmatrix} - \frac{K_{P_{\delta_F}}}{1-K_{P_{\delta_F}}\frac{\bar{L}_{\delta_F}}{m}}\begin{bmatrix} \frac{\bar{L}_{\delta_F}\bar{L}_\alpha}{m^2\bar{V}} & 0\\ -\frac{M_{\delta_F}\bar{L}_\alpha}{I_y m} & 0\end{bmatrix}\begin{bmatrix}\alpha\\ Q\end{bmatrix} + \frac{K_{P_{\delta_F}}C_W^{ref}}{1-K_{P_{\delta_F}}\frac{\bar{L}_{\delta_F}}{m}}\begin{bmatrix} -\frac{1}{m\bar{V}}\bar{L}_{\delta_F}\\ \frac{1}{I_y}M_{\delta_F}\end{bmatrix}$$

$$\begin{bmatrix}C_W\\ Q\end{bmatrix} = \begin{bmatrix} -\frac{1}{m}\bar{L}_\alpha & 0 \\ 0 & 1\end{bmatrix}\begin{bmatrix}\alpha\\ Q\end{bmatrix} - \frac{K_{P_{\delta_F}}}{1-K_{P_{\delta_F}}\frac{\bar{L}_{\delta_F}}{m}}\begin{bmatrix} \frac{\bar{L}_{\delta_F}\bar{L}_\alpha}{m^2} & 0\\ 0 & 0\end{bmatrix}\begin{bmatrix}\alpha\\ Q\end{bmatrix} + \frac{K_{P_{\delta_F}}C_W^{ref}}{1-K_{P_{\delta_F}}\frac{\bar{L}_{\delta_F}}{m}}\begin{bmatrix} -\frac{1}{m}\bar{L}_{\delta_F}\\ 0\end{bmatrix}$$

$$\begin{bmatrix}\dot{\alpha}\\ \dot{Q}\end{bmatrix} = \begin{bmatrix} -\frac{\bar{L}_\alpha}{m\bar{V}} - \left(\frac{K_{P_{\delta_F}}}{1-K_{P_{\delta_F}}\frac{\bar{L}_{\delta_F}}{m}}\right)\frac{\bar{L}_{\delta_F}\bar{L}_\alpha}{m^2\bar{V}} & 1\\ \frac{M_\alpha}{I_y} + \left(\frac{K_{P_{\delta_F}}}{1-K_{P_{\delta_F}}\frac{\bar{L}_{\delta_F}}{m}}\right)\frac{M_{\delta_F}\bar{L}_\alpha}{I_y m} & \frac{M_Q}{I_y}\end{bmatrix}\begin{bmatrix}\alpha\\ Q\end{bmatrix} + \begin{bmatrix} -\frac{\bar{L}_{\delta_F}}{m\bar{V}}\left(\frac{K_{P_{\delta_F}}}{1-K_{P_{\delta_F}}\frac{\bar{L}_{\delta_F}}{m}}\right)\\ \frac{M_{\delta_F}}{I_y}\left(\frac{K_{P_{\delta_F}}}{1-K_{P_{\delta_F}}\frac{\bar{L}_{\delta_F}}{m}}\right)\end{bmatrix}C_W^{ref} \tag{C.3.10}$$

$$\begin{bmatrix}C_W\\ Q\end{bmatrix} = \begin{bmatrix} -\frac{\bar{L}_\alpha}{m} & 0 \\ 0 & 1\end{bmatrix}\begin{bmatrix}\alpha\\ Q\end{bmatrix} - \frac{K_{P_{\delta_F}}}{1-K_{P_{\delta_F}}\frac{\bar{L}_{\delta_F}}{m}}\begin{bmatrix} \frac{\bar{L}_{\delta_F}\bar{L}_\alpha}{m^2} & 0\\ 0 & 0\end{bmatrix}\begin{bmatrix}\alpha\\ Q\end{bmatrix} + \begin{bmatrix} -\frac{\bar{L}_{\delta_F}}{m}\left(\frac{K_{P_{\delta_F}}}{1-K_{P_{\delta_F}}\frac{\bar{L}_{\delta_F}}{m}}\right)\\ 0\end{bmatrix}C_W^{ref} \tag{C.3.11}$$

let,

$$\Delta = \left(\frac{K_{P_{\delta_F}}}{1-K_{P_{\delta_F}}\frac{\bar{L}_{\delta_F}}{m}}\right) \tag{C.3.12}$$

Now,

$$\begin{bmatrix}\dot{\alpha}\\ \dot{Q}\end{bmatrix} = \begin{bmatrix} -\frac{\bar{L}_\alpha}{m\bar{V}} - \Delta\frac{\bar{L}_{\delta_F}\bar{L}_\alpha}{m^2\bar{V}} & 1\\ \frac{M_\alpha}{I_y} + \Delta\frac{M_{\delta_F}\bar{L}_\alpha}{I_y m} & \frac{M_Q}{I_y}\end{bmatrix}\begin{bmatrix}\alpha\\ Q\end{bmatrix} + \begin{bmatrix} -\frac{\bar{L}_{\delta_F}}{m\bar{V}}\Delta\\ \frac{M_{\delta_F}}{I_y}\Delta\end{bmatrix}C_W^{ref} \tag{C.3.13}$$

$$\begin{bmatrix}C_W\\ Q\end{bmatrix} = \begin{bmatrix} -\frac{\bar{L}_\alpha}{m} - \Delta\frac{\bar{L}_{\delta_F}\bar{L}_\alpha}{m^2} & 0\\ 0 & 1\end{bmatrix}\begin{bmatrix}\alpha\\ Q\end{bmatrix} + \begin{bmatrix} -\frac{\bar{L}_{\delta_F}}{m}\Delta\\ 0\end{bmatrix}C_W^{ref} \tag{C.3.14}$$

The transfer function for the NSA response to a reference NSA input is now determined.

Calculating the closed-loop characteristic equation,

$$p(s) = \det(s\mathbf{I} - \mathbf{A}) \tag{C.3.15}$$

thus,

$$
\begin{aligned}
p(s) &= \det\left(\begin{bmatrix} s + \frac{\bar{L}_\alpha}{m\bar{V}} + \Delta\frac{\bar{L}_{\delta_F}\bar{L}_\alpha}{m^2\bar{V}} & -1 \\ -\frac{M_\alpha}{I_y} - \Delta\frac{M_{\delta_F}\bar{L}_\alpha}{I_y m} & s - \frac{M_Q}{I_y} \end{bmatrix}\right) \qquad \text{(C.3.16)} \\
&= \left(s + \left(\frac{\bar{L}_\alpha}{m\bar{V}} + \Delta\frac{\bar{L}_{\delta_F}\bar{L}_\alpha}{m^2\bar{V}}\right)\right)\left(s - \left(\frac{M_Q}{I_y}\right)\right) - \left(-\frac{M_\alpha}{I_y} - \Delta\frac{M_{\delta_F}\bar{L}_\alpha}{I_y m}\right)(-1) \\
&= s^2 - s\left(\frac{M_Q}{I_y}\right) + s\left(\frac{\bar{L}_\alpha}{m\bar{V}} + \Delta\frac{\bar{L}_{\delta_F}\bar{L}_\alpha}{m^2\bar{V}}\right) - \left(\frac{M_Q}{I_y}\right)\left(\frac{\bar{L}_\alpha}{m\bar{V}} + \Delta\frac{\bar{L}_{\delta_F}\bar{L}_\alpha}{m^2\bar{V}}\right) \\
&\quad + \left(\frac{M_\alpha}{I_y} + \Delta\frac{M_{\delta_F}\bar{L}_\alpha}{I_y m}\right)(-1) \\
&= s^2 + s\left(\frac{\bar{L}_\alpha}{m\bar{V}} + \Delta\frac{\bar{L}_{\delta_F}\bar{L}_\alpha}{m^2\bar{V}} - \frac{M_Q}{I_y}\right) - \left(\frac{M_Q}{I_y}\frac{\bar{L}_\alpha}{m\bar{V}} + \frac{M_Q}{I_y}\Delta\frac{\bar{L}_{\delta_F}\bar{L}_\alpha}{m^2\bar{V}}\right) + \left(-\frac{M_\alpha}{I_y} - \Delta\frac{M_{\delta_F}\bar{L}_\alpha}{I_y m}\right)
\end{aligned}
$$

The zeros of the system are the roots of the equation,

$$z(s) = \mathbf{C}\text{adj}(s\mathbf{I} - \mathbf{A})\mathbf{B} + \mathbf{D}\det(s\mathbf{I} - \mathbf{A}) \tag{C.3.17}$$

solving the first part,

$$\begin{aligned}
\mathbf{C}\text{adj}(s\mathbf{I} - \mathbf{A})\mathbf{B} &= \begin{bmatrix} -\frac{\bar{L}_\alpha}{m} - \Delta\frac{\bar{L}_{\delta_F}\bar{L}_\alpha}{m^2} & 0 \\ 0 & 1 \end{bmatrix} \begin{bmatrix} s - \frac{M_Q}{I_y} & 1 \\ \frac{M_\alpha}{I_y} + \Delta\frac{M_{\delta_F}\bar{L}_\alpha}{I_y m} & s + \frac{\bar{L}_\alpha}{m\bar{V}} + \Delta\frac{\bar{L}_{\delta_F}\bar{L}_\alpha}{m^2\bar{V}} \end{bmatrix} \begin{bmatrix} -\frac{\bar{L}_{\delta_F}}{m\bar{V}}\Delta \\ \frac{M_{\delta_F}}{I_y}\Delta \end{bmatrix} \\
&= \begin{bmatrix} (-\frac{\bar{L}_\alpha}{m} - \Delta\frac{\bar{L}_{\delta_F}\bar{L}_\alpha}{m^2})(s - \frac{M_Q}{I_y}) & -\frac{\bar{L}_\alpha}{m} - \Delta\frac{\bar{L}_{\delta_F}\bar{L}_\alpha}{m^2} \\ \frac{M_\alpha}{I_y} + \Delta\frac{M_{\delta_F}\bar{L}_\alpha}{I_y m} & s + \frac{\bar{L}_\alpha}{m\bar{V}} + \Delta\frac{\bar{L}_{\delta_F}\bar{L}_\alpha}{m^2\bar{V}} \end{bmatrix} \begin{bmatrix} -\frac{\bar{L}_{\delta_F}}{m\bar{V}}\Delta \\ \frac{M_{\delta_F}}{I_y}\Delta \end{bmatrix} \\
&= \begin{bmatrix} \left[(-\frac{\bar{L}_\alpha}{m} - \Delta\frac{\bar{L}_{\delta_F}\bar{L}_\alpha}{m^2})(s - \frac{M_Q}{I_y})\right]\left[-\frac{\bar{L}_{\delta_F}}{m\bar{V}}\Delta\right] + \left[-\frac{\bar{L}_\alpha}{m} - \Delta\frac{\bar{L}_{\delta_F}\bar{L}_\alpha}{m^2}\right]\left[\frac{M_{\delta_F}}{I_y}\Delta\right] \\ \left[\frac{M_\alpha}{I_y} + \Delta\frac{M_{\delta_F}\bar{L}_\alpha}{I_y m}\right]\left[-\frac{\bar{L}_{\delta_F}}{m\bar{V}}\Delta\right] + \left[s + \frac{\bar{L}_\alpha}{m\bar{V}} + \Delta\frac{\bar{L}_{\delta_F}\bar{L}_\alpha}{m^2\bar{V}}\right]\left[\frac{M_{\delta_F}}{I_y}\Delta\right] \end{bmatrix}
\end{aligned} \tag{C.3.18}$$

now solve for,

$$\mathbf{D}\det(s\mathbf{I} - \mathbf{A}) = \begin{bmatrix} -\frac{\bar{L}_{\delta_F}}{m}\Delta \\ 0 \end{bmatrix} \left[s^2 + s\left(\frac{\bar{L}_\alpha}{m\bar{V}} + \Delta\frac{\bar{L}_{\delta_F}\bar{L}_\alpha}{m^2\bar{V}} - \frac{M_Q}{I_y}\right) - \left(\frac{M_Q}{I_y}\frac{\bar{L}_\alpha}{m\bar{V}} + \frac{M_Q}{I_y}\Delta\frac{\bar{L}_{\delta_F}\bar{L}_\alpha}{m^2\bar{V}}\right) + \left(-\frac{M_\alpha}{I_y} - \Delta\frac{M_{\delta_F}\bar{L}_\alpha}{I_y m}\right)\right] \tag{C.3.19}$$

combining the results of the two parts above,

$$z(s) = \mathbf{C}\text{adj}(s\mathbf{I} - \mathbf{A})\mathbf{B} + \mathbf{D}\det(s\mathbf{I} - \mathbf{A}) \tag{C.3.20}$$

$$= \begin{bmatrix} \left[(-\frac{\bar{L}_\alpha}{m} - \Delta\frac{\bar{L}_{\delta_F}\bar{L}_\alpha}{m^2})(s - \frac{M_Q}{I_y})\right]\left[-\frac{\bar{L}_{\delta_F}}{m\bar{V}}\Delta\right] + \left[-\frac{\bar{L}_\alpha}{m} - \Delta\frac{\bar{L}_{\delta_F}\bar{L}_\alpha}{m^2}\right]\left[\frac{M_{\delta_F}}{I_y}\Delta\right] \\ \left[\frac{M_\alpha}{I_y} + \Delta\frac{M_{\delta_F}\bar{L}_\alpha}{I_y m}\right]\left[-\frac{\bar{L}_{\delta_F}}{m\bar{V}}\Delta\right] + \left[s + \frac{\bar{L}_\alpha}{m\bar{V}} + \Delta\frac{\bar{L}_{\delta_F}\bar{L}_\alpha}{m^2\bar{V}}\right]\left[\frac{M_{\delta_F}}{I_y}\Delta\right] \end{bmatrix} + \begin{bmatrix} \left[-\frac{\bar{L}_{\delta_F}}{m}\Delta\right]\left[s^2 + s\left(\frac{\bar{L}_\alpha}{m\bar{V}} + \Delta\frac{\bar{L}_{\delta_F}\bar{L}_\alpha}{m^2\bar{V}} - \frac{M_Q}{I_y}\right) - \left(\frac{M_Q}{I_y}\frac{\bar{L}_\alpha}{m\bar{V}} + \frac{M_Q}{I_y}\Delta\frac{\bar{L}_{\delta_F}\bar{L}_\alpha}{m^2\bar{V}}\right) + \left(-\frac{M_\alpha}{I_y} - \Delta\frac{M_{\delta_F}\bar{L}_\alpha}{I_y m}\right)\right] \\ 0 \end{bmatrix}$$

$$= \begin{bmatrix} \left[-\frac{\bar{L}_\alpha}{m}s + \frac{\bar{L}_\alpha}{m}\frac{M_Q}{I_y} - \Delta\frac{\bar{L}_{\delta_F}\bar{L}_\alpha}{m^2}s + \Delta\frac{\bar{L}_{\delta_F}\bar{L}_\alpha}{m^2}\frac{M_Q}{I_y}\right]\left[-\frac{\bar{L}_{\delta_F}}{m\bar{V}}\Delta\right] + \left[-\frac{\bar{L}_\alpha}{m} - \Delta\frac{\bar{L}_{\delta_F}\bar{L}_\alpha}{m^2}\right]\left[\frac{M_{\delta_F}}{I_y}\Delta\right] \\ + \left[-\frac{\bar{L}_{\delta_F}}{m}\Delta\right]\left[s^2 + s\left(\frac{\bar{L}_\alpha}{m\bar{V}} + \Delta\frac{\bar{L}_{\delta_F}\bar{L}_\alpha}{m^2\bar{V}} - \frac{M_Q}{I_y}\right) - \left(\frac{M_Q}{I_y}\frac{\bar{L}_\alpha}{m\bar{V}} + \frac{M_Q}{I_y}\Delta\frac{\bar{L}_{\delta_F}\bar{L}_\alpha}{m^2\bar{V}}\right) + \left(-\frac{M_\alpha}{I_y} - \Delta\frac{M_{\delta_F}\bar{L}_\alpha}{I_y m}\right)\right] \\ \left[\frac{M_\alpha}{I_y} + \Delta\frac{M_{\delta_F}\bar{L}_\alpha}{I_y m}\right]\left[-\frac{\bar{L}_{\delta_F}}{m\bar{V}}\Delta\right] + \left[s + \frac{\bar{L}_\alpha}{m\bar{V}} + \Delta\frac{\bar{L}_{\delta_F}\bar{L}_\alpha}{m^2\bar{V}}\right]\left[\frac{M_{\delta_F}}{I_y}\Delta\right] \end{bmatrix}$$

$$= \begin{bmatrix} \left[-\frac{\bar{L}_{\delta_F}}{m}\Delta\right]\left[\left(-\frac{\bar{L}_\alpha}{m}s + \frac{\bar{L}_\alpha}{m}\frac{M_Q}{I_y} - \Delta\frac{\bar{L}_{\delta_F}\bar{L}_\alpha}{m^2}s + \Delta\frac{\bar{L}_{\delta_F}\bar{L}_\alpha}{m^2}\frac{M_Q}{I_y}\right)\left(\frac{1}{\bar{V}}\right) + \left(-\frac{\bar{L}_\alpha}{m} - \Delta\frac{\bar{L}_{\delta_F}\bar{L}_\alpha}{m^2}\right)\left(-\frac{m}{\bar{L}_{\delta_F}}\frac{M_{\delta_F}}{I_y}\right)\right. \\ \left. + \left(s^2 + s\left(\frac{\bar{L}_\alpha}{m\bar{V}} + \Delta\frac{\bar{L}_{\delta_F}\bar{L}_\alpha}{m^2\bar{V}} - \frac{M_Q}{I_y}\right) - \left(\frac{M_Q}{I_y}\frac{\bar{L}_\alpha}{m\bar{V}} + \frac{M_Q}{I_y}\Delta\frac{\bar{L}_{\delta_F}\bar{L}_\alpha}{m^2\bar{V}}\right) + \left(-\frac{M_\alpha}{I_y} - \Delta\frac{M_{\delta_F}\bar{L}_\alpha}{I_y m}\right)\right)\right] \\ \left[\frac{M_\alpha}{I_y} + \Delta\frac{M_{\delta_F}\bar{L}_\alpha}{I_y m}\right]\left[-\frac{\bar{L}_{\delta_F}}{m\bar{V}}\Delta\right] + \left[s + \frac{\bar{L}_\alpha}{m\bar{V}} + \Delta\frac{\bar{L}_{\delta_F}\bar{L}_\alpha}{m^2\bar{V}}\right]\left[\frac{M_{\delta_F}}{I_y}\Delta\right] \end{bmatrix}$$

$$= \begin{bmatrix} \left[-\frac{\bar{L}_{\delta_F}}{m}\Delta\right]\left[\left(-\frac{\bar{L}_\alpha}{m\bar{V}}s + \frac{\bar{L}_\alpha}{m\bar{V}}\frac{M_Q}{I_y} - \Delta\frac{\bar{L}_{\delta_F}\bar{L}_\alpha}{m^2\bar{V}}s + \Delta\frac{\bar{L}_{\delta_F}\bar{L}_\alpha}{m^2\bar{V}}\frac{M_Q}{I_y}\right) + \left(\frac{\bar{L}_\alpha}{\bar{L}_{\delta_F}}\frac{M_{\delta_F}}{I_y} + \Delta\frac{\bar{L}_\alpha M_{\delta_F}}{m I_y}\right) + s^2 + \left(\frac{\bar{L}_\alpha}{m\bar{V}}s + \Delta\frac{\bar{L}_{\delta_F}\bar{L}_\alpha}{m^2\bar{V}}s - \frac{M_Q}{I_y}s\right) - \left(\frac{M_Q}{I_y}\frac{\bar{L}_\alpha}{m\bar{V}} + \frac{M_Q}{I_y}\Delta\frac{\bar{L}_{\delta_F}\bar{L}_\alpha}{m^2\bar{V}}\right) + \left(-\frac{M_\alpha}{I_y} - \Delta\frac{M_{\delta_F}\bar{L}_\alpha}{I_y m}\right)\right] \\ \left[-\frac{\bar{L}_{\delta_F}}{m\bar{V}}\Delta\frac{M_\alpha}{I_y} - \frac{\bar{L}_{\delta_F}}{m\bar{V}}\Delta\Delta\frac{M_{\delta_F}\bar{L}_\alpha}{I_y m}\right] + \left[\frac{M_{\delta_F}}{I_y}\Delta s + \frac{M_{\delta_F}}{I_y}\Delta\frac{\bar{L}_\alpha}{m\bar{V}} + \frac{M_{\delta_F}}{I_y}\Delta\Delta\frac{\bar{L}_{\delta_F}\bar{L}_\alpha}{m^2\bar{V}}\right] \end{bmatrix}$$

$$= \begin{bmatrix} \left[-\frac{\bar{L}_{\delta_F}}{m}\Delta\right]\left[\left(\frac{\bar{L}_\alpha}{\bar{L}_{\delta_F}}\frac{M_{\delta_F}}{I_y}\right) + s^2 + \left(-\frac{M_Q}{I_y}s\right) + \left(-\frac{M_\alpha}{I_y}\right)\right] \\ \left[-\frac{\bar{L}_{\delta_F}}{m\bar{V}}\Delta\frac{M_\alpha}{I_y}\right] + \left[\frac{M_{\delta_F}}{I_y}\Delta s + \frac{M_{\delta_F}}{I_y}\Delta\frac{\bar{L}_\alpha}{m\bar{V}}\right] \end{bmatrix}$$

$$= \begin{bmatrix} \left[-\frac{\bar{L}_{\delta_F}}{m}\Delta\right]\left[s^2 - \frac{M_Q}{I_y}s + \left(\frac{\bar{L}_\alpha}{\bar{L}_{\delta_F}}\frac{M_{\delta_F}}{I_y} - \frac{M_\alpha}{I_y}\right)\right] \\ \left[\frac{M_{\delta_F}}{I_y}\Delta\right]\left[s - \frac{\bar{L}_{\delta_F}M_\alpha}{m\bar{V}} + \frac{\bar{L}_\alpha}{m\bar{V}}\right] \end{bmatrix}$$

The transfer function for a NSA response to a reference NSA input can therefore be written as,

$$G_{C_W^{ref}}^{C_W}(s) = \frac{\left[-\frac{\bar{L}_{\delta_F}}{m}\Delta\right]\left[s^2 - \frac{M_Q}{I_y}s + \left(\frac{\bar{L}_\alpha}{\bar{L}_{\delta_F}}\frac{M_{\delta_F}}{I_y} - \frac{M_\alpha}{I_y}\right)\right]}{s^2 + s\left(\frac{\bar{L}_\alpha}{m\bar{V}} + \Delta\frac{\bar{L}_{\delta_F}\bar{L}_\alpha}{m^2\bar{V}} - \frac{M_Q}{I_y}\right) - \left(\frac{M_Q}{I_y}\frac{\bar{L}_\alpha}{m\bar{V}} + \frac{M_Q}{I_y}\Delta\frac{\bar{L}_{\delta_F}\bar{L}_\alpha}{m^2\bar{V}}\right) + \left(-\frac{M_\alpha}{I_y} - \Delta\frac{M_{\delta_F}\bar{L}_\alpha}{I_y m}\right)} \tag{C.3.21}$$

The desired characteristic equation is,

$$\alpha_c(s) = s^2 + \alpha_1 s + \alpha_0 \tag{C.3.22}$$

equating the coefficients gives,

$$\begin{aligned} \alpha_1 &= \frac{\bar{L}_\alpha}{m\bar{V}} + \Delta\frac{\bar{L}_{\delta_F}\bar{L}_\alpha}{m^2\bar{V}} - \frac{M_Q}{I_y} \\ \alpha_0 &= -\frac{M_Q}{I_y}\frac{\bar{L}_\alpha}{m\bar{V}} - \frac{M_Q}{I_y}\Delta\frac{\bar{L}_{\delta_F}\bar{L}_\alpha}{m^2\bar{V}} - \frac{M_\alpha}{I_y} - \Delta\frac{M_{\delta_F}\bar{L}_\alpha}{I_y m} \end{aligned} \tag{C.3.23}$$

thus,

$$\Delta = \frac{m^2\bar{V}}{\bar{L}_{\delta_F}\bar{L}_\alpha}\left(\alpha_1 - \frac{\bar{L}_\alpha}{m\bar{V}} + \frac{M_Q}{I_y}\right) \tag{C.3.24}$$

and,

$$\alpha_0 = -\frac{M_Q}{I_y}\frac{\bar{L}_\alpha}{m\bar{V}} - \frac{M_Q}{I_y}\Delta\frac{\bar{L}_{\delta_F}\bar{L}_\alpha}{m^2\bar{V}} - \frac{M_\alpha}{I_y} - \Delta\frac{M_{\delta_F}\bar{L}_\alpha}{I_y m} \tag{C.3.25}$$

$$\begin{aligned} \frac{M_Q}{I_y}\Delta\frac{\bar{L}_{\delta_F}\bar{L}_\alpha}{m^2\bar{V}} + \Delta\frac{M_{\delta_F}\bar{L}_\alpha}{I_y m} &= -\alpha_0 - \frac{M_Q}{I_y}\frac{\bar{L}_\alpha}{m\bar{V}} - \frac{M_\alpha}{I_y} \\ \Delta\left(\frac{M_Q}{I_y}\frac{\bar{L}_{\delta_F}\bar{L}_\alpha}{m^2\bar{V}} + \frac{M_{\delta_F}\bar{L}_\alpha}{I_y m}\right) &= -\left(\alpha_0 + \frac{M_Q}{I_y}\frac{\bar{L}_\alpha}{m\bar{V}} + \frac{M_\alpha}{I_y}\right) \\ \Delta &= -\frac{\left(\alpha_0 + \frac{M_Q}{I_y}\frac{\bar{L}_\alpha}{m\bar{V}} + \frac{M_\alpha}{I_y}\right)}{\left(\frac{M_Q}{I_y}\frac{\bar{L}_{\delta_F}\bar{L}_\alpha}{m^2\bar{V}} + \frac{M_{\delta_F}\bar{L}_\alpha}{I_y m}\right)} \\ \Delta &= -\frac{\left(\alpha_0 I_y m^2\bar{V} + M_Q\bar{L}_\alpha m + M_\alpha m^2\bar{V}\right)}{\left(M_Q\bar{L}_{\delta_F}\bar{L}_\alpha + M_{\delta_F}\bar{L}_\alpha m\bar{V}\right)} \end{aligned}$$

Equating the above two equations of Δ gives,

$$\frac{m^2\bar{V}}{\bar{L}_{\delta_F}\bar{L}_\alpha}\left(\alpha_1 - \frac{\bar{L}_\alpha}{m\bar{V}} + \frac{M_Q}{I_y}\right) = -\frac{\left(\alpha_0 I_y m^2\bar{V} + M_Q\bar{L}_\alpha m + M_\alpha m^2\bar{V}\right)}{\left(M_Q\bar{L}_{\delta_F}\bar{L}_\alpha + M_{\delta_F}\bar{L}_\alpha m\bar{V}\right)} \tag{C.3.26}$$

$$\left(\alpha_1 - \frac{\bar{L}_\alpha}{m\bar{V}} + \frac{M_Q}{I_y}\right) = -\frac{\bar{L}_{\delta_F}\bar{L}_\alpha}{m^2\bar{V}}\frac{\left(\alpha_0 I_y m^2\bar{V} + M_Q\bar{L}_\alpha m + M_\alpha m^2\bar{V}\right)}{\left(M_Q\bar{L}_{\delta_F}\bar{L}_\alpha + M_{\delta_F}\bar{L}_\alpha m\bar{V}\right)}$$

$$\alpha_1 - \frac{\bar{L}_\alpha}{m\bar{V}} + \frac{M_Q}{I_y} = -\frac{\bar{L}_{\delta_F}}{m\bar{V}}\frac{\left(\alpha_0 I_y m\bar{V} + M_Q\bar{L}_\alpha + M_\alpha m\bar{V}\right)}{\left(M_Q\bar{L}_{\delta_F} + M_{\delta_F}m\bar{V}\right)}$$

$$\alpha_1\left(M_Q\bar{L}_{\delta_F} + M_{\delta_F}m\bar{V}\right) - \frac{\bar{L}_\alpha}{m\bar{V}}\left(M_Q\bar{L}_{\delta_F} + M_{\delta_F}m\bar{V}\right) + \frac{M_Q}{I_y}\left(M_Q\bar{L}_{\delta_F} + M_{\delta_F}m\bar{V}\right) = -\frac{\bar{L}_{\delta_F}}{m\bar{V}}\left(\alpha_0 I_y m\bar{V} + M_Q\bar{L}_\alpha + M_\alpha m\bar{V}\right) \tag{C.3.27}$$

$$\alpha_1\left(M_Q\bar{L}_{\delta_F} + M_{\delta_F}m\bar{V}\right) - \frac{\bar{L}_\alpha}{m\bar{V}}\left(M_Q\bar{L}_{\delta_F} + M_{\delta_F}m\bar{V}\right) + \frac{M_Q}{I_y}\left(M_Q\bar{L}_{\delta_F} + M_{\delta_F}m\bar{V}\right) = -\bar{L}_{\delta_F}\alpha_0 I_y - \frac{\bar{L}_{\delta_F}M_Q\bar{L}_\alpha}{m\bar{V}} - \bar{L}_{\delta_F}M_\alpha$$

$$\alpha_1\left(M_Q\bar{L}_{\delta_F} + M_{\delta_F}m\bar{V}\right) - \frac{\bar{L}_\alpha}{m\bar{V}}M_Q\bar{L}_{\delta_F} - \frac{\bar{L}_\alpha}{m\bar{V}}M_{\delta_F}m\bar{V} + \frac{M_Q}{I_y}\left(M_Q\bar{L}_{\delta_F} + M_{\delta_F}m\bar{V}\right) = -\bar{L}_{\delta_F}\alpha_0 I_y - \frac{\bar{L}_{\delta_F}M_Q\bar{L}_\alpha}{m\bar{V}} - \bar{L}_{\delta_F}M_\alpha$$

$$\alpha_1\left(M_Q\bar{L}_{\delta_F} + M_{\delta_F}m\bar{V}\right) - \bar{L}_\alpha M_{\delta_F} + \frac{M_Q}{I_y}\left(M_Q\bar{L}_{\delta_F} + M_{\delta_F}m\bar{V}\right) = -\bar{L}_{\delta_F}\alpha_0 I_y - \bar{L}_{\delta_F}M_\alpha$$

$$\alpha_1\left(M_Q\bar{L}_{\delta_F} + M_{\delta_F}m\bar{V}\right) + \frac{M_Q}{I_y}\left(M_Q\bar{L}_{\delta_F} + M_{\delta_F}m\bar{V}\right) - \bar{L}_\alpha M_{\delta_F} + \bar{L}_{\delta_F}M_\alpha = -\bar{L}_{\delta_F}\alpha_0 I_y$$

$$\alpha_1\left(M_Q\bar{L}_{\delta_F}I_y + M_{\delta_F}I_y m\bar{V}\right) + M_Q^2\bar{L}_{\delta_F} + M_Q M_{\delta_F}m\bar{V} - \bar{L}_\alpha M_{\delta_F}I_y + \bar{L}_{\delta_F}M_\alpha I_y = -\bar{L}_{\delta_F}\alpha_0 I_y^2$$

The characteristic equation can also be written as,

$$\alpha_c(s) = (s^2 + 2\zeta\omega_n s + \omega_n^2) \tag{C.3.28}$$

where the complex pole pair corresponds to the short period mode. Equating the coefficients allows an equation for the natural frequency ω_n to be determined,

$$2\zeta\omega_n \left(M_Q \bar{L}_{\delta_F} I_y + M_{\delta_F} I_y m\bar{V}\right) + M_Q^2 \bar{L}_{\delta_F} + M_Q M_{\delta_F} m\bar{V} - \bar{L}_\alpha M_{\delta_F} I_y + \bar{L}_{\delta_F} M_\alpha I_y = -\bar{L}_{\delta_F} I_y^2 \omega_n^2 \tag{C.3.29}$$

$$\bar{L}_{\delta_F} I_y^2 \omega_n^2 + 2\zeta\omega_n \left(M_Q \bar{L}_{\delta_F} I_y + M_{\delta_F} I_y m\bar{V}\right) + M_Q^2 \bar{L}_{\delta_F} + M_Q M_{\delta_F} m\bar{V} - \bar{L}_\alpha M_{\delta_F} I_y + \bar{L}_{\delta_F} M_\alpha I_y = 0$$

Now solve for the positive values of ω_n,

$$x = \frac{-b + \sqrt{b^2 - 4ac}}{2a} \tag{C.3.30}$$

$$b^2 = 4\zeta^2 \left(M_Q \bar{L}_{\delta_F} I_y + M_{\delta_F} I_y m\bar{V}\right)^2 \tag{C.3.31}$$

$$4ac = 4\bar{L}_{\delta_F} I_y^2 \left(M_Q^2 \bar{L}_{\delta_F} + M_Q M_{\delta_F} m\bar{V} - \bar{L}_\alpha M_{\delta_F} I_y + \bar{L}_{\delta_F} M_\alpha I_y\right) \tag{C.3.32}$$

$$b^2 - 4ac = 4\zeta^2 \left(M_Q \bar{L}_{\delta_F} I_y + M_{\delta_F} I_y m\bar{V}\right)^2 - 4\bar{L}_{\delta_F} I_y^2 \left(M_Q^2 \bar{L}_{\delta_F} + M_Q M_{\delta_F} m\bar{V} - \bar{L}_\alpha M_{\delta_F} I_y + \bar{L}_{\delta_F} M_\alpha I_y\right) \tag{C.3.33}$$

therefore,

$$\begin{aligned}\omega_n &= \frac{-2\zeta\left(M_Q\bar{L}_{\delta_F}I_y + M_{\delta_F}I_y m\bar{V}\right) + \sqrt{4\zeta^2\left(M_Q\bar{L}_{\delta_F}I_y + M_{\delta_F}I_y m\bar{V}\right)^2 - 4\bar{L}_{\delta_F}I_y^2\left(M_Q^2\bar{L}_{\delta_F} + M_Q M_{\delta_F}m\bar{V} - \bar{L}_\alpha M_{\delta_F}I_y + \bar{L}_{\delta_F}M_\alpha I_y\right)}}{2\bar{L}_{\delta_F}I_y^2} \\ &= \frac{-\zeta\left(M_Q\bar{L}_{\delta_F}I_y + M_{\delta_F}I_y m\bar{V}\right) + \sqrt{\zeta^2\left(M_Q\bar{L}_{\delta_F}I_y + M_{\delta_F}I_y m\bar{V}\right)^2 - \bar{L}_{\delta_F}I_y^2\left(M_Q^2\bar{L}_{\delta_F} + M_Q M_{\delta_F}m\bar{V} - \bar{L}_\alpha M_{\delta_F}I_y + \bar{L}_{\delta_F}M_\alpha I_y\right)}}{\bar{L}_{\delta_F}I_y^2} \\ &= \frac{-\zeta\eta + \sqrt{(\zeta\eta)^2 - \bar{L}_{\delta_F}I_y^2\left(M_Q^2\bar{L}_{\delta_F} + M_Q M_{\delta_F}m\bar{V} - \bar{L}_\alpha M_{\delta_F}I_y + \bar{L}_{\delta_F}M_\alpha I_y\right)}}{\bar{L}_{\delta_F}I_y^2}\end{aligned} \tag{C.3.34}$$

where,

$$\eta = M_Q\bar{L}_{\delta_F}I_y + M_{\delta_F}I_y m\bar{V} \tag{C.3.35}$$

Substituting the equation for ω_n into the two equations for Δ allows the derivation of two different but equivalent equations for the feedback gain $K_{P_{\delta_F}}$.

For the first Δ equation containing α_1,

$$\Delta = \frac{m^2\bar{V}}{\bar{L}_{\delta_F}\bar{L}_\alpha}\left(\alpha_1 - \frac{\bar{L}_\alpha}{m\bar{V}} + \frac{M_Q}{I_y}\right) \tag{C.3.36}$$

where,

$$\Delta = \left(\frac{K_{P_{\delta_F}}}{1 - K_{P_{\delta_F}}\frac{\bar{L}_{\delta_F}}{m}}\right) \tag{C.3.37}$$

now,

$$\left(\frac{K_{P_{\delta_F}}}{1 - K_{P_{\delta_F}}\frac{\bar{L}_{\delta_F}}{m}}\right) = \frac{m^2\bar{V}}{\bar{L}_{\delta_F}\bar{L}_\alpha}\left(\alpha_1 - \frac{\bar{L}_\alpha}{m\bar{V}} + \frac{M_Q}{I_y}\right) \tag{C.3.38}$$

$$K_{P_{\delta_F}} = \frac{m^2\bar{V}}{\bar{L}_{\delta_F}\bar{L}_\alpha}\left(\alpha_1 - \frac{\bar{L}_\alpha}{m\bar{V}} + \frac{M_Q}{I_y}\right)\left(1 - K_{P_{\delta_F}}\frac{\bar{L}_{\delta_F}}{m}\right)$$

$$K_{P_{\delta_F}} = \frac{m^2\bar{V}}{\bar{L}_{\delta_F}\bar{L}_\alpha}\left(\alpha_1 - \frac{\bar{L}_\alpha}{m\bar{V}} + \frac{M_Q}{I_y}\right) - K_{P_{\delta_F}}\frac{m\bar{V}}{\bar{L}_\alpha}\left(\alpha_1 - \frac{\bar{L}_\alpha}{m\bar{V}} + \frac{M_Q}{I_y}\right)$$

$$K_{P_{\delta_F}}\frac{m\bar{V}}{\bar{L}_\alpha}\left(\alpha_1 - \frac{\bar{L}_\alpha}{m\bar{V}} + \frac{M_Q}{I_y}\right) + K_{P_{\delta_F}} = \frac{m^2\bar{V}}{\bar{L}_{\delta_F}\bar{L}_\alpha}\left(\alpha_1 - \frac{\bar{L}_\alpha}{m\bar{V}} + \frac{M_Q}{I_y}\right)$$

$$K_{P_{\delta_F}} = \frac{\frac{m^2\bar{V}}{\bar{L}_{\delta_F}\bar{L}_\alpha}\left(\alpha_1 - \frac{\bar{L}_\alpha}{m\bar{V}} + \frac{M_Q}{I_y}\right)}{\frac{m\bar{V}}{\bar{L}_\alpha}\left(\alpha_1 - \frac{\bar{L}_\alpha}{m\bar{V}} + \frac{M_Q}{I_y}\right) + 1}$$

$$K_{P_{\delta_F}} = \frac{\frac{\bar{L}_\alpha}{m\bar{V}}\frac{m^2\bar{V}}{\bar{L}_{\delta_F}\bar{L}_\alpha}\left(\alpha_1 - \frac{\bar{L}_\alpha}{m\bar{V}} + \frac{M_Q}{I_y}\right)}{\frac{\bar{L}_\alpha}{m\bar{V}}\frac{m\bar{V}}{\bar{L}_\alpha}\left(\alpha_1 - \frac{\bar{L}_\alpha}{m\bar{V}} + \frac{M_Q}{I_y}\right) + \frac{\bar{L}_\alpha}{m\bar{V}}}$$

$$K_{P_{\delta_F}} = \frac{\frac{m}{\bar{L}_{\delta_F}}\left(\alpha_1 - \frac{\bar{L}_\alpha}{m\bar{V}} + \frac{M_Q}{I_y}\right)}{\alpha_1 - \frac{\bar{L}_\alpha}{m\bar{V}} + \frac{M_Q}{I_y} + \frac{\bar{L}_\alpha}{m\bar{V}}}$$

$$K_{P_{\delta_F}} = \frac{\frac{m}{\bar{L}_{\delta_F}}\left(\alpha_1 - \frac{\bar{L}_\alpha}{m\bar{V}} + \frac{M_Q}{I_y}\right)}{\alpha_1 + \frac{M_Q}{I_y}}$$

$$K_{P_{\delta_F}} = \frac{\frac{m}{\bar{L}_{\delta_F}}\left(\alpha_1 + \frac{M_Q}{I_y}\right) - \frac{\bar{L}_\alpha}{\bar{L}_{\delta_F}\bar{V}}}{\alpha_1 + \frac{M_Q}{I_y}}$$

$$K_{P_{\delta_F}} = \frac{m\left(\alpha_1 + \frac{M_Q}{I_y}\right) - \frac{\bar{L}_\alpha}{\bar{V}}}{\bar{L}_{\delta_F}\left(\alpha_1 + \frac{M_Q}{I_y}\right)}$$

$$K_{P_{\delta_F}} = \frac{m\left(\alpha_1 + \frac{M_Q}{I_y}\right)}{\bar{L}_{\delta_F}\left(\alpha_1 + \frac{M_Q}{I_y}\right)} - \frac{\frac{\bar{L}_\alpha}{\bar{V}}}{\bar{L}_{\delta_F}\left(\alpha_1 + \frac{M_Q}{I_y}\right)}$$

$$K_{P_{\delta_F}} = \frac{m}{\bar{L}_{\delta_F}} - \frac{\bar{L}_\alpha}{\bar{L}_{\delta_F}\bar{V}\left(\alpha_1 + \frac{M_Q}{I_y}\right)}$$

$$K_{P_{\delta_F}} = \frac{m}{\bar{L}_{\delta_F}} - \frac{\bar{L}_\alpha}{\bar{L}_{\delta_F}\bar{V}\left(2\zeta\omega_n + \frac{M_Q}{I_y}\right)}$$

For the second equation for Δ, containing α_0,

$$\Delta = -\frac{\left(\alpha_0 I_y m^2 \bar{V} + M_Q \bar{L}_\alpha m + M_\alpha m^2 \bar{V}\right)}{\left(M_Q \bar{L}_{\delta_F} \bar{L}_\alpha + M_{\delta_F} \bar{L}_\alpha m \bar{V}\right)} \tag{C.3.39}$$

where,

$$\Delta = \left(\frac{K_{P_{\delta_F}}}{1 - K_{P_{\delta_F}} \frac{\bar{L}_{\delta_F}}{m}}\right) \tag{C.3.40}$$

now,

$$\left(\frac{K_{P_{\delta_F}}}{1 - K_{P_{\delta_F}} \frac{\bar{L}_{\delta_F}}{m}}\right) = -\frac{\left(\alpha_0 I_y m^2 \bar{V} + M_Q \bar{L}_\alpha m + M_\alpha m^2 \bar{V}\right)}{\left(M_Q \bar{L}_{\delta_F} \bar{L}_\alpha + M_{\delta_F} \bar{L}_\alpha m \bar{V}\right)} \tag{C.3.41}$$

$$\left(\frac{K_{P_{\delta_F}}}{1}\right) = -\frac{\left(\alpha_0 I_y m^2 \bar{V} + M_Q \bar{L}_\alpha m + M_\alpha m^2 \bar{V}\right)}{\left(M_Q \bar{L}_{\delta_F} \bar{L}_\alpha + M_{\delta_F} \bar{L}_\alpha m \bar{V}\right)} (1 - K_{P_{\delta_F}} \frac{\bar{L}_{\delta_F}}{m})$$

$$K_{P_{\delta_F}} - K_{P_{\delta_F}} \frac{\bar{L}_{\delta_F}}{m} \frac{\left(\alpha_0 I_y m^2 \bar{V} + M_Q \bar{L}_\alpha m + M_\alpha m^2 \bar{V}\right)}{\left(M_Q \bar{L}_{\delta_F} \bar{L}_\alpha + M_{\delta_F} \bar{L}_\alpha m \bar{V}\right)} = -\frac{\left(\alpha_0 I_y m^2 \bar{V} + M_Q \bar{L}_\alpha m + M_\alpha m^2 \bar{V}\right)}{\left(M_Q \bar{L}_{\delta_F} \bar{L}_\alpha + M_{\delta_F} \bar{L}_\alpha m \bar{V}\right)}$$

$$m\left(M_Q \bar{L}_{\delta_F} \bar{L}_\alpha + M_{\delta_F} \bar{L}_\alpha m \bar{V}\right) K_{P_{\delta_F}} - K_{P_{\delta_F}} \bar{L}_{\delta_F} \left(\alpha_0 I_y m^2 \bar{V} + M_Q \bar{L}_\alpha m + M_\alpha m^2 \bar{V}\right) = -\frac{\left(\alpha_0 I_y m^2 \bar{V} + M_Q \bar{L}_\alpha m + M_\alpha m^2 \bar{V}\right)}{\left(M_Q \bar{L}_{\delta_F} \bar{L}_\alpha + M_{\delta_F} \bar{L}_\alpha m \bar{V}\right)} m\left(M_Q \bar{L}_{\delta_F} \bar{L}_\alpha + M_{\delta_F} \bar{L}_\alpha m \bar{V}\right)$$

$$K_{P_{\delta_F}} \left[m\left(M_Q \bar{L}_{\delta_F} \bar{L}_\alpha + M_{\delta_F} \bar{L}_\alpha m \bar{V}\right) - \bar{L}_{\delta_F} \left(\alpha_0 I_y m^2 \bar{V} + M_Q \bar{L}_\alpha m + M_\alpha m^2 \bar{V}\right)\right] = -\left(\alpha_0 I_y m^2 \bar{V} + M_Q \bar{L}_\alpha m + M_\alpha m^2 \bar{V}\right) m$$

$$K_{P_{\delta_F}} = -\frac{\left(\alpha_0 I_y m^2 \bar{V} + M_Q \bar{L}_\alpha m + M_\alpha m^2 \bar{V}\right) m}{\left[m\left(M_Q \bar{L}_{\delta_F} \bar{L}_\alpha + M_{\delta_F} \bar{L}_\alpha m \bar{V}\right) - \bar{L}_{\delta_F} \left(\alpha_0 I_y m^2 \bar{V} + M_Q \bar{L}_\alpha m + M_\alpha m^2 \bar{V}\right)\right]}$$

$$K_{P_{\delta_F}} = -\frac{\alpha_0 I_y m^2 \bar{V} + M_Q \bar{L}_\alpha m + M_\alpha m^2 \bar{V}}{\left(M_Q \bar{L}_{\delta_F} \bar{L}_\alpha + M_{\delta_F} \bar{L}_\alpha m \bar{V}\right) - \bar{L}_{\delta_F} \left(\alpha_0 I_y m \bar{V} + M_Q \bar{L}_\alpha + M_\alpha m \bar{V}\right)}$$

$$K_{P_{\delta_F}} = -\frac{\alpha_0 I_y m^2 \bar{V} + M_Q \bar{L}_\alpha m + M_\alpha m^2 \bar{V}}{M_{\delta_F} \bar{L}_\alpha m \bar{V} - \bar{L}_{\delta_F} \alpha_0 I_y m \bar{V} - \bar{L}_{\delta_F} M_\alpha m \bar{V}}$$

$$K_{P_{\delta_F}} = -\frac{\alpha_0 I_y m \bar{V} + M_Q \bar{L}_\alpha + M_\alpha m \bar{V}}{M_{\delta_F} \bar{L}_\alpha \bar{V} - \bar{L}_{\delta_F} \alpha_0 I_y \bar{V} - \bar{L}_{\delta_F} M_\alpha \bar{V}}$$

$$K_{P_{\delta_F}} = -\frac{\alpha_0 + \frac{M_Q \bar{L}_\alpha}{I_y m \bar{V}} + \frac{M_\alpha}{I_y}}{\frac{M_{\delta_F} \bar{L}_\alpha}{I_y m} - \frac{\bar{L}_{\delta_F} \alpha_0}{m} - \frac{\bar{L}_{\delta_F} M_\alpha}{I_y m}}$$

In summary

The natural frequency of the closed-loop poles is given by,

$$\omega_n = \frac{-\zeta\eta + \sqrt{(\zeta\eta)^2 - \bar{L}_{\delta_F} I_y^2 \left(M_Q^2 \bar{L}_{\delta_F} + M_Q M_{\delta_F} m\bar{V}\right)}}{\bar{L}_{\delta_F} I_y^2} \tag{C.3.42}$$

where,

$$\eta = M_Q \bar{L}_{\delta_F} I_y + M_{\delta_F} I_y m\bar{V} \tag{C.3.43}$$

The flaps feedback gain is give by either,

$$K_{P_{\delta_F}} = \frac{m}{\bar{L}_{\delta_F}} - \frac{\bar{L}_\alpha}{\bar{L}_{\delta_F}\bar{V}\left(2\zeta\omega_n + \frac{M_Q}{I_y}\right)} \tag{C.3.44}$$

or,

$$K_{P_{\delta_F}} = -\frac{\omega_n^2 I_y m\bar{V} + M_Q \bar{L}_\alpha + M_\alpha m\bar{V}}{M_{\delta_F}\bar{L}_\alpha\bar{V} - \bar{L}_{\delta_F}\omega_n^2 I_y\bar{V} - \bar{L}_{\delta_F} M_\alpha \bar{V}} \tag{C.3.45}$$

Pole placement therefore involves choosing a damping ratio ζ, then calculating the resultant natural frequency ω_n and the gain $K_{P_{\delta_F}}$.

C.4 Glide Path Offset

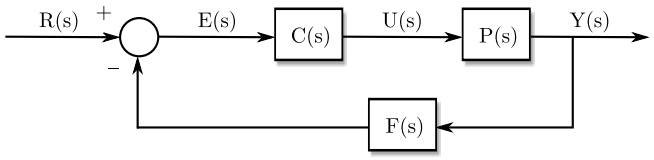

Figure C.1 – Control system block diagram

With reference to Figure C.1 the steady state altitude error is found as follows,

$$\frac{E(s)}{R(S)} = \frac{1}{F(s)P(s)C(s)} \tag{C.4.1}$$

$$= \frac{1}{1 + \frac{\tau_{CR}}{\tau_{CR}s + 1}\frac{1}{s}K_{P_h}} \tag{C.4.2}$$

For a ramp input $r(t) = At$, the final value theorem states,

$$e_{SS} = \lim_{t\to\infty} e(t) = \lim_{s\to 0}\left[s\frac{E(s)}{R(s)}\frac{A}{s^2}\right] \tag{C.4.3}$$

$$= \lim_{s\to 0}\left[s\frac{1}{1 + \frac{\tau_{CR}}{\tau_{CR}s + 1}\frac{1}{s}K_{P_h}}\frac{1}{s^2}\right] \tag{C.4.4}$$

$$= \frac{A}{\tau_{CR}K_{P_h}} \tag{C.4.5}$$

The altitude control is a type one system, therefore the steady state error to a ramp input is given by,

$$e_{SS} = \frac{A}{K_{Vec}} \tag{C.4.6}$$

where $K_{V_{ec}}$ is the velocity error constant. Thus,

$$K_{V_{ec}} = K_{P_h}\tau_{\mathrm{CR}} \tag{C.4.7}$$

where τ_{CR} is the time constant of the dominant closed-loop climb rate dynamics pole and K_{P_h} is the altitude feedback gain.

Appendix D

Additional Flight Test Information

D.1 Helderberg Radio Flyer's Airfield

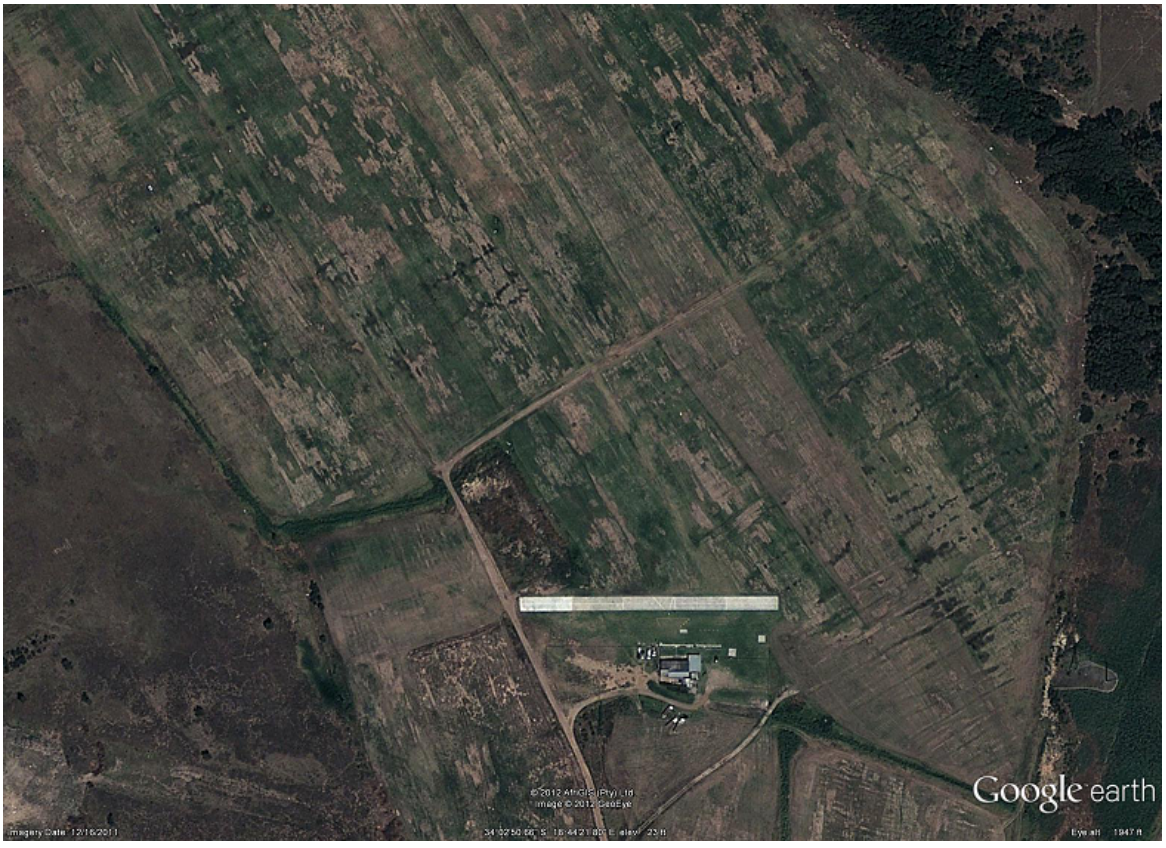

Figure D.1 – Satellite photo of Helderberg Radio Flyers (HRF) airfield. Source: Google Earth

D.2 Windspeed data - 29 November

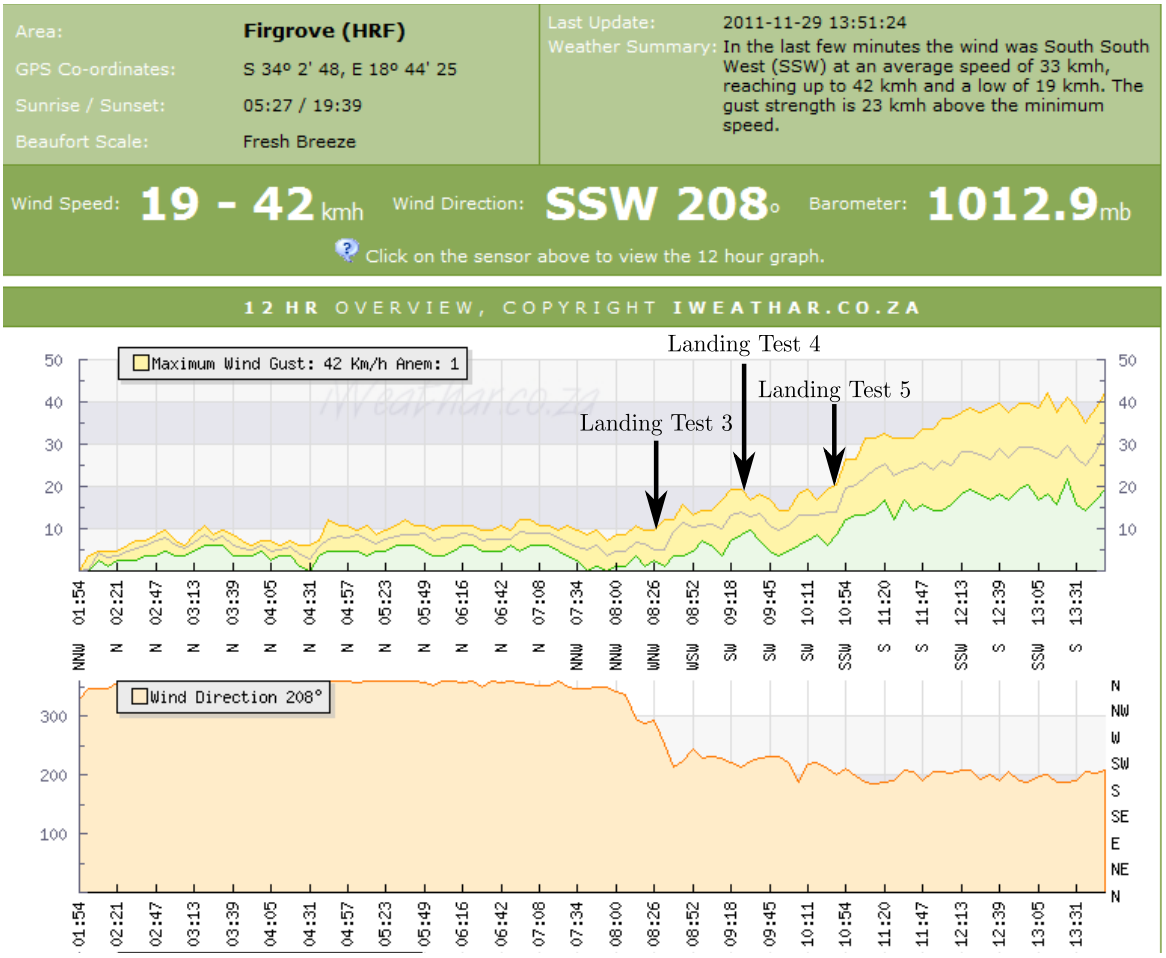

Figure D.2 – Wind speed during Landing Test 3,4 and 5

D.3 Flight Test Cards

D.3.1 Flight Test 1 - 25 July

TEST CARD: Fixed Wing ATOL

UAV: Phoenix

Electronic Systems Laboratory

Test Name:
Flight Test 1
Maiden flight test of the airframe

Test No:	Airframe Flt No:	Location:	Date:
1	n/a	HRF	25 July 2011

Test Coordinator:	Pilot:	Ground Station:	Test Leader:
Lionel Basson	Michael Basson	Nico Alberts	Nico Alberts

Configuration and Status:

This is the maiden flight test of the airframe and will be conducted exclusively under the control of the safety pilot. It serves to verify the airframe from a performance, stability and control perspective.

Restrictions:
Maximum flight time 5 minutes.
No excessive manoeuvres

Notes:

ESL Test Card Page 1 of 2

(a) Page 1 of 2

Take-Off #			1
Test #	*Test Goals*	*Pilot Information*	*Expected Behaviour*
1	Verify the airframe from a performance, stability and control perspective.	Safety Pilot uses best judgement to evaluate the airframe from a performance, stability and control perspective. If any adjustments are required, the aircraft should be landed and the control surfaces or weight distribution adjusted on the ground.	The aircraft will fly as per safety pilot commands

ESL Test Card Page 2 of 2

(b) Page 2 of 2

Figure D.3 – Flight test card - Flight Test 1 - 25 July

D.3.2 Flight Test 2 - 10 August

TEST CARD: Fixed Wing ATOL

UAV: Phoenix

Electronic Systems Laboratory

Test Name:
Flight Test 2
Controller Steps, Airspeed, Climb Rate, Altitude, Roll Angle and Dutch Roll Damper

Test No:	Airframe Flt No:	Location:	Date:
2	n/a	HRF	10 August 2011

Test Coordinator:	Pilot:	Ground Station:	Test Leader:
Lionel Basson	Michael Basson	Nico Alberts	Nico Alberts

Configuration and Status:

Changes since Flight Test 1 – 25 July flight:
None

The previous flight test confirmed the proper functioning of the aircraft, this flight test will commence testing of the controllers

This flight test makes use of the uBlox GPS module. Allowance for the future integration of the NovAtel DGPS unit and antenna has been made through the use of two dummy weights.

Restrictions:

Maximum flight time 5 minutes.
No excessive manoeuvres

Notes:

ESL Test Card Page 1 of 6

(a) Page 1 of 6

Take-Off # **1**

Test #	*Test Goals*	*Pilot Information*	*Expected Behaviour*
1	During this test the airspeed controller is tested. Airspeed Controller Gains set at: a = 0.5 zeta = 0.8	Safety Pilot takes off and engages autopilot on the transmitter **at the start of the FAR long leg** with the aircraft **straight and level** at around 60 m altitude Safety Pilot maintains control over all actuators **except for the throttle** Safety Pilot continues flying a relaxed circuit at **reasonably constant altitude.** Safety Pilot monitors aircraft for any strange behaviour and must retake control if airspeed or altitude become too low/high. Test Leader will inform Safety Pilot that test is complete. Safety Pilot disarms autopilot on the transmitter and takes full control of aircraft. **Land Aircraft:** Soft Landing should consist of a glide followed by a flare and touchdown.	Before takeoff the aircraft must be positioned accurately on the markings on the runway Safety Pilot takes off and engages autopilot on the transmitter **at the start of the FAR long leg** with the aircraft **straight and level** at around 60 m altitude The aircraft will fly as per safety pilot commands except that the airspeed is regulated by the controller Airspeed Controller will be given several references: Leg 1: 20 m/s Leg 2: 16 m/s 13 m/s Leg 3: 16 m/s If aircraft airspeed is judged too high/low Safety Pilot disengages autopilot and stabilises aircraft. Upon completion the Safety Pilot will be informed to retake control of the aircraft and land as close as possible to the take-off point.

ESL Test Card Page 2 of 6

(b) Page 2 of 6

Figure D.4 – Flight test card - Flight Test 2 - 10 August

Take-Off #			**2**
Test #	***Test Goals***	***Pilot Information***	***Expected Behaviour***
2	During this test the airspeed and climb rate controllers are tested concurrently. NSA Controller Gains set at: a = 4 zeta = 0.707 Nbar = 2 ClimbRate Controller Gains set at: Leg1: Kp = -0.5 Airspeed Controller Gains set at: a = 0.5 zeta = 0.8	Safety Pilot takes off and engages autopilot on the transmitter **at the start of the FAR long leg** with the aircraft **straight and level** at around 60 m altitude Safety Pilot maintains control over all actuators **except for throttle and elevator.** Safety Pilot maintains level wings as much as possible for the duration of the leg. Before reaching the end of the leg Safety Pilot disarms the autopilot. Safety Pilot is now in full control to make the turn. When the next leg is entered, the autopilot is armed once more. Safety Pilot monitors aircraft for any strange behaviour and must retake control if airspeed or altitude become too low. Look out for any **pitch oscillation**. Any visible oscillation will likely worsen and the Safety Pilot must **retake control immediately.** Test Leader will inform Safety Pilot that test is complete. Safety Pilot disarms autopilot on the transmitter and takes full control of aircraft. **Land Aircraft:** Soft Landing should consist of a glide followed by a flare and touchdown.	Before takeoff the aircraft must be positioned accurately on the markings on the runway Safety Pilot takes off and engages autopilot on the transmitter **at the start of the FAR long leg** with the aircraft **straight and level** at around 60 m altitude The aircraft will fly as per safety pilot commands except that the airspeed and climb rate is regulated by the controllers during the long legs The following references will be set: Airspeed: 15 m/s throughout Leg 1: Climb Rate: 0 m/s +2m/s Leg 2: Climb Rate: -2m/s 0m/s Upon completion the Safety Pilot will be informed to retake control of the aircraft and land as close as possible to the take-off point.

ESL Test Card Page 3 of 6

(c) Page 3 of 6

Take-Off #			**3**
Test #	***Test Goals***	***Pilot Information***	***Expected Behaviour***
3	During this test the airspeed and altitude controllers are tested concurrently. NSA Controller Gains set at: a = 4 zeta = 0.707 Nbar = 2 ClimbRate Controller Gains set at: Kp = -0.5 Altitude controller gain set at: Kp = 0.5 Airspeed Controller Gains set at: a = 0.5 zeta = 0.8	Safety Pilot takes off and engages autopilot on the transmitter **at the start of the FAR long leg** with the aircraft **straight and level** at around 60 m altitude Safety Pilot maintains control over all actuators **except for throttle and elevator.** Safety Pilot maintains level wings as much as possible for the duration of the leg. Before reaching the end of the leg Safety Pilot disarms the autopilot. Safety Pilot is now in full control to make the turn. When the next leg is entered, the autopilot is armed once more. Safety Pilot monitors aircraft for any strange behaviour and must retake control if airspeed or altitude become too low. Look out for any **pitch oscillation**. Any visible oscillation will likely worsen and the Safety Pilot must **retake control immediately.** Test Leader will inform Safety Pilot that test is complete. Safety Pilot disarms autopilot on the transmitter and takes full control of aircraft. **Land Aircraft:** Soft Landing should consist of a glide followed by a flare and touchdown.	Before takeoff the aircraft must be positioned accurately on the markings on the runway Safety Pilot takes off and engages autopilot on the transmitter **at the start of the FAR long leg** with the aircraft **straight and level** at around 60 m altitude The aircraft will fly as per safety pilot commands except that the airspeed and altitude is regulated by the controllers during the long legs The following references will be set: Airspeed: 15 m/s throughout Leg 1: Altitude Steps: + 25 m Leg 2: Altitude Steps: - 25 m Upon completion the Safety Pilot will be informed to retake control of the aircraft and land as close as possible to the take-off point.

ESL Test Card Page 4 of 6

(d) Page 4 of 6

Figure D.4 – Flight test card - Flight Test 2 - 10 August

Take-Off #			**4**
Test #	***Test Goals***	***Pilot Information***	***Expected Behaviour***
4	During this test the roll angle controller is tested Roll Angle Controller Gains Leg1: Roll Angle Pole = 4 Error Angle Pole = 2	Safety Pilot takes off and engages autopilot on the transmitter **at the start of the FAR long leg** with the aircraft **straight and level** at around 60 m altitude Safety Pilot maintains control over all actuators **except for ailerons.** Safety Pilot maintains altitude as much as possible for the duration of the leg. Before reaching the end of the leg Safety Pilot disarms the autopilot. Safety Pilot is now in full control to make the turn. When the next leg is entered, the autopilot is armed once more. . If the aircraft's roll angle is too high Safety Pilot disengages autopilot and stabilises aircraft Look out for any **roll oscillation**. Any visible oscillation will likely worsen and the Safety Pilot must **retake control immediately** Test Leader will inform Safety Pilot that test is complete. Safety Pilot disarms autopilot on the transmitter and takes full control of aircraft. **Land Aircraft:** Soft Landing should consist of a glide followed by a flare and touchdown.	Before takeoff the aircraft must be positioned accurately on the markings on the runway Safety Pilot takes off and engages autopilot on the transmitter **at the start of the FAR long leg** with the aircraft **straight and level** at around 60 m altitude The aircraft will fly as per safety pilot commands except that the roll angle is regulated by the controllers during the long legs The following references will be set: Leg 1: Roll angle: 0degrees +15 degrees Leg 2: Roll angle: 0degrees -15 degrees Upon completion the Safety Pilot will be informed to retake control of the aircraft and land as close as possible to the take-off point.

ESL Test Card Page 5 of 6

(e) Page 5 of 6

Take-Off #			**5**
Test #	***Test Goals***	***Pilot Information***	***Expected Behaviour***
5	During this test the Dutch Roll Damper is tested DRD Gains set at: DRD Pole = 0.333 DRD Gain = 0.3	Safety Pilot takes off and enters a relaxed circuit at a moderate altitude. Safety Pilot maintains control over all actuators. However, the rudder is also under control of the Dutch Roll Damper. Test Leader will arm the DRD controller and inform Safety Pilot. Safety Pilot engages autopilot on the transmitter **at the start of a long leg** with the aircraft **straight and level.** Safety Pilot maintains level flight as much as possible for the duration of the leg. Perform these tests on the closer leg so that the response can be visually seen. 1st Pass: **Controller disarmed:** Input rudder doublet to excite the Dutch roll, pilot should remember the range of the doublet that he used. 2nd Pass: **Arm controller:** Input rudder doublet to excite the Dutch roll, one should be able to visually see the damped response Upon completion the Safety Pilot will be informed to retake control of the aircraft and land as close as possible to the take-off point. **Land Aircraft:** Soft Landing should consist of a glide followed by a flare and touchdown. Flaps should be in the **middle position**.	Before takeoff the aircraft must be positioned accurately on the markings on the runway The aircraft will fly as per the safety pilot commands and attempt to dampen the dutch roll mode when the autopilot is armed. Upon completion the Safety Pilot will be informed to retake control of the aircraft and land as close as possible to the take-off point.

ESL Test Card Page 6 of 6

(f) Page 6 of 6

Figure D.4 – Flight test card - Flight Test 2 - 10 August

D.3.3 Flight Test 3 - 7 September

TEST CARD: Fixed Wing ATOL

UAV: Phoenix

ESL Electronic Systems Laboratory

Test Name:
Flight Test 3
Controller Steps, Navigation and glide path, Natural Elevator and Flaps response

Test No:	Airframe Flt No:	Location:	Date:
3	n/a	HRF	7 September 2011

Test Coordinator:	Pilot:	Ground Station:	Test Leader:
Lionel Basson	Michael Basson	Nico Alberts	Nico Alberts

Configuration and Status:
Changes since Flight Test 3 – 10 August flight:

None

Restrictions:
Maximum flight time 5 minutes.
No excessive manoeuvres

Notes:

ESL Test Card Page 1 of 6

(a) Page 1 of 6

Take-Off # 1

Test #	Test Goals	Pilot Information	Expected Behaviour
1	During this test the airspeed and climb rate controllers are tested concurrently. NSA Controller Gains set at: a = 4 zeta = 0.707 Nbar = 2 ClimbRate Controller Gains set at: Leg1: Kp = -0.5 Leg2: Kp = -0.5 Leg3: Kp = -0.8 Leg4: Kp = -1.0 Airspeed Controller Gains set at: a = 0.5 zeta = 0.8	Safety Pilot takes off and engages autopilot on the transmitter **at the start of the FAR long leg** with the aircraft **straight and level** at around 60 m altitude Safety Pilot maintains control over all actuators **except for throttle and elevator.** Safety Pilot maintains level wings as much as possible for the duration of the leg. Before reaching the end of the leg Safety Pilot disarms the autopilot. Safety Pilot is now in full control to make the turn. When the next leg is entered, the autopilot is armed once more. Safety Pilot monitors aircraft for any strange behaviour and must retake control if airspeed or altitude become too low. Look out for any **pitch oscillation**. Any visible oscillation will likely worsen and the Safety Pilot must **retake control immediately.** Test Leader will inform Safety Pilot that test is complete. Safety Pilot disarms autopilot on the transmitter and takes full control of aircraft. **Land Aircraft:** Soft Landing should consist of a glide followed by a flare and touchdown.	Before takeoff the aircraft must be positioned accurately on the markings on the runway Safety Pilot takes off and engages autopilot on the transmitter **at the start of the FAR long leg** with the aircraft **straight and level** at around 60 m altitude The aircraft will fly as per safety pilot commands except that the airspeed and climb rate is regulated by the controllers during the long legs The following references will be set: Airspeed: 18 m/s throughout Leg 1: Climb Rate: 0 m/s +3m/s(for 2 seconds) 0 m/s Leg 2: Climb Rate: 0m/s -3m/s(for 2 seconds) 0m/s Leg 3: Climb Rate: 0m/s +3m/s(for 2 seconds) 0m/s Leg 4: Climb Rate: 0m/s -3m/s(for 2 seconds) 0m/s Upon completion the Safety Pilot will be informed to retake control of the aircraft and land as close as possible to the take-off point.

ESL Test Card Page 2 of 6

(b) Page 2 of 6

Figure D.5 – Flight test card - Flight Test 3 - 7 September

Take-Off #			**2**
Test #	***Test Goals***	***Pilot Information***	***Expected Behaviour***
2	During this test the airspeed and altitude controllers are tested concurrently. NSA Controller Gains set at: a = 4 zeta = 0.707 Nbar = 2 ClimbRate Controller Gains set at highest stable from previous test: Kp = -1.0 Altitude Controller Gain set at: Kp = 0.5 Airspeed Controller Gains set at: a = 0.5 zeta = 0.8	Safety Pilot takes off and engages autopilot on the transmitter **at the start of the FAR long leg** with the aircraft **straight and level** at around 60 m altitude Safety Pilot maintains control over all actuators **except for throttle and elevator.** Safety Pilot maintains level wings as much as possible for the duration of the leg. Before reaching the end of the leg Safety Pilot disarms the autopilot. Safety Pilot is now in full control to make the turn. When the next leg is entered, the autopilot is armed once more. Safety Pilot monitors aircraft for any strange behaviour and must retake control if airspeed or altitude become too low. Look out for any **pitch oscillation**. Any visible oscillation will likely worsen and the Safety Pilot must **retake control immediately.** Test Leader will inform Safety Pilot that test is complete. Safety Pilot disarms autopilot on the transmitter and takes full control of aircraft. **Land Aircraft:** Soft Landing should consist of a glide followed by a flare and touchdown.	Before takeoff the aircraft must be positioned accurately on the markings on the runway Safety Pilot takes off and engages autopilot on the transmitter **at the start of the FAR long leg** with the aircraft **straight and level** at around 60 m altitude The aircraft will fly as per safety pilot commands except that the airspeed and altitude is regulated by the controllers during the long legs The following references will be set: Airspeed: 18 m/s throughout Leg 1: Altitude Command: 70 m 60 m Leg 2: Altitude Steps: 60 m 70 m Upon completion the Safety Pilot will be informed to retake control of the aircraft and land as close as possible to the take-off point.

ESL Test Card Page 3 of 6

(c) Page 3 of 6

Take-Off #			**3**
Test #	***Test Goals***	***Pilot Information***	***Expected Behaviour***
3	During this test the roll angle controller is tested Roll Angle Controller Gains Leg1: Roll Angle Pole = 4 Error Angle Pole = 2	Safety Pilot takes off and engages autopilot on the transmitter **at the start of the FAR long leg** with the aircraft **straight and level** at around 60 m altitude Safety Pilot maintains control over all actuators **except for ailerons.** Safety Pilot maintains altitude as much as possible for the duration of the leg. Before reaching the end of the leg Safety Pilot disarms the autopilot. Safety Pilot is now in full control to make the turn. When the next leg is entered, the autopilot is armed once more. . If the aircraft's roll angle is too high Safety Pilot disengages autopilot and stabilises aircraft Look out for any **roll oscillation**. Any visible oscillation will likely worsen and the Safety Pilot must **retake control immediately** Test Leader will inform Safety Pilot that test is complete. Safety Pilot disarms autopilot on the transmitter and takes full control of aircraft. **Land Aircraft:** Soft Landing should consist of a glide followed by a flare and touchdown.	Before takeoff the aircraft must be positioned accurately on the markings on the runway Safety Pilot takes off and engages autopilot on the transmitter **at the start of the FAR long leg** with the aircraft **straight and level** at around 60 m altitude The aircraft will fly as per safety pilot commands except that the roll angle is regulated by the controllers during the long legs The following references will be set: Leg 1: Roll angle: 0degrees +15 degrees(for 3 seconds) 0degrees repeat. Upon completion the Safety Pilot will be informed to retake control of the aircraft and land as close as possible to the take-off point.

ESL Test Card Page 4 of 6

(d) Page 4 of 6

Figure D.5 – Flight test card - Flight Test 3 - 7 September

Take-Off #			**4**
Test #	***Test Goals***	***Pilot Information***	***Expected Behaviour***
4	During this test the navigation controller is tested alongside a glide path NSA Controller Gains set at: a = 4 zeta = 0.707 Nbar = 2 ClimbRate Controller Gains set : Kp = -1.0 Roll Angle Controller Gains Leg1: Roll Angle Pole = 4 Error Angle Pole = 2	Safety Pilot takes off and engages autopilot on the transmitter **at the start of the FAR long leg** with the aircraft **straight and level** at around 60 m altitude Test Leader will arm the Navigation controller and inform Safety Pilot. Safety Pilot engages autopilot on the transmitter **at the start of the FAR long leg** with the aircraft **straight and level** at around 60 m altitude. Safety Pilot **does not** have control over **any actuators.** Safety Pilot monitors aircraft for any strange behaviour and must retake control if airspeed or altitude become too low. The controller can only **bank at 30 degrees**, if a steeper bank angle is judged to be occurring Safety Pilot must retake control. Safety Pilot will be informed if the Navigation Controller becomes disengaged for whatever reason. If this occurs the aircraft will keep flying straight and level indefinitely. Safety Pilot must retake control immediately. The approximate location of the waypoints will be discussed prior to flight. If the aircraft fails to turn when expected safety pilot must retake control. The Aircraft will be allowed to make one full circuit; the **glideslope controller** will then be activated. **No action is required** of the Safety Pilot for the activation. Upon completion the Safety Pilot will be informed to retake control of the aircraft and land as close as possible to the take-off point. **Land Aircraft:** Soft Landing should consist of a glide followed by a flare and touchdown. Flaps should be in the **middle position**.	Before takeoff the aircraft must be positioned accurately on the markings on the runway Safety Pilot takes off and engages autopilot on the transmitter **at the start of the FAR long leg** with the aircraft **straight and level** at around 60 m altitude The aircraft will fly the landing circuit, and on the second pass descend along the glide path. The Aircraft will be allowed to make one full circuit; the **glideslope controller** will then be activated. Setpoints: Airspeed: 18 m/s Altitude: 60 m Glide path height: 30m Upon completion the Safety Pilot will be informed to retake control of the aircraft and land as close as possible to the take-off point.

ESL Test Card Page 5 of 6

(e) Page 5 of 6

Take-Off #			**5**
Test #	***Test Goals***	***Pilot Information***	***Expected Behaviour***
5	During this test the natural response of the elevator and flaps is invetigated NSA Controller Gains set at: a = 4 zeta = 0.707 Nbar = 2 ClimbRate Controller Gains set : Kp = -1.0 Roll Angle Controller Gains Leg1: Roll Angle Pole = 4 Error Angle Pole = 2	Safety Pilot takes off and engages autopilot on the transmitter **at the start of the FAR long leg** with the aircraft **straight and level** at around 60 m altitude Safety Pilot maintains control over all actuators **except for the throttle.** Only the airspeed controller is activated and references between 15 – 18 m/s are set. **Flaps Response:** Safety Pilot flies straight, level and trimmed. Toggle Flaps to Middle position. This is a relatively small flaps deflection so **no elevator mixing will be done. The aircraft must be allowed to pitch naturally** (no change in elevator input). After 2 seconds, or if the pitch angle becomes excessive the flaps may be disengaged. If successfully executed, carry on with the next test. Otherwise repeat. **Elevator Response:** Safety Pilot flies straight, level and trimmed. "Toggle" Elevator. **The aircraft must be allowed to pitch naturally** After 2 seconds, or if the pitch angle becomes excessive the elevator may be returned Upon completion the Safety Pilot will be informed to retake control of the aircraft and land as close as possible to the take-off point. **Land Aircraft:** Soft Landing should consist of a glide followed by a flare and touchdown. Flaps should be in the **middle position**.	Before takeoff the aircraft must be positioned accurately on the markings on the runway Safety Pilot takes off and engages autopilot on the transmitter **at the start of the FAR long leg** with the aircraft **straight and level** at around 60 m altitude The aircraft will fly as per the safety pilot commands and attempt to maintain a constant airspeed Setpoints: Airspeed: 18 m/s Upon completion the Safety Pilot will be informed to retake control of the aircraft and land as close as possible to the take-off point.

ESL Test Card Page 6 of 6

(f) Page 6 of 6

Figure D.5 – Flight test card - Flight Test 3 - 7 September

D.3.4 Flight Test 4 - 20 September

TEST CARD: Fixed Wing ATOL

UAV: Phoenix

Electronic Systems Laboratory

Test Name:
Flight Test 4
Navigation Circuit , climbrate steps and glide path with DLC

Test No:	Airframe Flt No:	Location:	Date:
4	n/a	HRF	20 September 2011

Test Coordinator:	Pilot:	Ground Station:	Test Leader:
Lionel Basson	Michael Basson	Nico Alberts	Nico Alberts

Configuration and Status:
Changes since Flight Test 3 – 7 September 2011 flight:

None

Restrictions:
Maximum flight time 5 minutes.
No excessive manoeuvres

Notes:

ESL Test Card Page 1 of 4

(a) Page 1 of 4

Take-Off # 1

Test #	*Test Goals*	*Pilot Information*	*Expected Behaviour*
1	During this test the navigation controller is tested for both estimators. NSA Controller Gains set at: a = 4 zeta = 0.707 Nbar = 2 DLC Gains set at: Not used ClimbRate Kp = -1.0 Roll Angle Controller Gains Roll Angle Pole = 4 Error Angle Pole = 2	Safety Pilot takes off and engages autopilot on the transmitter **at the start of the FAR long leg** with the aircraft **straight and level** at around 60 m altitude Safety Pilot **does not** have control over **any actuators.** **Waypoint Navigation:** Test Leader will arm the Navigation controller and inform Safety Pilot. Safety Pilot engages autopilot on the transmitter **at the start of the FAR long leg** with the aircraft **straight and level** at around 60 m altitude. It is preferable for the controller to be **engaged at a higher altitude** instead of too low. Safety Pilot monitors aircraft for any strange behaviour and must retake control if airspeed or altitude become too low. The controller can only **bank at 30 degrees**, if a steeper bank angle is judged to be occurring Safety Pilot must retake control. Safety Pilot will be informed if the Navigation Controller becomes disengaged for whatever reason. If this occurs the aircraft will keep flying straight and level indefinitely. Safety Pilot must retake control immediately. The approximate location of the waypoints will be discussed prior to flight. If the aircraft fails to turn when expected safety pilot must retake control. The Aircraft will be allowed to fly **one and a half circuits.** Safety Pilot must land as the aircraft approaches him for the **second time**. The aircraft must be reset on the runway ready for takeoff. Test Leader will then reconfigure the estimator to the triad method and inform Safety Pilot when ready. Safety Pilot takes off as does exactly the same as previously. Test Leader will inform Safety Pilot that test is complete. Safety Pilot disarms autopilot on the transmitter and takes full control of aircraft. **Land Aircraft:** Soft Landing should consist of a glide followed by a flare and touchdown.	Before takeoff the aircraft must be positioned accurately on the markings on the runway Safety Pilot takes off and engages autopilot on the transmitter **at the start of the FAR long leg** with the aircraft **straight and level** at around 60 m altitude The Aircraft will be allowed to fly **one and a half circuits.** At a constant airspeed and altitude. Safety Pilot must land as the aircraft approaches him for the **second time**. Setpoints: Airspeed: 15 m/s Altitude: 50 m Upon completion the Safety Pilot will be informed to retake control of the aircraft and land as close as possible to the take-off point.

ESL Test Card Page 2 of 4

(b) Page 2 of 4

Figure D.6 – Flight test card - Flight Test 4 - 20 September

Take-Off #			**2**
Test #	***Test Goals***	***Pilot Information***	***Expected Behaviour***
2	During this test several climb rate steps will be performed with the DLC controller NSA Controller Gains set at: a = 4 zeta = 0.707 Nbar = 2 DLC Gains set at: Leg1: Kp = 0 CutoffFreq= 4 CCF = 0 Leg2: Kp = 0.2 CutoffFreq= 4 CCF = 0 Leg3: Kp = 0.5 CutoffFreq= 4 CCF = 0 Leg4: Kp = 0.7 CutoffFreq= 4 CCF = 0 Leg4: Kp = 0.7 CutoffFreq= 4 CCF = 0.1 Leg6: Kp = 0.7 CutoffFreq= 4 CCF = 0.15 Leg7: Kp = 0.7 CutoffFreq= 4 CCF = 0.2 Leg8: Kp = 0.7 CutoffFreq= 5 CCF = 0.2 ClimbRate Controller Gains set at: Kp = -1.0 Altitude Controller Gains set at: Kp = 0.5	Safety Pilot takes off and engages autopilot on the transmitter **at the start of the FAR long leg** with the aircraft **straight and level** at around 60 m altitude Safety Pilot maintains control over all actuators **except for throttle, elevator and flaps.** Safety Pilot maintains level wings as much as possible for the duration of the leg. Before reaching the end of the leg Safety Pilot disarms the autopilot. Safety Pilot is now in full control to make the turn. When the next leg is entered, the autopilot is armed once more If aircraft airspeed or altitude is judged too high/low Safety Pilot disengages autopilot and stabilises aircraft. Look out for any **pitch oscillation**. Any visible oscillation will likely worsen and the Safety Pilot must **retake control immediately.** Test Leader will inform Safety Pilot that test is complete. Safety Pilot disarms autopilot on the transmitter and takes full control of aircraft. **Land Aircraft:** Soft Landing should consist of a glide followed by a flare and touchdown	Before takeoff the aircraft must be positioned accurately on the markings on the runway Safety Pilot takes off and engages autopilot on the transmitter **at the start of the FAR long leg** with the aircraft **straight and level** at around 60 m altitude The following references will be set: Airspeed: 15 m/s throughout Leg 1: Climb Rate: 0 m/s +2m/s(for 2 seconds) 0 m/s Leg 2: Climb Rate: 0m/s -2m/s(for 2 seconds) 0m/s Leg 3: Climb Rate: 0m/s +2m/s(for 2 seconds) 0m/s Leg 4: Climb Rate: 0m/s -2m/s(for 2 seconds) 0m/s etc Upon completion the Safety Pilot will be informed to retake control of the aircraft and land as close as possible to the take-off point.

ESL Test Card Page 3 of 4

(c) Page 3 of 4

Take-Off #			**3**
Test #	***Test Goals***	***Pilot Information***	***Expected Behaviour***
3	During this test the navigation controller is enabled, and a glide path followed on the runaway leg NSA Controller Gains set at: a = 4 zeta = 0.707 Nbar = 2 DLC Gains set at: Not used ClimbRate Kp = -1.0 Roll Angle Controller Gains Roll Angle Pole = 4 Error Angle Pole = 2	Safety Pilot takes off and engages autopilot on the transmitter **at the start of the FAR long leg** with the aircraft **straight and level** at around 60 m altitude Safety Pilot **does not** have control over **any actuators.** The aircraft will fly the runway circuit. During the **runway leg**, the **aircraft will descend from 60 m down to 35 m** when it reaches the middle of the runway. Safety Pilot must take control if any **severe climb rate is observed**. The aircraft should be descending at around **2 m/s.** After the middle of the runway is passed, the aircraft will begin to **climb as well as turn left** at the next waypoint. Safety pilot must take control if the **airspeed drops significantly**. The Aircraft will be allowed to fly the circuit until the test time runs out Safety Pilot monitors aircraft for any strange behaviour and must retake control if airspeed or altitude become too low. The controller can only **bank at 30 degrees**, if a steeper bank angle is judged to be occurring Safety Pilot must retake control. Safety Pilot will be informed if the Navigation Controller becomes disengaged for whatever reason. If this occurs the aircraft will keep flying straight and level indefinitely. Safety Pilot must retake control immediately. The approximate location of the waypoints will be discussed prior to flight. If the aircraft fails to turn when expected safety pilot must retake control. Test Leader will inform Safety Pilot that test is complete. Safety Pilot disarms autopilot on the transmitter and takes full control of aircraft. **Land Aircraft:** Soft Landing should consist of a glide followed by a flare and touchdown.	Before takeoff the aircraft must be positioned accurately on the markings on the runway Safety Pilot takes off and engages autopilot on the transmitter **at the start of the FAR long leg** with the aircraft **straight and level** at around 60 m altitude The aircraft will fly the runway circuit. During the **runway leg**, the **aircraft will descend from 60 m down to 35 m** when it reaches the middle of the runway. Setpoints: Airspeed: 15 m/s Altitude: 60 m Upon completion the Safety Pilot will be informed to retake control of the aircraft and land as close as possible to the take-off point.

ESL Test Card Page 4 of 4

(d) Page 4 of 4

Figure D.6 – Flight test card - Flight Test 4 - 20 September

D.3.5 Flight Test 5 - 25 November

TEST CARD: Fixed Wing ATOL using DGPS

UAV: Phoenix

Electronic Systems Laboratory

Test Name:
Flight Test 5
DGPS confirmation through manual and automated flight

Test No:	Airframe Flt No:	Location:	Date:
5	n/a	HRF	25 November 2011

Test Coordinator:	Pilot:	Ground Station:	Test Leader:
Lionel Basson	Michael Basson	Nico Alberts	Nico Alberts

Configuration and Status:
Changes since Flight Test 4 – 20 September 2011 flight:

The uBlox GPS has been disabled. The DGPS dummy weights were removed and replaced with a NovAtel OEMV1-G rover and NovAtel antenna. The total mass, and balance of the aircraft are as before.

The introduction of the differential GPS has introduced a large number of changes to the way GPS is processed by the avionics. It has been tested in practical ground tests as well as HIL simulations. This flight test will confirm that the DGPS is functioning properly and that the EKF performs well. Automated flights will then be conducted.

Restrictions:
Maximum flight time 5 minutes.
No excessive manoeuvres

Notes:

ESL Test Card Page 1 of 4

(a) Page 1 of 4

Take-Off #			1
Test #	***Test Goals***	***Pilot Information***	***Expected Behaviour***
1	This flight will be RC only since it is the first flight with the NovAtel DGPS system. The main goals are to confirm: that the airframe is still in good flying condition avionics subsystems are fully operational in flight conditions that the DGPS system maintains the L1 integer solution for the entire flight envelope. that the EKF is functional in flight conditions.	The aircraft will be under safety pilot control for the entire test. No aggressive manoeuvres. Pilot should take off and fly a relaxed circuit at a moderate airspeed. After 5 minutes of flight the test should be concluded with a landing as close as possible to the take-off point.	Before takeoff the aircraft must be positioned accurately on the markings on the runway Since no AP will be armed during this test the behaviour is dictated by the safety pilot. After landing the aircraft must once again be positioned accurately on the markings on the runway to confirm the functioning of the estimator

ESL Test Card Page 2 of 4

(b) Page 2 of 4

Figure D.7 – Flight test card - Flight Test 5 - 25 November

Take-Off #			**2**
Test #	***Test Goals***	***Pilot Information***	***Expected Behaviour***
2	The Navigation controllers will be armed if the NovAtel system performed reliably in the previous test: Had continuous L1 Int fix Maintained well bounded sigmas (2cm for lat/lon, 4cm for altitude). The aircraft will fly the navigation loop until the test time runs out During this time several airspeed and altitude steps will be performed. NSA Controller Gains set at: a = 4 zeta = 0.707 Nbar = 2 DLC Gains set at: Kp = 0.02 CutoffFreq. = 4 CCF = 0.2 ClimbRate Controller Gains set at: Kp = -1.0 Altitude Controller Gains set at: Kp = 0.5	Safety Pilot takes off and engages autopilot on the transmitter **at the start of the FAR long leg** with the aircraft **straight and level** at around 60 m altitude Safety Pilot **does not** have control over **any actuators.** Safety Pilot monitors aircraft for any strange behaviour and must retake control if airspeed or altitude become too low. The controller can only **bank at 30 degrees**, if a steeper bank angle is judged to be occurring Safety Pilot must retake control. Safety Pilot will be informed if the Navigation Controller becomes disengaged for whatever reason. If this occurs the aircraft will keep flying straight and level indefinitely. Safety Pilot must retake control immediately. The approximate location of the waypoints will be discussed prior to flight. If the aircraft fails to turn when expected safety pilot must retake control. When the Direct-Lift flaps controller is armed the pitch behaviour of the aircraft must be closely observed. Safety Pilot must retake control immediately if any oscillations are seen.	Before takeoff the aircraft must be positioned accurately on the markings on the runway Safety Pilot takes off and engages autopilot on the transmitter **at the start of the FAR long leg** with the aircraft **straight and level** at around 60 m altitude After the autopilot has been armed the aircraft will begin to fly a navigation circuit at an altitude of 50 m and an airspeed of 18 m/s During this time the following steps will be performed. Airspeed: 18 m/s 15m/s 18 m/s Altitude: 55m 50m 55m 50m The Direct-Lift flaps controller will now be engaged and the following steps performed: **Pay close attention to aircraft pitch behaviour at this point** Altitude: 55m 50m 55m 50m More steps will be performed should time remain. For all runway legs, note the aircraft's path **offset from the middle of the runway** and inform test leader Upon completion the Safety Pilot will be informed to retake control of the aircraft and land as close as possible to the take-off point. After landing the aircraft must once again be positioned accurately on the markings on the runway to confirm the functioning of the estimator

ESL Test Card Page 3 of 4

(c) Page 3 of 4

Take-Off #			**3**
Test #	***Test Goals***	***Pilot Information***	***Expected Behaviour***
3	The Navigation + Landing Path controllers will be armed if the : NovAtel system performed reliably in the previous test: Had continuous L1 Int fix Maintained well bounded sigmas (2cm for lat/lon, 4cm for altitude). Analysis of the previous flight's data showed proper operation of the DLC controller The aircraft will fly the navigation loop until the test time runs out During this time mock landing paths will be flown on the runway leg of the circuit. NSA Controller Gains set at: a = 4 zeta = 0.707 Nbar = 2 DLC Gains set at: Kp = 0.02 CutoffFreq. = 4 CCF = 0.2 ClimbRate Controller Gains set at: Kp = -1.0 Altitude Controller Gains set at: Kp = 0.5	Safety Pilot takes off and engages autopilot on the transmitter **at the start of the FAR long leg** with the aircraft **straight and level** at around 60 m altitude Safety Pilot **does not** have control over **any actuators.** Safety Pilot monitors aircraft for any strange behaviour and must retake control if airspeed or altitude become too low. The controller can only **bank at 30 degrees**, if a steeper bank angle is judged to be occurring Safety Pilot must retake control. Safety Pilot will be informed if the Navigation Controller becomes disengaged for whatever reason. If this occurs the aircraft will keep flying straight and level indefinitely. Safety Pilot must retake control immediately. The approximate location of the waypoints will be discussed prior to flight. If the aircraft fails to turn when expected safety pilot must retake control.	Before takeoff the aircraft must be positioned accurately on the markings on the runway Safety Pilot takes off and engages autopilot on the transmitter **at the start of the FAR long leg** with the aircraft **straight and level** at around 60 m altitude After the autopilot has been armed the aircraft will begin to fly a navigation circuit at an altitude of **50 m** and an airspeed of 18 m/s During each runway leg the aircraft will descend down a glide slope of 7 degrees initially and 3 degrees finally until it reaches an altitude of around **20 m**. This will occur in the vicinity of the takeoff position markings. GlidePath origin set as: **--20 m** For all runway legs, note the aircraft's path **offset from the middle of the runway** and inform test leader Circuits will be flown until test time expires. Upon completion the Safety Pilot will be informed to retake control of the aircraft and land as close as possible to the take-off point. After landing the aircraft must once again be positioned accurately on the markings on the runway to confirm the functioning of the estimator

ESL Test Card Page 4 of 4

(d) Page 4 of 4

Figure D.7 – Flight test card - Flight Test 5 - 25 November

D.3.6 Flight Test 6 - 28 November

TEST CARD: Fixed Wing ATOL using DGPS

UAV: Phoenix

Electronic Systems Laboratory

Test Name:
Flight Test 6
Landing Approach flights with the possibility of full landing

Test No:	Airframe Flt No:	Location:	Date:
6	n/a	HRF	28 November 2011

Test Coordinator:	Pilot:	Ground Station:	Test Leader:
Lionel Basson	Michael Basson	Nico Alberts	Nico Alberts

Configuration and Status:
Changes since Flight Test 5 – November 25 2011 flight:

None

Restrictions:
Maximum flight time 5 minutes.
No excessive manoeuvres

Notes:

ESL Test Card Page 1 of 2

(a) Page 1 of 2

Take-Off # **1**

Test #	Test Goals	Pilot Information	Expected Behaviour
1	The Navigation + Landing controllers will be armed if the NovAtel system performed reliably in the previous test: Had continuous L1 Int fix Maintained well bounded sigmas (2cm for lat/lon, 4cm for altitude). Analysis of the previous flight's data showed good glide path following. The aircraft will fly the navigation loop until the test time runs out During this time mock landing paths will be flown on the runway leg of the circuit. The height of the mock landings will be adjusted downward for a low level flyby. During this flyby the pitch angle, descent rate, roll angle, offset from the middle of the runway and environmental factors will be judged by the Safety Pilot. A landing will only be attempted if the Safety Pilot feels comfortable with the above factors. NSA Controller Gains set at: a = 4 zeta = 0.707 Nbar = 2 DLC Gains set at: DLC not enabled ClimbRate Controller Gains set at: Kp = -1.0 Altitude Controller Gains set at: Kp = 0.5	Safety Pilot takes off and engages autopilot on the transmitter **at the start of the FAR long leg** with the aircraft **straight and level** at around 60 m altitude Safety Pilot **does not** have control over **any actuators.** Safety Pilot monitors aircraft for any strange behaviour and must retake control if airspeed or altitude become too low. The controller can only **bank at 30 degrees**, if a steeper bank angle is judged to be occurring Safety Pilot must retake control. Safety Pilot will be informed if the Navigation Controller becomes disengaged for whatever reason. If this occurs the aircraft will keep flying straight and level indefinitely. Safety Pilot must retake control immediately. The approximate location of the waypoints will be discussed prior to flight. If the aircraft fails to turn when expected safety pilot must retake control. The height of the mock landings will be adjusted downward for a low level flyby. During this flyby the pitch angle, descent rate, roll angle, offset from the middle of the runway and environmental factors must be judged by the Safety Pilot. A landing will only be attempted if the Safety Pilot feels comfortable with the above factors. During a landing the aircraft will **NOT flare**, the Safety Pilot should therefore judge the above parameters accordingly. During landing, the aircraft will strike the runway at the **takeoff markings.** **The instant that the aircraft strikes the runway the Safety Pilot must retake control.** The Safety Pilot should then either complete the landing, or take off again if landing is not feasible.	Before takeoff the aircraft must be positioned accurately on the markings on the runway Safety Pilot takes off and engages autopilot on the transmitter **at the start of the FAR long leg** with the aircraft **straight and level** at around 60 m altitude After the autopilot has been armed the aircraft will begin to fly a navigation circuit at an altitude of **40 m** and an airspeed of 18 m/s During each runway leg the aircraft will descend down a glide slope of 7 degrees initially and 3 degrees finally until it reaches an altitude of around **10 m**. This will occur in the vicinity of the takeoff position markings. GlidePath origin set as: **--10 m** If **adjustments** need to be made based on Safety Pilot feedback the circuit is flown again and re-checked. If the feedback from the Safety Pilot is good, the approach height is lowered for the next circuit. GlidePath origin set as: **--5 m** **IF** the Safety Pilot feels comfortable with a landing attempt: GlidePath origin set as: **+1.3 m and +1.5m** During a landing the aircraft will **NOT flare,** it will strike the runway close to the **takeoff markings.** **The instant that the aircraft strikes the runway the Safety Pilot must retake control.** The Safety Pilot should then either complete the landing, or take off again if landing is not feasible.

ESL Test Card Page 2 of 2

(b) Page 2 of 2

Figure D.8 – Flight test card - Flight Test 6 - 28 November

D.3.7 Flight Test 7 - 29 November

TEST CARD: Fixed Wing ATOL using DGPS

UAV: Phoenix

Electronic Systems Laboratory

Test Name:
Flight Test 7
Autonomous Landing

Test No:	Airframe Flt No:	Location:	Date:
7	n/a	HRF	29 November 2011

Test Coordinator:	Pilot:	Ground Station:	Test Leader:
Lionel Basson	Michael Basson	Nico Alberts	Nico Alberts

Configuration and Status:

No changes since Flight Test 6 – 28 November 2011.

Restrictions:

Maximum flight time 5 minutes.
No excessive manoeuvres

Notes:

ESL Test Card Page 1 of 2

(a) Page 1 of 2

Take-Off # **1**

Test #	*Test Goals*	*Pilot Information*	*Expected Behaviour*
1	During the previous flight test a successful autonomous landing was performed. During this test several more such landings will be attempted. The aircraft will fly the navigation loop and perform mock landing flybys until either the test time runs out, or an autonomous landing is performed. The height of the mock landings will be adjusted downward for a low level flyby. During this flyby the pitch angle, descent rate, roll angle, offset from the middle of the runway and environmental factors will be judged by the Safety Pilot. A landing will only be attempted if the Safety Pilot feels comfortable with the above factors. NSA Controller Gains set at: a = 4 zeta = 0.707 Nbar = 2 DLC Gains set at: Kp = 0.02 CutoffFreq. = 4 CCF = 0.2 ClimbRate Controller Gains set at: Kp = -1.0 Altitude Controller Gains set at: Kp = 0.5	Safety Pilot takes off and engages autopilot on the transmitter **at the start of the FAR long leg** with the aircraft **straight and level** at around 60 m altitude Safety Pilot **does not** have control over **any actuators.** Safety Pilot monitors aircraft for any strange behaviour and must retake control if airspeed or altitude become too low. The controller can only **bank at 30 degrees**, if a steeper bank angle is judged to be occurring Safety Pilot must retake control. Safety Pilot will be informed if the Navigation Controller becomes disengaged for whatever reason. If this occurs the aircraft will keep flying straight and level indefinitely. Safety Pilot must retake control immediately. The approximate location of the waypoints will be discussed prior to flight. If the aircraft fails to turn when expected safety pilot must retake control. The height of the mock landings will be adjusted downward for a low level flyby. During this flyby the pitch angle, descent rate, roll angle, offset from the middle of the runway and environmental factors must be judged by the Safety Pilot. A landing will only be attempted if the Safety Pilot feels comfortable with the above factors. . **The instant that the aircraft strikes the runway the Safety Pilot must retake control.** The Safety Pilot should then either complete the landing, or take off again if landing is not feasible.	Before takeoff the aircraft must be positioned accurately on the markings on the runway Safety Pilot takes off and engages autopilot on the transmitter **at the start of the FAR long leg** with the aircraft **straight and level** at around 60 m altitude After the autopilot has been armed the aircraft will begin to fly a navigation circuit at an altitude of **40 m** and an airspeed of either 18 m/s or 16 m/s During each runway leg the aircraft will descend down a glide slope of 7 degrees initially and 3 degrees finally until it reaches the **GlidePath origin height**. This will occur in the vicinity of the takeoff position markings. The GlidePath origin set as: **--20 m** or **-- 5 m** The aircraft will perform a low level flyby of the runway. If **adjustments** need to be made based on Safety Pilot feedback the circuit is flown again and re-checked. **IF** the Safety Pilot feels comfortable with a landing attempt: GlidePath origin set as: **+1.5 m** This will cause the aircraft to land approximately **20m from the takeoff markings** GlidePath origin set as: **+2 m** This will cause the aircraft to strike the runway close to the **takeoff markings.** **The instant that the aircraft strikes the runway the Safety Pilot must retake control.** The Safety Pilot should then either complete the landing, or take off again if landing is not feasible.

ESL Test Card Page 2 of 2

(b) Page 2 of 2

Figure D.9 – Flight test card - Flight Test 7 - 29 November

Bibliography

[1] Gaum, D.R.: *Aggressive Flight Control Techniques for a Fixed-Wing Unmanned Aerial Vehicle*. Master's thesis, Stellenbosch University, 2009.

[2] Peddle, I.K.: *Acceleration Based Manoeuvre Flight Control System for Unmanned Aerial Vehicles*. Ph.D. thesis, Stellenbosch University, 2008.

[3] Park, S.: *Avionics and Control System Development for Mid-Air Rendezvous of Two Unmanned Aerial Vehicles*. Ph.D. thesis, Massachusetts Institute of Technology, 2004.

[4] Peddle, I.K.: *Autonomous Flight of a Model Aircraft*. Master's thesis, Stellenbosch University, 2005.

[5] Roos, J.-C.: *Autonomous Take-Off and Landing of a Fixed Wing Unmanned Aerial Vehicle*. Master's thesis, Stellenbosch University, 2007.

[6] Hough, W.: *Autonomous Aerobatic Flight of a Fixed Wing Unmanned Aerial Vehicle*. Master's thesis, Stellenbosch University, 2007.

[7] Visser, B.J.: *Die Presisie Landing van 'n Onbemande Vliegtuig "The Precision Landing of an Unmanned Aircraft"*. Master's thesis, Stellenbosch University, 2008.

[8] Blaauw, D.: *Flight Control System for a Variable Stability Blended-Wing-Body Unmanned Aerial Vehicle*. Master's thesis, Stellenbosch University, 2009.

[9] de Hart, R.D.: *Advanced Take-Off and Flight Control Algorithms for Fixed Wing Unmanned Aerial Vehicles*. Master's thesis, Stellenbosch University, 2010.

[10] Basson, W.A.: *Fault Tolerant Adaptive Control of an Unmanned Aerial Vehicle*. Master's thesis, Stellenbosch University, 2011.

[11] Jeffrey, C.: *An Introduction to GNSS GPS, GLONASS, Galileo and other Global Navigation Satellite Systems*. First edition edn. NovAtel Inc., 2010.

[12] Pinsker, W.J.G.: The control characteristics of aircraft employing direct-lift control. Tech. Rep., Aerodynamics Dept., R.A.E., Bedford, 1970.

[13] Cook, M.V.: *Flight Dynamics Principles*. 2nd edn. Elsevier Ltd., 2007.

[14] Etkin, B. and Reid, L.D.: *Dynamics of Flight Stability and Control*. 3rd edn. John Wiley & Sons, Inc., 1996.

[15] Zipfel, P.H.: *Modeling and Simulation of Aerospace Vehicle Dynamics*. American Institute of Aeronautics and Astronautics Inc., 2000.

[16] Koen, M.: Modelling and simulation of an rpv for flight control system design purposes. *Department of Electronic and Computer Engineering, University of Pretoria*, 2006.

[17] Blakelock, J.: *Automatic Control of Aircraft and Missiles*. 2nd edn. JohnWiley & Sons, 1991.

[18] Gerrits, M.: *Direct Lift Control for the Cessna Citation II*. Master's thesis, Eindhoven University of Technology, 1994.

[19] Fitzgerald, P.: *Flight Control System Design for Autonomous UAV Landing*. Ph.D. thesis, Cranfield University, 2004.

[20] *Airplane Flying Handbook*. U.S. Department of Transportation, Federal Aviation Adminstration, Airman Testing Standards Branch, 2004.

[21] Smit, P.E.: *Development of a 3-DOF Motion Simulation Platform*. Master's thesis, Stellenbosch University, 2010.

[22] de Jager, A.M.: *The design and implementation of vision-based autonomous rotorcraft landing*. Master's thesis, Stellenbosch University, 2011.